A Validated Computational Fluid Dynamics Methodology for Characterisation of Fluid Flow & Heat Transfer in Unsteady Jets

Trinity
College
Dublin
The University of Dublin

by

Sajad Alimohammadi

A dissertation submitted to the University of Dublin for the Degree of Doctor of Philosophy. Department of Mechanical & Manufacturing Engineering, Trinity College, Dublin, Dublin 2.

February 2016

Declaration

I declare that this thesis has not been submitted as an exercise for a degree at this or any other university and it is entirely my own work.

I agree to deposit this thesis in the University's open access institutional repository or allow the library to do so on my behalf, subject to Irish Copyright Legislation and Trinity College Library conditions of use and acknowledgement..

Signed,

Sajad Alimohammadi,

February 2015

Abstract

To improve reliability and avoid premature failure in electronic devices, more effective techniques must be used to dissipate the heat generated by devices. Thermal simulations can enable engineers to investigate and verify appropriate techniques at a very early stage of the design of the electronic device. It helps to improve cooling techniques by providing a visual representation of the complicated heat dissipation phenomenon inside the device. Due to high heat transfer coefficients and the enhanced efficiency, impinging jets are known as a desirable method of heat removal. This thesis reports on a comprehensive project which aimed to establish and validate a robust yet low-cost computational fluid dynamics (*CFD*) methodology to predict the fluid flow and heat transfer of steady and unsteady impinging jets, using in-house detailed experimental measurements for validation. A major focus in this study is on improving the accuracy of unsteady heat transfer simulations. This is done through three major stages, namely, steady jets, pulsating jets, and synthetic jets. The idea is to investigate these three stages considering the incremental progression of complexity in the flow configurations. This can lead to a modelling methodology which is capable of handling a wide range of application and conditions, e.g. steady or unsteady jets, free or impinging jets, and fixed or moving geometries. For steady jets, one of the main goals is to show that the model is valid for a wide range of operational and geometrical parameters, while keeping the computational cost low. The motivation in the second stage for pulsating jets is to characterise the stagnation and area-averaged enhancements (or degradations) in convective heat transfer rate achieved by an unsteady flow such as pulsating jet, when compared to a steady jet, for an extended range of operating conditions. The results is analysed in terms of the effect of different key parameters. This is accomplished by developing fitted correlations as functions of groups of modified dimensionless numbers that best collapse the averaged and stagnation heat transfer enhancement. At the final stage, the most complicated case of unsteady synthetic jet with a moving geometry is studied. The formation, evolution and interaction of a pair of adjacent synthetic jets is investigated numerically using computational fluid dynamics and experimentally using particle image velocimetry (*PIV*). Full jet cavity simulations incorporating the diaphragm motion is performed using Mesh Deformation techniques. The results for both cases of phase-locked and out-of-phase jet flows are compared versus *PIV* measurements. This leads to a better understanding of the fluid mechanics of adjacent synthetic jets and delivers a theoretical basis to be used in the future for their application.

Acknowledgement

I would like to thank all of those who have provided me with assistance in my research throughout the first stage of my PhD program. This work would not have been possible without the help and support of the following people.

Foremost, I would like to especially thank my Supervisors, Prof. Darina B. Murray and Dr. Tim Persoons for sharing their knowledge, and for their constant support, generosity and willingness to help me with my research objectives. I could not have imagined having a better advisors and mentors for my PhD study.

I wish to express my sincere thanks to for the financial support of my School of Engineering Studentship provided through various exciting projects I have worked on during the course of the PhD with research groups of Dr. Tony Robinson and Dr. Gareth Bennett, lecturers in the Department of Mechanical and Manufacturing Engineering at Trinity College Dublin, and Prof. Suresh V. Garimella, the director of Cooling Technologies Research Centre at Purdue University, USA. Also I would like to thank Dr. Bennett as the internal examiner of my confirmation report.

I thank Mick Reilly, Gerry Byrne, and John Gaynor for their technical and administrative assistance.

To my fellow researchers: Eoin Fanning, Seamus Michael O Shaughnessy, Cian Quinn, Diarmuid Jackson, Rudi O'Reilly Meehan, Daniel Keogh, Quentin Pelletier, Alberto Pellegrino, Kevin Tarrant, Kun Zhao and Jason Botha, for the stimulating discussions and support, and for all the enjoyable moments we have had in the last three years.

Last but not least, I would like to thank my family: my wife Sepideh for her love, encouragement and constant support, and my parents and my sister and brother for their many years of support and unwavering faith in me.

Table of Contents

Nomenclature

A	surface area, m^2
D	nozzle pipe inner diameter, m
f	pulsation frequency, Hz
f_h	Helmholtz resonance frequency, Hz
h	heat transfer coefficient, W/(m$^{2}\cdot$K)
H	nozzle-to-impingement surface spacing, m
H_C	cavity height, m
k	turbulent kinetic energy, m^2/s^2 and thermal conductivity, W/(m.K)
K	jet orifice damping coefficient
Nu	local Nusselt number
Nu_0	stagnation Nu
$\overline{Nu}$	area-averaged Nu
L	nozzle length, m
L'	effective jet orifice length, m
L_o	stroke length, m
Pr	Prandtl number
Pr_t	turbulent Prandtl Number
q	local convective heat flux, W/m^2
r_C	cavity or speaker radius, m
Re	Reynolds number
$\tilde{R}e_{\theta t}$	local transition onset momentum thickness Reynolds number
S	strain rate tensor modulus, 1/s
Sr	Strouhal number, fD/U_m
T	local surface temperature, K
T_{ref}	fluid temperature in jet nozzle, K
Tu	local turbulence intensity, %
t_{pipe}	nozzle pipe wall thickness, m
U	local velocity magnitude, m/s
U_m	mean flow velocity, m/s

u_j	velocity vector, m/s
u, v	radial, axial velocity components, m/s
u', v'	radial and axial fluctuating u and v, m/s
x, r	axial and radial coordinate (main flow), m
y	normal distance from the wall, m
y^+	non-dimensional distance from the wall
	Greek letters
Δ_A, ε_A	absolute and relative uncertainty on quantity A
β	acoustic radiation end correction
ρ	density of fluid, kg/m^3
γ	intermittency
α_N	vectoring angle, °
$\delta\emptyset$	left and right jet phase angles, °
υ	kinematic viscosity of fluid, m^2/s
μ	molecular viscosity, kg/(m.s)
μ_t	turbulent viscosity, kg/(m.s)
ω	specific turbulence dissipation rate, 1/s
ω_z	vorticity, normal to {x,r} plane, 1/s
Ω	vorticity tensor modulus, 1/s
	Subscripts
0	stagnation point
T	transition onset
θ	momentum thickness

List of Figures

List of Tables

1 Introduction

1.1 Introduction

Data centres are massive facilities, which reportedly number more than 3 million worldwide and account for up to 1.5% of global electricity use (Fig. 1-1).

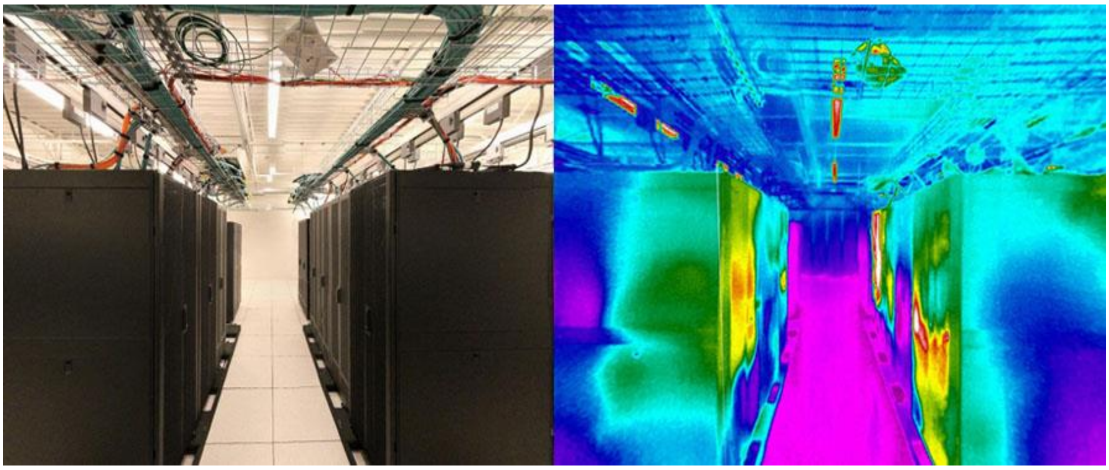

Figure 1-1. Data centre IR infrared thermal mapping (produced by DataCentIR™)

As shown in Fig. 1-2, in a broad review of the energy usage of the information technology (IT) industry, Garimella et al. [1] have reported that combined worldwide electricity consumption of data centres has increased from 71 billion kWh per year (in 2000) to approximately 238 billion kWh per year (in 2010). This accounts for a growth of almost 11% per year over the last decade. There is an essential demand for realisable energy management for these systems.

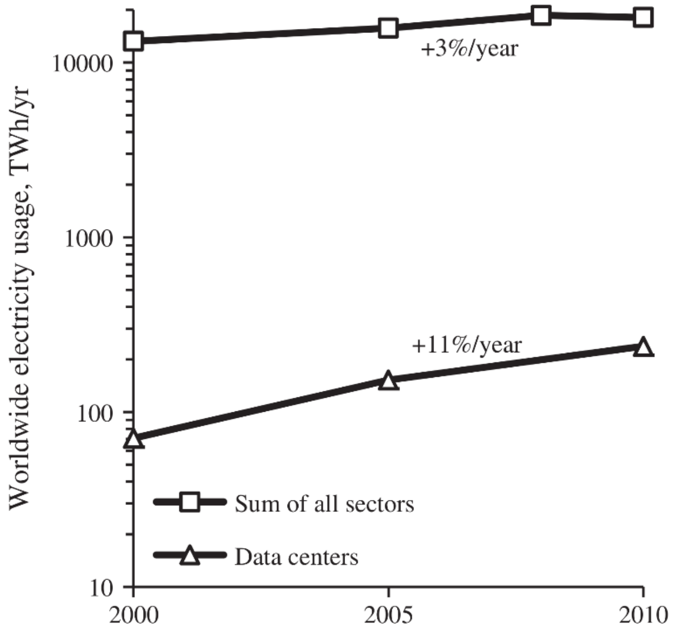

Figure 1-2. Variation of the global electricity usage compared to the sum of all sectors [1]

In a traditional air-cooled data centre a significant portion of this energy is used to cool the equipment so it does not overheat and fail. This poses huge opportunities for energy savings (Fig. 1-3).

Increased awareness about the energy consumption of data centres and telecommunication systems have made electronics thermal management a very active research field. Research activities cover a wide range of cooling techniques, from high density heat transport and two-phase convection systems, to high and moderate density cooling using forced liquid and air convection in micro-structured heat sinks. Impinging jets, consisting of fluid issued from a nozzle hitting a solid surface, can achieve high local heat transfer rates [1]-[2].

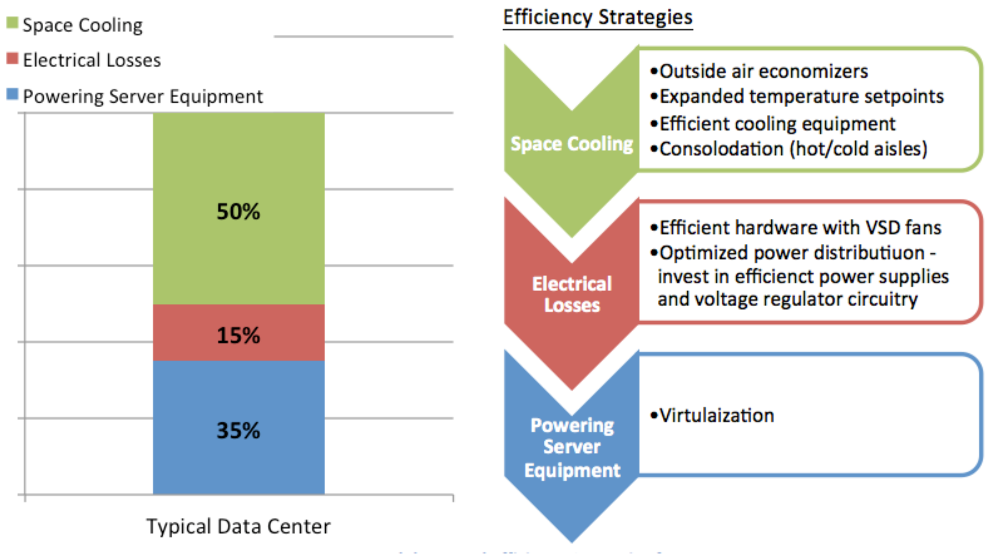

Figure 1-3. Energy use breakdown and efficiently strategies for data centres (produced by Schneider Electric's Data Centre Science Centre)

1.2 Impinging jets

Impinging jets have been used in many cooling/heating engineering applications, including cooling of electronic devices and turbine blades, de-icing of aircraft, and drying of textiles, among many others.

An impinging jet on a flat surface can be classified into different regions as specified in Fig. 1-4. In theory Schlichting et al. [3] and Jambunathan et al. [4] have defined them as follows:

- **Potential core**

This is the core of the jet which remains unaffected by the surrounding fluid; the velocity profile is identical to that of the jet exiting the nozzle and the turbulence intensity is low [5].

- **Shear layer**

The shear layer is where the turbulence of the jet fluid is much higher than that in the centre, entraining fluid from the ambient surroundings and causing a reduction in jet velocity. This entrainment also leads to the radial expansion of the jet. O'Donovan and

Murray [5]-[6] and Schlichting et al. [1] demonstrate this proportional reduction in centreline jet velocity with the distance from the end of the potential core.

- **Free Jet Region**

The shear layer will continue to grow and develop as the jet moves further away from the nozzle eventually enveloping the potential core. This results in reduced jet velocity and increased turbulence intensity.

- **Stagnation Zone**

The stagnation point is the point where the mean velocity of the jet is equal to zero and there is a rise in static pressure. This region is also referred to as the deflection zone as it is here that the jet is deflected radially along the surface. This may also be referred to as the impingement region.

- **Wall Jet Region**

In this region the local jet velocity increases, resulting in a maximum jet velocity at the wall reducing proportionally to the distance from the wall. Due to the increase in turbulence caused by the shear layer between the ambient air and the wall jet, there is more heat transfer in this region. This increased turbulence makes its way to the boundary layer at the wall. Again, the entrainment of the ambient air causes this wall jet to expand and reduce in velocity, but increase in flow area.

The dramatic increase in turbulence in the wall jet region allows for more heat transfer to take place [4]. This is summarised by Pakhomov and Terekhov [7] who state that the main features of impinging jets are thinner hydrodynamic and thermal boundary layers and increased turbulence.

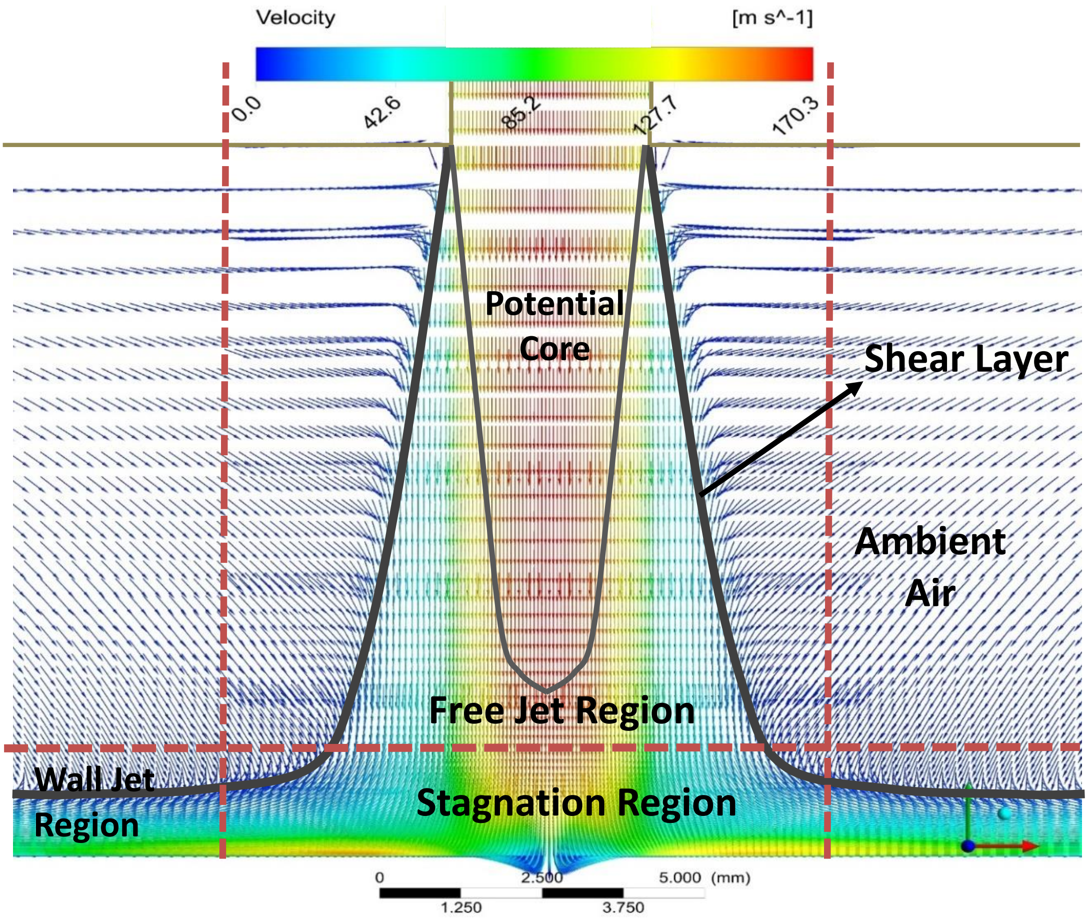

Figure 1-4. Classification of distinct regions of an impinging jet on a flat surface (velocity vectors from *CFD* simulations results on an axisymmetric steady air jet; chapter 4)

Impinging jets have been chosen as the basis of this study, due to their remarkable flow characteristics and their influence on heat transfer. To conduct a fundamental investigation of the complex fluid flow and heat transfer mechanisms of the jets, the first step is to perform a comprehensive review of the previous research studies performed in this field.

2 Literature Review

The present study focuses mainly on convective heat transfer of steady and unsteady jets, with an exclusive attention into the fluid mechanics of the jets. The emphasis is mainly on the development of the numerical model, and presenting detailed experimental results to allow for validation of the modelling technique.

Jet impingement is widely used in applications for high heat flux cooling like gas turbine blades and high-density electronic equipment, so its heat transfer performance has been the subject of many studies both numerically and experimentally in the last decades, [8]-[13].

2.1 Steady jets

Some studies have experimentally examined the heat transfer to steady impinging jets issuing from a long pipe nozzle [8]-[10] showing that the heat transfer rates are very sensitive to alterations in flow conditions (e.g., velocity and/or turbulence profile), [4] and [10]. Jambunathan et al. [4], Viskanta [10], and Persoons et al. [13] have presented comprehensive overviews of stagnation Nusselt number correlations for a steady impinging jet on a flat surface. The reported differences between empirical heat transfer correlations are due to variations in the nozzle geometry and the heat transfer performance enhancement from intensified velocity gradients and fluctuations. The temporal nature of both the fluid flow and heat transfer of impinging air jets has been experimentally investigated by O’Donovan and Murray [5]; their results show that the evolution of vortices with distance from the jet exit has an influence on the magnitude of heat transfer coefficient along the wall. In another study [6], the same authors have shown that at low nozzle-to-target ratios ($H \leq 2D$), secondary peaks in the radial heat transfer distributions are due to an abrupt increase in the turbulence in wall jet.

Thanks to the progress in computational performance, various numerical investigations have been performed to study the heat transfer coefficient distributions of impinging jet flows.

A number of numerical studies have qualitatively predicted the main flow features and heat transfer trends; however the results for local heat transfer distributions do not consistently produce acceptable quantitative agreement with experiments [14]-[15]. Furthermore, there are few studies recommending a reliable computational methodology for transitional jet impingement. This is the main motivation of the current study, which uses the established experimental methodologies of previous studies by the authors, O'Donovan and Murray [5]-[6] and Persoons et al. [13], for validation. As described by Caggese et al. [16], the inlet turbulence intensity has a strong effect on the heat transfer coefficient distribution, so the inlet turbulence profile must be chosen appropriately in order to fit the numerical model with experimental data. As will be described in section 4.1.1, the profiles of velocity and turbulence intensity exiting the nozzle are mapped from a separate model for the long inlet nozzle pipe to make the inlet boundary conditions more realistic.

In computational fluid dynamics, turbulence modelling coupled with appropriate near-wall treatment of grids is critical for the achievement of accurate flow and heat transfer predictions in impinging jet flows. There is no clear consensus in the literature on the most robust turbulence model which yields the best results for a wide range of operating and geometrical conditions. Although some recent studies using the large eddy simulation (*LES*) approach have proposed some enhancements in the accuracy of *CFD* results when referenced against experiments [17]-[19], the methods are not computationally efficient enough for a typical industrial design and engineering environment. Thus, performance evaluation of computationally efficient turbulence models is a crucial objective for this study. Table 2-1 presents an overview of the main parameter ranges and turbulence models used in some selected numerical studies from the literature. Different *CFD* models have been used, for a range of *Re* and *H/D* values (see Fig. 2-1).

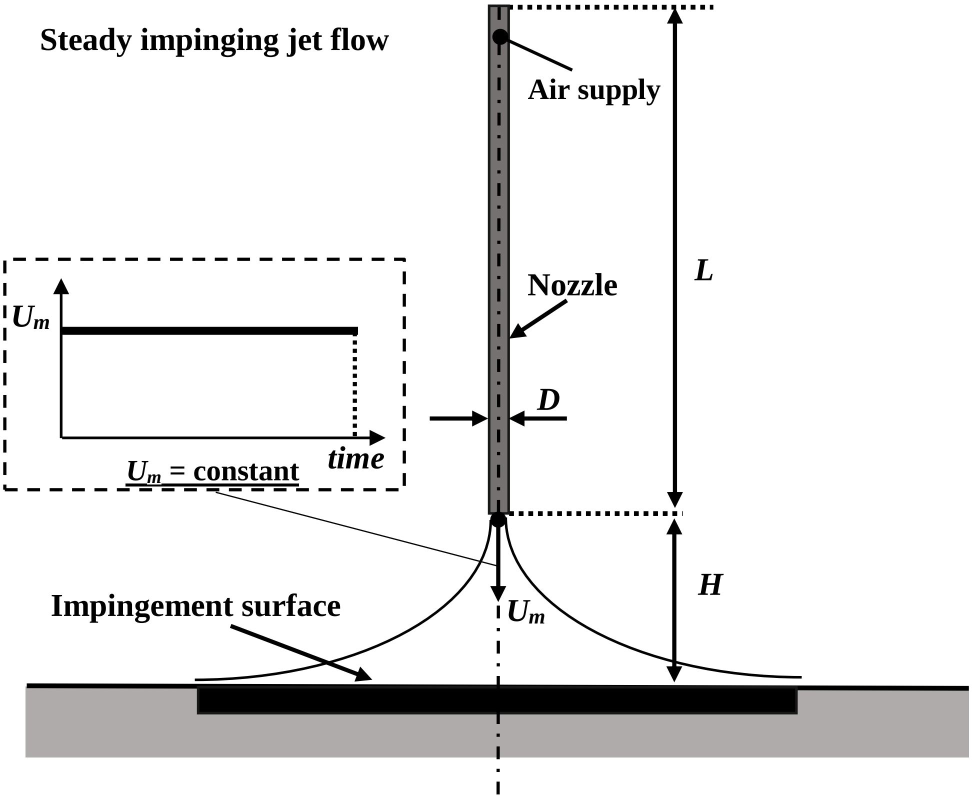

Figure 2-1. Schematic diagram of steady impinging jet flow

Table 2-1.Overview of parameter ranges and turbulence models used in selected numerical studies

	Re	*H/D*	**Turbulence model**
Draksler and Koncar [15]	20,000-23,000	1-2	*SST*
Caggese et al. [16]	16,500-41,800	0.5-1.5	*SST*
Hadziabdic and Hanjalic [17]	20,000	2	*LES*
Cziesla et al. [18]	5,800	8-12	*LES*
Kubacki and Dick [19]	13,500-20,000	4-10	*Hybrid RANS/LES*

In addition, when the simulation domain contains laminar, transitional and turbulent flows at the same time in different regions, the laminar-turbulent boundary layer transition should be modelled correctly. Although other numerical jet impingement studies typically use a fully turbulent model in the domain [16], an alternative is to employ a transition turbulence model called the *Gamma-Theta* model [20]-[22]. This model is based on two transport equations for intermittency and the transition momentum thickness Reynolds number, which determine the state of the boundary layer. The model becomes more useful in wall-bounded flows, in which the wall shear stress or the surface heat transfer rate are of interest. It is designed to predict the location and extent of laminar to turbulent flow transition which in turn significantly affects the heat transfer coefficient distribution. For impinging jet heat transfer at low values of nozzle-to-surface ratio ($H \leq 2D$, O'Donovan and Murray [5]), the local increase in wall-normal velocity fluctuations due to the transition of the wall jet flow from the laminar to turbulent mode coincides with a secondary peak in the heat transfer coefficient distribution along the wall (see also Colucci and Viskanta [23]). A recent study by Caggese et al. [16] on circular jet impingement shows that although numerical modelling can accurately predict the main heat transfer characteristics in the stagnation zone, it is more difficult to accurately predict this secondary peak.

2.2 Pulsating jets

Steady impinging jets are considered as an effective technique to achieve convective heat transfer due to a very thin thermal boundary layer forced over a surface [5] and [24]. Pulsating or intermittent impinging jets, shown in Fig. 2-2, are generally believed to enhance heat transfer when compared to steady jets, although there remains a lack of consensus on the level of enhancement; for some conditions the heat transfer can even be impaired [25]-[33]. The intermittent nature of a pulsating jet effectively redevelops and breaks up the boundary layer within each pulsation period, which may result in a thinner boundary layer than that of an equivalent steady jet. This can be achieved using little additional energy with no need to increase the pressure or flow rate [25]. The shortening and spreading of the pulsating jet also allows for higher turbulence levels and promotes flow instabilities [29].

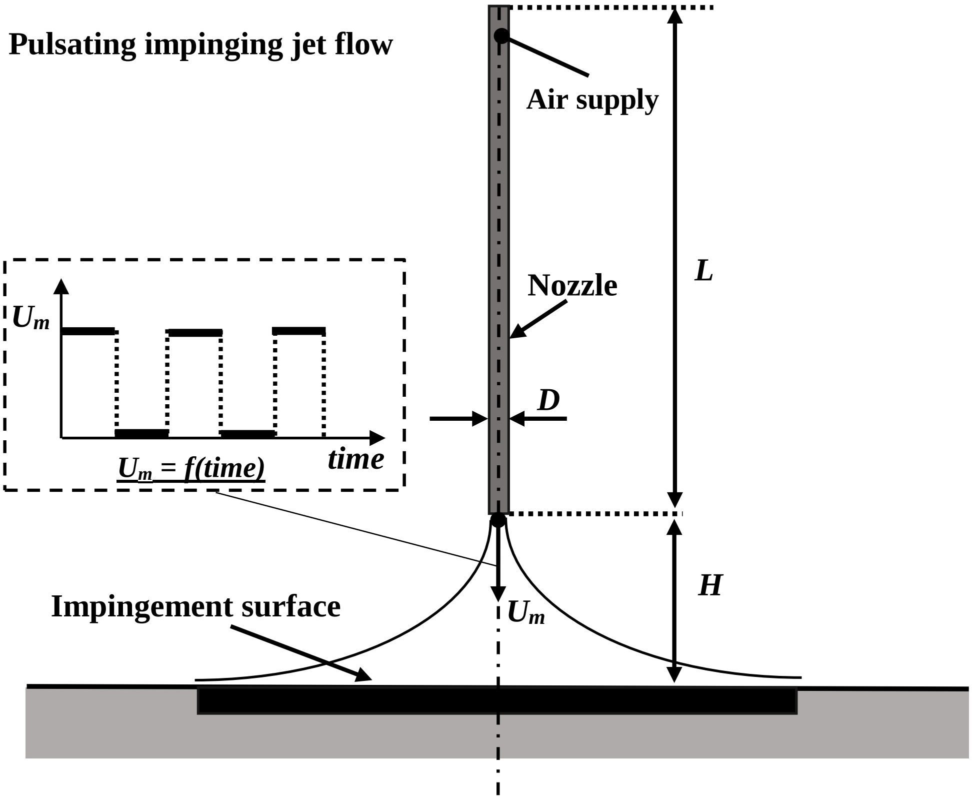

Figure 2-2. Schematic diagram of pulsating impinging jet flow

There is a lack of consensus in the scientific literature about the effect of flow pulsation on convective heat transfer enhancement. Although many studies have been carried out, the findings about the potential heat transfer enhancement induced by pulsating jets are quite varied [26]-[32]. Thus, some researchers report a significant heat transfer enhancement [26]-[29], while other studies reported no enhancement or even a reduction of the heat transfer using pulsating jet impingement [30]-[32]. Camci and Herr [26] found enhancement factors in stagnation heat transfer of up to 70% for Re = 14,000, H/D = 24, and f = 100 Hz (Sr = 0.033). Intermittent pulsation with a square-wave form has been experimentally investigated by Zumbrunnen and Aziz [27]; they reported significant heat transfer enhancement of up to 100% using the square-wave pulsation at high frequency f = 142 Hz (Sr = 0.37). Different waveform shapes were also investigated by Herwig and Middelberg [28], showing that a square-wave form pulsation produces much higher enhancement (for Sr = 0.08, δNu_0= 25%) than triangular or sinusoidal forms. The numerical results presented by Xu et al. [29] show that increase in the Reynolds number and pulsation frequency augments the Nusselt number compared to steady flow (up to 47%). In contrast, Liu and Sullivan [30] have measured changes in heat transfer due to pulsation of -10% to +10%, depending on the pulsation frequency and H/D. Using an acoustically excited air jet from a contoured nozzle, O'Donovan and Murray [31] have also reported a heat transfer reduction of up to -21% for $10{,}000 \le Re \le 30{,}000$ and $0.5 \le H/D \le 2$. This lack of consistency in findings is mainly due to the different ranges of parameters used in different investigations. Persoons et al. [24] have recently observed a change in behaviour due to flow pulsation in an axisymmetric impinging jet. Thus, for H/D=1 and a low pulsation frequency (Sr < 0.025), a reduction in stagnation point heat transfer rate by 13% is observed, increasing to positive enhancements for $Sr.(H/D)$ > 0.1 up to a maximum enhancement of 48% at $Sr\,(H/D)$ = 0.6.

Since direct numerical simulations (*DNS*) and even large eddy simulations (*LES*) remain impractical for many current industrial engineering environments, there is a need to establish a reliable numerical methodology to investigate the fluid flow and heat transfer of unsteady impinging jets at low computational costs ([13], [24], [31] and [34]-[38] and). This can be achieved by using the computationally efficient Unsteady Reynolds-Averaged Navier Stokes (*TRANS*) turbulence modelling method. However to ensure good accuracy, the numerical methodology should be accompanied by experimental validation of heat transfer results. There have been few studies in this field with a major focus on enhancing the accuracy of unsteady heat transfer results using computationally low-cost turbulence modelling schemes [29] and [32]-[33]. The current study tries to achieve accurate simulations by validating the results via thorough comparisons against experimental data.

2.3 Synthetic jets

A synthetic jet is typically generated from a partially closed cavity with an orifice and an oscillating diaphragm (see Fig. 2-3). Vibration of the diaphragm draws in and ejects ambient fluid through the orifice. This results in a train of vortex rings at the orifice outlet, to form the external jet flow. The train of vortex rings is able to entrain surrounding air into the high momentum jet core, resulting in increased flow controlling capabilities [13].

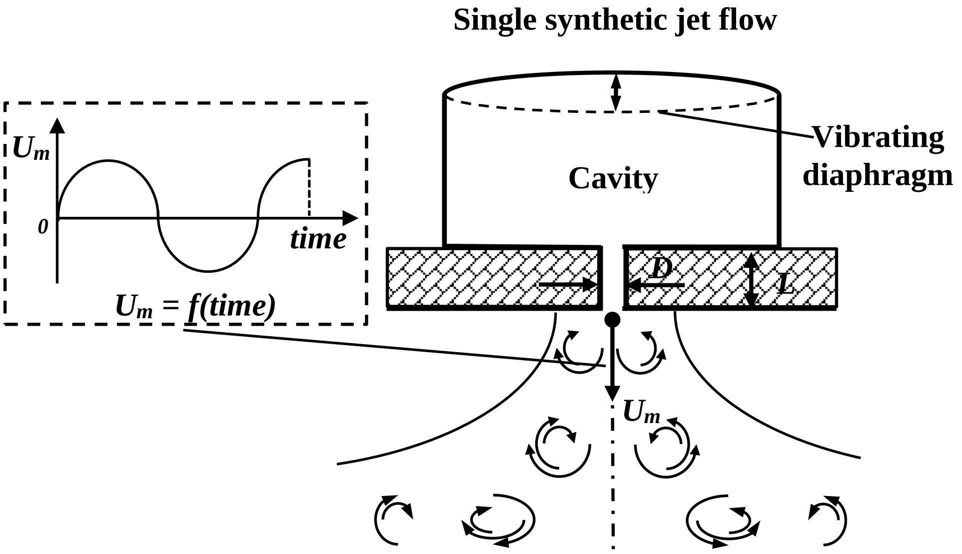

Figure 2-3. Schematic diagram of single synthetic jet flow

For an orifice diameter or slot width, D, the Reynolds number, $Re = \rho U_0 D/\mu$, and stroke length, L_0, govern the flow field of a free synthetic jet as defined by Smith and Glezer [79]. The stroke length is defined as the distance that a slug of fluid travels away from the orifice during the ejection portion of the cycle Holman et al. [80]. The stroke length L_0 is defined as:

$$L_0 = \frac{1}{A}\int_0^{1/(2f)} \int_A v(x,z,t)\, dA\, dt \ = \frac{U_0}{f} \tag{2-1}$$

The variables $v(x,z,t)$ and f are the instantaneous orifice velocity and the driving frequency of the synthetic jet, respectively. A is the cross-sectional area of the orifice.

Several applications of free synthetic jets in flow control techniques have been numerically and experimentally studied; for instance, applications in separation control by Zhang and Samtaney [81], Mittal and Rampunggoon [82], and Ozawa et al. [83], mixing enhancement by Jabbal and Zhong [84], Liu et al. [85], and Xia and Zhong [86], thrust-vectoring by Ibrahim and Skote [87] and virtual surface shaping by Mittal and Rampunggoon [82].

Furthermore, synthetic jets have become an interesting method of electronics cooling, resulting in continued research activities in this field. The local convective heat transfer of an impinging synthetic jet has been shown to rival that of a steady impinging jet as reported by Campbell et al. [88], Smith and Swift [89], Mahalingam [90] and Persoons et al. [13]. The major advantage of synthetic jets is their zero net mass-flux nature, since the jets recycle the ambient fluid. Thus, the system does not require any additional components making synthetic jets advantageous for cooling in confined geometries, such as microelectronic thermal management.

Single synthetic jets have been experimentally investigated in various studies to date; see Smith and Glezer [79], Glezer and Amitay [91], Shuster and Smith [92], Valiorgue et al. [44], and Persoons et al. [13]. Persoons et al. [13] have provided an objective comparison of axisymmetric impinging synthetic jets versus steady jets through a wide range of operating conditions.

In addition to experimental investigations, several studies have used numerical modelling to understand the behaviour of synthetic jets. Provided the models are diligently validated, computational fluid dynamics can provide valuable additional information to better gain insight into the complicated nature of the fluid mechanics of synthetic jets.

2.3.1 Numerical investigations of single synthetic jet flows

Some specific features of synthetic jets make *CFD* an effective approach for investigation. Firstly, the configuration for a synthetic jet can be small and it is not always practically feasible to measure different parameters within the device. Secondly, synthetic jet flow fields involve a wide range of spatial and temporal scales, which adds to the complexity of their measurement; see Mohseni and Mittal [93]. Challenges and limitations associated with *CFD* modelling of synthetic jets have to contend with complex flow phenomena including flow separation, compressibility, unsteadiness, vortex dynamics and boundary layer formation.

Some numerical studies performed in this field have used an oscillating boundary condition at the exit of the orifice slot. This is done by setting an empirical harmonic function as the inlet velocity to the jet domain, $\overline{U_{\iota n}}$, defined as:

$$\overline{U_{\iota n}} = U_A f(\eta) \sin(2\pi f t) \tag{2-2}$$

where U_A is the amplitude of the harmonic function, and η is the cross-stream direction. These values are usually approximated using an experimental study performed at the corresponding parameter settings of the numerical model under investigation. The simplified inlet boundary condition (*I.B.C.*) truly reduces the amount of the complexity and the computational time during the solution procedure. However, this leads to an over-simplification of boundary conditions in the numerical model which is known to be the major challenge in this field of study. Table 2-2 summarizes a comprehensive overview of various numerical studies performed to evaluate single synthetic jets (*S. J.*). This table also points out the major features and characteristic parameters used by different studies, namely the configuration under investigation, stroke length (L_0/D), Reynolds number (*Re*), actuation frequency (*f*), and method used for simulation. The latter represents two items: first the turbulence model used in each study and second the method practiced to simulate the dynamic flow phenomenon in the cavity, which can be either a simplified inlet boundary condition (*I.B.C.*) at the orifice slot or *Dynamic Mesh* (*DM*) scheme. Dynamic Mesh scheme has been used in a limited number of studies to date (see Table 2-2).

As an early stage effort in this field, Kral et al. [94] have used a boundary condition to simulate an isolated synthetic jet actuator using the *RANS* approach. The actuator model simulates the orifice as a suction/blowing boundary condition. Three different velocity distributions along the orifice were tested and all three cases result in the same flow features. It has been demonstrated that the modelled boundary condition captures the essential features of the jet without modelling the detailed breakdown of the vortices or the details of the cavity flow.

Using the unsteady compressible *Navier–Stokes* equations, both the interior of the actuator cavity and the external jet flow field were investigated by Rizzetta et al. [95]. Both the spatial and temporal quality of the results were established via mesh-size and time-step studies. The internal results are generated with an overset deforming zonal mesh system, whereas the jet flow field is obtained by a high-order compact-difference scheme. A comparison is made with experimental data in terms of the mean and fluctuating components of the jet velocity. Simulations captured span wise instabilities that led to a breakup of the coherent vortex structure. They reported that with sufficient computational resources and complete knowledge of physical details of the actuating device, complex synthetic jet flow fields can be accurately simulated.

Turbulence modelling of statistically periodic flows applied to synthetic jet into quiescent air has been studied by Carpy and Manceau [96]. Since the flow inside the cavity was not simulated, unsteady *Dirichlet* boundary conditions were specified at the slot exit. This simplified inlet boundary condition *I. B. C.*, which was imposed as vertical velocity over the centre of the slot as a function of phase, was extracted from *PIV* data and used as inlet conditions. Comparisons of the performance of the models with experimental data show that the evolution of the vortex dipole generated by inviscid mechanisms is not correctly reproduced by the k - ε model. The Reynolds-stress model gives much more realistic predictions. However, several characteristics are not well predicted, such as the convection velocity, since the turbulence is far from equilibrium in the region close to the slot exit. It is also difficult for a Reynolds-stress model to reproduce accurately the interaction between the turbulence and the vortex dipole. A detailed analysis shows that the vortex dipole dynamics are essentially inviscid during the early blowing phase, when the flow is more transitional than fully turbulent. Turbulence develops and influences the dynamics of the vortices only at a later stage of the blowing phase. Consequently, it is of importance that the turbulence models do not predict erroneously high levels of turbulence. Moreover, the correct prediction of the region of negative production that appears during the deceleration of the blowing velocity, due to the misalignment of the strain and anisotropy tensors, is crucial. Therefore, linear eddy-viscosity models must be discarded for these types of pulsed flows, in particular for flow control using synthetic jets. Comparisons of long-time-averaged quantities are misleading because of the propagation of errors. When phase-averaged quantities are compared in detail, the deficiencies of linear eddy-viscosity models clearly appear. In order to evaluate the ability of the models to reproduce the unsteady dynamics of the flow, it is much more relevant to focus on the behaviour of the vortex dipole, in terms of location, intensity, convection velocity and penetration into the ambient fluid: the Reynolds-stress model is able to reproduce the correct dynamics, contrary to the $k - \varepsilon$. Rumsey et al. [97] arrived at the opposite conclusion reporting that linear eddy-viscosity models produce the best results among *URANS* models.

Rumsey et al. [97] have explored two different synthetic jet flows issuing into a turbulent boundary layer crossflow through a circular orifice. The use of *URANS* was shown to be appropriate for synthetic jet flows. The computations demonstrated good prediction of the qualitative behaviour of the synthetic jet flow field. However, quantitatively there were many specific differences. A major reason for the discrepancies between the *URANS* and the experimental results, was noted by the authors to be related to the time-dependent boundary condition which was applied at the centre of the orifice exit (simplified *I. B. C.*). They have finally emphasized the importance of including the region inside the cavity when modelling synthetic jets, and concluded that use of *I. B. C.* was an oversimplification that failed to capture the complex nature of the flow field near the orifice, particularly during the ejection phase of the cycle.

With an aim to develop a numerical predictive model for future designs of synthetic jet based active cooling substrates, Wang et al. [98] utilized a *LES* turbulence modelling scheme to perform the 3D simulations. To reduce the complexity of the model and the computational time of simulations, the vibration diaphragm boundary condition is simulated as a sine wave velocity boundary.

To simulate the displacement of the membrane, an actual mesh deformation in the vicinity of the membrane has been taken into account in a study of synthetic jets for heat transfer enhancement in air cooled micro-channels Timchenko et al. [99]. It was demonstrated that the compressibility of air is very significant. The effects of varying the frequency of the jet for a fixed pressure difference between the ends of the channel, and with a fixed jet Reynolds number, have been studied with air as the working fluid. The flow field results were not compared to experimental data in their study.

Ozawa et al. [83] have simulated the interaction between a synthetic jet and a laminar separation bubble caused by adverse pressure gradient in a boundary layer. In the numerical model including the synthetic jet actuator, the synthetic jet velocity at the exit of the cavity was defined as an input. To perform *LES*, a *Dynamic Smagorinsky* model was used for the sub-grid scale stress (*SGS*) terms. Their model was capable of capturing the basic features, including the transition from laminar to turbulent flow. However, simulating the transition from laminar to turbulent flow still remains a challenge.

The moving diaphragm can be modelled with a moving piston boundary condition as well as with a moving wall boundary condition. This is performed by Jain et al. [101] to investigate the effect of various cavity parameters on the ensuing synthetic jet flow, by use of a laminar flow model. It is observed that the approximations of the boundary condition in terms of a velocity inlet with a top hat profile or in terms of a sinusoidal moving piston do not simulate the actual behaviour of a vibrating diaphragm.

Bazdidi-Tehrani et al. [102], Harinaldi and Rhakasywi [103], and Silva and Ortega [104] have also used a sinusoidal wave function to simulate the movement of the piezoelectric membrane in the cavity. They have presented a numerical simulation of synthetic jets impinging on a heated wall. For applications associated with micro-mixers and high-viscosity fluids (very low Reynolds numbers), Xia et al. [105] have used sinusoidal *I. B. C.* to provide a way of designing more effective synthetic jet actuators for enhancing mass and momentum transfer.

Table 2-2. Review of *CFD* studies for single synthetic jets

	Configuration	L_0/D	*Re*	*f* (Hz)	Method
Kral et al. [94]	*S. J. into quiescent air*	2.7 – 16.5*	500 – 3,000	1,000	*I. B.C.* *Spalart-Allmaras*
Rizzetta et al. [95]	*S. J. actuator*	4.1 – 8.2*	750 – 1,500	1,000	*D. M.* *DNS*
Carpy and Manceau [96]	*S. J. into quiescent air*	29.7*	2,400	444.7	*I. B.C.* *URANS*
Wang et al. [98]	*S. J. based active cooling substrates*	-	600	-	*I. B.C.* *LES*
Rumsey et al. [97]	*S. J. in crossflow*	-	-	24 - 150	*I. B.C.* *URANS*
Timchenko [99]	*S. J. in micro-channels*	18.9 - 56.7*	103	10 - 30	*D. M.* *Laminar Model*
Ozawa et al. [83]	*S. J. for active flow control*	27.5*	500	100	*I. B. C.* *LES*
Jain et al. [101]	*Axisymmetric S. J.*	0.83 – 42.5*	167 – 1,544	200 – 1,100	*I. B.C. & D. M.* *Laminar Model*
Harinaldi and Rhakasywi [103]	*Impinging S. J.*	48.8 – 195*	1,421 - 2,843	80 - 160	*I. B. C.* *SST*
Silva and Ortega [104]	*Impinging S. J.*	2.33 - 6.9*	508	400 – 1,200	*I. B. C.* *Laminar Model*
Bazdidi-Tehrani et al. [102]	*Impinging S. J.*	0.55 – 27.6	2210	30 - 2500	*I. B. C.* *V^2-f Model*
Xia et al. [105]	*S. J. at low Reynolds numbers*	0.52 - 11.1	14.8 – 553	2 - 10	*I. B. C.* *Laminar Model*

Notes: *I. B. C.* = Inlet boundary condition, *D. M.* = Dynamic Mesh, *S. J.* = Synthetic Jet.

*Values are not provided by the authors (estimated).

Due to the limitations of piezoelectric material, it has been hard to modify the controlling efficiency of small-scale synthetic jet actuators for the limited maximum amplitude. A high-power synthetic jet actuator can fulfil the efficiency and power requirements of full-scale flow control applications; see Liu et al. [85]. However, the newly designed actuators are not compact enough to be utilized conveniently into high-density electronic equipment and other devices. To meet the "strength" and "micro-" requirements in various applications, it is necessary to investigate the optimization design methods of adjacent synthetic jets actuators; see Ritchie and Seitzman [106].

2.3.2 Numerical investigations of adjacent synthetic jet flows

The strong entrainment of the surrounding flow which is induced by the jet in the vicinity of the cavity outlet can be used to dynamically vector the jet. A pair of side-by-side synthetic jets can form a larger jet, as experimentally studied by Smith and Glezer [78]. They have studied two adjacent synthetic jets 0.5 mm wide placed apart from each other. Their results show that if the jets are in phase, the inner vortices cancel each other, resulting in a single merged jet. The combined jet has stronger controlling ability compared with a single synthetic jet. When one of the jets is leading in phase, its vortex pair and the suction effect from the adjacent jets deflects the vortex pair directions and the merged jet is vectored toward the actuator leading in phase. The relative phase difference of the jet actuators can be used to manipulate the merged jet which results in a great effect on the controlling ability of the synthetic jet actuator.

The vectoring phenomenon in adjacent synthetic jets is not yet broadly discussed in the literature. It is essential to review different studies performed to assess the interaction of a pair of adjacent synthetic jets *(A. S. J.)*, separately. This has been experimentally investigated by Smith and Glezer [78], Luo and Xia [107], Persoons et al. [108] and Fanning et al. [109]. The vectoring mechanism which occurs by applying a phase difference between actuating signals is characterised as an 'attract-impact causing deflection' by Luo and Xia [107], causing the combined jet to be vectored in the direction of the jet leading in phase; a very similar trend is reported by Smith and Glezer, Smith and Glezer [78] and Persoons et al. [108]. Persoons et al. [108] have also reported that this effect induces a cross-flow proving entrainment of fresh cooling air to the merged jet. This effect prevents recirculation of heated fluid to the cavity without the need for an external cross-flow (e.g. driven by a fan) and was shown to enhance the convective heat transfer performance of the jet pair. Heat transfer and *PIV* measurements by Persoons et al. [108] suggest an optimum phase difference region of $90° < \delta\emptyset < 120°$ for constant values of $Re = 300$, $L_0/D = 29$ and an orifice-to-orifice centre separation $S = 3D$. In this range of phase difference an effective cross-flow was set up whilst maintaining strong vortex mixing at impingement, resulting in the highest convective heat transfer rates. Using *PIV* and infrared thermography Fanning et al. [109] have recently presented a wide range of heat transfer measurement and discussed the mechanism of cross-flow induced by the out-of-phase synthetic jets.

A very limited number of studies have considered interaction of a pair of adjacent twin jets. This becomes the case especially when the major focus is on the effect of phase difference between adjacent cavities on vectoring of the merged jet. A summarized overview of numerical studies performed to evaluate adjacent synthetic jets is presented in Table 2-3.

In the study of Guo et al. [110], the cavity geometry is included in the simulations and the actuator boundary conditions using Eq. (2-2) are applied at the bottom of the two cavities. *RANS* equations are solved to simulate the interaction of two adjacent synthetic jet actuators. Cases with different relative phases between the adjacent jets are simulated. For a phase difference of 130 °, the vortex pairs generated by the blowing strokes of the two jets are both vectored towards the left wall even before they separate from the jets, and travel away from the synthetic jets along the wall and dissipate gradually. They have also noted that for relatively higher phase differences between two jets, the direction of the merged jet is sensitive to the initial phases.

Hewakandamby [100] have used a laminar flow model to simulate an array of oscillatory impinging jets located on top of a heated surface. The model is actually a pair of adjacent synthetic jets with 90° phase difference. The exit velocity of the jet is defined as a sinusoidal function of time. They report that the oscillatory jets result in almost 100% enhancement of heat transfer compared to a steady jet.

Luo et al. [107] have investigated a novel piezoelectric-driven actuator. Synthetic jet actuator is composed of two emitting slots, two sealed cavities bounded on one end by a single PZT diaphragm, and a slide block. This can be regarded as a pair of adjacent jets with a constant phase difference of 180°. The study mainly focuses on introducing the adjustable actuator design. The numerical results are based on an *I. B. C.* and $k-\varepsilon$ model are only limited to velocity contours of flow field into quiescent air, without a comparison to experiments. The same turbulence model and boundary condition is used by Liu et al. [85] to evaluate the mechanism of adjacent synthetic jets and the influence of phase difference on the mixing of coaxial jets. Their results indicate that a phase difference between the jets can lead to reduced vortex size, reduced vortex strength to a greater degree, and finally, decreased controlling ability. The unsteadiness mainly results from the vortex-vortex interaction and energy exchange, and the detailed mechanism needs further investigation in the future.

To investigate the benefits of dual circular orifice synthetic jets over a single one for higher circulation production, Riazi and Ahmed [111] have used an incompressible laminar model to study single and two-orifice synthetic jet actuators. The diaphragm motion is replaced with an expression for flow velocity as an *I. B. C.*. This is an in-phase *A. S. J.* with one actuator. They have reported that the circulation can be enhanced by more than 160% with a fixed input energy by use of orifices with smaller diameters but higher dimensionless stroke lengths in two-orifice actuators.

Table 2-3. Review of *CFD* studies for adjacent synthetic jets

	Configuration	***L_0/D***	***Re***	***f* (Hz)**	**Method**
Guo et al. [110]	*Interaction of A. S. J.*	29D	300	600	*I. B.C.* *Spalart-Allmaras*
Luo et al. [112]	*S. J. with two emitting slots: 180°A. S. J.*	-	-	500	*I. B.C.* $k-\varepsilon$ *Model*
Hewakandamby [100]	*Array of impinging jets: 90°A. S. J.*		100 – 1,200	1 - 500	*I. B.C.* *Laminar Model*
Liu et al. [85]	*Mixing Control in Coaxial Jets with A. S. J.*	-	-	500	*I. B.C.* $k-\varepsilon$ *Model*
Riazi and Ahmed [111]	*Two-orifice synthetic jet: In phase (0°) A. S. J.*	1 – 3.49	-	50	*I. B.C.* *Laminar Model*

Notes: *I. B. C.* = Inlet boundary condition, *A. S. J.* = Adjacent Synthetic Jets

To the best of our knowledge, there has not been an effort thus far to integrate the oscillating diaphragm motion in the simulation of *a pair of adjacent synthetic* jets and which is accompanied with experimental validations.

The complicated vortex structures in shear layer must be accurately calculated in order to understand the vortex-vortex and vortex-wave interactions which are difficult to understand. The intricate mechanism of adjacent synthetic jets and the effect of phase difference on vectoring of the merged jet is the major focus in this study.

As discussed above, the simulation of the actuator diaphragm is still a crucial challenge in the numerical modelling of synthetic jets which is overlooked in a lot of studies (see Table 2-2 and Table 2-3).

This study describes a complete simulation of an adjacent synthetic jet case including the whole cavity, nozzle slot, and jet evolution domain into quiescent air; this is expected to lead to a non-empirical numerical model with more accurate results. This also adds much more flexibility to the numerical model, which makes it independent from a backup experimental setup. Any change in dimensional or operational parameters of the cavity, for instance the aspect ratio of the cavity orifice, the frequency and amplitude of vibration will be automatically updated inside the model without any need to modify the empirical boundary condition, shown in Eq. (2-2).

Alimohammadi et al. [38] have previously shown that the *CFD* model can reliably predict the fluid flow and heat transfer to steady and pulsating impinging jets for an extensive range of operating conditions. To predict the fluid flow behaviour of synthetic jets using numerical modelling, the previously validated transient numerical model for pulsating impinging jets [38] is extended to synthetic jets. This is done for both single jets and a pair of adjacent jets, considering the case of jets inssuing into quiescent air. This model is designed so as to overcome the previously described deficiency in the numerical modelling of synthetic jets. The oscillating wall of the cavity is simulated in the new model by means of dynamic mesh techniques. The results are compared to the results reported by Smith and Glezer [78], Persoons et al. [108], and Fanning et al. [109] and a set of experimental data obatined in this study on adjacent synthetic jets using Particle Image Velocimetry (*PIV*) techniques.

According to the literature review, a limited number of studies have been performed on a wide-ranging numerical-experimental methodology for unsteady impinging jets. With the knowledge gained from the literature review as shown earlier in this chapter, the major objectives of this study can be defined in the first place. Based on the research objectives the main structure and the pathway of the research can be established.

3 Research Objectives and Outline

3.1 Research objectives

This work aims to develop an experimentally validated numerical model for a wide range of jet flows for heat transfer applications in a progressive manner.

The main objectives of this study are the following:

- Verification of a computational fluid dynamics model to predict the fluid flow & heat transfer of steady and unsteady impinging jets, using detailed experimental measurements for validation.
- The effect of Reynolds number, jet-to-surface distance, nozzle diameter, pulsation frequency on heat transfer enhancement for pulsating jets.
- Quantification of the stagnation and area-averaged heat transfer enhancements achieved by flow pulsation.
- Proving an insight into the near-wall behaviour in the viscous sublayer to realize the governing heat transfer mechanisms.
- A full simulation of the internal flow in the jet cavities, as well as the external jet flow, for a pair of adjacent synthetic jets, using dynamic mesh techniques.
- Investigation of the vectoring phenomenon in adjacent synthetic jets.

3.2 Thesis outline

Steady, pulsating and synthetic jets are three important manifestations of jet flows suitable for electronics cooling and thermal management applications, each having their own specific challenges to model numerically. This is mainly represented in chapters 4, 5 and 6, for steady, pulsating, and synthetic jets, respectively. Each chapter attempts to show the step-by-step procedure to extend the numerical model for each specific case. Every chapter includes the required descriptions about the numerical and experimental methodologies together with validation of *CFD* model for each specific case (e.g. steady jets, pulsating jets, synthetic jets). This is accompanied by a specific results and discussion section for each chapter and also a conclusion which bridges each chapter to the next one.

The remainder of this thesis is organised as follows:

Chapter 4 aims to establish and verify a robust *RANS* (Reynolds-averaged Navier-Stokes) computational fluid dynamics (*CFD*) methodology to accurately predict the local heat transfer coefficient for a circular steady impinging jet, using our own detailed experimental measurements for validation. The main goal is to capture the transition to turbulence in the wall jet and to ensure the model is valid over a wide range of operational and geometrical parameters, while keeping the computational cost low. This chapter is the first step towards a robust numerical methodology for unsteady impinging flows such as pulsating and synthetic jets ([13], [34]-[38]).

In **chapter 5** the main motivation is to characterise the stagnation and area-averaged enhancements (or degradations) in convective heat transfer rate achieved by flow pulsation, when compared to steady jets, for an extended range of operating conditions. The results were analysed in terms of the effect of different key parameters such as Reynolds number *Re,* dimensionless nozzle-to-surface distance *H/D*, nozzle diameter *D*, and so on. This is accomplished by developing fitted correlations as functions of groups of modified dimensionless numbers that best collapse the averaged and stagnation heat transfer enhancement.

Following rigorous experimental validation, the *CFD* model is used as a stable tool to simulate operating conditions beyond the frequency range for reliable operation of the experimental pulsating valve. This shows how the numerical model helps the investigation to be extrapolated to much higher frequency jets.

As another motivation in this research, to better understand the potential heat transfer enhancement introduced by the flow pulsation, some of the effective near-wall flow characteristics, namely the radial velocity gradient, the normal vorticity, and the Reynolds stress components, are monitored. This approach reveals that these flow characteristics are directly proportional to the heat transfer distribution of steady and pulsating jets over the impingement surface, and shows the variation of jet frequency itself can affect the enhancement.

Chapter 6 reports the numerical and experimental study performed on synthetic jets. The formation, evolution and interaction of a pair of adjacent synthetic jets is investigated numerically using computational fluid dynamics and experimentally using particle image velocimetry techniques. Both jet actuators are operated at the same condition but with an adjustable phase difference. The investigation considers a jet pair issuing into quiescent air. Simulation of full jet cavity incorporating the diaphragm motion is performed using Mesh Deformation techniques.

The effect of phase difference between the pair of adjacent synthetic jets on the vectoring of the merged jet is investigated. This leads to a better understanding of the fluid mechanics of adjacent synthetic jets and delivers a theoretical basis to be used in the future for their application.

Chapter 7 highlights the main conclusions of this study, considering the incremental progression of complexity in the flow configurations from steady jets to pulsating jets and finally a pair of adjacent synthetic jets. This is done apart from the conclusion sections which are reported at the end of each chapter linking the findings to the next chapter.

Chapter 8 reports an overall summary of achievements during this PhD study.

4 Steady Impinging Jet Flows

This chapter presents a computational fluid dynamics (*CFD*) methodology to accurately predict the heat transfer characteristics of an unconfined steady impinging air jet in the transitional flow regime, impinging on a planar constant-temperature surface (see Fig. 4-1). The *CFD* methodology is validated using detailed experimental measurements of the local surface heat transfer coefficient. The numerical model employs a transitional turbulence model that captures the laminar-turbulent transition in the wall jet which precisely predicts the intensity and extent of the secondary peak in the radial Nusselt number distribution. This chapter proposes a computationally low-cost turbulence model which yields the most accurate results for a wide range of operating and geometrical conditions. A detailed analysis of the effect of mesh grid size and properties, inflow conditions, turbulence model, and turbulent Prandtl number Pr_t is presented. The numerical uncertainty is quantified by the grid convergence index (*GCI*) method. In the range of Reynolds number $6{,}000 \leq Re \leq 14{,}000$ and nozzle-to-surface distance $1 \leq H/D \leq 6$, the model is in excellent agreement with the experimental data. For the case of $H/D = 1$ and $Re = 14{,}000$, the maximum deviations are 6%, 4% and 3% in terms of local, area-averaged and stagnation point Nusselt numbers, respectively. Experimental and numerical correlations are presented for the stagnation point Nusselt number.

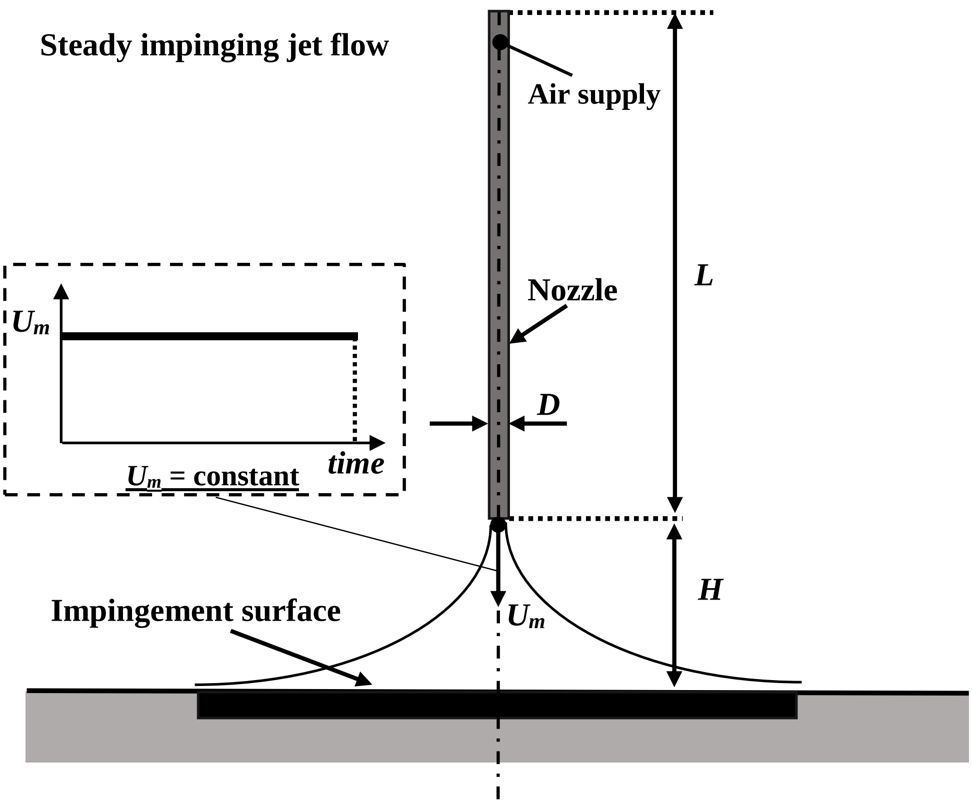

Figure 4-1. Schematic diagram of steady impinging jet flow

4.1 Numerical methodology

For the numerical simulation of jet impingement, the commercial tool ANSYS CFX 14 is employed. This package uses an element-based finite volume method. This is done by integrating and discretising conservation equations, namely continuity, momentum and energy equations, plus the appropriate turbulence equations according to the selected turbulence model as a closure [39]-[40]. CFX uses a vertex-centred solver, so the solution variables are stored at the mesh vertices (nodes). To describe the way a variable changes across each element, solution fields and gradients at integration points are approximated using finite-element shape function. Likewise, following the standard finite-element approach, shape functions are used to evaluate spatial derivatives for the diffusion terms. The resulting linear system of equations that arises by applying the finite volume method to all elements are discrete conservation equations, which are solved using a coupled solver to reduce the number of iterations for convergence.

Attention is focused on the near-wall region since it is the most important for convective heat transfer. Some previous studies on heat transfer to impinging jets only qualitatively predict the flow physics, with a limited degree of quantitative accuracy for the solution of the energy equation which is closely linked to the convective heat transfer. The current chapter aims to improve the accuracy of heat transfer simulations by validating the results via comparison with experimental local heat transfer coefficient data (see Sections 4.2, 4.3 and 4.4).

4.1.1 Computational domain: geometry and boundary conditions

Figure 4-2 displays the two-dimensional axisymmetric computational domain and mesh used in the simulation of an unconfined round jet impinging on a flat plate. The dimensions are identical to that of the experimental setup used for validation (see Section 4.2.1). An assumption of axisymmetric flow in the domain provides a good approximation while saving time to achieve a satisfactory convergence (Alimohammadi et al. [37]), as verified by the comparison of CFD to experimental results presented in sections 4.3 and 4.4. The computational domain extends far enough from the area of interest (up to a radial distance of 16D from the jet centreline) to prevent outlet boundary effects on the results.

The boundary conditions applied to the domain are shown in Fig 4-2. The governing equations were formulated to eliminate all gradients in the circumferential direction (see [39]). This assumption imposed an axial symmetry condition, and reduced the necessary simulated region to a radial slice through the domain. The velocity profile at the nozzle exit is calculated using a separate simulation for a long nozzle pipe and mapped from the nozzle exit to the domain inlet. The spatially and time-averaged velocity in the nozzle is set to match the Reynolds number (based on the diameter D = 13 mm and the mean nozzle velocity) used in the experiments.

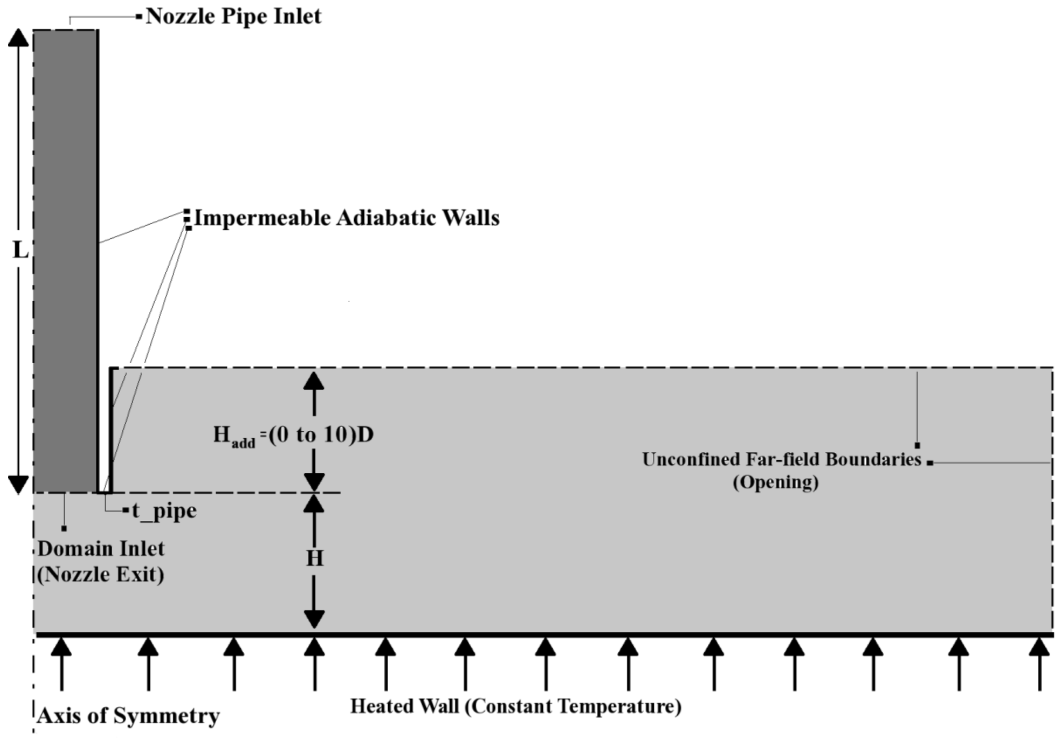

Figure 4-2. Computational domain, boundary conditions

The turbulence intensity at the domain inlet is also determined by means of the same mapping procedure of profiles obtained for the turbulent kinetic energy from a separate simulation. However, it should be noted that the turbulence intensity value at the nozzle inlet, remains unknown at this stage; the procedure to estimate the averaged turbulence intensity at the nozzle pipe inlet is described in section 4.3.5.

At the radial outlet and unconfined top boundaries of the domain, as the far-field boundaries which are free to the environment, an opening boundary condition with a constant temperature of 25 ℃ and zero relative pressure is used to allow the flow to leave and re-enter the domain, thereby enabling potential flow re-circulation. The planar heated wall surface at the bottom of the domain is set to a constant temperature of 60 ℃, in agreement with the experiments (see Section 4.2.1).

4.1.2 Mesh generation

The generated mesh is designed to resolve the important flow features as a function of the main parameters (e.g., *Re* and *H/D*), using suitable methods such as grid refinement inside the wall boundary layer. The mesh topology is generated based on the structured approach with a hexahedral mesh to maintain the orthogonality in the domain (see Fig.

4-3); afterwards, it is refined and adapted iteratively in regions with large velocity, pressure, temperature and turbulence gradients in order to attain a stable solution. To have a computationally efficient model in low-gradient regions a coarse mesh scheme is applied, resulting in better control on the physical distance of the first grid point from the wall (y^+). The adequate value of near-wall cell thickness is ensured by keeping the y^+ below unity for the near-wall cells.

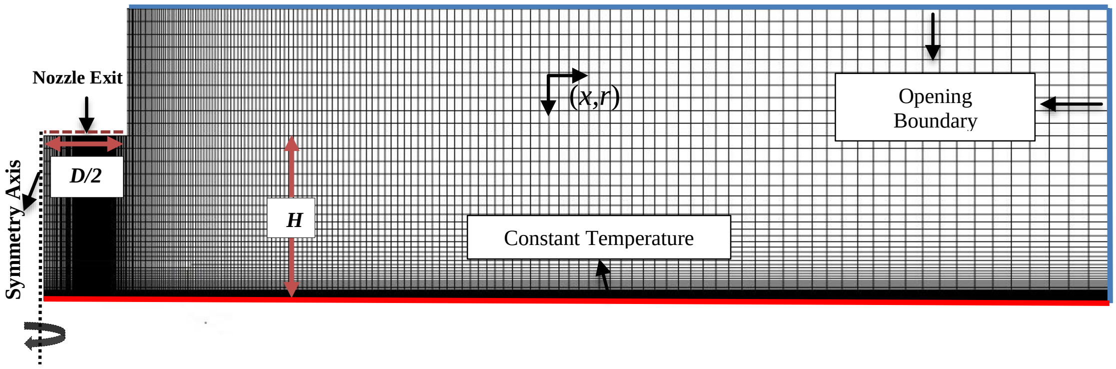

Figure 4-3. Mesh used in the simulation of the unconfined axisymmetric impinging jet

Additionally, at least ten nodes are applied inside the viscous sub-layer within a small distance from the wall (of the order of $10^{-6} \times D$ for the present problem). The final grid is generated to have a larger concentration of nodes close to the impingement wall and the jet mixing region, which take places between the jet and the surrounding entrained air. Section 4.3.1 shows the details of five different mesh sizes used for the grid independency study and their effect on heat transfer results.

4.1.3 Fluid properties

Fluid compressibility is negligible in the current problem since the local Mach number does not exceed 0.05. However since temperature differences of up to 35 ℃ may occur in the domain, a moderate change in air properties can be expected. A linear property table is employed to calculate the density, viscosity and thermal conductivity for the range of 25 ℃ to 60 ℃ in the domain, to include the effect of compressibility and changing fluid properties. As a result, the difference between the heat transfer results extracted from incompressible and compressible models for the applicable range of Re numbers in this study (between 6000 and 14,000) is calculated to be less than 1%.

The relative importance of buoyancy forces (natural convection) due to the temperature variations in a mixed convection flow can be estimated using Richardson number (*Ri*) the ratio of Grashof number to the squared Reynolds number, which is proportional to the domain length scale. Due to the small length scale of the domain (with a maximum of 0.1 m, approximately), the maximum value of this ratio for the current problem is of the order of 0.002. Thus, buoyancy is neglected in the simulation.

4.1.4 Turbulence modelling and governing equations

As observed in impinging jet flow experiments, both laminar and turbulent flow occurs simultaneously in different regions. For laminar flow, the numerical solution of the momentum and continuity equations with a suitable grid is sufficient to resolve the flow phenomenon (see section A.4.2), but for turbulent or transitional flows, a turbulence model is required. Turbulence strongly affects the important global features of the flow, so the accurate and reliable prediction of turbulent flow phenomena is essential.

The decision regarding the appropriate model for simulations of turbulence in the domain is based on the flow physics and computational requirements depending on the generated grid and accuracy. Due to the boundary layer separation, a wall function is not an appropriate method to resolve the boundary layer [17]. Instead, directly resolving the boundary layer can provide accurate results. One of the major considerations is generating a near-wall mesh which is fine enough to resolve the laminar part of the boundary layer (viscous sub-layer) over a very small distance from the wall. The *RANS* turbulence models are broadly used in practical modelling for suitable accuracy and efficiency. The *RANS* turbulence models evaluated in the present study are*:* k-ε, *RNG* k-ε, k-ω, and *SST* with and without a transition model. Section 4.3.6 describes the effect of the different turbulence models on the results and the procedure for selection of an appropriate turbulence model in comparison with experimental data.

The *CFD* simulations are performed based on the well-known conservation laws for incompressible flow, namely continuity, momentum and energy equations, plus the appropriate turbulence equations according to the final selected turbulence model (*SST*, as will be described in section 4.3.6) as a closure [40]. In addition, the present study employs an accurate and realizable laminar-turbulent transition model called *Gamma-Theta* model (γ-Re_θ). This model employs new empirical correlations developed by Langtry and Menter [16-18], which have been broadly validated to work with the *SST* turbulence model.

Firstly, the transport equations for turbulent kinetic energy (k) and its specific dissipation rate (ω) of the modified *SST* model to work with the γ-Re_θ transition model are as follows ([20]-[22]):

$$\rho\frac{Dk}{Dt}=\frac{\partial}{\partial x_j}\left[(\mu+\sigma_k\mu_t)\frac{\partial k}{\partial x_j}\right]+\left(\gamma_{eff}\mu_t S^2-\ \rho k\frac{\partial u_j}{\partial x_j}\right) - min\left[max\left(\gamma_{eff},0.1\right),1\right]\rho\beta^*\omega k \tag{4-1}$$

$$\rho\frac{D\omega}{Dt}=\ \frac{\partial}{\partial x_j}\left[(\mu+\sigma_\omega\mu_t)\frac{\partial\omega}{\partial x_j}\right]+\alpha\left(\mu_t S^2-\ \rho k\frac{\partial u_j}{\partial x_j}\right)-\rho\beta\omega^2 + 2\rho(1-F_1)\sigma_{\omega 2}\frac{1}{\omega}\frac{\delta k}{\delta x_j}\frac{\delta\omega}{\delta x_j} \tag{4-2}$$

where u_j is the velocity vector, μ is the molecular viscosity, ρ is the density, S is the strain rate tensor modulus and γ_{eff} is the effective intermittency. Note that the production term in the transport equation of ω is not amended. The turbulent viscosity (μ_t) is defined as:

$$\mu_t=\rho kT,\qquad T=min\left[\frac{1}{max[\omega,SF_2/a_1]},\frac{0.6}{\sqrt{3}S}\right] \tag{4-3, 4-4}$$

the functions F_1 and F_2 are calculated as:

$$F_1=\max[F_3,tanh(arg_1^4)],\qquad arg_1=max\left[min\left(\frac{\sqrt{k}}{0.09\omega y},\frac{500\upsilon}{\omega y^2}\right),\frac{2k}{y^2CD_{k\omega}}\right] \tag{4-5, 4-6}$$

$$CD_{k\omega}=max\left(\frac{1}{\omega}\frac{\delta k}{\delta x_j}\frac{\delta\omega}{\delta x_j}\right) \tag{4-7}$$

$$F_2 = tanh(arg_2^2), \qquad arg_2 = max\left(\frac{2\sqrt{k}}{0.09\omega y}, \frac{500\upsilon}{\omega y^2}\right) \tag{4-8, 4-9}$$

$$F_3 = exp\left(-\left(\frac{R_y}{120}\right)^8\right), \qquad R_y = \rho y k^{1/2}/\mu \tag{4-10, 4-11}$$

where y is the normal distance from the nearest wall, and R_y is wall-distance based turbulent Reynolds number. The coefficient ϕ, which is a general term for σ_k, σ_ω, β and α in the equations (4-1) and (4-2), is estimated from the blending function (F_1) as follows:

$$\phi = F_1\phi_1 + (1 - F_1)\phi_2 \tag{4-12}$$

where the coefficients ϕ_1, ϕ_2 are:

$$\sigma_{k1} = 0.85, \sigma_{\omega 1} = 0.65, \beta_1 = 0.075, \alpha_1 = \beta_1/\beta^* - \sigma_{\omega 1}\kappa^2/\sqrt{\beta^*}$$

$$\sigma_{k2} = 1.0, \sigma_{\omega 2} = 0.856, \beta_2 = 0.0828, \alpha_2 = \beta_2/\beta^* - \sigma_{\omega 2}\kappa^2/\sqrt{\beta^*}$$

and $a_1 = f0.3, \kappa = 0.41, \beta^* = 0.09$.

The γ-Re_θ transition model is made of two transport equations for the intermittency (γ) and the transition momentum thickness Reynolds number ($\tilde{R}e_{\theta t}$) which are written as follows ([20]-[21]):

$$\rho\frac{D\gamma}{Dt} = \frac{\partial}{\partial x_j}\left[\left(\mu + \frac{\mu_t}{\sigma_\gamma}\right)\frac{\partial\gamma}{\partial x_j}\right] + F_{length}c_{a1}\rho S(\gamma F_{onset})^{0.5}(1 - c_{e1}\gamma) + c_{a2}\rho\Omega\gamma F_{turb}(1 - c_{e2}\gamma) \tag{4-13}$$

$$\rho\frac{D\tilde{R}e_{\theta t}}{Dt} = \frac{\partial}{\partial x_j}\left[\sigma_{\theta t}(\mu + \mu_t)\frac{\partial\tilde{R}e_{\theta t}}{\partial x_j}\right] + c_{\theta t}\frac{(\rho U)^2}{500\mu}(Re_{\theta t} - \tilde{R}e_{\theta t})(1 - F_{\theta t}) \tag{4-14}$$

where Ω is the vorticity tensor modulus, and U represents the local velocity magnitude. The parameters F_{length} and F_{onset} are empirical correlations which control the length of transition region and transition onset, respectively. F_{turb} and $F_{\theta t}$ are controllers of the destruction/re-laminarisation of the boundary layer and the boundary layer detector, respectively.

The above described controller functions are written as:

$$F_{onset} = max(F_{onset2} - F_{onset3}, 0) \tag{4-15}$$

$$F_{turb} = exp[-(R_T/4)^4] \tag{4-16}$$

$$F_{onset2} = min\left[\max\left(F_{onset1}, {F_{onset1}}^4\right), 2\right] \tag{4-17}$$

$$F_{onset1} = \frac{R_v}{(2.193Re_{\theta c})} \tag{4-18}$$

$$F_{onset3} = max\left(1 - \left(\frac{R_T}{2.5}\right)^3, 0\right) \tag{4-19}$$

$$F_{\theta t} = min\left\{max\left[F_{wake}.exp\left[-\left(\frac{U^2}{375\Omega v\tilde{R}e_{\theta t}}\right)^4\right], 1 - \left(\frac{c_{e2}\gamma - 1}{c_{e2} - 1}\right)^2\right], 1\right\} \tag{4-20}$$

$$F_{wake} = exp[-(R_\omega/10^5)^2] \tag{4-21}$$

$$R_v = \frac{\rho S y^2}{\mu},\ R_T = \frac{\rho k}{\mu\omega},\ R_\omega = \frac{\rho\omega y^2}{\mu} \qquad \text{(4-22, 4-23, 4-24)}$$

where R_v is the strain-rate Reynolds number, R_T is a turbulent Reynolds number (generally known as the viscosity ratio). $Re_{\theta c}$ is the critical momentum thickness Reynolds number at the threshold of intermittency occurrence in the boundary layer.

The constant coefficients are:

$c_{a1} = 2.0,\ c_{e1} = 1.0,\ c_{a2} = 0.06,\ c_{e2} = 50.0,\ c_\alpha = 0.5,\ c_\gamma = 1.0,\ \sigma_{\theta t} = 2.0,\ c_{\theta t} = 0.03$

The effective intermittency, γ_{eff}, is calculated as follows:

$$\gamma_{eff} = max(\gamma, \gamma_{sep}) \tag{4-25}$$

$$\gamma_{sep} = min\left[2max\left(\frac{R_v}{3.235Re_{\theta c}} - 1,0\right)F_{reattach}, 2\right]F_{\theta t} \tag{4-26}$$

$$F_{reattach} = exp[-(R_T/20)^4] \tag{4-27}$$

The boundary condition for $\tilde{R}e_{\theta t}$ at a wall is zero flux. The boundary condition at an inlet should be calculated from the empirical correlation based on the inlet turbulence intensity.

Three empirical correlations are proposed for $Re_{\theta t}$, $Re_{\theta c}$ and F_{length} to close the γ-Re_θTransition model. F_{length} and $Re_{\theta c}$ are both reported as empirical correlations which depend on the transition momentum thickness Reynolds number $\tilde{R}e_{\theta t}$. Based on experimental data by Langtry and Menter [20]-[22], two empirical correlations have been proposed for the transition onset momentum thickness Reynolds number $Re_{\theta t}$, defined in the free stream. This empirical correlation is a function of the local turbulence intensity Tu and the Thwaites pressure gradient coefficient λ_θ:

$$Re_{\theta t} = f(Tu, \lambda_\theta) \tag{4-28}$$

$$\lambda_\theta = \frac{\theta^2}{v}\frac{dU}{ds}, \qquad \frac{dU}{ds} = \frac{\partial u_j}{\partial x_j}\frac{u_i u_j}{U^2} \qquad \text{(4-29, 4-30)}$$

$$Tu = \frac{(2k/3)^{1/2}}{U}100\% \tag{4-31}$$

where dU/ds is the acceleration in the stream-wise direction.

In order to capture the laminar and transitional boundary layers correctly, the location of the nearest grid cell to the wall should approximate y^+ = 1 (section 4.1.2). The transition onset location moves upstream with increasing y^+. It is advisable to use a 2nd order upwind discretization scheme for the mean flow, turbulence and transition equations [21]. Further details of various turbulence models used in this study are presented in the Appendix (also see 0).

4.1.5 Solution approach

Second order discretization schemes produce more accurate results for heat transfer, yet are less stable in convergence compared to first order schemes, especially for the energy equation which is very important for this study. To improve the convergence a multi-step approach is used: firstly, the entire domain is initialized by inlet flow conditions and the solution starts using the first order upwind discretization scheme.

When the solution meets the convergence criteria of 10^{-6} for all the equations, the next step of solution starts with a blend of 1st and 2nd order discretization schemes based on the same convergence criteria, initialized by the results of the previous step; the blend factor is successively increased from 0 to 1 in order to ensure a full 2nd order scheme at the final step of simulation. Section 4.3.3 shows that the heat transfer results are improved by using the above mentioned approach.

4.2 Experimental methodology

4.2.1 Facility and instrumentation

The validation experiments were performed on an impinging jet test facility used for fluid dynamics and local heat transfer coefficient measurements by the authors O'Donovan and Murray [5]-[6] and Persoons et al. [13]. The geometry is identical to the numerical model shown in Fig. 4-2. An air jet issues from a nozzle consisting of a smooth brass pipe with inner diameter $D = 13mm$ and length $L = 32D$, with a sharp edged exit, shown schematically in Fig. 4-4. The pipe length exceeds the hydraulic development length by about 50% for $6000 \leq Re \leq 14,000$. The air flow to the nozzle pipe (a) at a temperature of approximately 25 ℃ is supplied by the building air compressor and dehumidification system, via a pressure regulator (c) and a mass flow controller (b) (MKS 1579A, 0-300 standard litre/min, combined uncertainty of ±3 standard litre/min).

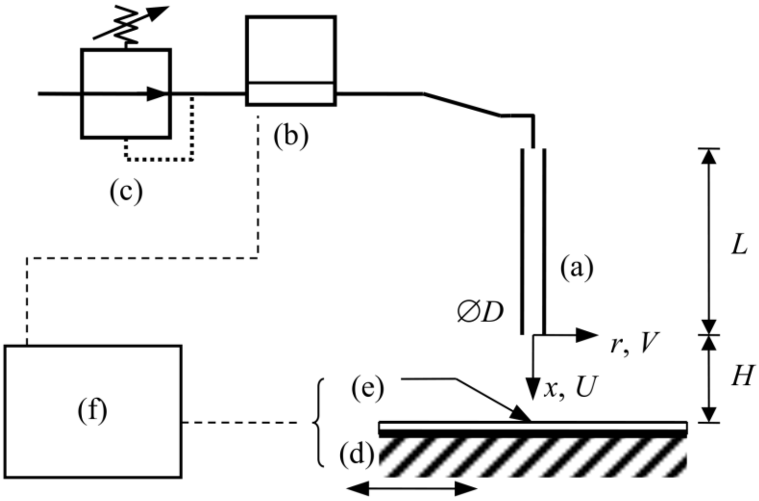

Figure 4-4. Schematic diagram of the experimental setup; (a) pipe nozzle, (b) mass flow meter, (c) pressure reducer valve, (d) instrumented isothermally heated plate, (e) embedded heat flux sensor, (f) data acquisition unit and computer

The heated impingement surface (d) consists of a flat copper plate (425×550 *mm*^{2}, 5 *mm* thick). Electrical power is supplied by a DC voltage source to a 1.1 *mm* thick silicone rubber mat with embedded wire heaters, glued with thermally conductive adhesive to the underside of the copper plate. The plate assembly is insulated underneath the heater mat. For typical jet Reynolds numbers, the representative Biot number equals 0.0013 for the copper plate. The plate approximates a constant wall temperature boundary condition which is near uniform in space and time-invariant, as verified in earlier studies [5]. The system is operated at a fixed surface temperature of 60 °*C* and an ambient temperature of about 25 °*C*, identical to the *CFD* simulations.

The local convective heat transfer coefficient is defined as $h = Nu\,(k/D) = q/(T - T_{ref})$ where q is the local convective heat flux and T is the local surface temperature. Since the flow velocity remains well below the speed of sound in these tests ($Ma < 0.05$), the reference temperature T_{ref} is taken as the jet temperature recorded with a T-type thermocouple mounted in the air supply line upstream of the pipe nozzle.

The local convective heat flux q is measured with a factory-calibrated RdF Micro-Foil^{TM} differential thermopile heat flux sensor (e), which measures the temperature difference across a well-defined thermal barrier.

4.2.2 Experimental uncertainty

The uncertainty in the Reynolds number is determined as $\varepsilon_{Re} = \Delta_{Re}/Re \cong [(\Delta_M/M)^2 + (\Delta_D/D)^2]^{1/2}$ where Δ_M represents the uncertainty in the mass flow rate and $\Delta_D \cong 0.25$ *mm* is the uncertainty in the nozzle diameter. The resulting uncertainty is $\varepsilon_{Re} \cong$ 3-6% for the investigated range based on a 95% confidence level. For steady flow, the turbulence intensity at the nozzle exit is below 8.5% of the mean velocity, based on a previous study using the same test setup [5].

The uncertainty in the reference and surface temperature is $\Delta_T < 0.1$K, based on a 95% confidence level.

The manufacturer's calibration coefficient for the heat flux sensor ($0.093\mu V/(W/m^2)$) is within 3% of the values obtained from a calibration experiment for the stagnation point Nusselt number in an impinging steady jet issuing from a long pipe nozzle (length = 80D) with a fully developed velocity profile [10]. For the experimental conditions encountered in this study, the radiation heat loss from the sensor accounts for about 3-6% of the convection heat flux near the stagnation point, up to a maximum of about 15% at $r/D \cong 4$. For the stagnation point, this effect is intrinsically contained in the heat flux sensor calibration, which is performed at the same surface and ambient temperature. The resulting uncertainty in the Nusselt number $\varepsilon_{Nu} = \Delta_{Nu}/Nu \cong [(\Delta_q/q)^2 + 2(\Delta_T/(T - T_{ref}))^2]^{1/2}$ is estimated to be approximately 6% based on a 95% confidence level, with a spatial resolution of about 1 mm in the radial direction [5]. The experimental uncertainties are shown as an error band and/or within the figure caption in the results.

4.2.3 Experimental results

Shadlesky [12] used laminar flow theory to derive a lower bound for the stagnation heat transfer rate to an impinging steady jet with a uniform nozzle velocity profile, $Nu_0 = 0.5856Re^{0.5}Pr^{0.4}$. This theoretical relationship (represented by the thin solid line in Fig. 4-5) is valid for approximately $H/D < 2$. The proportionality constant depends on the square root of the radial velocity gradient at the stagnation point, $Nu_0/(Re^{0.5}Pr^{0.4}) \propto \beta_0^{1/2}$. Since the gradient is steeper for a non-uniform velocity profile, $Nu_0/(Re^{0.5}Pr^{0.4}) = 0.5856$ can be considered a lower bound for the stagnation point heat transfer rate to an impinging pipe jet. Figure 4-5 includes experimental data from other researchers for stagnation point heat transfer for impinging jet flows from long smooth pipe nozzles. Lytle and Webb [8] used a pipe of 78*D* length ($0.1 \le H/D \le 1$, $3600 \le Re \le 27600$), as did Lee and Lee [9] ($2 \le H/D \le 10$, $5000 \le Re \le 30{,}000$). Katti and Prabhu [10] used a pipe of 83*D* long ($0.5 \le H/D \le 8$, $12{,}000 \le Re \le 28{,}000$).

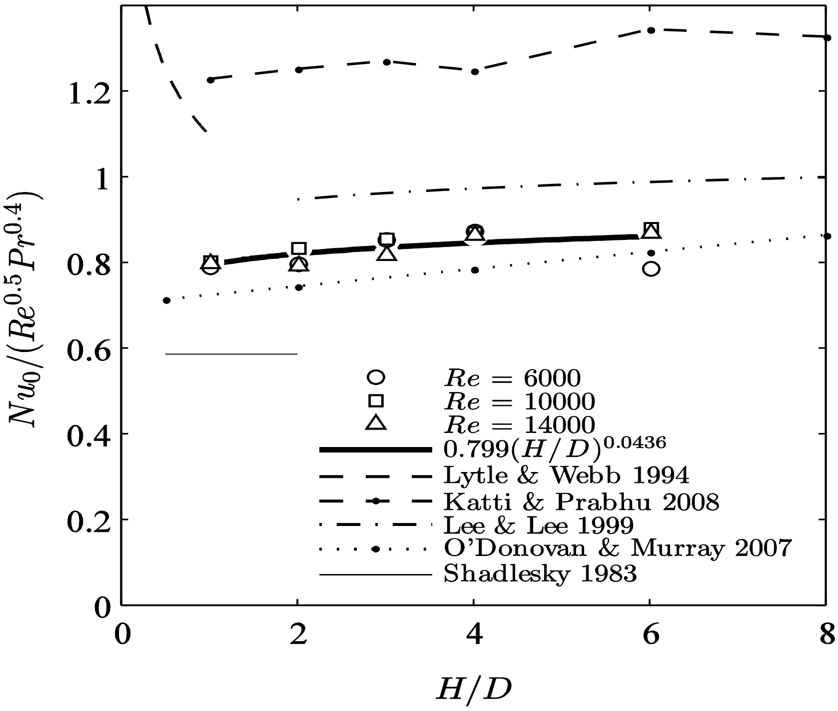

Figure 4-5. Heat transfer coefficient at the stagnation point of a steady impinging jet plotted as $Nu_0/(Re^{0.5}Pr^{0.4})$ as a function of nozzle-to-surface spacing *H/D* [5] and [13]

The hollow markers in Fig. 4-5 represent the current experiments for a steady impinging pipe jet at H/D = 1, 2, 3, 4, 6 and Re = 6000 (○), 10,000 (□) and 14,000 (△). The thick solid line represents a least squares fitted power law correlation as:

$$Nu_0 = 0.799 Re^{0.5} Pr^{0.4} (H/D)^{0.0436} \qquad (R^2 = 0.42) \qquad (4\text{-}32)$$

The Nu_0 values are at the lower end of those obtained in the other pipe flow studies, which may be attributed [8]-[10] to a lower turbulence level or to the shorter pipe length ($L = 32D$ compared to 78-83D) , [5], [12].

4.3 CFD validation and sensitivity analysis

The following sections present a comprehensive sensitivity analysis of the most influential methods and parameters in the numerical modelling. Each section discusses an individual aspect of the *CFD* methodology using the experimental data for validation. For the sake of clarity, only the comparisons to the experimental data for *Re* = 6,000 and *H/D* = 1 are presented. In all subsequent figures, experimental data are represented by hollow markers and numerical results by lines without markers. Although not shown here, the *CFD* methodology has been verified for the entire range of Reynolds number and nozzle-to-surface spacing. The effects of *Re* and *H/D* on the heat transfer coefficient distributions are presented in Section 4.4.

4.3.1 Grid independency and numerical uncertainty

A detailed sensitivity analysis on the grid density is performed to confirm grid independence of the final solution. This is performed using 5 sequentially refined grids generated from a baseline mesh $F1$ (coarse, with 60×20 nodes) by multiplying the cell number by a grid factor (*F*) of 2 to 5 in all directions. The details of different grids and their respective heat transfer results, namely the stagnation point Nusselt number (Nu_0) and the area averaged Nusselt number over the whole surface ($Nu_{ave-domain} = \frac{2}{R^2}\int_{r=0}^{R} Nu(r)rdr;\ here: R = 6D$) plus the deviation of the results from the finest mesh size (i.e. grid factor 5) are shown in Table 4-1. The Nusselt number is defined as $Nu = hD/k$ where $h = q/(T_{surf} - T_{ref})$ and k is the thermal conductivity of the fluid.

According to Table 4-1, for the grid factor 4, the deviation of Nu_{ave_Domain} values from the reference grid factor is almost negligible. The radial distribution of Nusselt number for different mesh sizes is shown in Fig. 4-6(a). The results associated with *F4* and *F5* almost coincide, except for a minor difference (less than 1%) in the stagnation region with *r/D* < 1. A more rigorous numerical uncertainty analysis is also performed using the method recommended by ASME Journal of Fluids Engineering [45]. The grid convergence index (*GCI*) method (see section 0), performed using three different sets of grids, represents the discretization error in the solution which is indicated by an error band on the numerical results.

Table 4-1. Details of different grids and their heat transfer results (Nu_0 *and* Nu_{ave_Domain}) with deviation of Nu_{ave_Domain} (%) from grid *F5* and maximum uncertainties (GCI_{max} %) for grid independency study

Grid factor (*F*)	**Size ($n_x \times n_y$)**	**Nu_0**	**Nu_{ave_Domain}**	**Deviation of Nu_{ave_Domain} %**	**GCI_{max} %**
F1	85×30	50.64	17.96	1.21	-
F2	170×60	51.60	17.99	1.05	-
F3	255×90	52.58	18.06	0.66	12
F4	340×120	54.38	18.15	0.16	4.7
F5	425×150	54.89	18.18	-	1.3

Fig. 4-6(b) shows the local calculated *GCI* error band for Nusselt number distribution using the grid *F4*; the global order of accuracy for grid *F4* is 0.9 as oscillatory convergence occurs at 14% of the grid points in Fig. 4-6(b). The *GCI* distribution has some peaks in the region of $1 < r/D < 2$ (Fig. 4-6(b)). The maximum numerical uncertainty (GCI_{max}) for different grids is also shown in Table 4-1, indicating that solutions are within the asymptotic range of convergence. Thus the grid factor 4, with a reasonably low *GCI* according to Table 4-1, provides an acceptable level of accuracy, and as a compromise between accuracy and computational time, it is not necessary to employ a finer grid than *F4*. The selected resolution (*F4*, with 340 and 120 nodes in x and y directions, respectively, for $H/D = 1$) is kept constant through all the following sections of sensitivity analysis, as long as the domain size is not changed. For further details about the GCI method used in this study see Appendix (0).

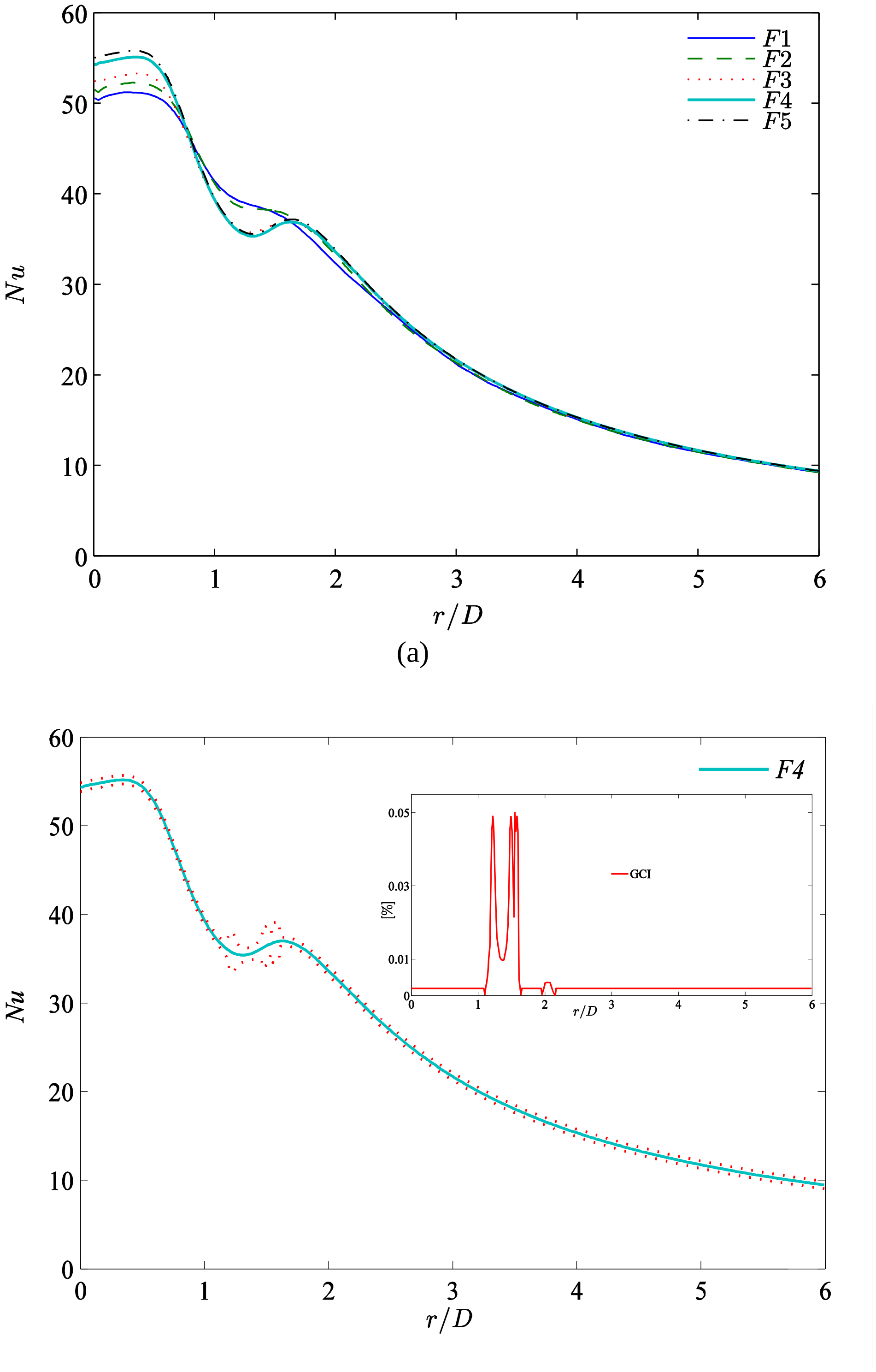

(a)

(b)

Figure 4-6. (a). Radial distribution of Nusselt number for different mesh sizes, *F1* to *F5*, listed in Table 4-1 (*Re* = 6,000, *H/D* = 1); (b). Local distribution of numerical uncertainty (GCI (%)) as error band on the selected mesh size for simulation (*F4*)

Determination of the minimum required vertical distance to the unconfined far-field top boundary is performed by simulating different distances from the heated plate, $H + H_{add}$ where H_{add} = 0-10D were simulated (see Fig. 4-2). For H/D = 1 as the main experimental case, a distance of $H + 3D$ from the impingement wall has the closest agreement with experimental data. A further increase no longer affects the Nusselt number distribution. Gao and Ewing [49] have studied the influence of confinement on the heat transfer to a round turbulent impinging jet. Their results show that the differences in heat transfer between a confined and an unconfined jet are negligible for $H/D \geq 2$, in which case it is possible to impose either a confined or an unconfined boundary.

4.3.2 Mesh skewness

Skewness is defined as the difference between the shape of the cell and the shape of an equilateral cell of equivalent volume. The mesh skewness is an appropriate indicator of the mesh quality. A poor quality grid will cause inaccurate solutions and/or slow convergence. According to the definition of the skewness, a value of 0 indicates an equilateral cell (best quality) and a value of 1 indicates a completely degenerate cell. Degenerate cells are characterized by nodes that are nearly coplanar. Cells with a skewness value above 1 are invalid. Highly skewed cells and faces are unacceptable because the equations being solved assume that the cells are relatively equilateral/equiangular. A statistical analysis of the mesh quality is implemented on the generated mesh for the current study, reporting the quality of the generated mesh. This is shown in Fig. 4-7, listing the number the grids versus the calculated mesh skewness for them. A major number of the girds (above 97%) are having a skewness of smaller than 0.15 which is considered as an excellent level of quality. Based on Fig. 4-7, maximum mesh skewness equals 0.92834, which guarantees the best analysis results for the problem with improved predictive capabilities.

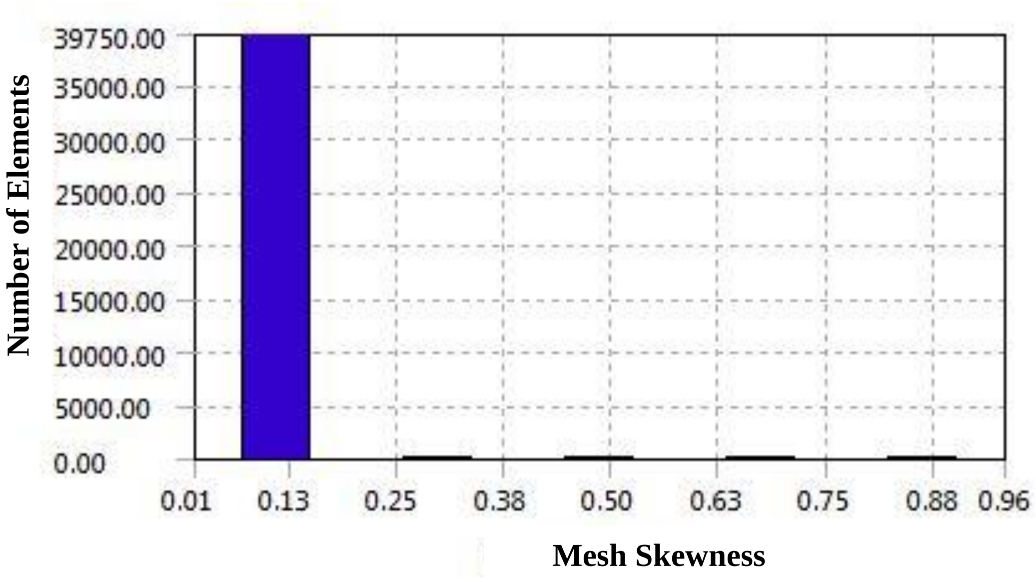

4-7. Investigation of mesh quality (skewness)

4.3.3 Discretization scheme

Employing a higher order discretization scheme for the convection term in the conservation equations is known to increase the simulation accuracy for impinging jet problems ([17]). Figure 4-8 demonstrates how a successive enhancement of the discretization scheme from first order to second order (described in section 4.1.5) improves the calculated Nusselt number results compared to the experimental values. The 2nd order scheme resolves the domain to capture the second peak in Nusselt number distribution in the radial direction. The first order scheme is inconsistent with the experimental data for the region with *r/D* < 2, which is mainly attributed to unstable convergence of the transition equations.

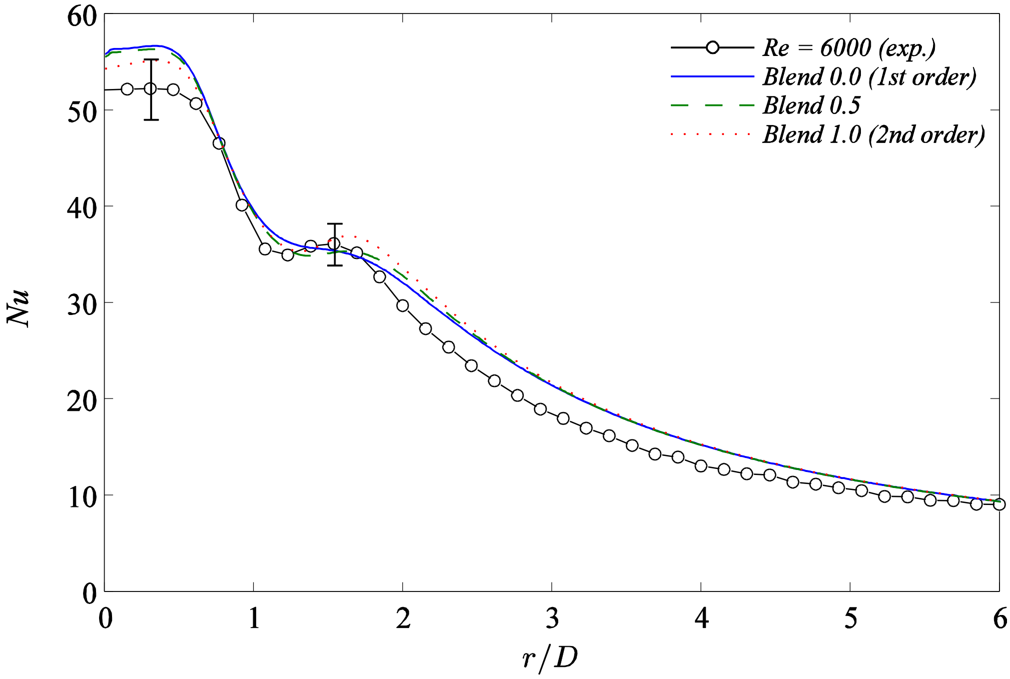

Figure 4-8. Comparison of radial distribution of Nusselt number for different discretization schemes to experimental data (*Re* = 6,000, *H/D* = 1; error bars display exp. uncertainty)

4.3.4 Inlet velocity profile

The heat transfer rate strongly depends on the inlet conditions such as the velocity profile and turbulence intensity. Figure 4-9 compares the heat transfer results obtained for different velocity profiles at the nozzle exit (domain inlet). The fully developed velocity profile is characterized by a higher flow momentum in the centre of the jet compared to the uniform flow, thereby leading to a steeper radial velocity gradient in the stagnation zone, which Shadlesky [12] has shown to be linked to higher stagnation Nusselt number. In the present study, the fully developed velocity profile produces a local Nusselt number distribution in the stagnation region with a maximum deviation of 5% from the experimental data. By contrast, for the uniform velocity profile with the same mean velocity, the local Nusselt number distribution exhibits a significant deviation from measured data, especially in the stagnation and transition regions up to *r/D* = 2 where the uniform and developing profiles under-predict the radial Nusselt number distribution.

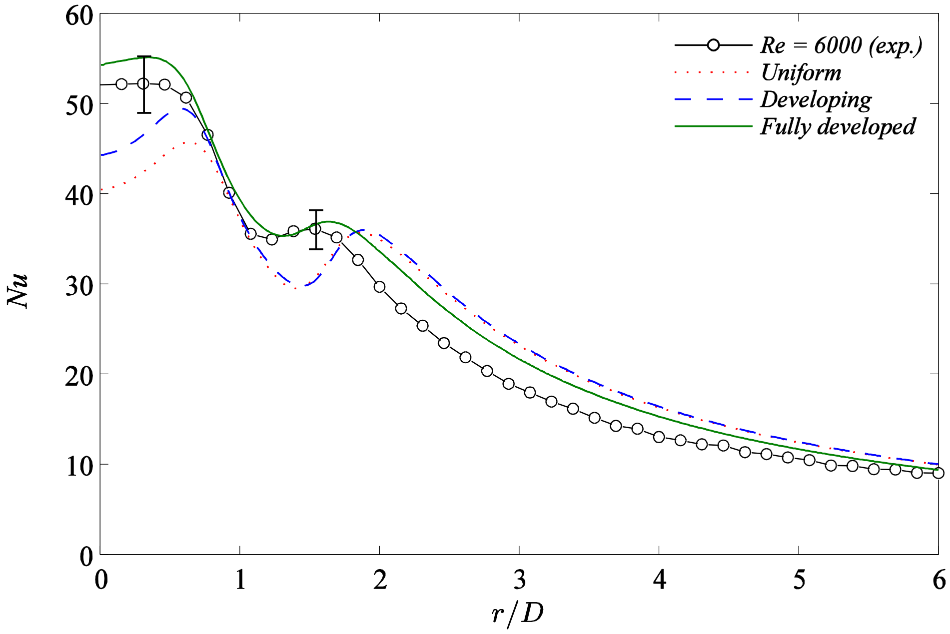

Figure 4-9. Comparison of radial distribution of Nusselt number for different inlet velocity profiles to experimental data (*Re* = 6,000, *H*/*D* = 1; error bars display exp. uncertainty)

Figure 4-10 provides a better understanding by comparing the radial distribution of normalized turbulent kinetic energy in the near-wall region (here: 0.01*D* from the wall, inside the momentum boundary layer) for different inlet velocity profiles. The heat transfer coefficient is closely related to the turbulence intensity and radial velocity gradient. As shown in Fig. 4-10, the turbulent kinetic energy in the region $r/D < 2$ is lower for a uniform nozzle exit profile which helps to explain the Nusselt number deviation from experimental data. For the fully developed profile, the location of the peak turbulence intensity reasonably matches the secondary peak in the Nusselt number distribution, corresponding to the laminar-to-turbulent transition. This agrees with the findings of O'Donovan and Murray [5] and Colucci and Viskanta [23].

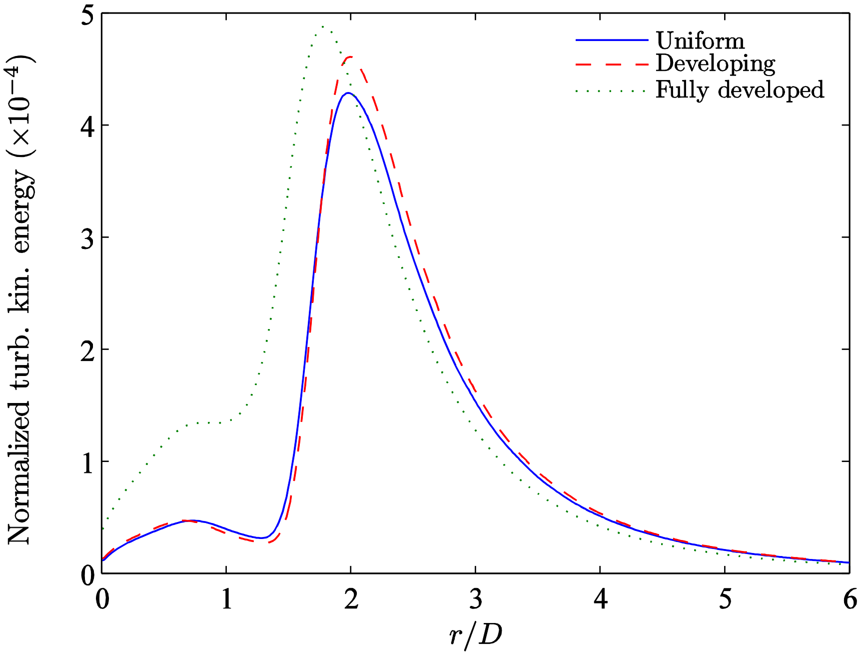

Figure 4-10. Radial distribution of normalized turbulence kinetic near the wall (at 0.01*D*) for different inlet velocity profiles (*Re* = 6,000, *H/D* = 1)

The radial velocity gradient in the near-wall region is shown in Fig. 4-11. The jet flow with the fully developed velocity profile exhibits the steepest radial velocity gradient accompanied by a strong radial acceleration. The subsequent abrupt deceleration of the wall jet flow coincides with the laminar to turbulent transition, which is reflected in the secondary Nusselt number peak in Fig. 4-9. The further radial development of the wall jet (*r/D* > 2) shows a monotonic reduction of Nusselt number (Fig. 4-9) and a decaying negative velocity gradient (Fig. 4-11) as the flow spreads out radially.

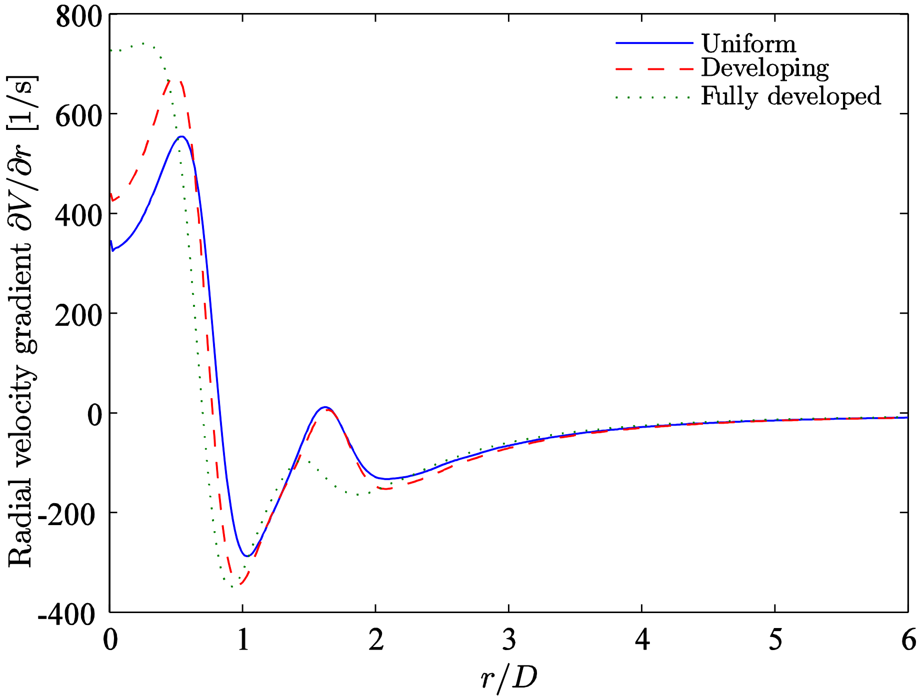

Figure 4-11. Radial distribution of radial velocity gradient (s^{-1}) near the wall (at 0.01*D*) for different inlet velocity profiles (*Re* = 6,000, *H/D* = 1)

4.3.5 Inlet turbulence intensity

Consideration should be given to the correct estimation of the turbulence intensity at the nozzle inlet (Fig.1-4). As described in section 4.1.1, this is performed using a separate simulation for a long nozzle pipe, and turbulence intensity profiles are mapped from the nozzle exit to the domain inlet of the main simulation. The variation in turbulence intensity at the nozzle inlet affects the turbulence intensity profile at the nozzle exit, and consequently the surface heat transfer, especially at low *H/D*. Figure 4-12 shows the effect of the nozzle inlet turbulence intensity on the Nusselt number distribution. High turbulence enhances the momentum diffusion in the jet which reduces the potential core length.

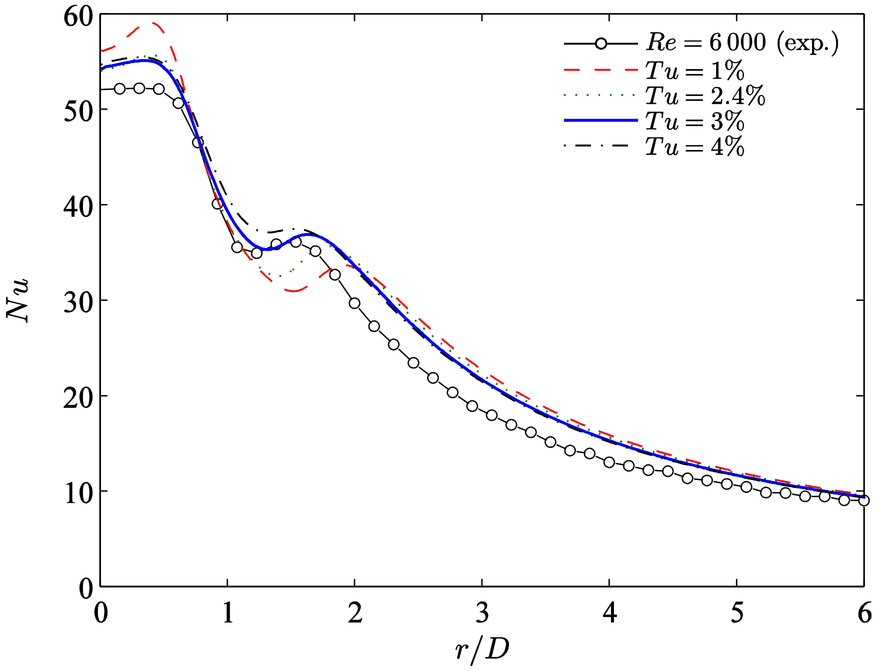

Figure 4-12. Comparison of radial distribution of Nusselt number for different inlet turbulence intensities (%) to experimental data (*Re* = 6,000, *H/D* = 1; Exp. uncertainty = 6%)

As seen in Fig. 4-12 different turbulence levels mainly affect the intensity and location of the secondary peak in the Nusselt number distribution. This is known as the transition region (1 < *r/D* < 2). With the exception of the low turbulence case (*Tu* = 1%), the different values from *Tu* = 2% to 4% produce approximately the same heat transfer results in the stagnation region (*r/D* < 1) and developing wall jet region (*r/D* > 2). Upon comparison with the experimental data, a turbulence intensity of *Tu* = 3% is selected as the final value for further numerical investigation of this case. As described by Viskanta [10] and Jambunathan et al. [4], the inlet turbulence intensity does not have a significant impact for larger values of *H/D* where the turbulence created in the shear layer becomes dominant.

4.3.6 Turbulence model

As described in section 4.1.4 the turbulence models evaluated in the present study are: *k-ε, RNG k-ε, k-ω, SST* with and without transition model. Figure 4-13 shows the effect of the turbulence model on the simulation results, with the corresponding experimental data included as markers. The *k-ε, RNG k-ε* and *k-ω* models fail to predict the correct trend of the Nusselt number distribution, as they are mostly associated with an unstable convergence. Generally, the k-ε model is not ideal for the prediction of separation, swirling flows, and flows with strong streamline curvatures. The *k-ω* model works well for the outer region (*r/D* > 2) but is unreliable for *r/D* < 2 where it considerably over-predicts the experimental Nusselt number.

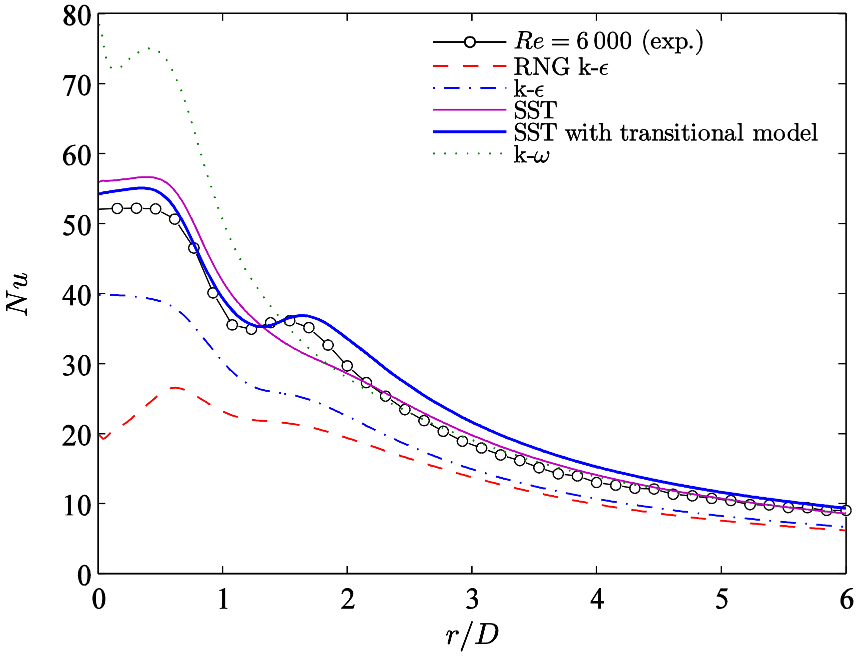

Figure 4-13. Comparison of radial distribution of Nusselt number for different turbulence models to experimental data (*Re* = 6,000, *H*/*D* = 1; Exp. uncertainty = 6%)

For flows containing recirculation zones, the Shear Stress Transport (*SST*) model is a better turbulence model, to be used without additional damping function. One advantage of the *SST* model is the near-wall treatment for flow computations at low values of turbulent Reynolds number in the viscous sub-layer. The *SST* formulation also switches to the k-ε behaviour in fully turbulent flow fields and thus avoids the common k-ε problem where the model is excessively sensitive to the inlet free stream turbulence properties [17]. A comparison of the different turbulence models for a numerical study of jet impingement heat transfer has been performed by Zuckerman and Lior [50]. Large errors (up to 60%) were reported in estimated Nusselt number distributions for most versions of *k-ε, k-ω* and Reynolds stress models. The authors recommend the *SST* model for its low computational cost when secondary peaks in the Nusselt number distribution are not expected. Models that capture the secondary peak are the v^2f model with a moderate computational cost, and large eddy simulation (*LES*) and direct numerical simulation (*DNS*) with high computational costs. Therefore, the *SST* model is chosen, coupled with a complementary transition model, as a compromise between low computational cost and reliably capturing the laminar-to-turbulent transition which is characteristic for these impinging jet flows.

A critical point in the present study is the correct modelling of the laminar-to-turbulent boundary layer transition which occurs in the wall jet flow, and directly affects the heat transfer results. According to Fig. 4-13, the selected transition model coupled with the *SST* formulation (section 4.1.4) accurately predicts the intensity, position and extent of the secondary peak in the radial Nusselt number distribution. This is the only model which shows a satisfactory agreement with the experimental data, while the *SST* without transition model fails to capture the secondary peak. The current study complements the recent findings of Caggese et al. [16], confirming that the primary factor in achieving accurate results is the choice of turbulence model, rather than the other investigated parameters; see Appendix A.5.

4.3.7 Turbulent Prandtl number

The turbulent Prandtl Number, Pr_t, is the ratio of eddy diffusivities for momentum and heat transfer. The value of Pr_t in the near-wall region becomes very important in the prediction of turbulent heat transfer, since it directly affects heat diffusion. Reynolds [51] reports that the most common way of relating variations of time-averaged velocity and temperature across a turbulent shear layer is through the introduction of uniform values for the turbulent Prandtl number. He also suggests values of $Pr_t = 0.7$ for round jets and $Pr_t = 0.5$ for other shear flows (e.g., mixing layers, plane jets, and wakes). There have been many discussions in the literature about the parameters that affect the turbulent Prandtl number in the boundary layer, resulting in quite a lot of semi-empirical correlations which show the combined dependence of Pr_t on Reynolds number, molecular Prandtl number and non-dimensional distance from the wall, $Pr_t = f\{Re, Pr, y^+\}$ ([53]-[59]). Antonia and Kim [52] have evaluated Pr_t in turbulent wall shear flows, confirming that Pr_t tends to a constant value irrespective of the molecular

Prandtl number in the near-wall region. Table 4-2 shows a brief review of various results for Pr_t from different studies, for the configurations used in the present study.

Table 4-2. Turbulent Prandtl number values suggested by different studies for various applications

Mayer & Divoky [53]	*plane turbulent jets & wakes*	0.42–0.83
Patankar & Spalding [54]	*boundary layer h. t.*	0.9
Browne & Antonia [55]	*Plane jet*	0.65
Kays [56]	*boundary layer h. t.*	0.85
Kawamura et al. [57]	*h. t. in a channel flow*	1
Chidambaram et al. [58]	*axisymmetric round jets*	0.7
Churchill [59]	*boundary layer h. t*	0.7-0.94

The range of values for Pr_t shown in Table 4-2 suggests that the correct value may be different from the default of 0.9 in the Ansys CFX software. The appropriate value for the present case is calculated by comparison of experimental and numerical results, as shown in Fig. 4-14. Values ranging from 0.7 to 0.8 generate roughly the same results, except for a minor difference beyond the transition region (Fig. 4-14).

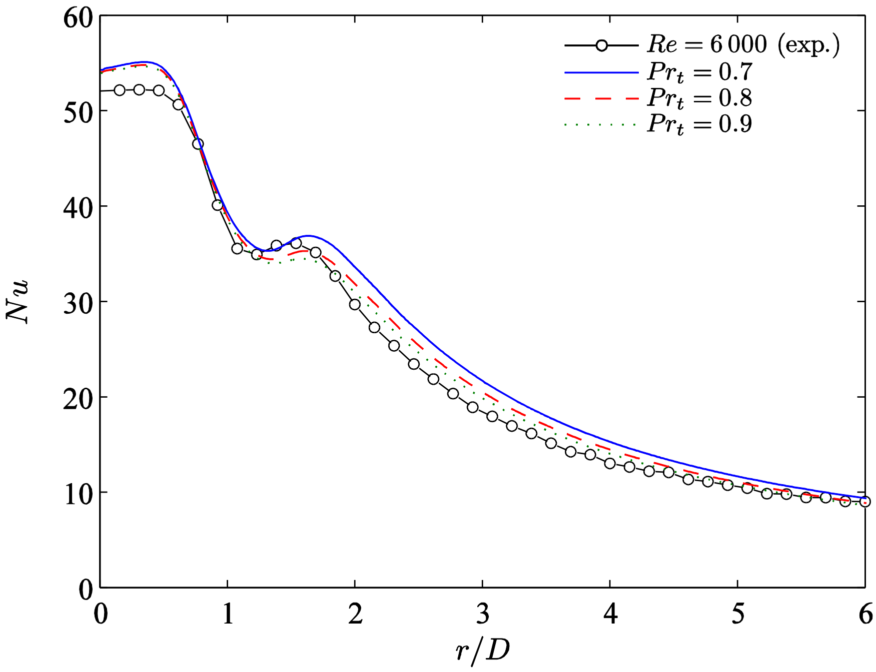

Figure 4-14. Comparison of radial distribution of Nusselt number for different turbulent Prandtl numbers to experimental data (*Re* = 6,000, *H/D* = 1; Exp. uncertainty = 6%)

To accurately capture the intensity and the location of the secondary peak in the *Nu* number distribution, a value of $Pr_t = 0.7$ is chosen here, which agrees well with values suggested by the other studies in Table 4-2. However, it is worth mentioning that a value of $Pr = 0.9$ provides a slightly better prediction of the area-averaged Nusselt number over the whole region ($0 < r/D < 6$).

4.4 Numerical results and discussion

4.4.1 Effect of Reynolds number

The heat transfer to the impinging jet strongly depends on the Reynolds number which is directly associated with the flow momentum. Figure 4-15 compares the numerical and experimental radial Nusselt number data for Reynolds numbers of 6000, 10,000 and 14,000 for $H/D = 1$. The nozzle inlet turbulence intensity to ensure best agreement with the experimental data is $Tu = 3\%$ for $Re = 6000$, $Tu = 2\%$ for $Re = 10{,}000$ and $Tu = 1.5\%$ for 14,000. Apart from the nozzle inlet turbulence intensity, all other numerical parameters are maintained as described in Section 4.3.

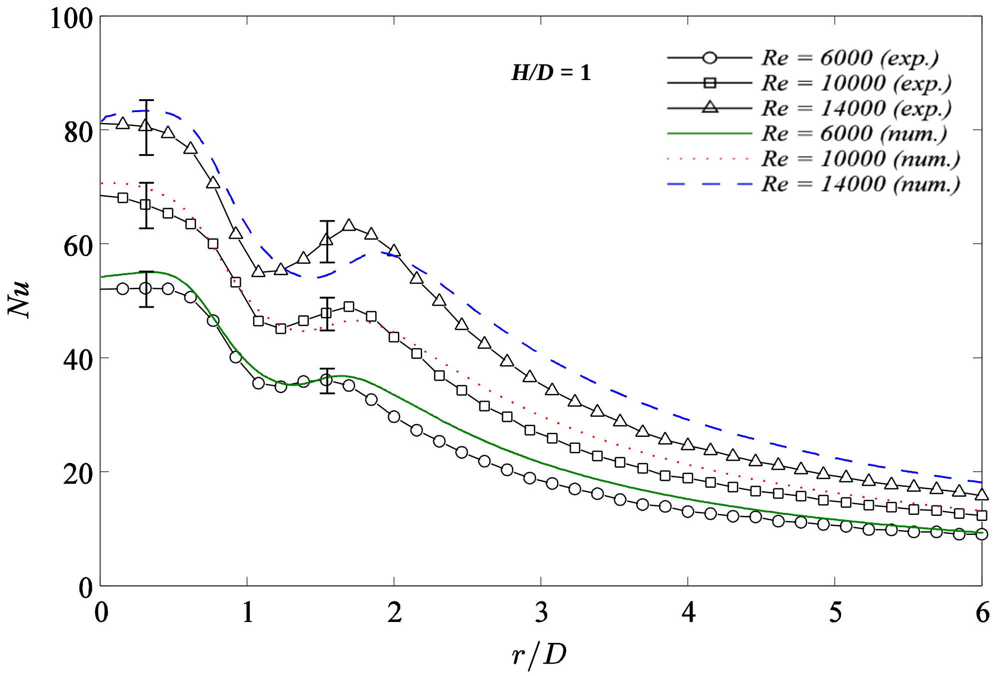

Figure 4-15. Comparison of radial distribution of Nusselt number for different Reynolds numbers to experimental data (*H*/*D* = 1; *Re* = 6,000, 10,000 and 14,000; error bars display exp. uncertainty)

As shown in Fig. 4-15, the data for different Reynolds numbers are in acceptable agreement with the experiments, exhibiting a maximum deviation of 6%, 4% and 3% for *Re* = 14,000 in terms of local (*Nu*), area-averaged ($Nu_{ave\text{-}domain}$) and stagnation point (Nu_0) Nusselt numbers, respectively. However even for this case the model correctly predicts the heat transfer for $r/D < 1$, with the main deviation in the transition region ($1 < r/D < 2$). Nevertheless the trend is correctly predicted. This deviation is partly due to the elongation of the potential core at larger Reynolds number which corresponds to higher jet exit velocities, and partly because of the numerical and experimental uncertainties which increase with Reynolds number in the transition region.

4.4.2 Second peak in *Nu* distribution

Numerical investigation of the complex flow field of an unsteady impinging jet can help to understand the effect of vortical structures on the heat transfer, and specifically the nature of turbulence fluctuations in the stagnation point and developing wall jet zone.

The secondary peak in radial distribution of *Nu* is one of the major characteristics of impinging jets for small jet to surface spacings. The flow acceleration in the developing region of the boundary layer is closely related to the secondary peak in the radial distribution of Nusselt number. Further downstream, the developing wall jet region is interrupted by the impinging turbulent shear layer. The combined effect of the radially accelerated wall jet and the vertically impinging shear layer results in transition of the wall jet flow from the laminar to the turbulent mode around the region with $r / D \approx 2$. The consequent local increase in the wall-normal velocity fluctuations, or the turbulence in the wall jet, results in a local thinning of the thermal boundary layer which is found as one of the main reasons for the jump in *Nu* distribution.

The numerical method developed in this study employs a transitional turbulence model that captures the local increase in the wall-normal velocity fluctuations which helps to precisely predict the transition region. Therefore, the intensity and the extent of the secondary peak in the radial *Nu* distribution can be modelled.

At larger values of *H/D*, the axial velocity of the radial wall jet is smaller and its combined effect with the following impinging shear layer (with reduced turbulent levels at larger *H/D*) does not cause the same wall jet flow development as for small *H/D* values, and conclusively, no secondary peak is visible.

4.4.3 Effect of nozzle-to-impingement surface distance

As described in section 4.3.1, the computational mesh size has been kept the same for all the previous sections, because the domain remained unchanged. The required mesh size to resolve the flow field and heat transfer in the boundary layer is unique for each nozzle-to-surface distance, and a distinct mesh is generated for each *H/D* value according to the procedure in section 4.3.1.

The position of the secondary Nusselt number peak is a function of both *Re* and *H/D*, and both the experimental and numerical results in Fig. 4-16 confirm this. O’Donovan and Murray [5] report that for higher values of *H/D* the shear layer penetrates to the stagnation point, resulting in a diminished velocity and increased turbulence intensity at the centreline. In this case the turbulence created in the shear layer becomes dominant.

As shown in Fig. 4-16, the influence of the inlet conditions becomes negligible. For the case of *H/D* = 2, the secondary peaks in numerical predictions are visible with some degree of deviation in the transition region. This can mainly be attributed to the slight increase in numerical uncertainty which occurs in the region $1 < r/D < 2$ (see section 4.3.1). This is the reason for the deviation of the results in the same region for larger values of *H/D* as well. Also, at larger values of *H/D* the axial velocity of the jet in the region with $r/D < 1$ is smaller and does not cause the same wall jet flow development as for small *H*/*D* values. Conclusively, the profile does not have an evident secondary peak in the Nusselt number distribution due to a more uniform turbulence distribution level, as shown in Figs. 4-16 (c) and (d) for *H/D* = 4 and 6, respectively.

As with the experimental results (Eq. (1)), two least squares fitted power law correlations of the stagnation point Nusselt number are derived from the numerical results:

$$Nu_0 = 0.784Re^{0.5}Pr^{0.4}(H/D)^{0.064} \qquad (R^2 = 0.978) \qquad (4\text{-}33)$$

$$Nu_0 = 0.663Re^{0.518}Pr^{0.4}(H/D)^{0.064} \qquad (R^2 = 0.978) \qquad (4\text{-}34)$$

Eq. (4-32) is based on the assumption of a fixed value for the power of *Re* number (here 0.5, see Shadleskey [12]), while Eq. (4-34) uses a least-square fitted value for the power of *Re* number.

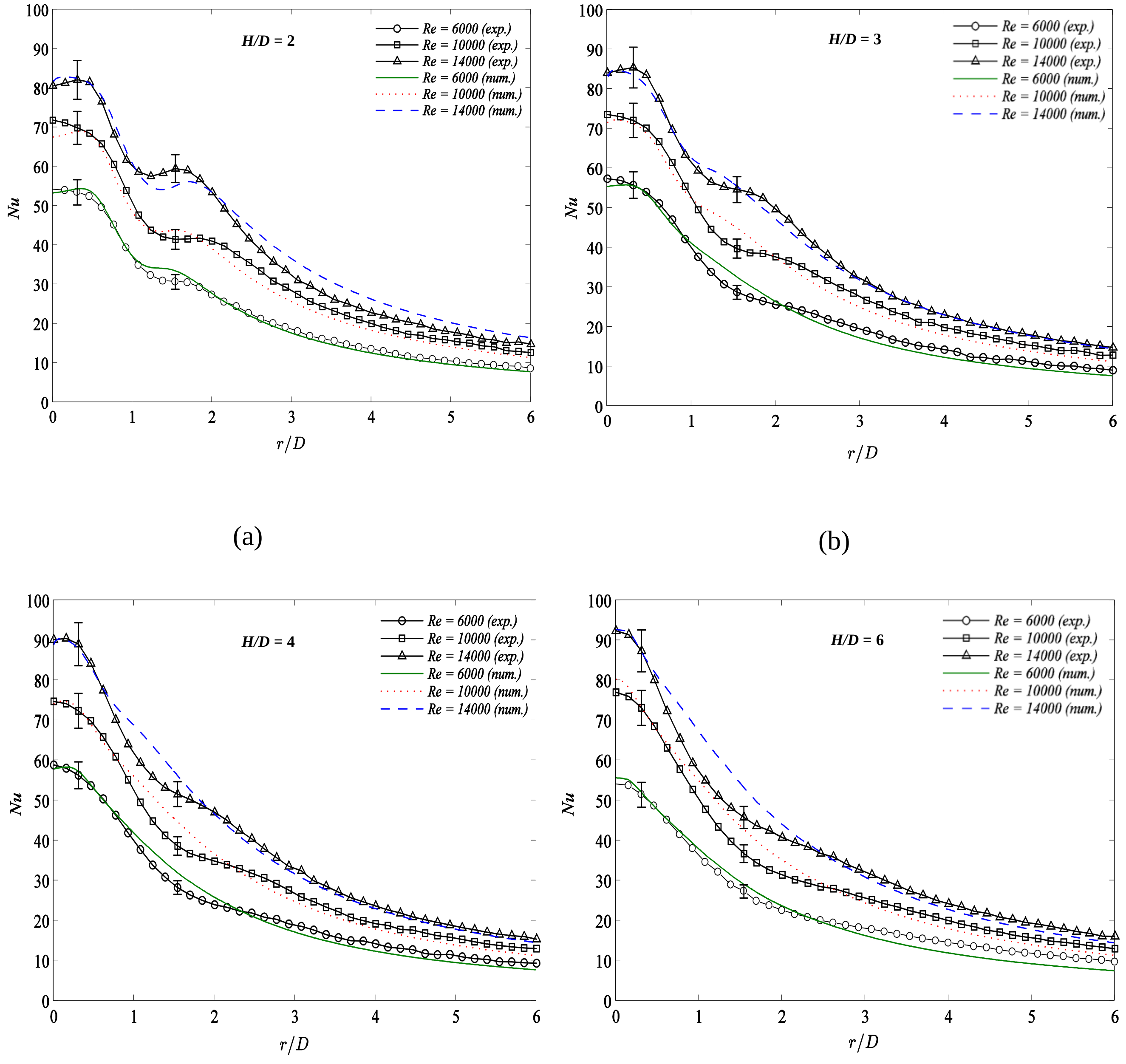

(a) (b)

(c) (d)

Figure 4-16. Comparison of radial distribution of Nusselt number for different nozzle-to-surface distances to experimental data: (a) *H/D* = 2, (b) *H/D* = 3, (c) *H/D* = 4 and (d) *H/D* = 6 (*Re* = 6,000, 10,000 and 14,000; error bars display exp. uncertainty)

4.5 Conclusion

The performance evaluation of computationally efficient turbulence models shows that with realistic configurations of boundary conditions, computational domain, fluid properties and solution approach, numerical modelling is able to accurately predict the local heat transfer coefficient for a circular steady impinging jet.

The results for the *SST* turbulence model coupled with the *Gamma-Theta* Transition model, as a computationally low cost model, show improvements in accurate prediction of the position, intensity and extent of the secondary peak in the local Nusselt number distribution, as determined from a comparison with detailed experimental measurements for validation.

Furthermore, by iteratively adapting the grid density in the near-wall region, the large velocity, temperature and turbulence quantity gradients in the momentum and thermal boundary layers are well captured. Correlations based on the experimental and numerical heat transfer coefficient data are generated for the stagnation point Nusselt number for a wide range of operating conditions, incorporating the effect of Reynolds number ($6000 \leq Re \leq 14{,}000$), nozzle-to-surface distance ($1 \leq H/D \leq 6$) in the standard formulation $Nu_0 = a.Re^{0.5}Pr^{0.4}(H/D)^n$ with $a = 0.799$ and $n = 0.0436$ for the experiments and $a = 0.784$ and $n = 0.064$ for the numerical model (see Equations (4-32) and (4-33)).

The turbulent Prandtl number in the near-wall region has proven an important parameter in the prediction of turbulent heat transfer since its value directly affects the level of heat diffusion. Here, to most accurately capture the intensity and location of the secondary peak in the Nusselt number distribution, a turbulent Prandtl number value $Pr_t = 0.7$ is proposed for the simulations, which is in line with the values suggested by other studies (see Table 4-2). However, a value of $Pr_t = 0.9$ would yield slightly more accurate results in terms of the overall area-averaged Nusselt number.

By accurately reproducing the experimental boundary conditions in the numerical model, the simulated Nusselt number distributions in the stagnation region deviate less than 4% from the experimental results. For the entire range of Reynolds numbers, a maximum deviation of 6% is found with the experimental local Nusselt numbers, for the case of *Re* = 14,000. The location of the secondary peak in the Nusselt number distribution in the region $1 < r/D < 2$ is captured well. It is not affected significantly by the inlet turbulence intensity for larger values of *H/D* where the turbulence created in the shear layer becomes dominant. The position of the secondary Nusselt number peak varies consistently with *Re* and *H/D*, both in the experiments and numerical results.

The effect of Reynolds number and nozzle-to-surface spacing shows that the computational model is robust enough for a wide range of geometrical and operational conditions. This provides an encouraging starting point to extend this numerical methodology towards unsteady impingement flows such as synthetic or pulsating jets [13], [24]-[35] as discussed in the next chapter.

Some of the findings presented in this chapter have been published in Alimohammadi et al. [34].

5 Pulsating Impinging Jet Flows

This chapter presents the second part of a comprehensive numerical-experimental study performed on unsteady impinging jets with flow pulsation and builds on an experimentally validated numerical Reynolds-averaged Navier Stokes (*RANS*) *CFD* model for fluid flow and heat transfer simulations of steady impinging jets. The model accounts for intermittent pulsation with a square-wave form as the inlet velocity signal (see Fig. 5-1). Comparing against experimental local heat transfer data as reference, accurate *CFD* simulation results are presented. The study is performed over an extensive range of operating conditions for an axisymmetric air jet impinging on a flat surface for nozzle-to-surface distances $1 \leq H/D \leq 6$, Reynolds numbers $1{,}300 \leq Re \leq 2{,}800$ and Strouhal number $0.0029 \leq Sr \leq 0.333$ (pulsation frequency $5\ \mathrm{Hz} \leq f \leq 260\ \mathrm{Hz}$). The numerical model is used to extend the findings beyond the experimental range and simulates considerably higher pulsation frequencies. The numerical results also provide a more detailed insight into the near-wall behaviour in the viscous sub-layer, which helps to understand the governing heat transfer mechanisms. Correlations for the averaged and stagnation point Nusselt number enhancement in pulsating flow have been least-square fitted to the numerical data as a function of suitably modified Strouhal numbers.

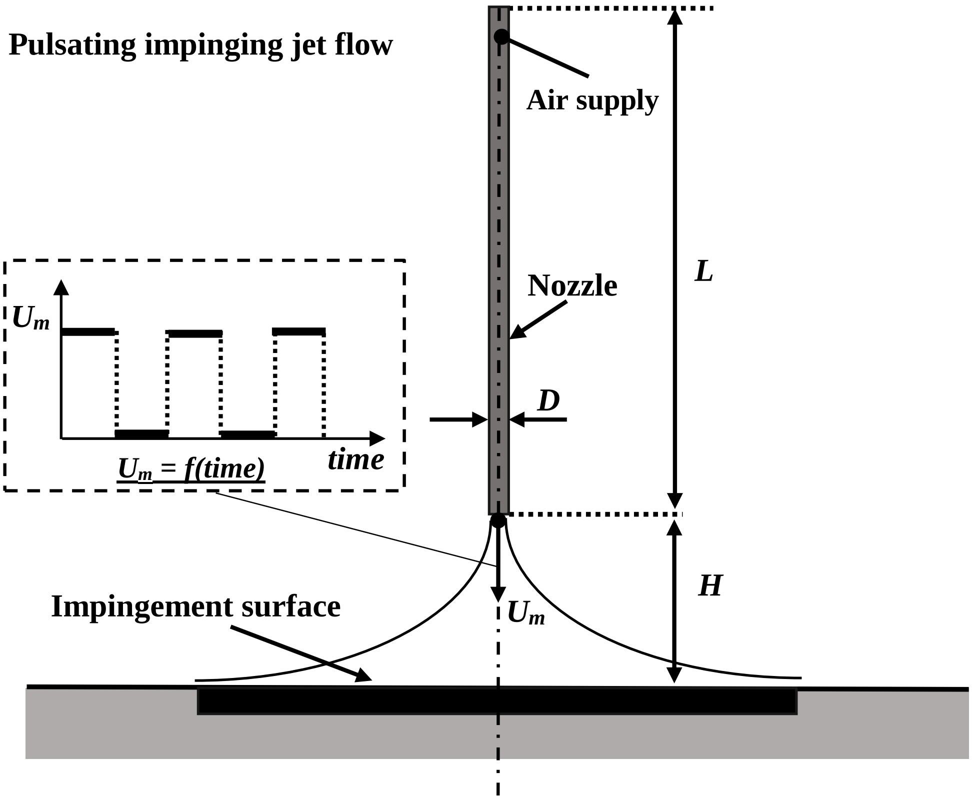

Figure 5-1. Schematic diagram of pulsating impinging jet flow

5.1 Numerical approach

The step-by-step approach toward the development of the unsteady *CFD* simulation methodology is briefly described in this section. For the sake of brevity, this section does not repeat the descriptions given earlier in section 4.1 about the development of the numerical model for a steady jet, and it only provides required information for the improvement of the model toward simulation of unsteady flows applied to pulsating jets.

Figure 5-2 depicts the solution domain, the generated mesh and the boundary conditions used in the simulation. The *CFD* model reproduces the exact configuration used in the accompanying experiments (see section 5.2). As for the steady impinging jet flow, an axisymmetric two-dimensional section of the domain is simulated. The computational domain extends far enough from the area of interest (up to a radial distance of 16*D* from the jet centreline) to prevent any outlet boundary effects on the results.

The boundary conditions are the same as those shown in section 4.1 for a steady jet. The major difference is the inlet velocity profiles which are defined as a function of time to account for flow pulsation at the nozzle inlet. This is described in detail later in this section. The procedure to determine the minimum required vertical distance from the unconfined top boundary (distance above the nozzle exit) is also explained in section 4.1. This is done to show that the entrainment from the surrounding region above the nozzle exit is modelled correctly. The planar heated wall surface at the bottom of the domain is set to a constant temperature of 60 ℃, in accordance with the experiments (see section 5.2).

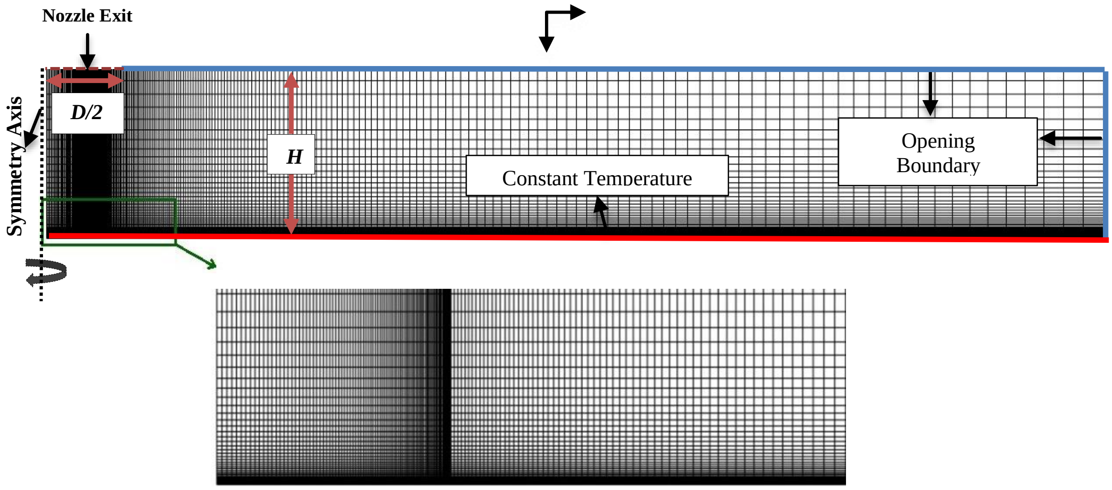

Figure 5-2. Schematic representation of the solution domain, the generated mesh and boundary conditions used for the numerical simulation

Contrary to the numerical model prepared for a steady jet, to prevent complications due to back flow into the nozzle exit between two ejection phases, the nozzle and jet domain are solved together in a single model. So the flow at the outlet of the nozzle is no longer mapped into the jet domain from a separate solution, but it is taken directly during the solution as the nozzle and jet domain are coupled to each other in the same model.

In the same manner as that of steady jets, the basic mesh topology is produced based on the structured approach with a quadrilateral mesh; the mesh is then adapted iteratively in regions with large gradients, such as the impingement wall region and the mixing region of jet and surrounding entrained air, in order to achieve a stable solution. This is shown in Fig. 5-3.

Step 1 295× 120	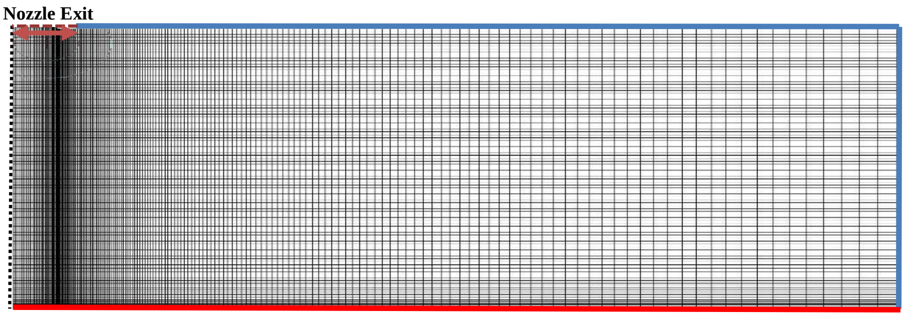
Step 2 335×150	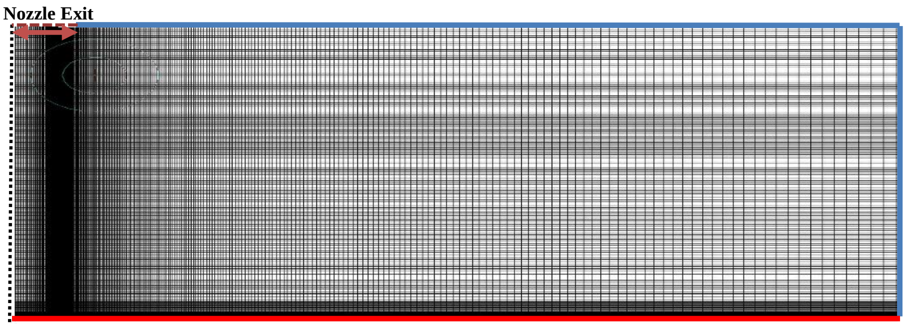
Step 3 390×180	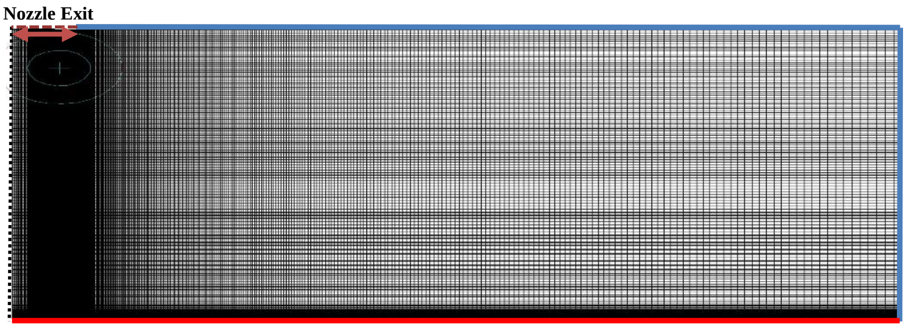

Figure 5-3. Progressive images showing the mesh refinement and adaption procedure

An essential question in numerical *CFD* analysis is what level of mesh resolution is appropriate for the solution. Due the increased complexity of simulations from steady to unsteady jet modelling, this issue is further investigated in this chapter.

Traditional methods of estimating discretisation error define it as the error in the solution due to the choice of space and time resolution. This method is useful when the exact solution of the problem is known to determine the error and illustrate the rate of convergence. However, the numerical solution in this method will never be totally mesh-independent. So there is a distinction between the results which approach an asymptotic numerical value, and the results which approach the true solution. There still may exist some deviation (error) between the asymptotic numerical value and the correct physical answer. As a result, there should be a confirmed threshold below which the mesh is considered to be independent.

In this study, a Grid Convergence Index (*GCI*) study is performed to quantify the discretisation error [45]. This method is suggested by Roache [60] as a consistent approach for reporting the results of grid convergence investigations. As an advantage of this method, it is not necessary to *double* the resolution in each step to obtain the finer grid. In fact, a non-integer grid refinement factor should be used, because doubling the resolution may put the solution out of the asymptotic range. *GCI* is reported as a percentage error and supplies a confidence bound on the estimated error band within which the numerically converged solution will likely stand. This is performed using three different sets of grids. The method provides an estimate of the numerical uncertainty of the solution, and it predicts how a further grid refinement will change the solution.

The *GCI* study performed for this study is reported in Table 5-1. The presented results are for the case with Re = 1,300, H/D = 1, f = 40 Hz. This is done by comparison of grid size versus area-averaged Nusselt number $\overline{Nu}$ for 1st and 2nd order discretisation schemes. The maximum numerical uncertainties (GCI_{max}) for different grids are also shown for both schemes in Table 5-1, indicating that the solutions are within the asymptotic range of convergence.

Table 5-1. Grid independency study using different grid refinement factor, area-averaged Nusselt number $\overline{Nu}$, and maximum uncertainties (*GCImax* %) for 1st and 2nd order discretisation schemes

Grid refinement factor	Size ($n_x \times n_y$)	$\overline{Nu}$ *1st order*	Deviation %	$\overline{Nu}$ *2nd order*	Deviation %	GCI_{max} % *1st order*	GCI_{max} % *2nd order*
1	25,000 (250×100)	8.517	25.35	9.231	19.84	-	-
1.4	35,000 (295× 120)	9.654	15.38	10.156	11.80	-	-
2	50,000 (335×150)	10.620	6.92	10.862	5.68	10.09	7.39
2.8	70,000 (390×180)	11.268	1.1	11.452	0.55	4.23	1.64
3.5	87,500 (450×195)	11.409	-	11.516	-	2.14	1.17

The area-averaged *Nu* for 1st and 2nd order discretisation schemes is also depicted for each grid size in Fig. 5-4. For a coarse mesh the solution is both grid-spacing and spatial discretization-order dependent, indicating that both of these numerical aspects affect the results. For finer meshes with 2nd order scheme, reduced GCI_{max} values confirm that the solution has a small dependence on the grid spacing. Conversely, the 1st order method is still dependent on grid spacing, as this method obviously requires a finer mesh to reach grid independence [61]. The reason behind the fact that 2nd order scheme is superior on coarser meshes is the global truncation error. This is defined as accumulation of the local truncation error of an infinite phenomenon over all of the iterations, assuming perfect knowledge of the true solution at the initial time step. This error is higher for 1st order scheme at a given grid size [62].

Through a uniform grid refinement procedure, shown in Table 5-1, the finer grids are generated by multiplying the refinement factor to the base-line grid size with 25,000 nodes. The grid refinement factor of 2.8, with 70,000 nodes, is the best choice as a compromise between accuracy and computational cost, so it is not necessary to employ a finer grid.

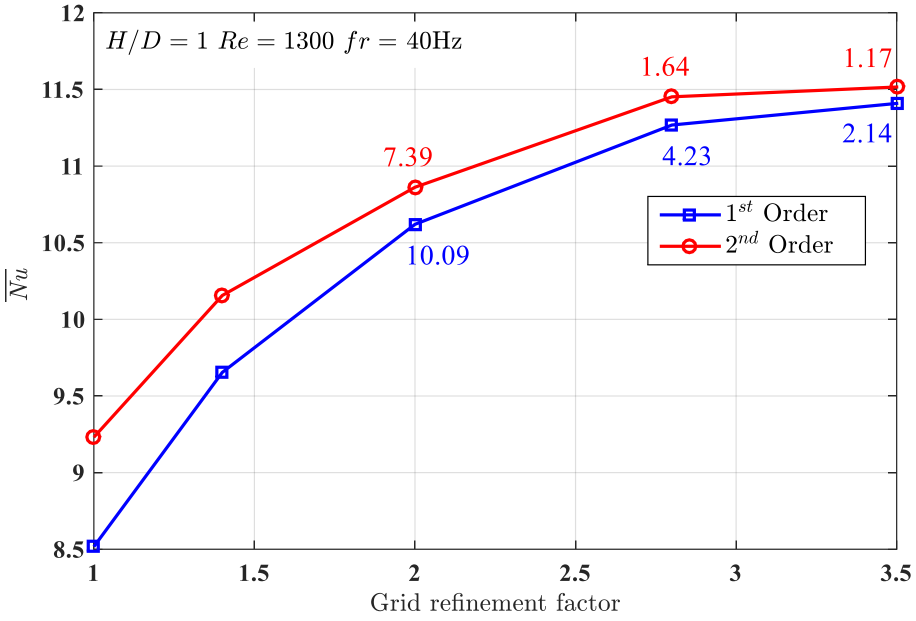

Figure 5-4. Area-averaged Nusselt number versus grid refinement factor together with maximum Grid Convergence Index (GCI_{max} %) values for 1st and 2nd order discretisation schemes

All the other details such as the chosen turbulence model, turbulent Prandtl number, and etc. are kept the same as for the steady jet model (see section 4.1 and 4.3).

The results presented in chapter 4 confirm that the developed numerical steady jet model, as the baseline model, can be extended for simulation of unsteady jet impingement problems such as pulsating flows.

Further modifications are implemented in the model to account for the intermittent pulsation with a square-wave form with exponential decay/growth as the inlet velocity signal [29]. In terms of the finite difference scheme implementation, a second order backward Euler scheme is used to integrate with respect to time. This approach minimises the discretisation error in time which would otherwise tend to numerically diffuse steep temporal gradients. As a result of the sensitivity study on the time-step, 2000 iterations per cycle are used to achieve the convergence criteria of 1^{e-5}.

Figure 5-5(a) shows the pulsating inlet velocity component, which consists of a step function passed through a first order filter, resulting in exponential decay/growth transitions.

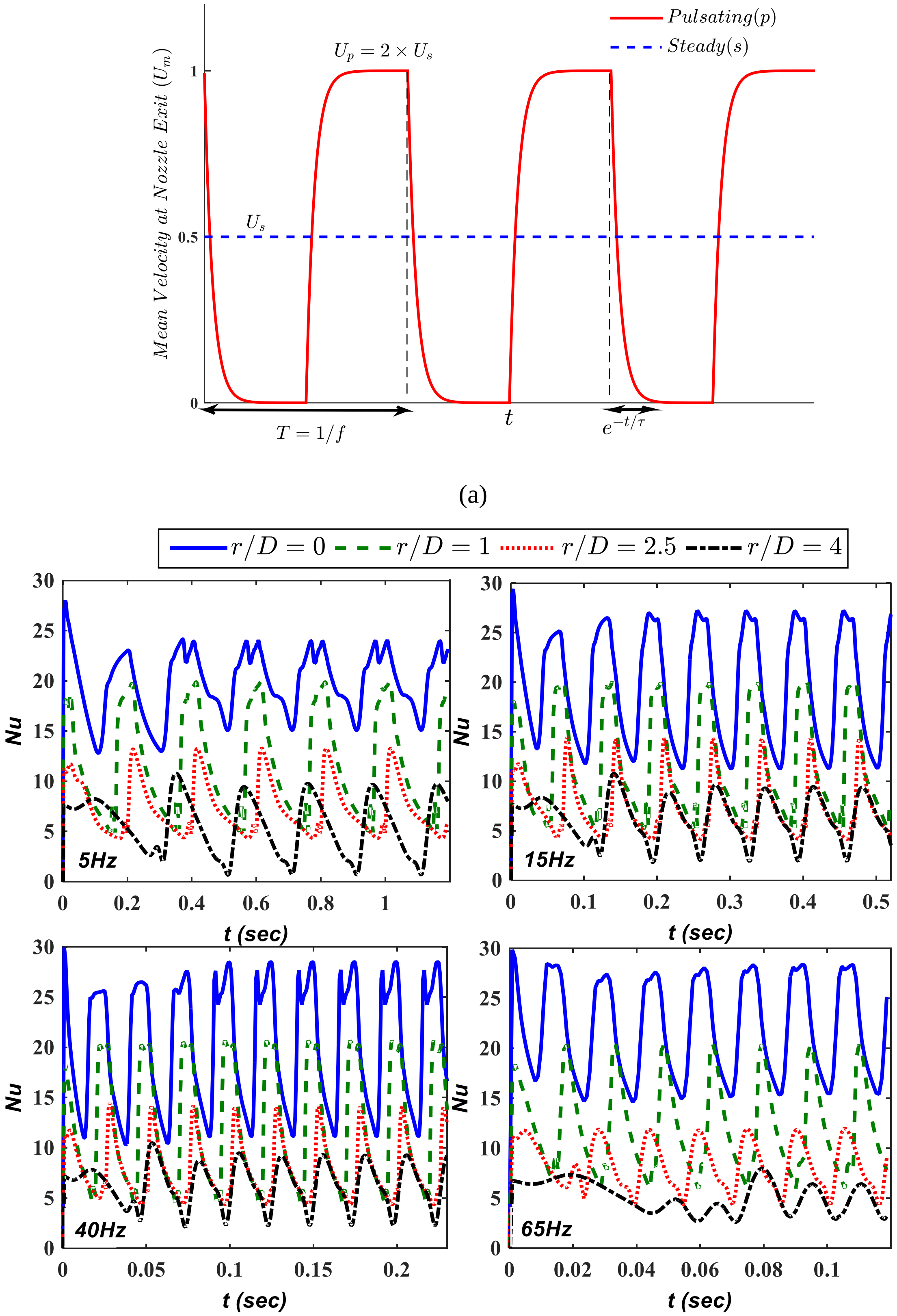

(a)

(b)

Figure 5-5. (a). Steady and pulsating mean velocities at the inlet to the nozzle; (b). temporal variation of local *Nu* at four different radial distances (*r/D* = 0, 1, 2.5, and 4) for different frequencies (*f* = 5 Hz, 15 Hz, 40 Hz, and 65 Hz) and *H/D* = 1 from the start of the simulation

The exponential transitions (with decay time constant τ) take into consideration the response time of the pneumatic solenoid valve which generates the pulsating flow in the experimental setup; its response time is approximately 2 milliseconds according to the manufacturer’s specifications (see section 5.2). From a numerical point of view, the exponential transitions have a stabilizing effect on the solution by avoiding sudden changes of the inlet pulsating flow (Fig. 5-5(a)). The time-averaged mean velocity of the signal is used in the definition of the Reynolds number, so that the exponential transition in the signals (and the time constant) does not affect the time-averaged velocity.

The value of the decay constant is maintained at $\tau = 2$ ms, in agreement with the response time of the electromagnetically actuated pneumatic valve used in the validation experiments. The solution is continued up to several cycles until all the monitored local *Nu* values over the wall become periodic; then, time-averaging is performed over the final cycle. The solution is considered periodic when the root-mean-squared deviation on the time-averaged *Nu* in different radial distances, up to $r/D = 6$, between two successive cycles does not exceed 1%. The solution over the whole domain of interest, up to $r/D = 6$, becomes periodic after around 7 iterative cycles. Figure 5-5(b) shows the numerical results for temporal variations of local *Nu* distribution at four different radial distances (r/D = 0, 1, 2.5, and 4) and four pulsation frequencies (f = 5 Hz, 15 Hz, 40 Hz, and 65 Hz) from the start of the simulation until a periodic solution is reached.

5.2 Experimental setup

Figure 5-6(a) shows the experimental apparatus used to measure the distribution in local heat transfer coefficient for a pulsating impinging axisymmetric air jet. The main components and the experimental procedure are depicted schematically in Fig. 5-6(b). The air was supplied from the building compressed air supply having passed through a number of filters (a) and a plenum chamber (b) in order to rid the flow of any fluctuations and impurities.

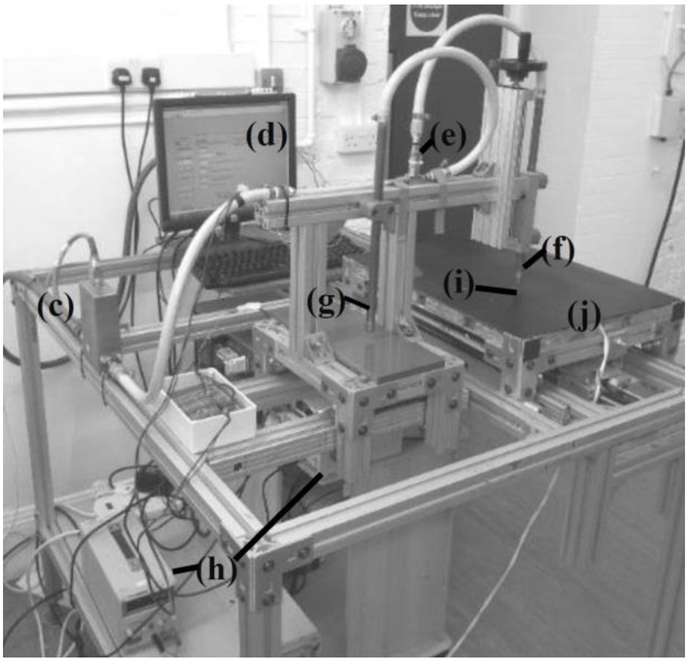

(a)

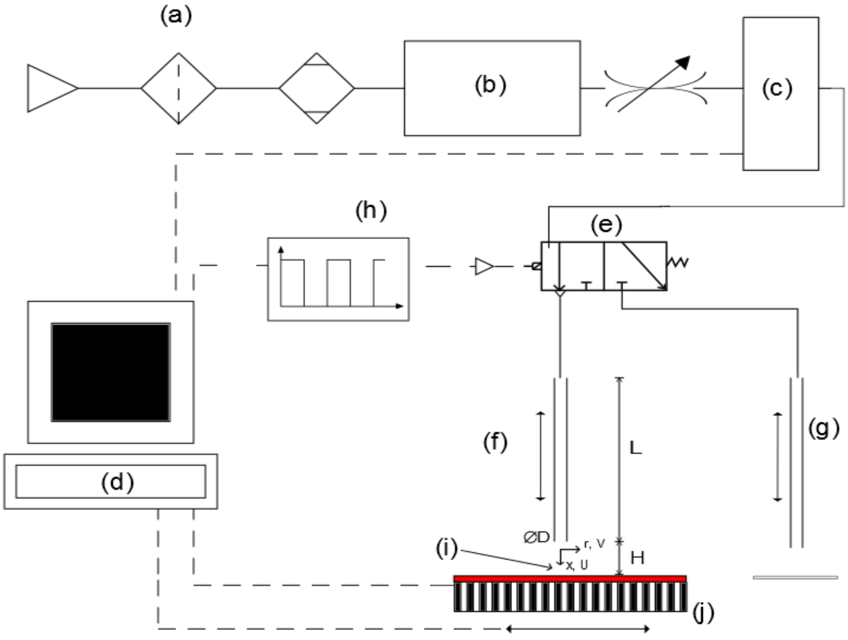

(b)

Figure 5-6. (a). Experimental apparatus, (b) Schematic representation: (a) Air Compressor, Filter and Dryer, (b) Plenum Chamber, (c) Mass Flow Meter, (d) Data Acquisition System, (e) Pneumatic solenoid valve, (f) Testing Pipe Nozzle, (g) Secondary Nozzle, (h) Function Generator, (i) Microfoil Sensor Flush with Hot Plate, (j) Heated impingement Plate

The air is then passed through (c) a digital mass flow controller (300 standard litre/min, combined uncertainty of ±1%), controlled by a data acquisition (DAQ) computer system at (d), through to the pneumatic solenoid valve (e). This valve divides the flow between the testing pipe (f) and the secondary pipe (g), at a frequency specified by the amplified signal from the function generator (h). Both the testing and secondary nozzles are identical, straight edged pipes with a diameter $D = 5$ mm and length $L = 80D$. The secondary pipe is used so as to allow for air to be expelled to the ambient when the valve is closed, preventing pressure build up in the system. The height of the testing pipe, H, is adjusted together with the height of the secondary pipe in order to maintain the same boundary conditions at both pipes, providing equal back pressures in each pipe. The testing pipe was centred over an RDF Microfoil™ sensor at (i) which was installed flush with the hot plate at (j). This sensor was connected to the DAQ computer (d) along with three T-type thermocouples allowing for the ambient, plate, and inlet flow temperature to be measured, together with the local surface heat flux. This hot plate could be traversed radially using a stepper motor controlled by the DAQ computer (d), to provide radial Nusselt number profiles. Uncertainty margins in nozzle diameter, mass flow rate, Reynolds number, the reference and surface temperature, and Nusselt number are reported in section 4.2.1. Further information on the rig and the sensors used for measurements are described in greater details in [41]-[42].

The Parker 9 series 3-way solenoid valve, shown in Fig. 5-6 and Fig. 5-7, receives an amplified signal from the function generator and switches the flow between the two pipe nozzles. The frequency at which the flow is switched is dictated by the setting specified in the function generator. The function generator for this study produces a square wave pulse in order to produce a duty cycle of 50%. The compressibility of air will have a significant impact on this square-wave signal, causing it to become more sinusoidal as predicted by Persoons et al. [2]. The duty cycle is be measured via a hot wire to confirm that the response of the valve replicates the signal produced by the function generator. The valve has a response time of <5ms allowing for rapid replication of the square wave signal supplied to it [42].

Figure 5-7. Parker 9 series 3-way solenoid valve (pulsating valve) [43]

The Jet impingement plate is a 5 mm thick copper plate, heated from below by an electrical heater and well insulated to minimize heat loss from the base. The microfoil heat flux sensor and thermocouple are flush mounted to the top surface, which is maintained at a near constant temperature of 60˚C with the ambient air remaining at around 22˚C. The plate has been found to preserve a uniform wall temperature boundary condition according to previous studies [5]. The three T-type thermocouples in use on the experimental rig were calibrated by McGuinn [41] using a thermostatically controlled water bath and a Resistance Temperature Detector (*RTD*). The jet angle of impingement for all tests was 90˚, maintaining the same experimental setup from previous studies [24]. The instrumentation used to measure surface heat flux is calibrated against the correlation of Shadlesky [12] who utilised laminar flow theory and assumptions in order to develop the following expression $Nu_o = 0.585 Re^{0.5} Pr^{0.4}$ for *H/D* < 2. This is performed to provide an accurate calibration for the 5 mm diameter straight pipe nozzles. The heat transfer coefficient was determined from $h = q''/(T_{surf} - T_{ref})$ where the heat flux was provided by the RDF Microfoil™. The results reported here are in the form of Nusselt number $Nu = hD/k$.

Hot wire measurements were carried out using a Dantec 55P14 one-dimensional right-angle hot wire probe connected to a Dantec MiniCTA™ 54T30 constant temperature anemometer (bandwidth 10 kHz). The probe was positioned about 0.5 mm downstream from the nozzle exit, and was clamped to the stepper motor controlled traverse system to give radial profiles of the axial velocity and turbulence intensity of the nozzle exit flow. The data in all heat transfer tests was sampled at a rate of 8192 Hz. Although earlier studies were sampled at the higher rate of 16384 Hz, this change was found to have little effect on measurements obtained when carrying out the current study. A number of profiles were re-tested at the higher rate with no difference in value being detected. The sampling frequency was then varied as required when the hot wire probe was integrated into the system, so as to provide a high resolution of 100 samples per period for a pulsating jet. This meant simply multiplying the sampling frequency by 100. The measurements taken were instantaneous, allowing for the time step to be obtained from the sampling frequency providing a measure of the changes of velocity with time [42].

5.3 Results

5.3.1 Validation of the numerical model using local experimental *Nu* profiles

The experimental jet test facility was previously used in [24] and [34] which contain a full account of the experimental data.

This section illustrates the validation of the *CFD* model against corresponding experimental data. Alimohammadi et al. [34] have previously shown that the *CFD* model reliably predicts the local heat transfer rate distribution to a steady axisymmetric impinging jet for an extensive range of operating conditions (see section 4.3). Here the target is to validate the unsteady part of the *CFD* model for pulsating jets.

For this purpose, the radial *Nu* distributions of experimental and numerical results are plotted together in Fig. 5-8. This is done for both steady and pulsating jets for the lowest and highest nozzle-to-surface distances $H = 1D$ and $6D$ and for time-averaged *Re* of 1,300 and 2,800 at two sample pulsation frequencies $f = 5$ Hz and 40 Hz.

The goal is to investigate the performance of an operating condition-independent numerical model. However, to improve the agreement versus experimental data, the decay constant of the pulsating flow input signal, τ, is varied between 1.5 ms to 2 ms in the model. All of the other model parameters, configurations and settings are kept constant in the numerical model, when changing the operating conditions, (*Re*, *H/D*, etc).

The numerical and experimental data shown in Fig. 5-8 exhibit reasonable agreement in terms of the local distribution of *Nu* in the radial direction, from the stagnation point at $r = 0$ up to $r = 6D$. The maximum normalized deviation between the numerical and experimental data for the steady and pulsating jets are 6% and 10%, respectively. The deviation is greater for the pulsating jet (and increases with pulsation frequency). Deviations in the lower *r/D* region (and increases with pulsation frequency) can be partly attributed to numerical and experimental uncertainties, which are generally higher at the stagnation point [34].

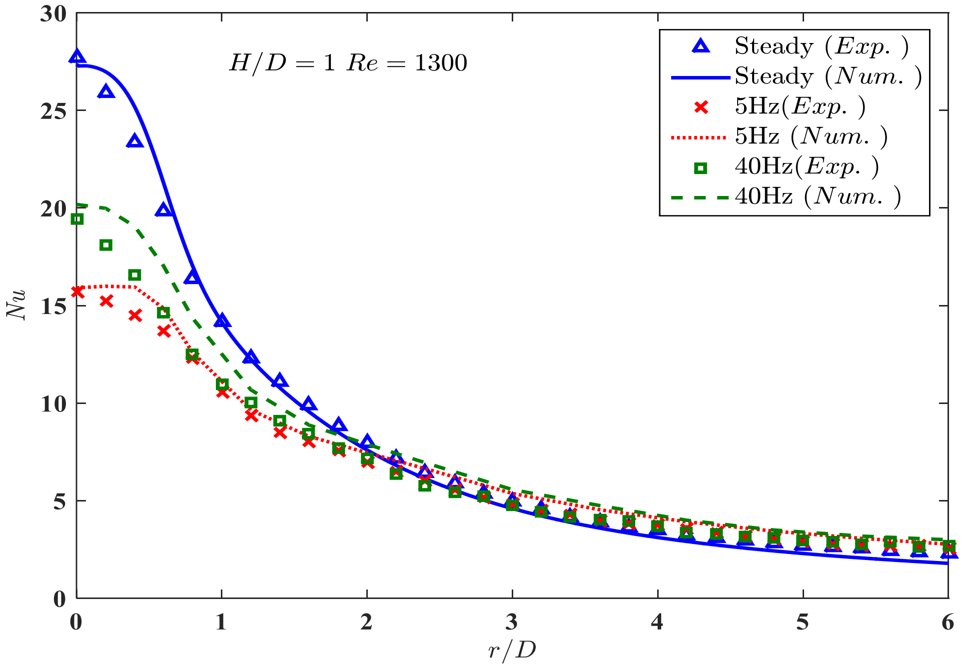

$H/D = 1$ $Re = 1300$
Steady (*Exp.*)
Steady (*Num.*)
5Hz(*Exp.*)
5Hz (*Num.*)
40Hz(*Exp.*)
40Hz (*Num.*)
Nu
r/D
30
25
20
15
10
5
0
0
1
2
3
4
5
6

(a)

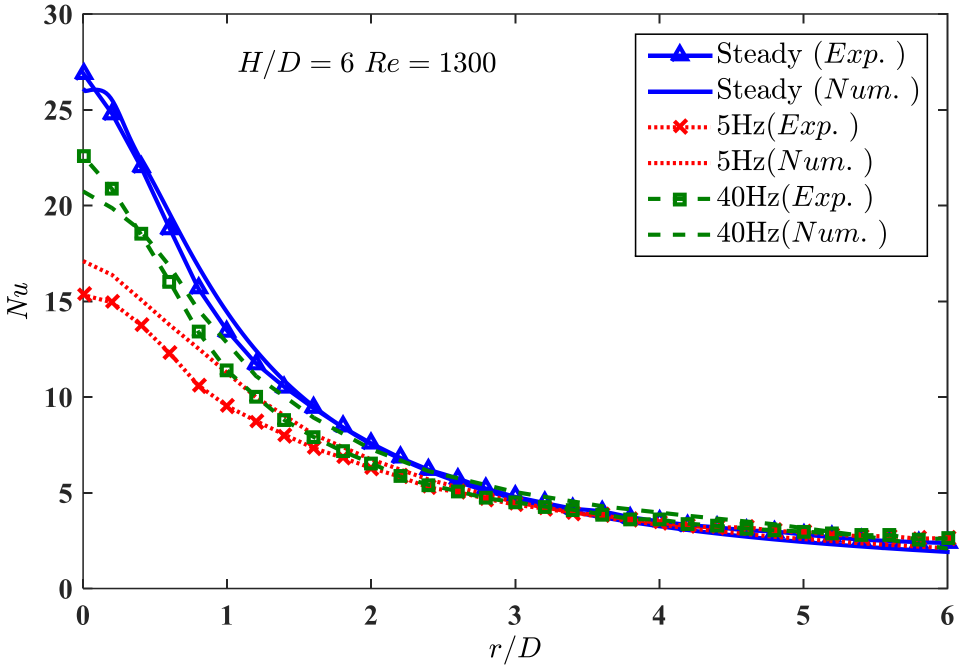

$H/D = 6$ $Re = 1300$
Steady (*Exp.*)
Steady (*Num.*)
5Hz(*Exp.*)
5Hz(*Num.*)
40Hz(*Exp.*)
40Hz(*Num.*)
Nu
r/D
30
25
20
15
10
5
0
0
1
2
3
4
5
6

(b)

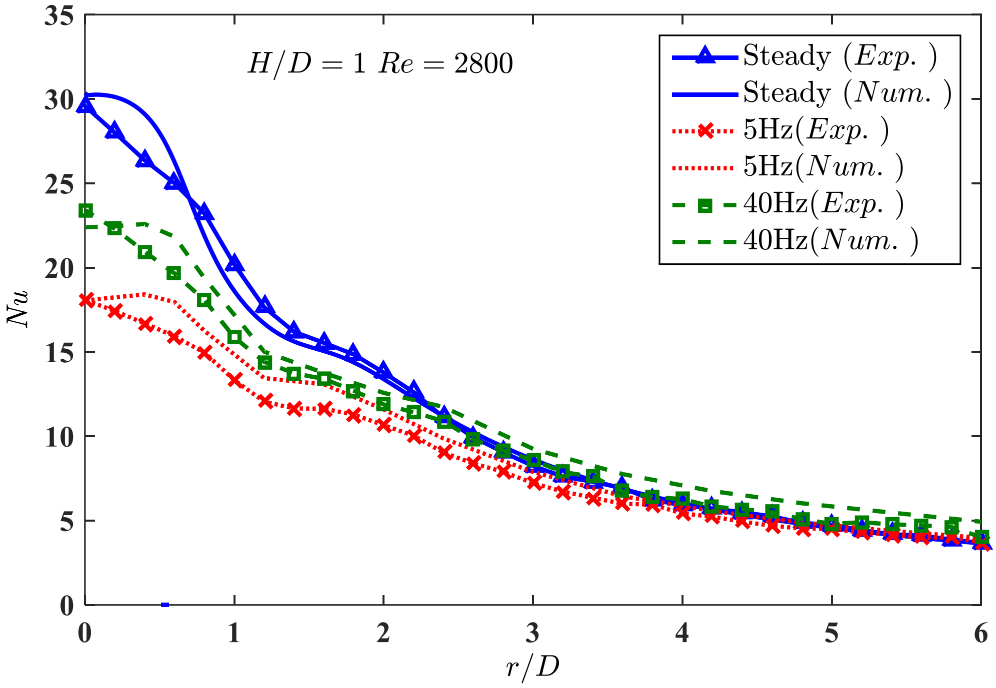

(c)

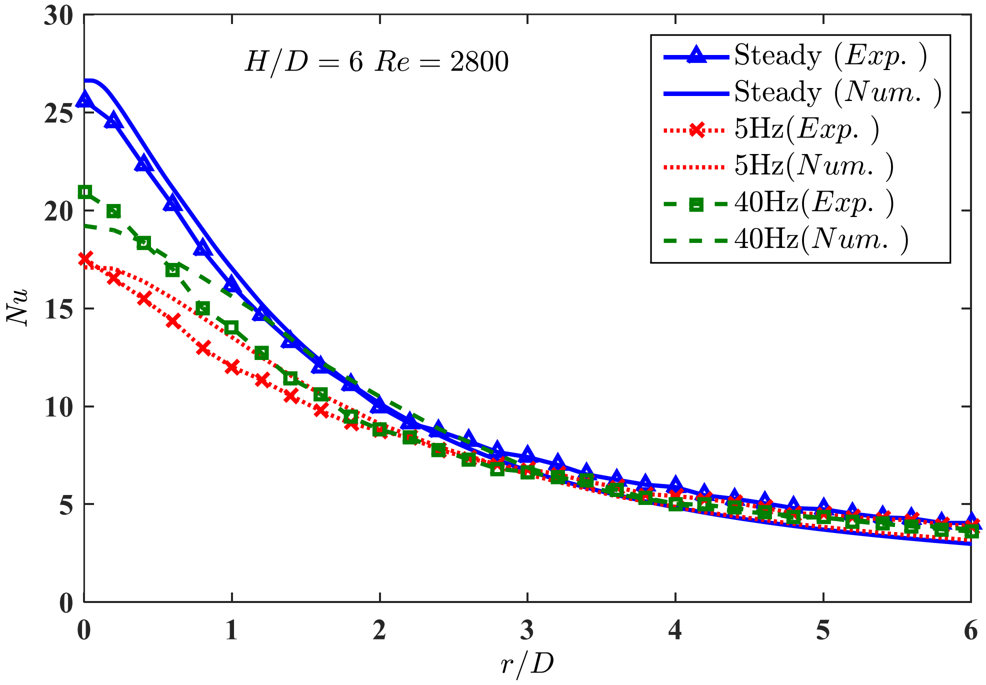

(d)

Figure 5-8. Comparison of numerical results for local *Nu* using steady and pulsating jets (*f* = 5 Hz and 40 Hz) to experimental data for validation at (a) *H/D* =1, *Re* = 1,300; (b *H/D* =6, *Re* = 1,300; (c) *H/D* =1, *Re* = 2,800; and (d) *H/D* =6, *Re* = 2,800

To be more specific, the false (numerical) diffusion which arises from discretisation of continuous conservation equations can be a major contributor to deviations from experimental data [63]. More diffusive discretisation schemes are prone to behave differently than the intended physical system. False diffusion depends on various parameters, including the alignment of the local streamlines with respect to the grid, grid element size, and discretisation scheme [63]. Aligning the successively refined grids with the flow as well as employment of a higher order discretisation scheme, as shown in section 4.3.3, can help to reduce this error. Also, when it comes to discretisation in time as another source of deviation, false diffusion of steep temporal gradients (Fig. 5-8) may be reduced by means of a second order time integration scheme, as described in section 0. However, the creation of some nonphysical oscillations in time is possible depending on the nature of the chosen method.

The intermittent nature of pulsating jet impingement results in a reduction in the stagnation Nusselt number δNu_0 compared to the equivalent steady jet at the same Reynolds number. When it comes to area-averaged Nusselt number, $\delta\overline{Nu}$, a slight enhancement in the heat transfer is observed over the domain. Both improved by increasing the frequency from 5 Hz to 40 Hz. Change in heat transfer due to flow pulsation is investigated in section 5.3.3 in more detail.

The stagnation point experiences the highest heat transfer, as shown in Fig. 5-8. The highest velocity and the lowest temperature difference are observed at this point, causing a corresponding increase in Nu due to the well documented dependencies on $Re^{0.5}$ and ΔT [70].

No sizeable “saddle back” profiles are detected in Fig. 5-8, except for the case with the highest Reynolds number and lowest jet to surface spacing, as shown in Fig. 5-8(c). This secondary peak in $Nu(r)$ is one of the major characteristics of impinging jets for small jet to surface spacings. The local increase in wall-normal velocity fluctuations due to the transition of the wall jet flow from the laminar to turbulent mode is known as one of the main reasons for this jump in $Nu(r)$, [9] and [5].

At larger values of *H/D*, the axial velocity of the jet in the region up to *r/D* of 1 is smaller and does not cause the same wall jet flow development as for small *H*/*D* values, and conclusively, no secondary peak in *Nu(r)* is visible [34]. This trend is also described by Lytle and Webb [8], that the second peak becomes visible at higher *Re* when *H/D* is decreased. Consequently, the saddle back profile can appear at $H/D \le 1$, depending on the jet Reynolds number. According to Fig. 5-8(c), the secondary peak was marginally detectable in this investigation, at $H/D = 1$ and $Re = 2{,}800$, a result consistent with that of Persoons et al. [24].

A secondary peak in Nusselt number was also identified in the previous studies performed with a 13 mm round pipe nozzle by Persoons et al. [24] and Alimohammadi et al. [34]. This is consistent with the significantly higher *Re* which was examined by the aforementioned studies using the same experimental rig. The lower *Re* and therefore slightly higher Strouhal number also means that the potential core of the jet diminishes at a quicker rate, as shown above.

5.3.2 Numerical results for extended parameter range

5.3.2.1 High frequency jets

The experimental pulsating valve described in section 5.2 is technically suitable for frequencies lower than 70 Hz, the upper limit at which the performance of the valve starts to deteriorate. At higher frequencies, the valve generates faulty signals [24] and [36]. In the higher frequency range, the validated *CFD* model can be used as a more stable tool to simulate conditions beyond the experimental capabilities.

For this purpose additional simulations were performed at f = 130Hz (Sr = 0.1667 and 0.0747 for Re =1,300 and 2,800, respectively) and 260 Hz (Sr = 0.3333 and 0.1494 for Re =1,300 and 2,800, respectively). These frequencies are two and three times larger, respectively, than the experimentally validated maximum f = 65 Hz. The numerical results for highest $H/D = 6$ and $Re = 2{,}800$, in the range of $5\text{ Hz} \le f \le 260\text{ Hz}$ ($0.0029 \le Sr \le 0.1494$), are shown in Fig. 5-9.

When pulsation is used, as shown in the above figure, the stagnation Nusselt number Nu_0 is lower than that of the stagnation jet for all operating points. This is consistent with the results of Azevedo et al. [25] who reported that flow pulsation reduces heat transfer at the stagnation point for all *H/D* values. They have reported reductions in magnitude of more than 25% for stagnation point heat transfer.

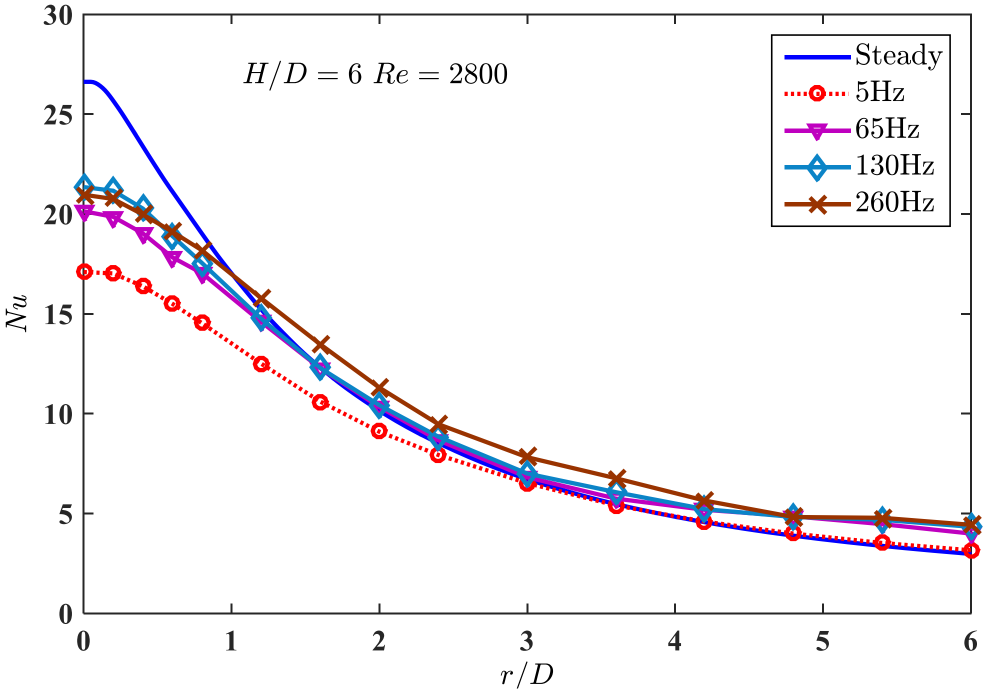

Figure 5-9. Radial distribution of *Nu* for extended ranges of frequency, 5 Hz $\leq f \leq$ 260 Hz, and Strouhal number $0.0029 \leq Sr \leq 0.1494$ (*Re* = 2,800, *H/D* = 6)

Increasing the pulsation frequency accelerates the enhanced mixing and decay rate of the potential core and consequently increases *Sr*, as discussed in [70] and [72]. This results in visible improvements of the stagnation and area-averaged heat transfer by increasing the frequency from 5 Hz to 130 Hz, as shown in Fig. 5-9, although the results are still well below the steady jet case. The area-averaged Nusselt number $\overline{Nu}$ was defined as the average over a circular impingement area of radius *R* = 6*D* around the stagnation point: $\overline{Nu} = \frac{1}{\pi R^2}\int_0^R Nu(r) 2\pi r\, dr$. For f = 260 Hz, the stagnation enhancement drops to a slightly lower value than that of 130 Hz jet, while the area-averaged enhancement over the entire impingement domain still increases. The approximate value of *f* = 130 Hz is considered as upper limit for the applications with specific interest in heat transfer enhancement in the stagnation zone.

5.3.3 Change in heat transfer due to flow pulsation

The numerically predicted variations in stagnation and area-averaged Nusselt numbers with pulsation frequencies f = 5 Hz to 260 Hz, for Re = 1,300 and 2,800 and H/D = 1 and 6, are shown in Fig. 5-10. This corresponds to a Strouhal number, Sr, range of $0.0029 \leq Sr \leq 0.3333$ where $Sr = fD/U_m$ and U_m is the nozzle-averaged axial velocity. The enhancements are defined by the following expression:

$$\delta\overline{Nu} = [\overline{Nu}(\text{Pulsating})/\overline{Nu}(\text{Steady}) - 1]\ . \qquad (5\text{-}1)$$

The stagnation Nusselt number δNu_0 experiences an appreciable degradation when pulsation is used, but the level of decrease reduces with increasing frequency from 5 Hz to 65 Hz for both Re of 1,300 and 2,800. For Re of 2,800, this improvement in δNu_0 continues up to f = 130 Hz for both H/D = 1 and 6, then starts to drop at higher frequencies. However, for Re =1,300, the gradual recovery in stagnation heat transfer continues only up to f = 65 Hz.

The change in area-averaged Nusselt number, $\delta\overline{Nu}$, can generally produce a better prediction of the global performance of the impinging jets. $\delta\overline{Nu}$ exhibits a near monotonic increase with frequency (and Strouhal Number) at different H/D and Re values. For both Re = 1,300 and 2,800, $\delta\overline{Nu}$ shows an increasing level of enhancement as the pulsation starts from 5 Hz. For $f \geq 130$ Hz ($Sr \geq 0.1667$), at Re = 1,300, $\delta\overline{Nu}$ reaches to more or less constant values of 36% and 40% enhancement for H/D = 1 and 6, respectively, then remains almost constant for higher frequencies up to 260 Hz, Sr = 0.03333 (Fig. 5-10(a)).

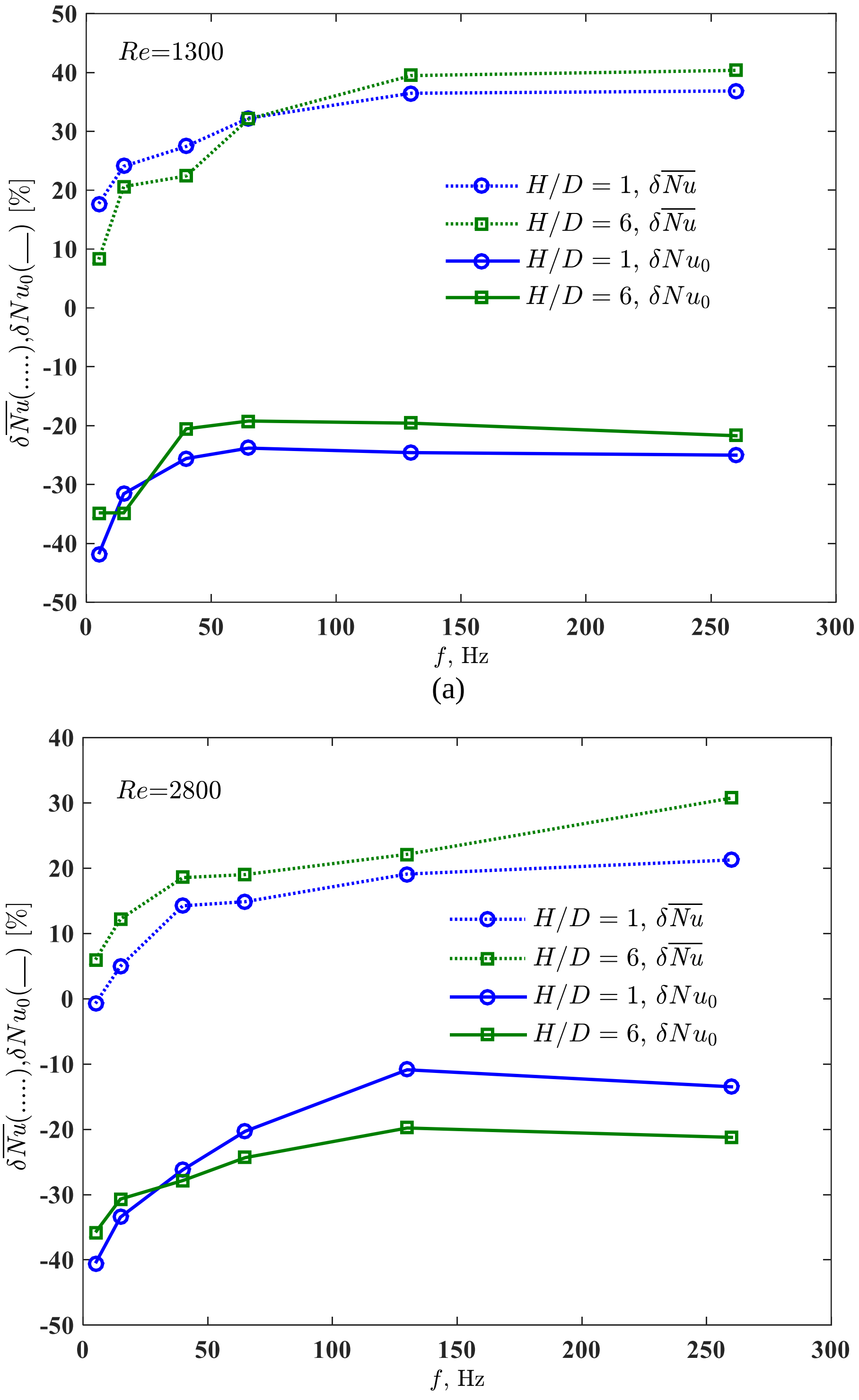

(a)

(b)

Figure 5-10. Numerical results for change in Stagnation and area-averaged Nusselt numbers, δNu_0 and $\delta\overline{Nu}$, using pulsating jets for H/D = 1 to 6 at different frequencies f = 5 Hz to 260 Hz and Strouhal numbers: (a). $0.0054 \le Sr \le 0.3333$; (b). $0.0029 \le Sr \le 0.1494$

For the higher Reynolds number, which has a higher averaged jet velocity, the pulsating jet experiences lower values of *Sr* than that of the jet with *Re* = 1,300. Figure 5-10 shows that for the identical pulsation frequencies, $\delta\overline{Nu}$ for the jet with *Re* = 2,800 attains lower values than the enhancements induced by the jet with *Re* = 1,300.

As can be seen in Fig. 5-10(b) at *f* = 260 Hz (*Sr* = 0.1494) for *H/D* = 6, there appears to be potential to achieve higher area-averaged enhancement than 30% by increasing the pulsation frequency. This means that *Sr* is still lower than the threshold at which the increase in $\delta\overline{Nu}$ saturates and reaches an approximately constant value, as in Fig. 5-10(a).

The stagnation and area-averaged changes in heat transfer can be summarized as follows: -42% $\leq \delta Nu_0 \leq$ -10% and -1% $\leq \delta\overline{Nu} \leq$ 40%. Thus, if area-averaged heat transfer is of particular interest, there is merit in introducing pulsation to the flow.

5.3.3.1 Numerical flow visualization

With the aim of providing insight into the mechanisms of convective heat transfer provided by pulsating impinging jets, Fig. 5-11 (a-c) shows a number of sequential snapshots of the evolving normalized velocity ($\sqrt{u^2+v^2}/U_m$) and vorticity ($\omega_z D/U_m$) contours for pulsating impinging jet simulations at *Re* = 2,800, *H/D* = *6*, and *f* = 65 Hz.

As the pulsating jet impinges on the flat surface, the potential jet core remains not much affected by the surrounding flow. Away from the centreline of the jet, the turbulence becomes considerably larger, in the shear layer, where entrainment from surrounding flow and a reduction in jet velocity occurs. The amplified turbulence made by the flow pulsation results in higher entrainment, mixing and turbulence in the shear layer, causing accelerated degradation in the potential jet core. This allows turbulent structures to penetrate the thermal boundary layer. In the wall jet region, the local radial jet velocity increases, resulting in a maximum value at the wall followed by a reduction as the radial distance from the stagnation point increases [5].

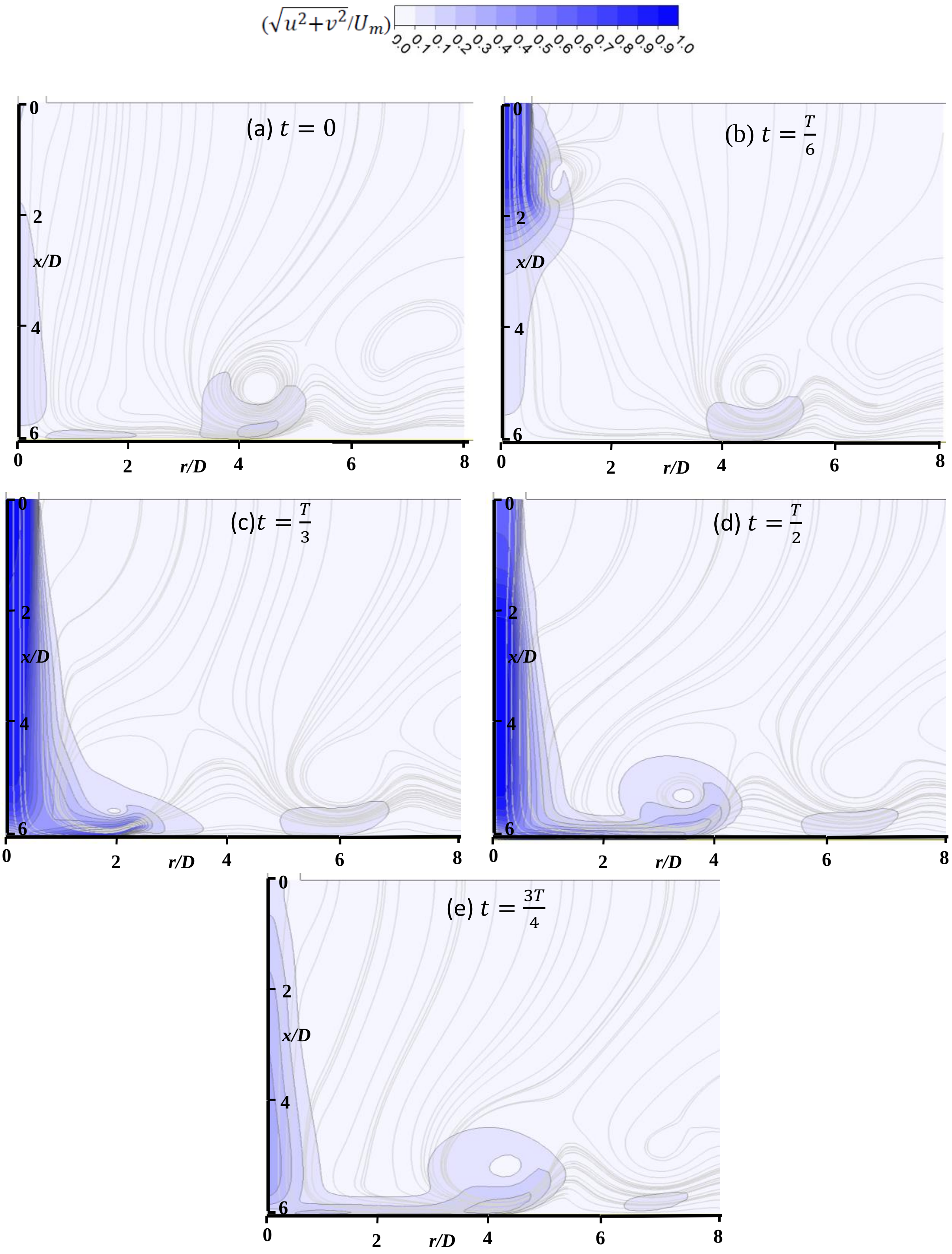

Figure 5-11. Sequential snapshots of the normalized velocity ($\sqrt{u^2+v^2}/U_m$) contours for pulsating impinging jet simulations for *Re* = 2,800, *H/D* = 6, and *f* = 65 Hz at (a) $t = 0$, (b) $t = \frac{T}{6}$, (c) $t = \frac{T}{3}$, (d) $t = \frac{T}{2}$, and (e) $t = \frac{3T}{4}$ (*T is* pulsation period)

From the start of the ejection phase, very strong toroidal vortices impinging on the surface can be observed for the pulsating impinging jets, while the vortices in the steady impinging jet are weak. The relatively strong vortices, as shown in Fig. 5-12, are considered to intensify the mixing and flow entrainment from the surrounding flow which contributes to the enhanced heat transfer offered by pulsating jets. However, the beneficial effect of the ordered, periodic vortices provided by the flow pulsations does not rival the heat transfer at the stagnation point of a steady jet until they have penetrated the core of the jet at larger values of *H/D.* At higher values of *H/D* the potential core of the jet would be completely wrapped by the shear layer, allowing for increased turbulence intensity across the jet [73]. This increased turbulence intensity and enhanced mixing compensates for the loss in mean velocity when compared to a steady jet, as described in [70], [72]- [73].

The primary vortices formed in the shear layer of the jet are detectable, as seen in Fig. 5-12. A remarkable feature is the additional inverse vortices moving along the wall, causing a local flow reversal, and inducing separation. Turbulent fluctuations of axial and radial velocity components together with fluctuations of pressure gradient are considered as the reason for the formation of these counter rotating vortices [50].

Mladin and Zumbrunnen [72] have reported that as the velocity decreases radially and the turbulence intensity increases, enhanced mixing and increase in turbulence intensity occurs, causing increased heat transfer. As shown earlier, the stagnation point heat transfer does not show any positive enhancement for the range of operating conditions investigated here (Fig. 5-10). A comparison of the radial velocity profile for steady and pulsating jets shows that the mean velocity of the pulsating jet is considerably smaller at the stagnation point, whereas it increases to much higher peak values compared to a steady jet at the same distance from the stagnation point. This does contribute to the degradation in heat transfer at the stagnation point, while higher instantaneous velocities result in a small positive heat transfer enhancement for the pulsating jet at radial distances away from the stagnation point, as demonstrated by the effect on the area-averaged Nusselt number [74].

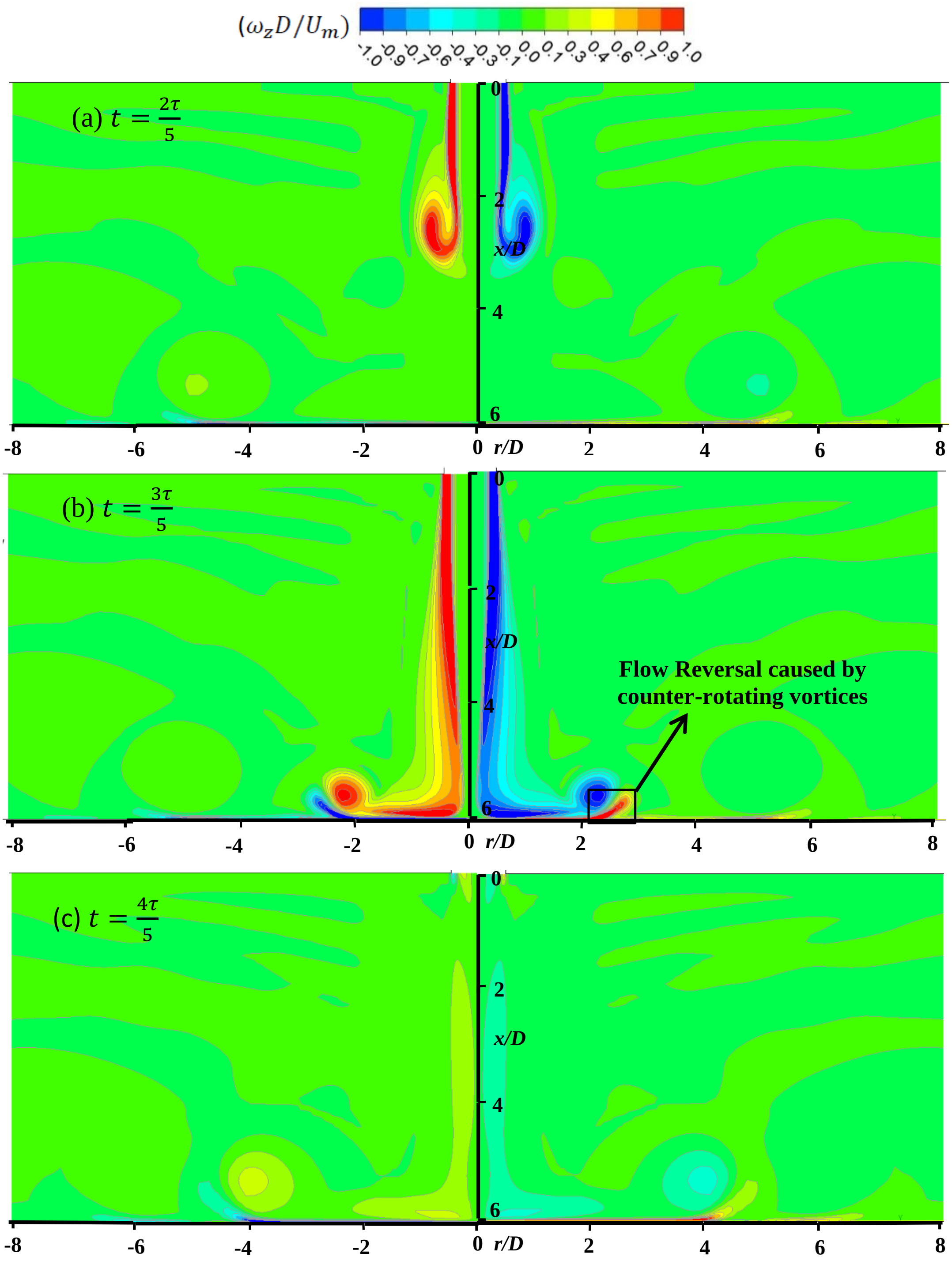

Figure 5-12. Sequential snapshots of the normalized vorticity ($\omega_z D/U_m$) contours for pulsating impinging jet simulations at Re = 2,800, H/D = 6, and f = 65 Hz at (a). $t = \frac{2T}{5}$, (b). $t = \frac{3T}{5}$, (c). $t = \frac{4T}{5}$

Numerical results can provide a closer perspective into the adjacent wall cells in the viscous sub-layer, by monitoring a few essential near-wall components. This contributes to improved understanding of the potential heat transfer enhancement (or reduction) introduced by pulsating jets. To avoid the data loss due to the pulsating behaviour of the jet in the flow field, when the target flow component is oscillating between negative and positive values during a full pulsation period *T*, time-averaging of the monitored quantity is performed on absolute values of that quantity. Figure 5-13(a) depicts the distribution of time-averaged values of instantaneous, absolute radial velocity gradient, $\overline{\left|\frac{\partial u}{\partial x}\right|}$, the convective acceleration term, for the steady and pulsating jets (*f* = 5 Hz and 65 Hz) with *Re* = 200, *H/D* = *6*. This is done by averaging the values at four equally distributed vertical distances from the impingement surface up to *y* = 0.05*D*. This corresponds to the results shown in Fig. 5-9. A point-by-point comparison of the results from Fig. 5-13(a) with results for radial *Nu* distributions in Fig. 5-9 indicates a reasonable degree of correspondence between the local Nusselt number and $\overline{\left|\frac{\partial u}{\partial x}\right|}$ results. The distributions of radial velocity gradient for both steady and pulsating jets present identical trends; interestingly, differences in the magnitudes mirror the same differences for *Nu(r)* in Fig. 5-9. In particular, Figs. 5-9 and 5-13(a) respectively show that *Nu(r)* and $\overline{\left|\frac{\partial u}{\partial x}\right|}$ for the pulsating jet with *f* = 65 Hz are slightly higher than that of the jet with *f* = 5 Hz over the entire impingement surface, and at $r/D \approx 3$, the 65 Hz jet rises to values higher than that of the steady jet, while the steady jet still remains at values larger than the 5 Hz jet. Figure 5-13(b) shows the radial distribution of time-averaged normal vorticity term, defined as $\omega_z = (\frac{\partial v}{\partial x} - \frac{\partial u}{\partial y})$, over a pulsation period. This distribution also displays the same behaviour as described above which makes the result for ω_z consistent with *Nu* shown in Fig. 5-9 and Fig. 5-13(b) also supports the theory that at *f* = 65 Hz, when compared to 5 Hz jet, the primary vortices shaped in the shear layer of the jet, which can penetrate into the viscous boundary layer, and also the additional vortices generated by the turbulent flow field along the wall can enhance heat and mass transfer rates at higher frequencies.

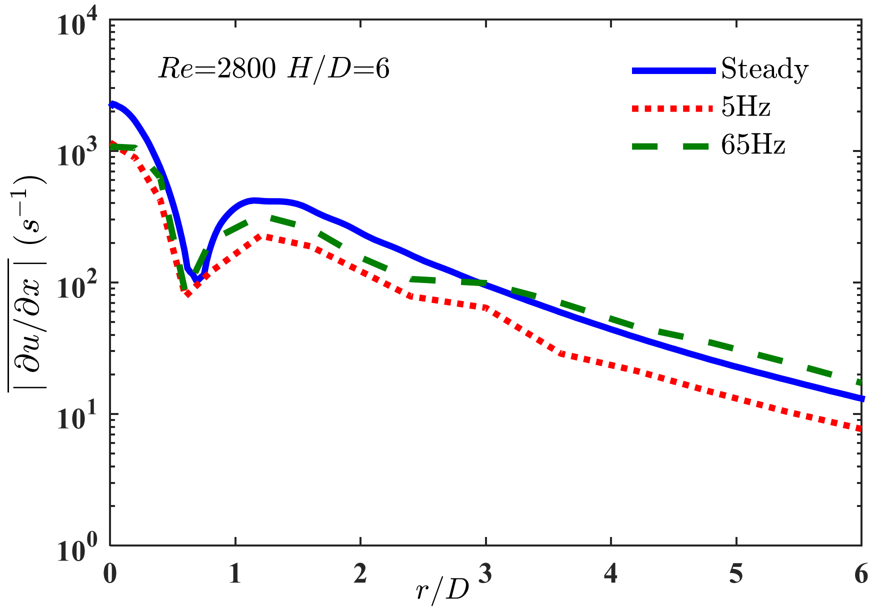

(a)

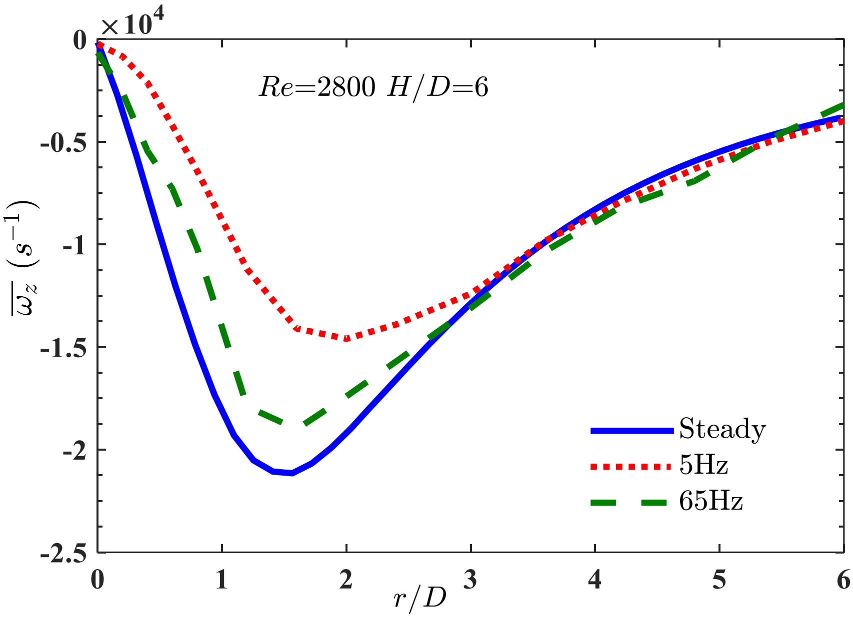

(b)

Figure 5-13. Comparison of local distribution of time-averaged (a) absolute radial velocity gradient $\left|\frac{\partial u}{\partial x}\right|$, (b) normal vorticity term ω_z at *Re* = 2,800, *H/D* = 6 for steady and pulsating jets (*f* = 5 Hz and 65 Hz)

Using the Reynolds decomposition, the instantaneous velocity, $u_j(x,t)$, is decomposed into the mean velocity, $U_j(x,t)$, and the fluctuating part of the velocity due to turbulence in the flow field, $u_j'(x,t)$, according to,

$$u_j = U_j + u_j' \tag{5-2}$$

By averaging the Navier-Stokes equations to account for turbulent fluctuations in the fluid momentum, the resulting equation of motions contain additional turbulent stress terms, known as the Reynolds stresses [75]-[76]. Turbulent Reynolds stress components, shear stress $-\rho\langle u'v'\rangle$ and normal stresses $-\rho\langle u'^2\rangle$ and $-\rho\langle v'^2\rangle$, which are solved using the closure turbulence model described in section 4.1.4, can be monitored to better illuminate the effect of flow pulsation on the wall heat transfer. Figure 5-14 displays the radial distribution of time-averaged values of absolute Reynolds stress components over a single pulsation period T. This is done by averaging the values at four equally distributed vertical distances from the impingement surface up to y = 0.05D. It is worth noting that the term $\langle u'v'\rangle$ is a time-averaged value of product of radial and axial fluctuating velocity components, u' and v', over each time step of solution Δt. From a physical viewpoint, a simple manipulation shows that the component $-\rho\langle u'v'\rangle$ can be related to the mean transport of instantaneous momentum, ρu, by the fluctuating velocity, v', [75]-[76]. The Reynolds stresses imply that convective transport caused by the turbulent fluctuating velocity will act to augment mixing over and above that caused by thermal fluctuations at the molecular level. The isotropic turbulence model used in this study returns equal values for the magnitudes of normal components $\overline{|\langle u'^2\rangle|}$ and $\overline{|\langle v'^2\rangle|}$, while the shear components $\overline{|\langle u'v'\rangle|}$ = 0. The use of an anisotropic turbulence model (e.g., Reynolds Stress model) is not within the scope of this study. As a result, at higher frequencies, velocity fluctuations take place at a larger length scale, and turbulent fluxes are larger than molecular ones. Figure 5-14 shows that all Reynolds stress components for the 65 Hz jet are higher than those of the jet with f = 5 Hz.

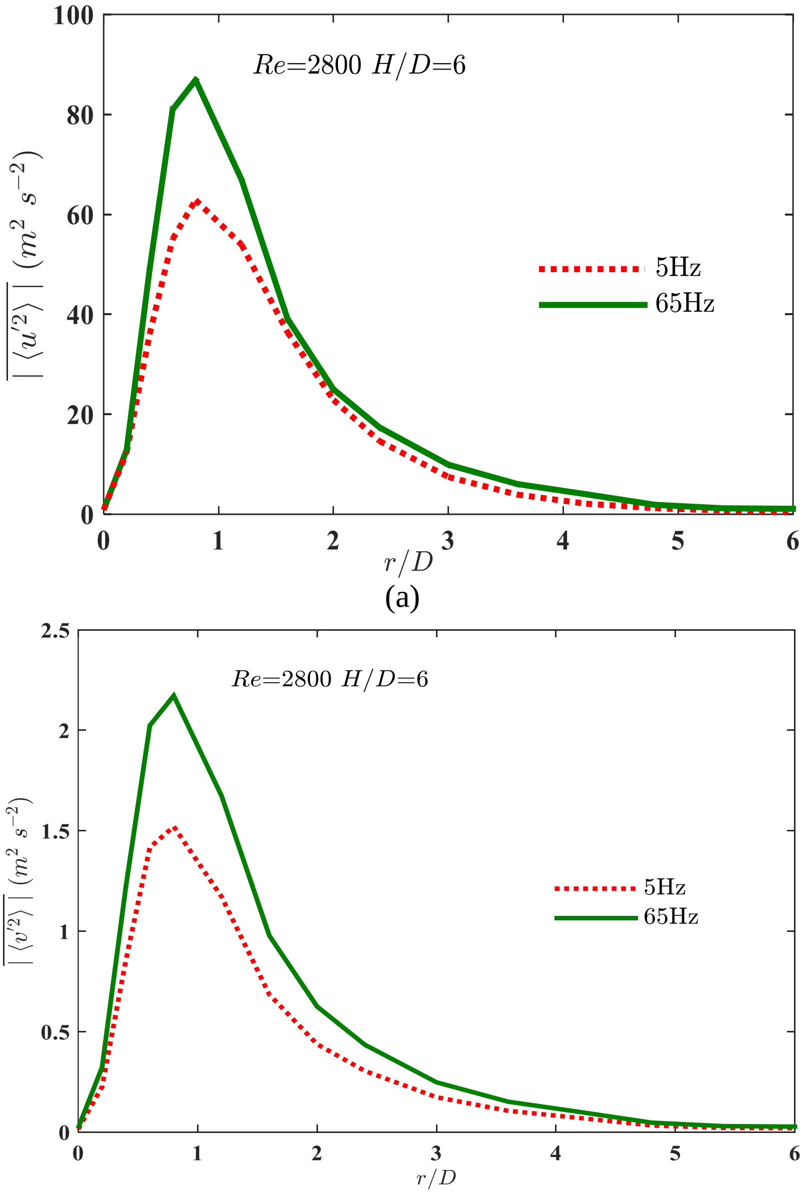

(a)

(b)

Figure. 5-14. Comparison of local distribution of time-averaged absolute Reynolds stress components (a). $|\langle u'^2 \rangle|$, and (b). $|\langle v'^2 \rangle|$ at *Re* = 2,800, *H/D* = 6 for pulsating jets (*f* = 5 Hz and 65 Hz)

5.3.3.2 Thermal Boundary Layer

The presence of a thin fluid layer of the nearly stagnant fluid held on the heated surface by viscous forces is considered as a major limitation of the heat transfer over surfaces. This layer acts as a thermal insulator. The heat and mass transport has to cross this layer by conduction, a process much less effective (by several orders of magnitude in the case of gas) than convection.

The boundary layer within the wall jet begins in the stagnation region, where it has a typical thickness of no more than 1% of the jet diameter.

One possibility to remove this main obstacle is applying pulsation to demolish the stagnant layer. The thickness of the stagnant fluid layer (and hence its resistance to the conduction transport) increases with increasing time after the fluid is set into motion. The increase in thickness is the effect of viscous momentum transfer action, diffusing away from the wall. In the oscillatory regime, the thickness regrows within each pulsation period. Therefore, the time-mean thickness decreases and the resistance to the conductive transport is lower.

The vortices in pulsating jets periodically break up the thermal boundary layer, forcing it to redevelop at the driving frequency of the jet. If these vortices remain close to the surface, they have the potential to alter the surface heat transfer. The observed effects of the square-wave pulsation can be attributed to higher turbulence, larger vortexes, increased flow entrainment and mixing promoted by flow instabilities, as well as reduced instantaneous hydrodynamic and thermal boundary layers. Unsteady boundary layers on the surface may produce higher or lower heat transfer coefficients, depending primarily on frequencies, dimensions, and jet Reynolds number.

5.3.3.3 Scaling heat transfer enhancements

As depicted in Fig. 5-11(b), enhancement of area-averaged heat transfer induced by the pulsating jet requires a high frequency of pulsation f and low mean flow velocity U_m (or Re). Therefore, a certain dependency on the Strouhal number is noted, where $Sr = fD/U_m$, as reported by others [24], [27], [35], and [72]-[73]. Moreover, Fig. 5-11 indicates that the pulsating jets have dissimilar impacts at the stagnation point and over the entire wall impingement surface, in terms of heat transfer enhancement. As a result, in this section the dimensionless Sr is used to scale δNu_0 and $\delta\overline{Nu}$ for the entire range of operating conditions investigated. To have a broader range of parameters, a previous set of results from a numerical-experimental study performed using the same setup and numerical model but with a nozzle pipe of diameter 13 mm for Re = 6,000 and 9 Hz $\leq f \leq$ 55 Hz ($0.017 \leq Sr \leq 0.102$) by Alimohammadi et al. [35] is also included with the current set of data. Further details of heat transfer simulation results for the 13 mm nozzle are presented in the Appendix (see A.1)

Persoons et al. [24] have used a scaling scheme to analyse the convective heat transfer due to pulsating flow for their experimental data. The same statistical analysis is performed here to scale the stagnation and the area averaged enhancements as functions of different sets of dimensionless parameters, separately. Stagnation enhancement, δNu_0, is found to be best fitted as a function of $SrRe^2$, whereas area-averaged enhancement can be properly correlated as a function of $Sr(H/D)^{0.5}$. Figure 5-15 demonstrates the variation of δNu_0 and $\delta\overline{Nu}$ with these two modified Strouhal numbers for the whole set of investigated conditions, together with a least-square fitted correlation curve for each figure (shown with solid lines).

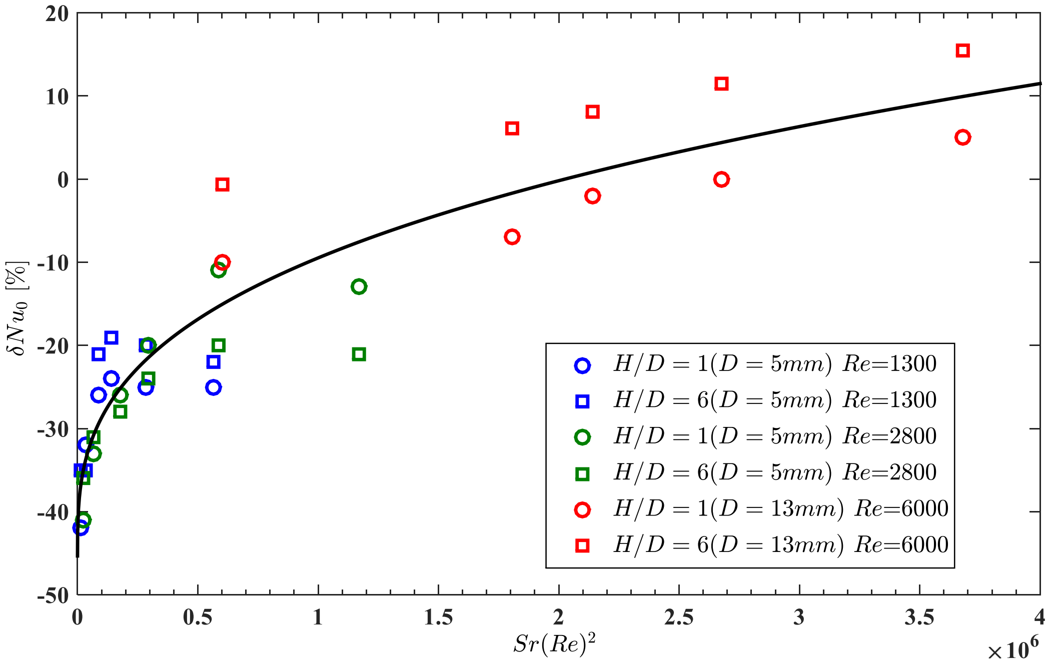

(a)

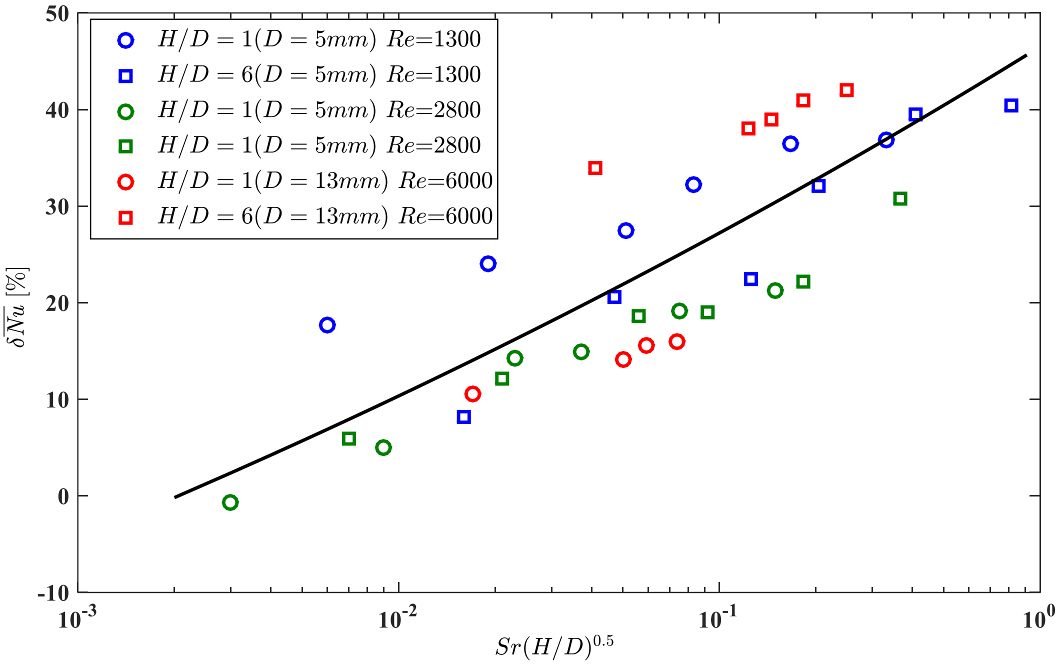

(b)

Figure 5-15. Variation of (a) δNu_0 with $SrRe^2$ and (b) $\delta\overline{Nu}$ with $Sr(H/D)^{0.5}$ as modified Strouhal numbers for the whole set of investigated conditions (D = 13 mm for Re = 6,000, 9 Hz ≤ f ≤ 55 Hz, 0.017 ≤ Sr ≤ 0.102; and D = 5 mm for Re = 1,300 to 2,800, 5 Hz ≤ f ≤ 260 Hz, 0.0029 ≤ Sr ≤ 0.333) for H/D = 1 and 6, together with least-square fitted curves

The power law correlations derived for $\delta Nu_0 = \mathrm{f}(SrRe^2)$ and $\delta\overline{Nu} = \mathrm{f}(Sr\left(\frac{H}{D}\right)^{0.5})$ are shown in equations (5-3) and (5-4) as follows:

$$\delta Nu_0 \cong 0.3739(SrRe^2)^{0.3307} - 45.53;\ R^2 = 0.85 \tag{5-3}$$

$$\delta\overline{Nu} \cong\ 77.84\left(Sr\left(\frac{H}{D}\right)^{0.5}\right)^{0.1319} - 31.61; R^2 = 0.71 \tag{5-4}$$

where R^2 is the coefficient of determination, indicating how well the data fit the correlations shown above [77].

The results plotted in Fig. 5-15(a) show that for the same range of modified Strouhal number $SrRe^2$, the enhancement of stagnation Nusselt number can be improved by employing a larger nozzle diameter (13 mm), for all *H/D* values. Specifically, at *H/D* = 6, the larger nozzle alters the reduction (< 0) in stagnation heat transfer to enhancement (> 0) for Sr > 0.017 ($SrRe^2$ = 0.6×10^6); for *H/D* = 1 this occurs only for Sr > 0.07 ($SrRe^2$ = 2.6×10^6). When it comes to the change in area-averaged Nusselt number, the larger nozzle only delivers an improvement for *H/D* = 6, while for *H/D*=1, $\delta\overline{Nu}$ drops to lower values than the corresponding values for the 5 mm nozzle; this can be seen in Fig. 5-15(b).

The results reported here confirm that the heat transfer performance of pulsating jets depends strongly on parametric and operating conditions. Thus, to obtain the maximum enhancement in heat transfer, all these mutually dependent conditions must be methodically investigated and understood for the effective optimization of performance.

5.4 Conclusion

In this chapter a comprehensive numerical-experimental study had been performed to investigate the effect of flow pulsation on fluid flow and heat transfer for axisymmetric air jets impinging on a flat surface. It is concluded that a properly designed numerical model can be used for accurate investigations of the fluid flow and the heat transfer phenomena in unsteady impinging jets. This is of great value for the simulation of the operating conditions beyond experimental capabilities. In this study, this holds specifically for considerably higher pulsation frequencies, 130 Hz and 260 Hz, than the maximum experimental limit (65 Hz). This helps to identify the threshold of *f* and *Sr* at which the heat transfer enhancement reaches an approximately constant value, where a further increase in frequency drops the enhancement.

Through a step-by-step procedure, the techniques toward accomplishment of the final *CFD* model are described. Using detailed experimental data, the developed *CFD* model is validated for a large range of operating conditions. This is done for both steady and pulsating jets at $H = 1D$ and $6D$ and *Re* of 1,300 and 2,800 for two sample pulsation frequencies $f = 5$ Hz and 40 Hz. The deviations of the *CFD* results from the experimental data in terms of local *Nu* are calculated as 6% and 10% for the steady and pulsating jets, respectively.

Using pulsating impinging jets over the investigated range of conditions, the area-averaged *Nu* exhibits larger enhancements showing a monotonic increase with frequency at different *H/D* values, while the stagnation *Nu* undergoes a reduction. For *Sr* range of $0.0029 \leq Sr \leq 0.3333$, the stagnation and area-averaged heat transfer modifications, when compared to the corresponding steady jet, are calculated as -42% $\leq \delta Nu_0 \leq$ -10% and -1% $\leq \delta\overline{Nu} \leq$ 40%. This confirms that the augmented $\delta\overline{Nu}$ outweighs the reductions in δNu_0.

A closer look at the radial distribution of near-wall components is presented using the numerical flow visualization of velocity and vorticity contours in the computational domain. This shows how periodic re-development of the jet flow can affect the fluid flow and heat transfer in the domain. Primary vortices and additional reverse vortices in the viscous sub-layer are captured. The radial velocity gradient, the normal vorticity, and Reynolds stress components are monitored. This method shows a direct dependency between the heat transfer behaviour of steady and pulsating jets over the impingement surface and the monitored flow components.

Overall, pulsating jet cooling technology shows great potential for thermal management applications such as compact electronic systems. Pulsating jets highly depend on operating conditions, and adjusting the effective parameters appropriately can cause a significant enhancement.

The developed numerical model for steady and pulsating jets is extended further in the next chapter for simulation of the intricate fluid flow in synthetic jets.

Some of the findings presented in this chapter have been published in Alimohammadi et al. [35], [36] and [38].

6 Synthetic Jet Flows

This chapter presents the numerical and experimental study performed on synthetic jets. The previously validated transient numerical model for pulsating impinging jets is extended to synthetic jets. Flow vectoring by a pair of synthetic jets is suitable for modification of the global flow characteristics with practical applications in active flow control and adaptive heat convection. The formation, evolution and interaction of a pair of adjacent synthetic jets issuing from adjacent rectangular slot orifices are in is investigated numerically using computational fluid dynamics and experimentally using particle image velocimetry. Both jet actuators are operated at the same condition but with an adjustable phase difference $\delta\phi$. The investigation considers a jet pair issuing into quiescent air.

As shown in Fig. 6-1, a synthetic jet is typically generated from a partially closed cavity with an orifice and an oscillating diaphragm. Vibration of the diaphragm draws in and ejects ambient fluid through the orifice. This results in a train of vortex rings at the orifice outlet, to form the external jet flow. The previously developed knowledge in numerical modelling of pulsating impinging jets is extended in this chapter to predict the fluid flow in synthetic impinging jets.

To achieve the most realistic calculation of the flow induced by synthetic jets, a full transient simulation is performed of the internal flow in two cavities as well as the external jet flow. The actuator diaphragm deformation is treated using a dynamic mesh technique which is the most suitable scheme to reproduce the essential flow features.

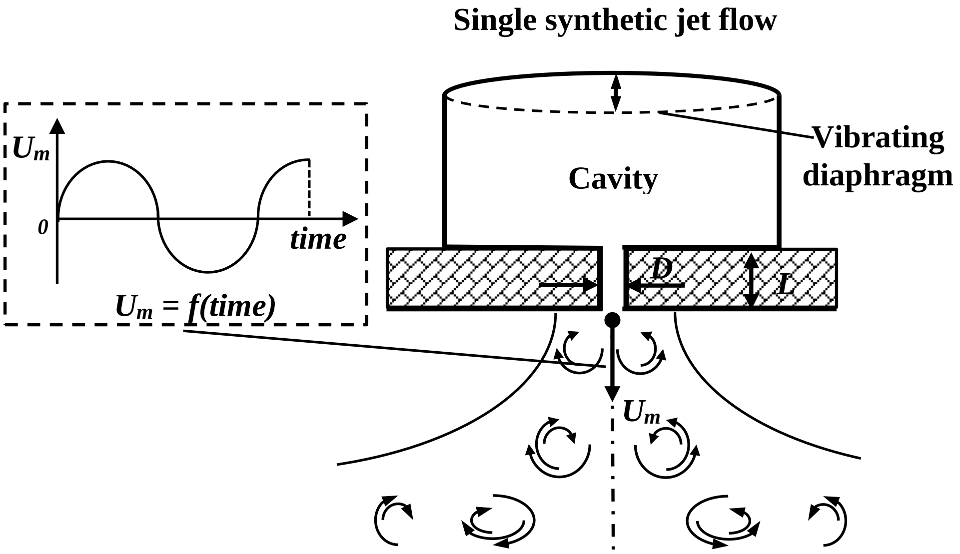
Single synthetic jet flow

Figure 6-1. Schematic diagram of synthetic jet flow

The results show a reasonable quantitative agreement with *PIV* measurements performed by Smith and Glezer [78] as well as new measurements presented in this chapter for jets issuing into quiescent air.

These results give confidence that the developed *CFD* approach can be utilized to predict the intricate flow vectoring phenomenon induced by adjacent synthetic jets.

The effect of phase difference between the pair of adjacent synthetic jets on the vectoring of the merged jet is investigated. The near-field entrainment of surrounding flow into the jet is highly affected by the vortex formation process. The combined or merged jet is vectored in the direction of the cavity that is leading in phase, with a similar trend shown by the experimental and numerical results of instantaneous and time-averaged vortical structures. This leads to a better physical understanding of the fluid mechanics of adjacent synthetic jets, and enhances the theoretical basis needed to promote their practical application.

6.1 Numerical approach

This section briefly describes the unsteady compressible numerical model used for the simulation of a flow field for adjacent synthetic jets. The computational flow-field, as well as the boundary conditions, and driving signals that define the displacement of the deforming diaphragms are shown in Fig. 6-2. Two cavities are located adjacent to each other with the orifice slot at their side wall. The driving signals for left and right cavities are represented by $\emptyset_L$ and $\emptyset_R$, respectively. To have a more realistic deformation of cavity diaphragm, maximum displacement is applied at the centre of diaphragm, decreasing in a parabolic manner toward the edges. With the diaphragm vibrating harmonically in time, the diaphragm geometry is parabolic at any instant in time. The method by which the out-of-phase deformation of adjacent diaphragms is defined in the numerical model, is schematically depicted in Fig. 6-2 (a-b). The computational domain consists of three distinct regions, namely cavity, orifice slot, and the region through which the jet is developed. The sensitivity analysis suggests that the far-field boundary conditions should be developed far enough downstream in order to guarantee the computational results are not affected by the atmospheric pressure boundary condition, therefore, they are established at 80*D* in span-wise, *x*, and 100*D* in axial, *y*, directions.

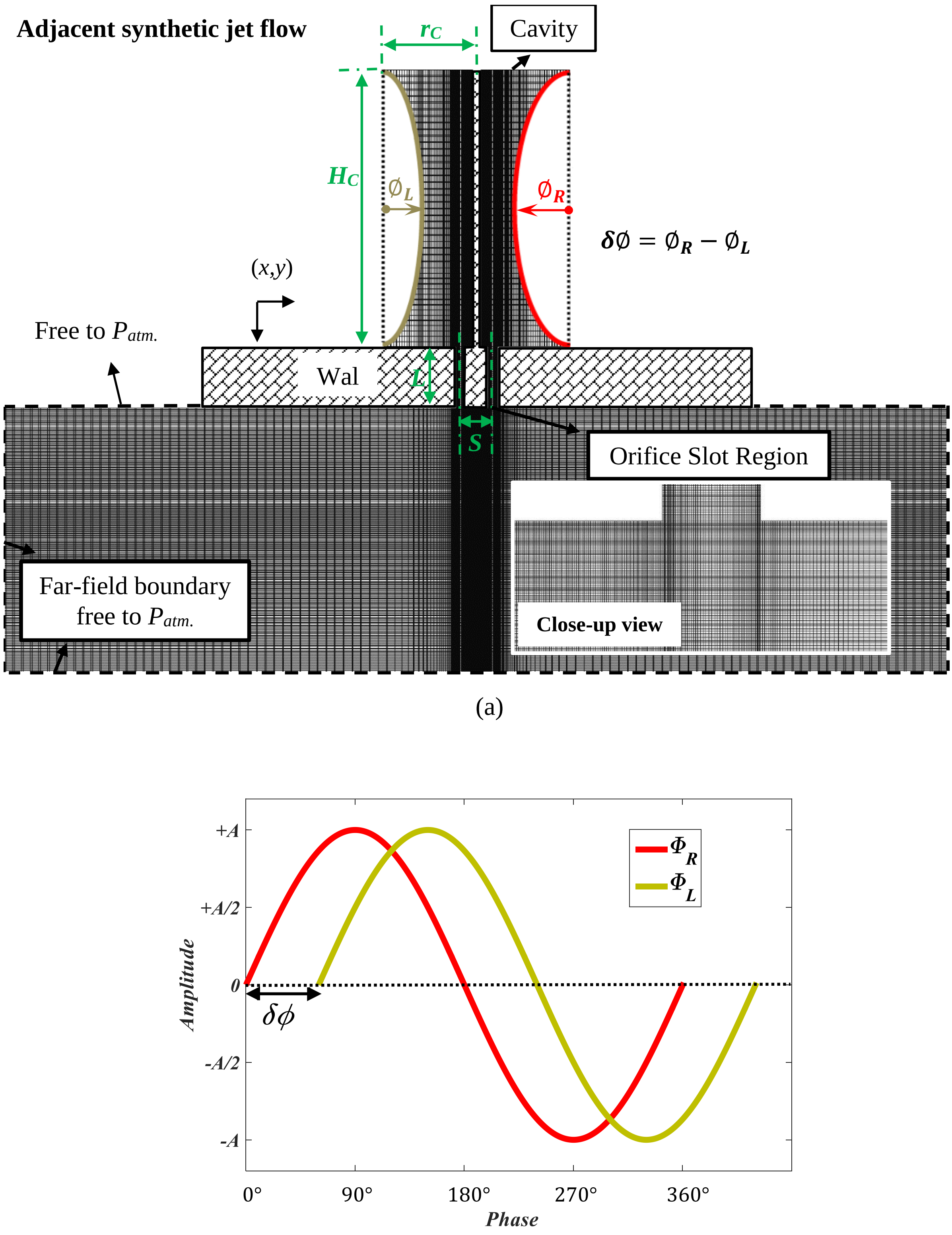

(a)

(b)

Figure 6-2. a) Computational flow-field (diaphragm deformations are exaggerated for clarification of phase difference); b) harmonic driving signals used to define the displacement of side-by-side deforming diaphragms

Cavity parameters, which are kept the same in both experimental and numerical investigations, are listed in Table 6-1. With a fixed value of diaphragm oscillation frequency, the value of diaphragm amplitude is varied in order to produce a stroke length of $L_0 = 29D$, and Reynolds number of $Re = 300$. This keeps the operating conditions identical to that of the accompanying experiments.

Table 6-1. Operating conditions and sizes

Parameter	**Value**
Orifice slot width (D)	1.65 mm
Jet orifice length (L)	$5.81D$
Diaphragm amplitude (A)	0.58 mm
Diaphragm frequency	57 Hz
Cavity or diaphragm radius (r_C)	$45.45D$
Cavity height (H_C)	60.6 mm
orifice-to-orifice centre distance (S)	$3.3D$
Cavity volume (V_C)	101.5 cm^3
Helmholtz resonance frequency (f_h)	485 Hz

For two dimensional simulations of flow field, almost 200,000 grid points are used. An adequate value of near-wall cell thickness is ensured by keeping the y^+ (non-dimensional distance of the first grid point off the wall, scaled with the local friction velocity and kinematic viscosity) below unity for the near-wall cells. As a numerical uncertainty analysis, a Grid Convergence Index (*GCI*) study is performed to show that solutions are in the asymptotic range of convergence Celik et al. [45] and Alimohammadi et al., [34]. 2nd order discretisation scheme is used for all of the simulations. The shear stress transport (*SST*) model coupled with modified curvature correction and also the *Gamma-Theta* transition model has been found to best capture the flow field of unsteady jets Alimohammadi et al. [35]-[36] and [38] (see also sections 4.1 and 0).

A major challenge lies in simulating the time dependent diaphragm motion. Employment of proper dynamic meshing techniques to capture this motion and also fluid-structure interaction between the diaphragm and air inside the cavity are the most important aspects.

The model requires an original mesh to be input, together with a specification of all regions that deform with time. For each deforming region of the computational grid, the point motion grids are specified on the domain boundaries by a user defined function (*UDF*). This is achieved using a *FORTRAN* based routine integrated into the *CFD* model. The motions of the other regions are determined by a mesh motion model, called *Displacement Diffusion*. In this model, the displacements specified on domain boundaries are diffused to other regions by solving the following equation at the start of each time step [39]:

$$\nabla.\left(\Gamma_{disp}\nabla\delta\right) = 0 \tag{6-1}$$

where, δ is the relative displacement with respect to the previous mesh and Γ_{disp} is the stiffness of the mesh. The latter defines the degree to which the mesh regions deform together. For a constant value of Γ_{disp}, deformation determined in the domain will be uniformly diffused through the mesh. A variable Γ_{disp} can produce a more realistic distribution of fine near-boundary regions. This can be done by assigning a higher stiffness near small mesh volumes so that the mesh quality will benefit from having larger cells that undergo bigger deformations. To determine the variable mesh stiffness, the equation below is used:

$$\Gamma_{disp} = (\frac{L_{ref}}{d})^{C_{stiff}} \tag{6-2}$$

Increasing the distance from the nearest boundary, *d*, will decrease Γ_{disp}. In the above equation L_{ref} is the reference length, representing a typical element length in the domain, and the exponent C_{stiff} specifies how quickly the change in stiffness occurs. This exponent is set to 2 by default.

Integral conservation equations are modified to account for deformation of control volumes with time. By use of Leibnitz integral rule, differential conservation equations of mass and momentum are respectively shown as follows:

$$\frac{d}{dt}\iiint \rho dV + \iint \rho\left(U_j - W_j\right)dn_j = 0 \tag{6-3}$$

$$\frac{d}{dt}\iiint \rho U_j dV + \iint \rho\left(U_j - W_j\right)U_j dn_j = -\iint P dn_j + \iint \mu_{eff}\left(\frac{\partial U_i}{\partial x_j} + \frac{\partial U_j}{\partial x_i}\right)dn_j + \iiint S_{U_i} dV \tag{6-4}$$

where U_j and W_j are fluid velocity and deforming control volume boundary velocity, respectively. In the above equations, the advection term (second term) takes into account the net advective transport across the moving boundaries of control volume [39].

1000 iterations per cycle are used based on the sensitivity study of the time-step size for simulations. Convergence criteria for all of the iterative equations are set to 1^{e-5}. The solution is continued up to several cycles until all the monitored values of characteristic fluid flow parameters, namely components of velocity, velocity gradients, vorticity, and pressure, in different locations through the computational domain become periodic. The solution is considered periodic when the root-mean-squared deviation on the time-averaged magnitude of the monitored parameters between two successive cycles does not exceed 1%.

Further information about the computational procedure and sensitivity analysis on the effect of grid density, turbulence model are reported in sections 4.1 and 5.1 and Alimohammadi et al. [34]-[38], where a comprehensive study on the fluid flow and heat transfer to steady and pulsating impinging jets is presented.

6.2 Experimental setup

6.2.1 Adjacent synthetic jet facility

The experimental setup used to validate the numerical results is shown in Fig. 6-3. The synthetic jet pair are driven with two *Visaton FR 8* speakers inside polyamide rectangular cavities. The speakers force ambient air through an accurately machined acrylic orifice plate 10 mm in thickness with a slot width of D = 1.65 mm and span of 44.5 mm (aspect ratio = 27:1).

Estimating the jet orifice velocity and hence the Reynolds number in a synthetic jet flow can be difficult, due to compressibility effects of the fluid. This is further complicated by a jet pair since the adjacent pressure fields cause interference; see Smith and Glezer [113]. Therefore, a calibration model described by Persoons and O'Donovan [114] and Persoons [115] is used to maintain Re and L_0 of the jet pair at fixed values during *PIV* measurements. *PIV* measurements can subsequently be used to verify the jet orifice velocity. The cavity pressure amplitude $|p_c|$ is measured by placing a high pressure microphone (*G.R.A.S.* 40BH, 0.5mV/Pa) inside one of the cavities. The jet velocity amplitude $|U_m|$ is then obtained from the relationship shown below:

$$\frac{\rho a|U_m|}{|p_c|} = \left(\frac{2V_c}{AL'}\right)^{\frac{1}{2}} \times \left(\left(\frac{f}{f_h}\right)^2 + \left[\left(\frac{f}{f_h}\right)^4 + \left(\frac{KV_C}{AL'}\frac{|p_c|}{\rho a^2}\right)^2\right]^{\frac{1}{2}}\right)^{-\frac{1}{2}} \tag{6-5}$$

where a is the speed of sound, f_h is the Helmholtz resonance frequency (= $a/(2\pi L')[AL'/V_C]^{1/2}$ = 343 Hz), V_C is the cavity volume, A is the orifice cross sectional area and the effective orifice length $L' = L(1 + 2\beta D)$. The empirical parameter β represents an acoustic radiation end correction (here, $\beta = 2.6 \pm 0.2$) and K represents fluidic damping in the orifice ($K = 1.81 \pm 0.15$), the values of which are determined in an initial calibration by Persoons and O'Donovan [114] and Persoons [115]. The model accurately predicts the behaviour up to a geometry-dependent limit frequency in excess of the Helmholtz frequency f_h. The time-averaged jet ejection velocity $U_0 = |U_m|/\pi$, for sine wave excitation, and hence *Re* and L_0 can be quantified. The high pressure microphone allows control of the cavity pressure p_c, *Re* and L_0 to a fixed value.

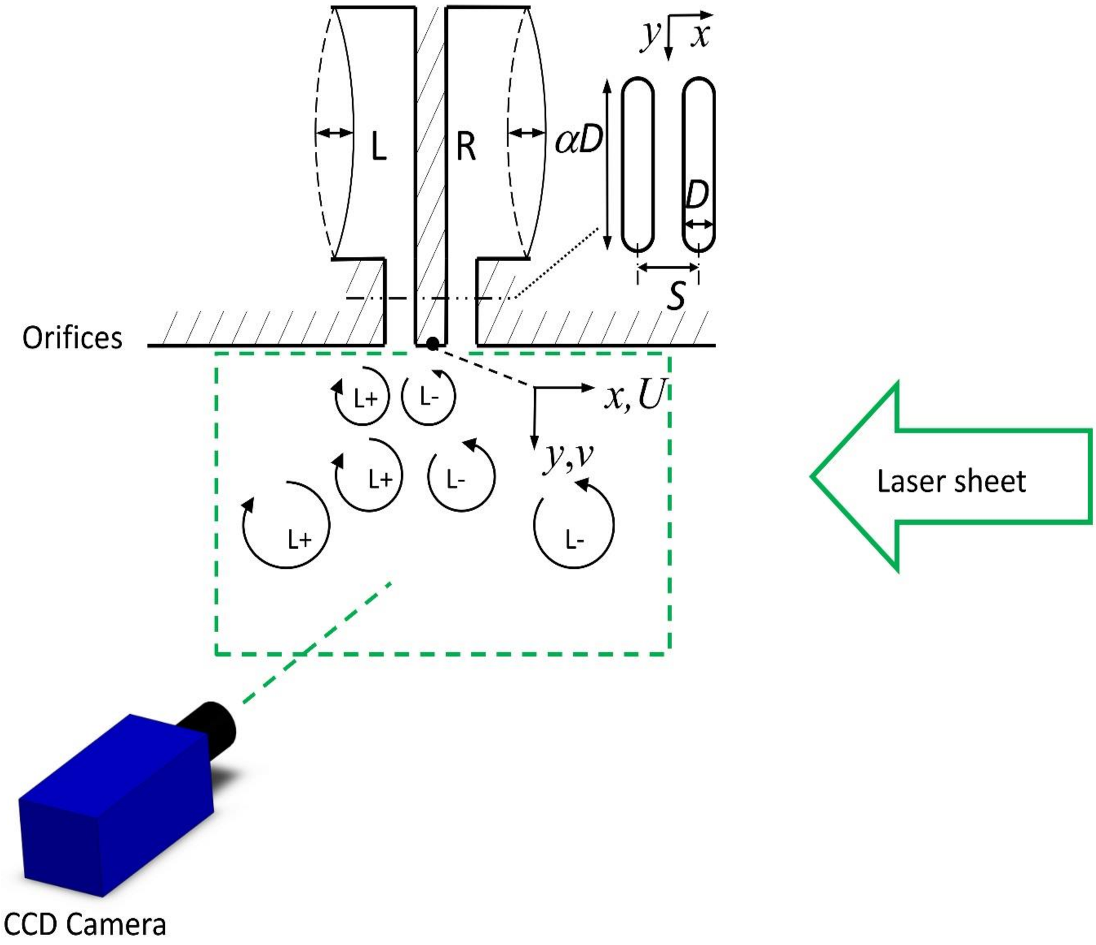

Figure 6-3. Synthetic jet *PIV* measurement setup

6.2.2 *PIV* Flow field measurements

Flow velocity measurements have been performed using particle image velocimetry (*PIV*), as shown in Fig. 6-3. The PIV system comprises a *New Wave Solo-II Nd:YAG* twin cavity laser (30 mJ per pulse at 15 Hz) and a *PCO Sensicam*^{TM} thermo-electrically cooled *CCD* camera (1280×1024 px^2, 12 bit) with 28 mm lens. A glycol-water aerosol is used for seeding, with a mean particle diameter of 0.25 µm. The laser beam passes through customized optics to form a 0.3 mm thick light sheet aligned to the plane of the jet pair midway across the orifice slot length (x, y, 0) as shown in Fig. 6-3. The *CCD* camera is mounted perpendicular to the light sheet. The image resolution is about

36 μm/px. A narrow band pass filter is used with fluorescent paint which absorbs the reflections on the orifice plate. This maximizes the signal-to-noise ratio near the walls.

The *PIV* system is phase-locked to the synthetic jet actuators by means of a trigger signal, which synchronised the rising flank zero passage of one actuator's voltage waveform with zero phase angle in the *PIV* measurement. Images are acquired for 24 phases, θ**,** per cycle ($\theta = 0{:}15{:}360^\circ$) and 32 vector fields are averaged for each phase. The *PIV* system is limited to a laser pulse frequency, f_p, of 15 Hz whereas the frequency of the jet f is 57 Hz. Therefore, each 15 ° interval measurement is taken N cycles apart (i.e. $\theta = 0^\circ, 15 + N\times360^\circ, 30 + 2N\times360^\circ \ldots 360^\circ + 24N\times360^\circ$) where N is an integer such that $N > f/f_p$. The laser pulse separation time is determined such that no vectors are dropped in the highest shear regions of the jet.

6.2.3 Post-processing of *PIV* measurements

The velocity fields are processed with *Lavision Davis* 7.2.2 software, using multi-grid cross-correlation with continuous window shifting and deformation. An interrogation window size decreasing from 64×64 to 32×32 px^2 at 75% overlap is used with Whittaker reconstruction in the final pass. The seeding density is sufficiently high to assume an order of magnitude displacement uncertainty of 0.1 pixel; see Stanislas et al. [116], which yields an uncertainty in the velocity field between 1% for the high velocity region and 20% for the low velocity regions. *PIV* measurements confirm the ejection velocity values of the jet pair measured from the calibration model which is discussed in section 2.1. *PIV* measurements performed in this study are only done for the in-phase adjacent jets test case with $\delta\emptyset = 0°$.

Reynolds decomposition of the velocity field in a quasi-periodic flow is used to extract the required phase-resolved and time-averaged velocity components, as follows:

$$u(\theta,t) = \underbrace{\tilde{u}(\theta)}_{\substack{\text{phase-}\\ \text{resolved}}} + \underbrace{u_t(\theta,t)}_{\text{unresolved}} \tag{6-6}$$

where $\tilde{u}(\theta)$ represents the phase-averaged velocity, defined as the following ensemble average:

$$\tilde{u}(\theta) = \frac{1}{N_c}\sum_{c=1}^{N_c} u(\theta, t) \tag{6-7}$$

where c and N_c are the cycle index and number of cycles used (here: $N_c = 64$).

The time-averaged velocity is defined as:

$$\bar{u} = \frac{1}{N_p}\sum_{p=1}^{N_p} \tilde{u}(\theta) \tag{6-8}$$

where p and N_p are the phase index and number of phase angles per period (here: $N_p = 24$).

The turbulent velocity fluctuation is defined as:

$$u'(\theta) = \sqrt{\frac{1}{N_c}\sum_{c=1}^{N_c} u_t^2(\theta, t)} \tag{6-9}$$

6.3 Validation of the numerical model

Firstly, the numerical model is used to simulate a pair of adjacent synthetic jets expelling into quiescent air. The objective is to compare numerical results of different flow features for phase-locked ($\delta\emptyset = 0°$) and out-of-phase ($\delta\emptyset \neq 0°$) jets, against experimental data. The numerical results are compared with experimental results from the current study and with the results of Smith and Glezer [78].

Secondly, the validated numerical model is used in a more detailed analysis of the flow vectoring phenomenon for two free adjacent synthetic jets issuing into quiescent fluid.

6.3.1 Free adjacent synthetic jets

To assess the performance of the *CFD* model, the results are first carefully compared with experimental data. The target case to perform an experimental validation of *CFD* model is a pair of adjacent synthetic jets with a separation distance $s = 3.3D$, stroke length $L_0 = 29D$, and Reynolds number $Re = 300$. This is identical to the operating condition used in *PIV* measurements of this study, which aims to reproduce the same operating conditions as Smith and Glezer [78].

The validation of the numerical model is presented in Fig. 6-4. The variation of non-dimensional stream-wise time-averaged centreline velocity, $\bar{v}/U_o$ at $x/D = 0$, with stream-wise distances from the orifice exit plane, *y/D*, for in-phase adjacent jets ($\delta\emptyset = 0°$) is shown in Fig. 6-4 for both experimental data and numerical results.

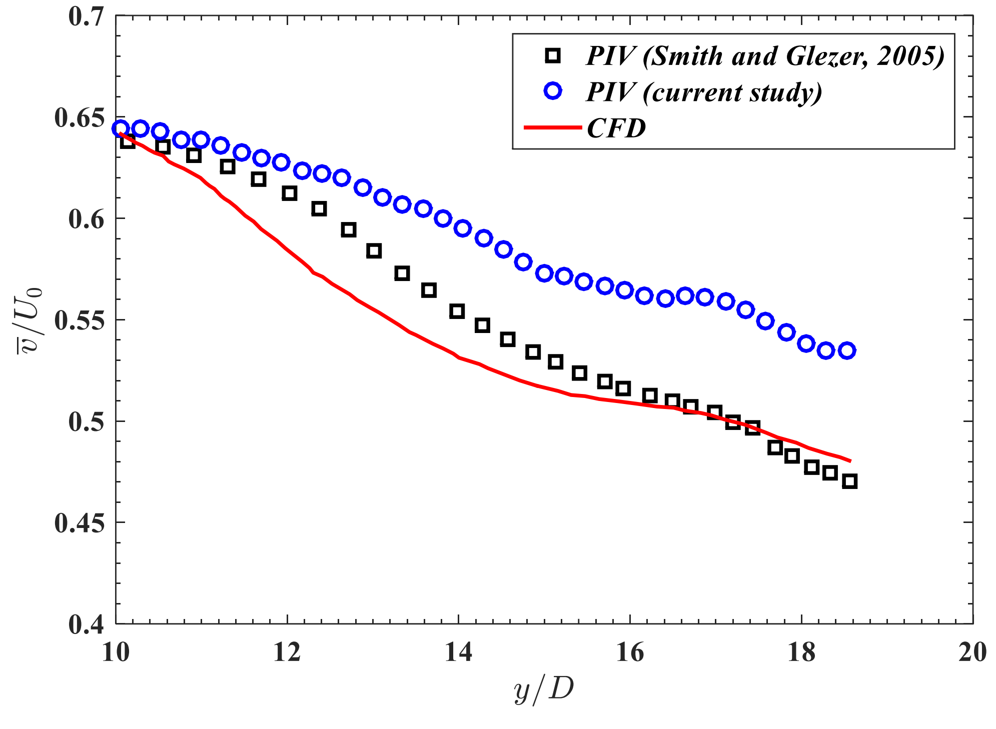

Figure 6-4. Comparison of CFD and experimental data Smith and Glezer [78]: variation of non-dimensional stream-wise centreline velocity, $\bar{v}/U_o$ at $x/D = 0$, with stream-wise distances from the orifice exit plane, *y/D*, for in-phase adjacent jets ($\delta\emptyset = 0°$)

It is clear that the stream-wise velocity decreases with increasing distance from orifice outlet along the centreline. This comparison confirms the numerical model accurately replicates the trend of the experimental stream-wise centreline velocity distribution for a pair of in-phase adjacent jets. Maximum deviation of numerical results from the PIV measurements of Smith and Glezer [78] is quantified as 10%. The jet is formed by a rapid time-harmonic motion, however the far-field behaviour of the jet is comparable to a steady blowing jet. Interestingly, the decay rate of the jet pair exhibits a very similar trend to a conventional two-dimensional turbulent jet (v/U_0).

The agreement of the numerical result is considerably better when compared to *PIV* measurements performed by Smith and Glezer [78], while the deviation from *PIV* measurements in this study does not exceed a percentage error of 11% in $10 < y/D < 20$. This is mainly attributed to the fillet-type edges of the nozzle slots used for *PIV* measurements in this study, whereas straight edge slots are used in both the numerical study and the measurement done by Smith and Glezer [78]. Nevertheless, the numerical results and *PIV* data from the present study and Smith and Glezer [78] all show similar trends and inflection points at comparable axial locations.

To further illustrate the agreement of the numerical results with *PIV* measurements done in this study, Fig. 6-5 shows cross-stream distribution of axial and span-wise velocities (v and u normalized with U_0, respectively) at a stream-wise distance from the orifice exit plane of $y/D = 25$. Figure 6-5 shows that the numerical model captures a qualitatively and quantitatively comparable trend to that of *PIV* measurements for both $\bar{v}/U_o$ and $\bar{u}/U_o$ over a range spanning $-18 < x/D < +18$.

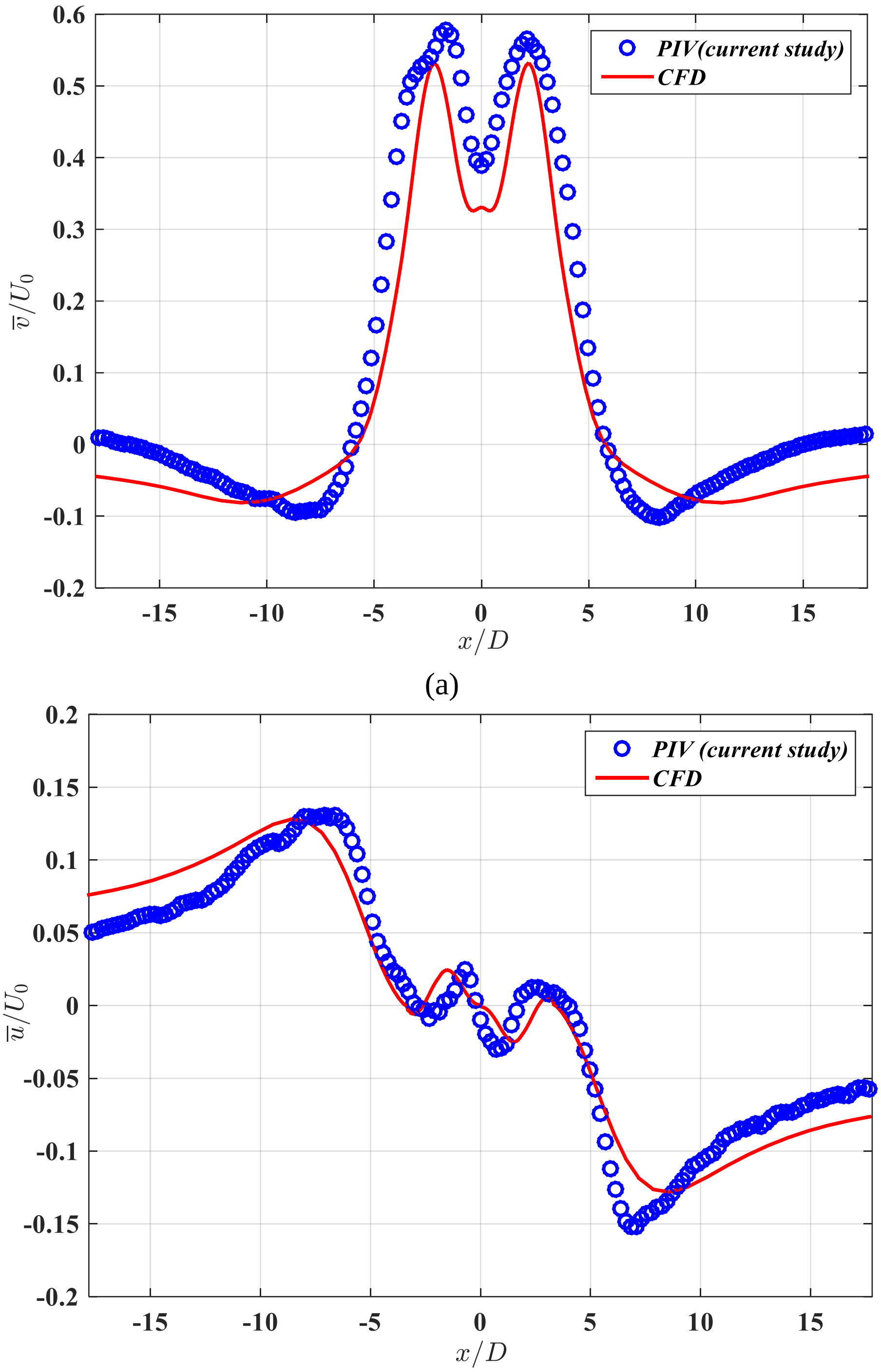

(b)

Figure 6-5. Comparison of *PIV* data versus numerical results for cross-stream distribution of (a). normalized axial velocity, $\bar{v}/U_o$, and (b). normalized span-wise velocity, $\bar{u}/U_o$, at a stream-wise distance from the orifice exit plane of *y/D* = 25

In terms of fluctuating components of velocity, the comparison of numerical results versus *PIV* measurements is shown in Fig. 6-6.

Regarding the numerical results, the isotropic turbulence model used in this study returns the same value for the magnitudes of fluctuation components $\overline{u'}$ and $\overline{v'}$, here called $\overline{u'}_{isotropic}$. The isotropic fluctuating component of velocity, $\overline{u'}_{Isotropic}$, is defined as:

$$\overline{u'}_{isotropic} = \frac{2}{3}\sqrt{\bar{k}} \tag{6-10}$$

where turbulent kinetic energy, $\bar{k}$, is the time-averaged kinetic energy per unit mass of the turbulent fluctuations, defined as:

$$\bar{k} = \frac{1}{2}(\overline{u'}^2 + \overline{v'}^2 + \overline{w'}^2) \tag{6-11}$$

Turbulent velocity fluctuation extracted through post-processing of *PIV* measurements is reported in eq. (6-9). This provides values for fluctuations in *x* and *y* directions, $\overline{u'}^2$ and $\overline{v'}^2$ respectively, based on the 2*D* concept of *PIV* measurements. Assuming that the missing component of velocity fluctuations in *PIV* measurements, $\overline{w'}^2$, is equal to the span-wise fluctuation component, $\overline{u'}^2$, $\bar{k}$ for *PIV* data is redefined as:

$$\bar{k} = \frac{1}{2}(\overline{2u'}^2 + \overline{v'}^2) \tag{6-12}$$

Figure 6-6 shows that while the cross-stream distribution shows a similar trend for $\overline{u'}_{Isotropic}$, the values calculated with the numerical model are significantly smaller than the fluctuation experienced in the measurements. This is mainly because of the nature of the two dimensional *Reynolds-Averaging* concept used for the turbulence modelling in this study, resulting in a reduction of the fluctuating velocity component.

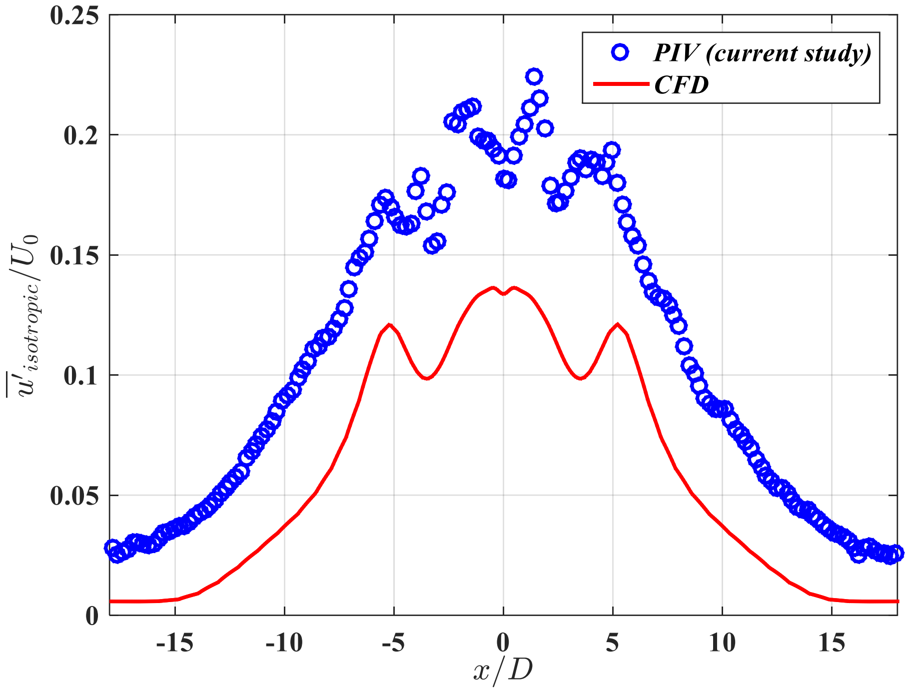

Figure 6-6. Comparison of *PIV* data versus numerical results for cross-stream distribution of fluctuating velocity component, $\overline{u'}_{isotropic}/U_0$, at a stream-wise distance from the orifice exit plane of *y/D* = 25

6.4 Results and discussion on synthetic jet vectoring

6.4.1 Time-averaged flow field: experimental versus numerical results

Smith and Glezer [78] have experimentally shown that the combined jet vectors toward the actuator that is leading in phase. The time-averaged streamlines determined by the authors for adjacent jets with various phase differences, $\delta\emptyset = 0°,\ 60°,\ 70°,\ 80°,$ and $130°$, are compared to the numerical results in Fig. 6-7(a-e). The streamlines are mapped together with velocity contours and vectors in the numerical results to better reveal some major flow features.

It can be seen that the merged jet is vectored to the right (i.e., toward the cavity that is leading in phase) with a very similar trend between experimental and numerical results. This is especially interesting since the shape and size of the cavity used in experiments by Smith and Glezer [78] is unknown, yet the predicted flow structure of the jet is remarkably similar. This suggests that the formation and evolution of the jet is relatively independent of the cavity geometry and only depends on its volume. It is also unknown how far the domain is physically confined in both span-wise and axial directions in the experiments by Smith and Glezer [78]. Except for the two non-dimensional characteristic parameters of synthetic jets, stroke length (L_0) and Reynolds number (*Re*), almost all of the dimensions and parameters in the *CFD* model, namely orifice slot width, diaphragm amplitude and frequency, cavity sizes, are different from the experiment (see Table 6-1).

The time-average streamlines in Fig. 6-7, demonstrate zero net mass flow rate through the orifice. For a pair of phase-locked jets ($\delta\emptyset = 0°$), Fig. 6-7 (a), the symmetric streamlines of the merged jet (around the domain centreline) entrain surrounding air and transports the flow at a higher flow rate, compared to a single synthetic jet Smith and Glezer [78]. The authors reported that the flow rate transferred by the merged jet is approximately two times larger than that of a single synthetic jet. The arrow markers on the experimental data and velocity vectors on the numerical results show how the fluid from the wider surroundings is entrained into the core of the merged jet.

The flow fields of out of phase jets (right hand side is leading in phase) are presented in Fig. 6-7 (b-e). For $\delta\emptyset = 60°$, Fig. 6-7 (b), the merged jet is vectored toward the right with a nominal angle of $\alpha_N = 17°$ based on the *PIV* results. In comparison, for the numerical results, the asymmetric streamlines of the merged jet show an approximate vectoring angle of $19°$. It is worth noting that significant aspects of the physical phenomenon are not captured properly with *2D Reynolds-Averaged* turbulence modelling. However, the *CFD* model benefits here from the utilisation of mesh deformation techniques for simulation of the cavity. This compensates for the disadvantages described earlier in section 6.1 and enables the *CFD* model to realistically capture the physical phenomena with reasonable computational costs.

A slight increase of phase difference between adjacent jets by 10° can significantly change the vectoring of the jets. For $\delta\emptyset = 70°$, the time-averaged streamlines demonstrate further attraction of the jet pair in the direction of the jet leading in phase and resulting in a larger recirculation zone on the right. The reversing section of this zone is close to the confinement plate on the right. The nominal vectoring, α_N, also increases by $\delta\emptyset$. This is noticeable in both the *CFD* and *PIV* results as shown in Fig. 6-7 (c).

With further increase of phase difference to $\emptyset = 80°$, not shown here, the recirculation region becomes considerably smaller forming a confined compact zone between the merged jet and the confinement (orifice) plate, as the region is attached to the plate on one side. The entrained ambient air is now directed towards the right almost parallel to the orifice plate. Smith and Glezer [78] have idnicated that for this case the flow rate entrained and transferred by the adjacent jets becomes considerably smaller for $\delta\emptyset = 80°$. This can be attributed to the recirculation of a large part of the merged jet on the right hand side of the jet pair which prevents some of the fluid from being entrained.

The size of the recirculation region reduces continuously by increasing the phase difference, $\delta\emptyset$. Fig. 6-7 (d) shows that for $\delta\emptyset = 130°$ the merged jet is fully vectored toward the right with an approximate nominal angle of $\alpha_N = 90°$, almost parallel to the confinement plate. The recirculation zone is very small as shown in the numerical results. This is not fully captured in *PIV* results, mainly because of the limited spatial data points in the domain and the specific filtering and smoothing techniques used in the post processing stage of the results. This can discard some of the extremely small-scale phenomena in *PIV* measurements. The arrow markers illustrate that for this case air is entrained from every direction and subsequently transported entirely toward the right. Smith and Glezer [78] have sub-divided these observations into three main scenarios based on the phase difference between adjacent jets: ‘free vectoring flow’ for $\delta\emptyset \leq 70°$, ‘vectored flow with a recirculating flow domain’ for $80 \leq \delta\emptyset \leq 110°$, and ‘nominally attached flow’ with $\delta\emptyset > 110°$. This agrees well with the corresponding simulations performed using CFD according to Fig. 6-7.

Consequently, this set of results shows that by only maintaining the non-dimensional L_0 and *Re* the same, without fully-defined cavity and slot geometry, the numerical model produces a jet pair structure very similar to that observed in experiments. By making this comparison with other studies, the results suggest that the numerical model is almost independent of so called operating or synthetic jet formation conditions. The adjacent synthetic jets may experience the same 'Vectoring Phenomenon' under different conditions (e.g. frequency, cavity geometry, orifice slot width, etc.), so long as their L_0 and *Re* and phase differences are equivalent.

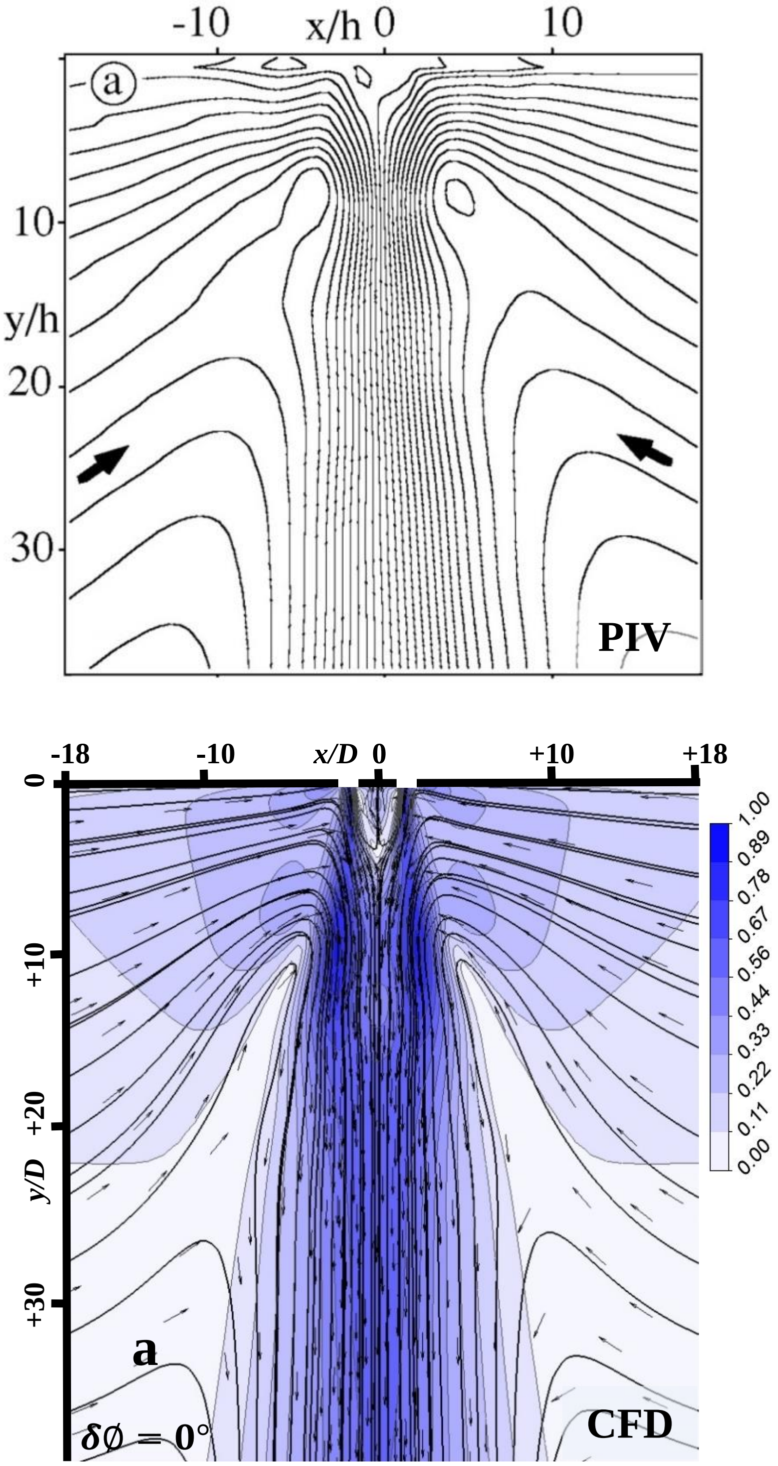

Figure 6-7 (a; continued on the next page). comparison of numerical results to experimental data [78] on time-averaged streamlines for adjacent jets with various phase differences, $\delta\emptyset = 0^\circ,\ 60^\circ,\ 70^\circ,\ 80^\circ,$ and 130°; numerical streamlines are mapped together with velocity contours and vectors

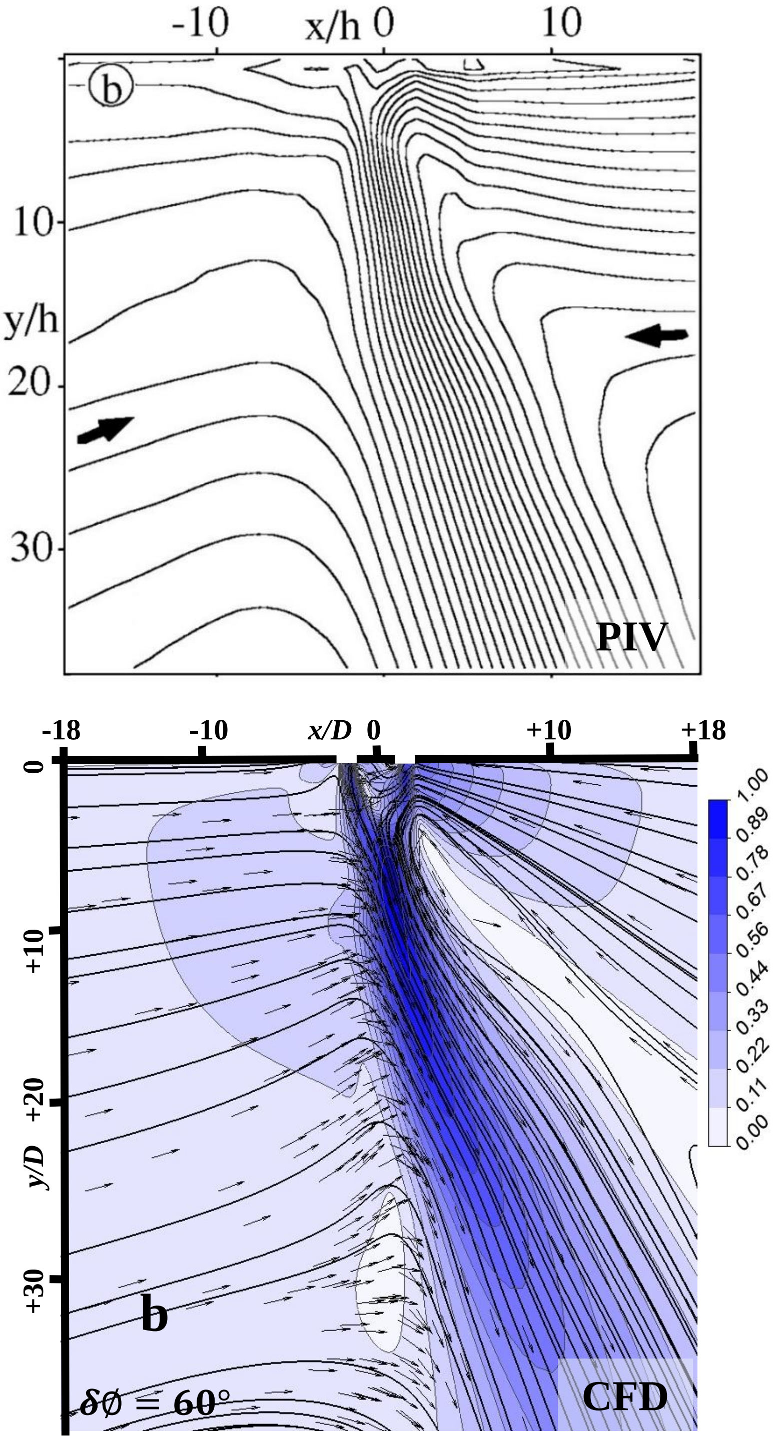

Figure 6-7 (b; continued on the next page)

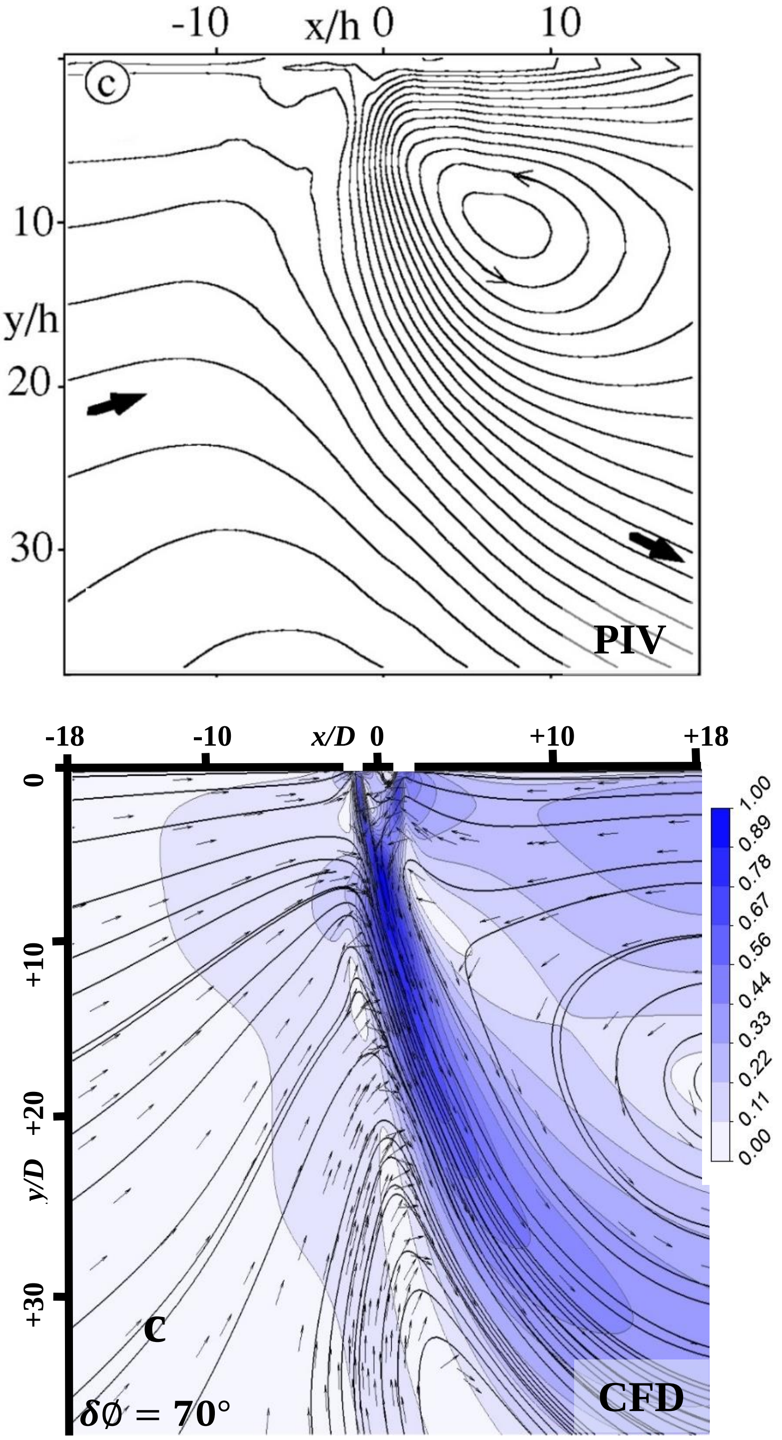

Figure 6-7 (c; continued on the next page)

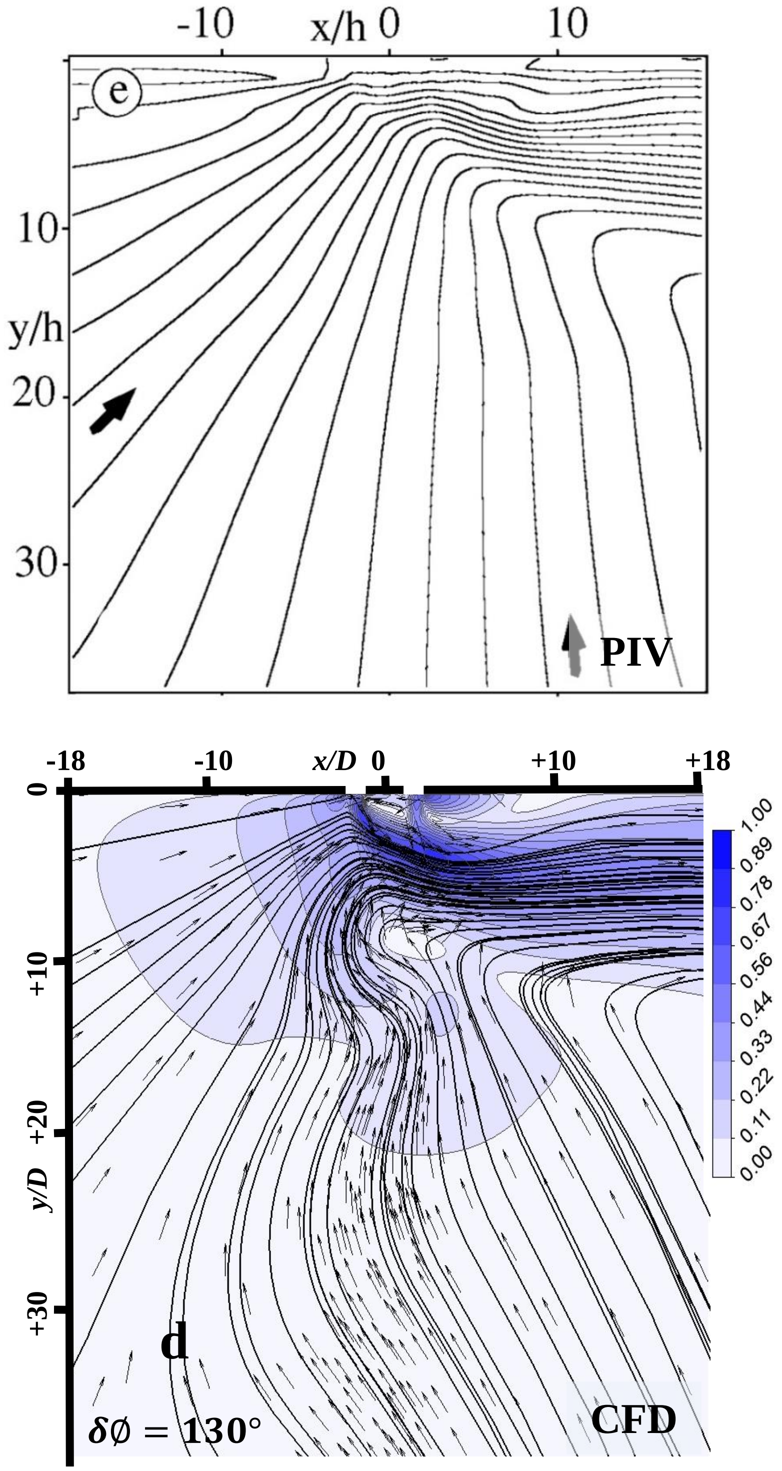
-10
x/h 0
10
e
10
y/h
20
30
PIV
-18
-10
x/D 0
+10
+18
0
+10
+20
y/D
+30
d
δ∅ = 130°
CFD
1.00
0.89
0.78
0.67
0.56
0.44
0.33
0.22
0.11
0.00

Figure 6-7 (d)

6.4.2 Phase-resolved flow fields

PIV results for contours of normalized vorticity ($\omega D/U_0$) at consecutive phase-resolved points in a full jet period, every 15°, are shown in Fig. 6-8.

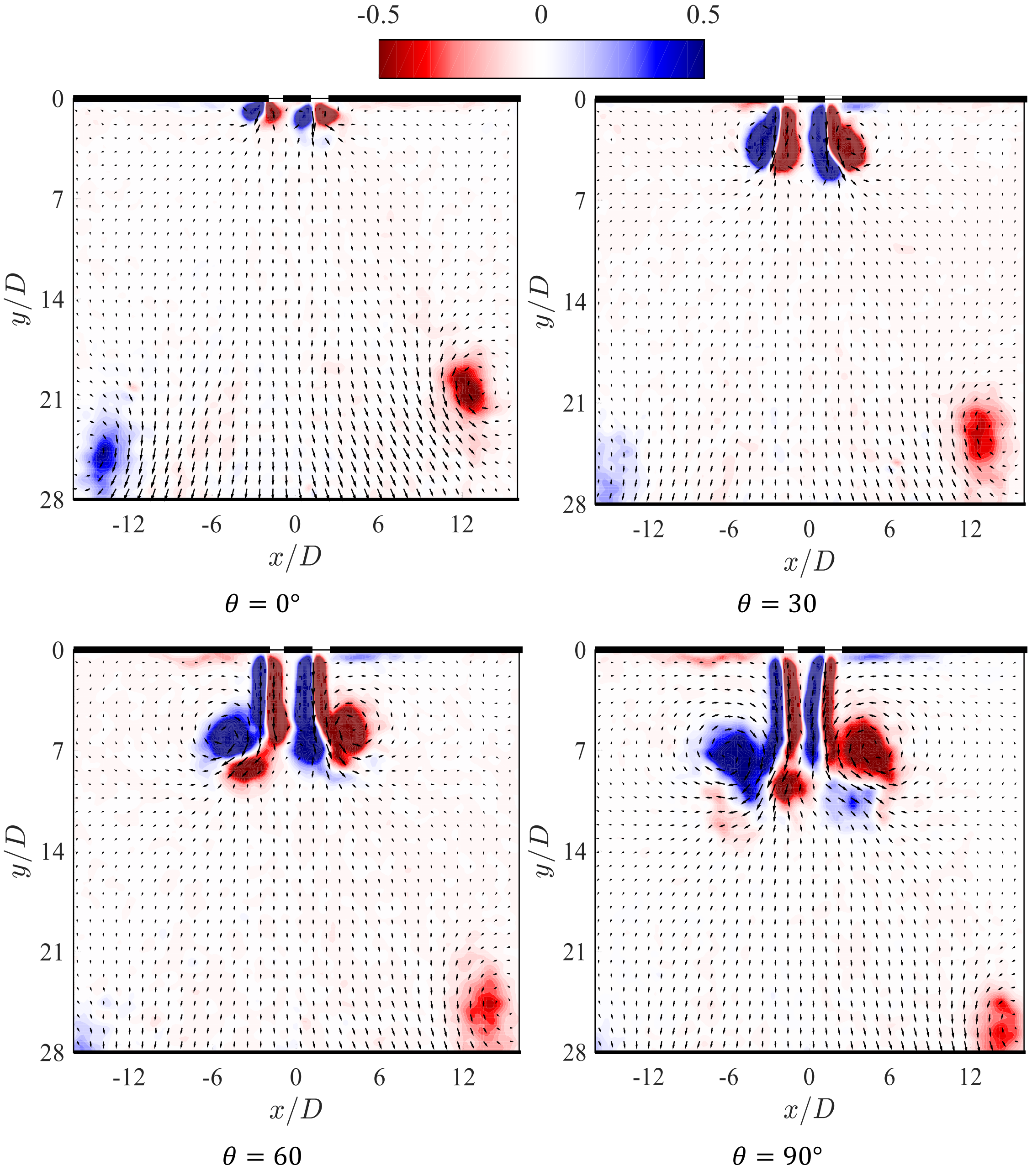

$\theta = 0°$

$\theta = 30$

$\theta = 60$

$\theta = 90°$

Figure 6-8. PIV results for normalized vorticity ($\omega D/U_0$) at consecutive phase-resolved points in a full jet period (for $\delta\emptyset = 0°$): $\theta = 0°$ to $330°$; step $= 15°$ (continued on the next page)

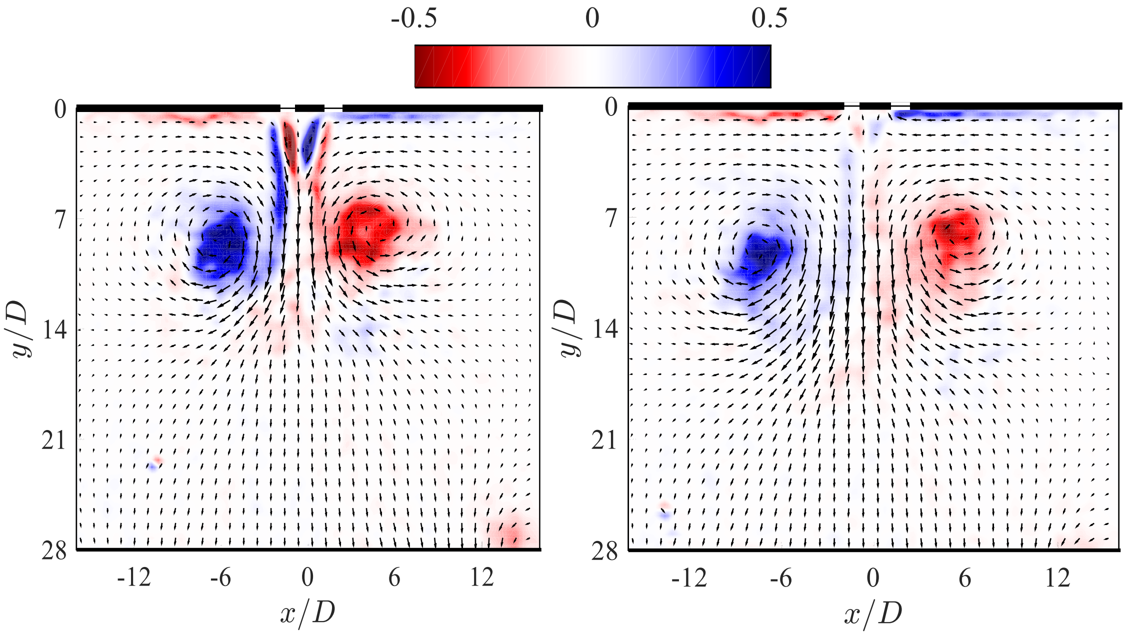

$\theta = 120°$ $\theta = 150°$

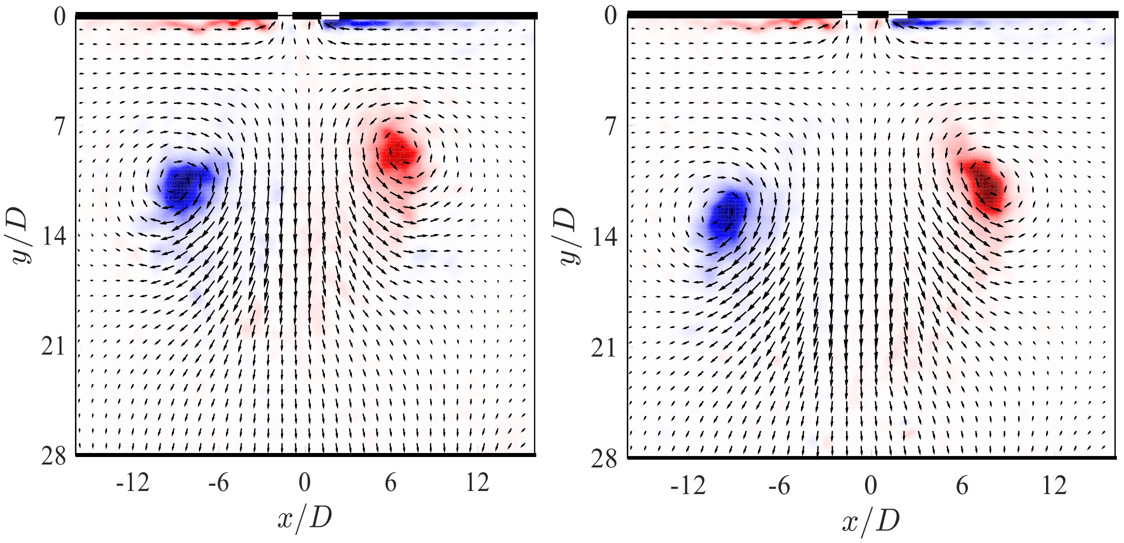

$\theta = 180°$ $\theta = 210$

Fig. 6-8 (continued on the next page)

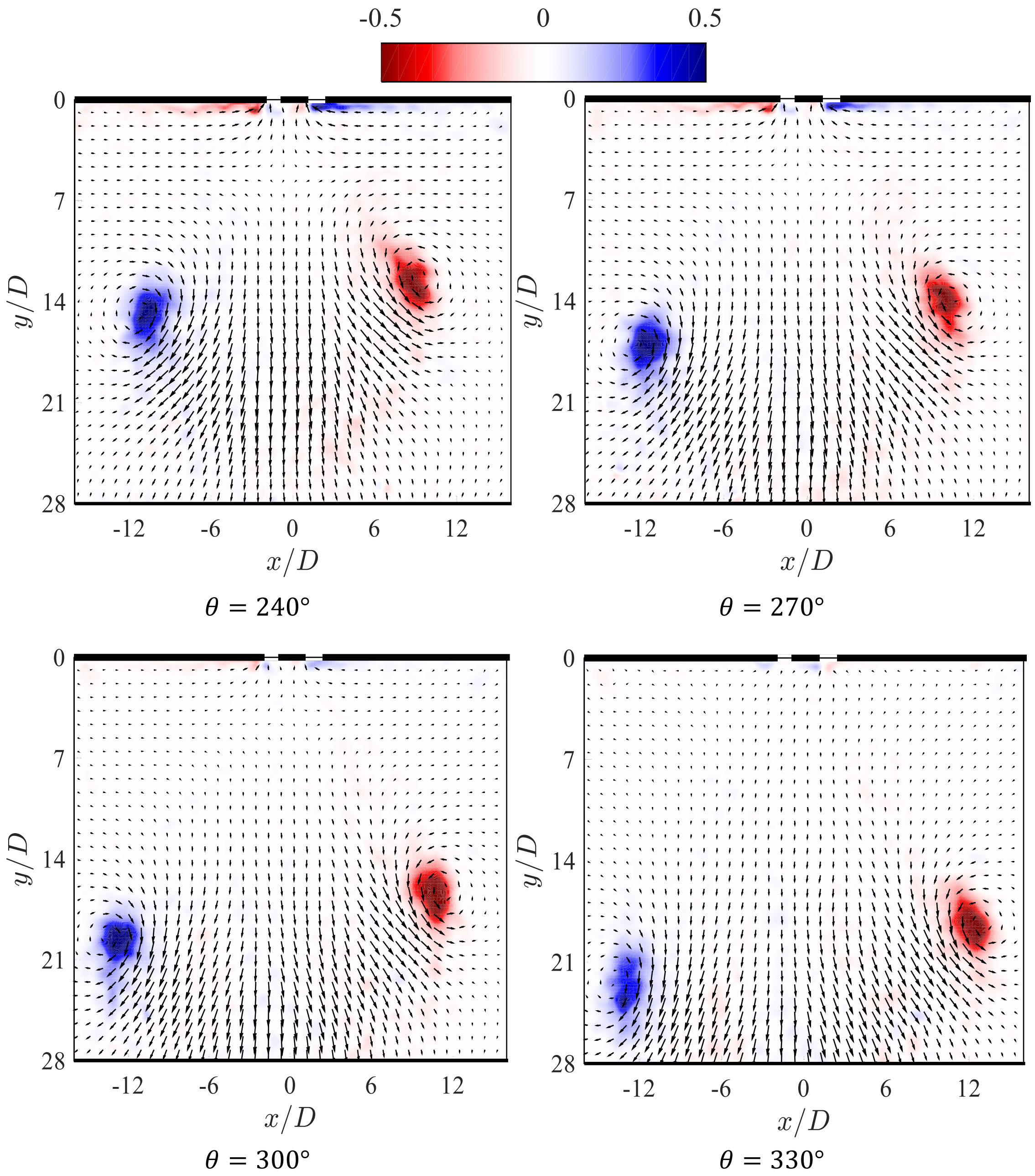

$\theta = 240°$ $\theta = 270°$

$\theta = 300°$ $\theta = 330°$

Fig. 6-8

Two adjacent vortex pairs exit the plane of orifice slots and start to roll down into the air. The remnants of the vortices form the last blowing stroke are noticeable downstream. The cores of the pair of counter-rotating vortices stretch in the direction of the flow. For phase-locked jets, the results demonstrate an almost symmetric evolution of adjacent jets.

CFD enables us to investigate through complicated flow features, therefore three cases with $\delta\emptyset = 0°, 60°$ and $130°$ are investigated in more detail to achieve a deeper understating of vectoring of adjacent synthetic jets. Contours of normalized velocity magnitude ($\sqrt{u^2+v^2}/U_0$) and vorticity ($\omega D/U_0$) for 4 consecutive phase-resolved points in a full jet period, i.e. $\theta = 0°, 90°, 180°$ and $270°$, are shown below. θ here is the phase in the leading jet period as depicted in Fig. 6-9, 6-11 and 6-13. Also, the span-wise-distribution of the axial velocity, *v*, and the static pressure, *P*, at different non-dimensional stream-wise distances from the orifice exit plane, *y/D* = 0.125 and 2 for 4 consecutive points of the jet period are also investigated. This is done for three phase differences of $\delta\emptyset = 0°, 60°$ and $130°$, respectively, as shown in Figs. 6-10, 6-12 and 6-14.

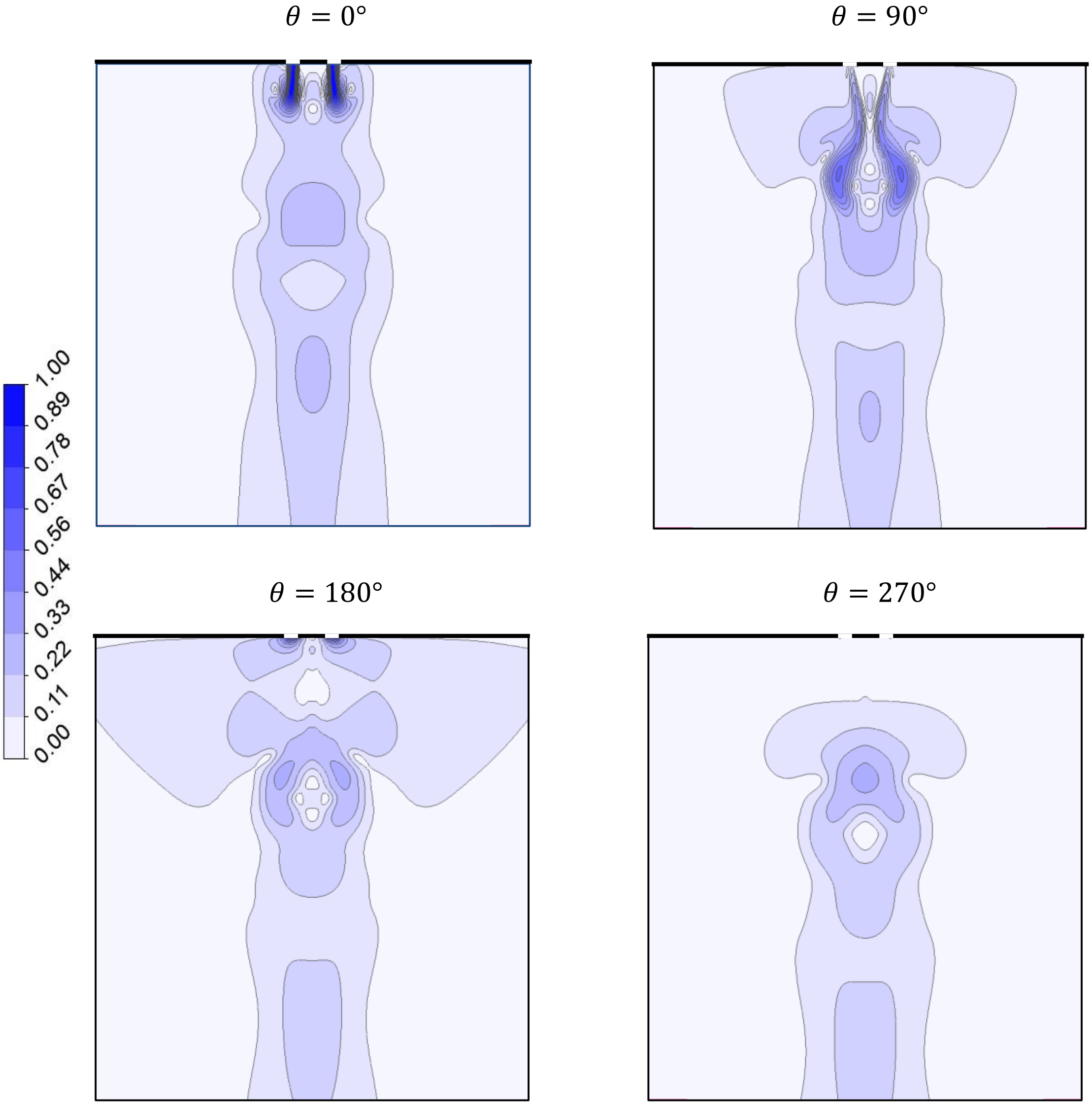

(a)

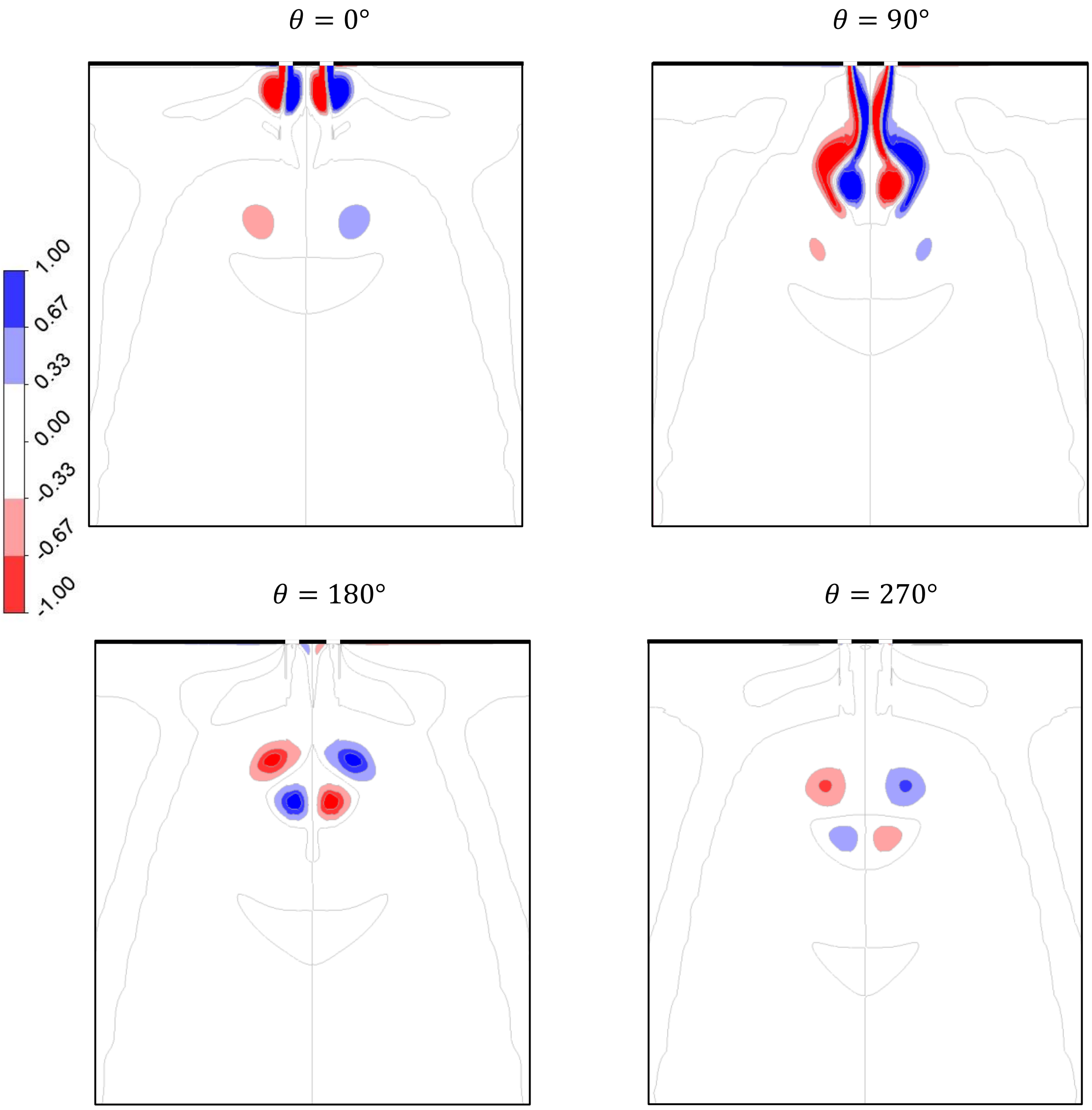

(b)

Figure 6-9. Numerical results for contours of (a). normalized velocity magnitude $(\sqrt{u^2 + v^2}/U_0)$ and (b). vorticity $(\omega D/U_0)$ at 4 consecutive phase-resolved points in a full jet period: $\theta = 0°, 90°, 180°$ and $270°$ for $\delta\emptyset = 0°$

One possible reason for vectoring of the merged jet toward the cavity leading in phase is that the actuator leading in phase accomplishes the ejection stroke primarily. Therefore, the momentum flux into the quiescent air and the generated vortices around it result in a low pressure region in the vicinity of the jet compared to the surrounding flow. The pressure drop results in vectoring of the phase-lagging adjacent jet toward the leading jet (towards the low pressure region). When the leading jet enters the suction stroke, the phase-lagging jet is still being vectored. This vectoring effect is shown in Figs. 6-11 to 6-14. On the contrary, the velocity and vorticity contours (Fig. 6-9) and the span-wise distributions of v and P (Fig. 6-10), for phase-locked jets, $\delta\emptyset = 0°$ demonstrate a fully symmetric evolution of adjacent jets. For out-of-phase jets, $\delta\emptyset = 60°$ and 130°, the aforementioned pressure drop in the vicinity of the leading jet is clearly noticeable from the span-wise pressure distributions shown in Figs. 6-12(b) and 6-14(b). This results in attraction of the lagging jet toward the right. The pressure drop and the component of velocity in the direction of the leading jet is a function of the phase difference; see Appendix A.6 for the inner cavity flow filed results.

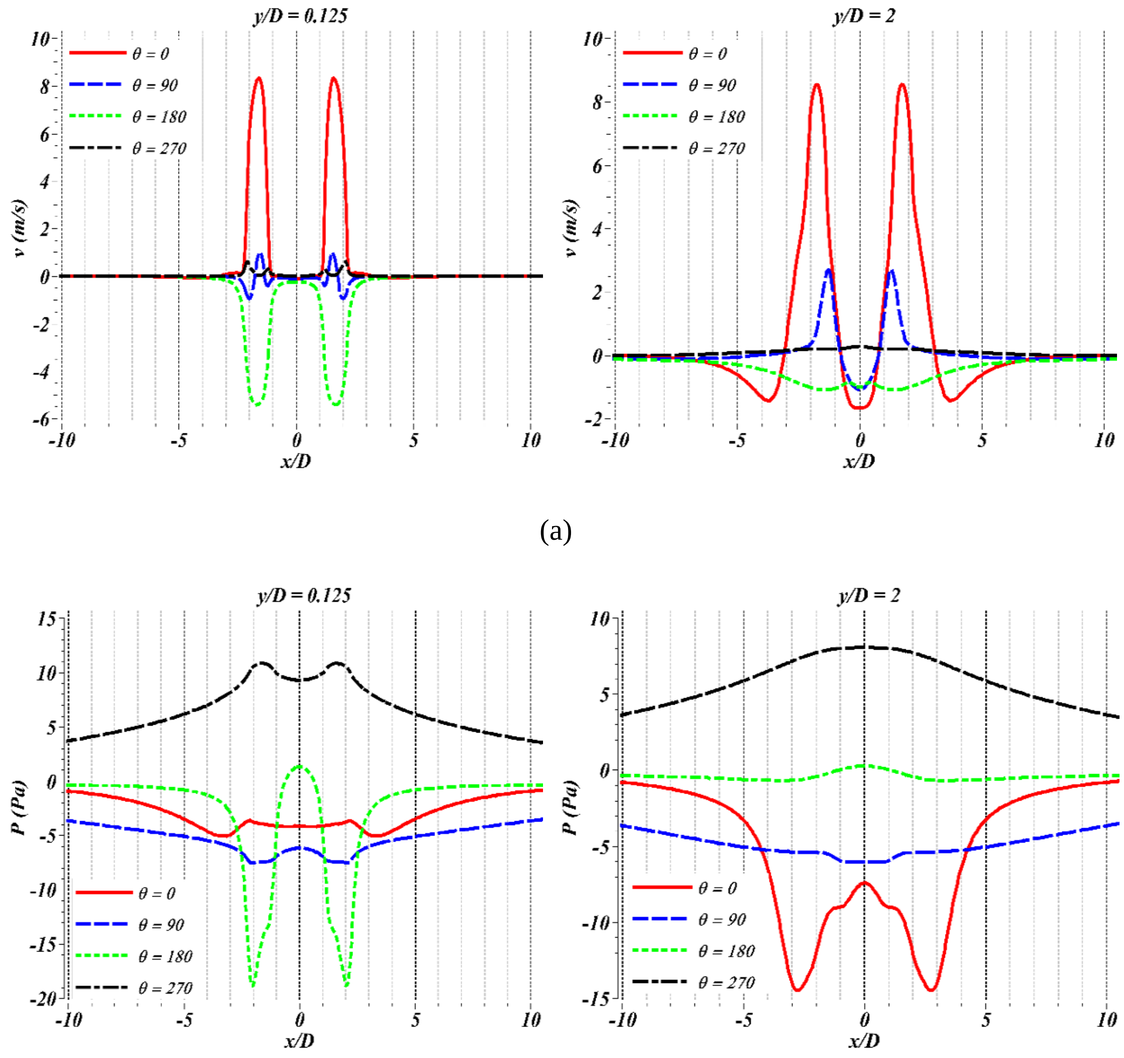

(a)

(b)

Figure 6-10. Numerical results for span-wise-distribution of (a). axial velocity, v, and (b). static pressure, P, at different non-dimensional stream-wise distances from the orifice exit plane, y/D = 0.125 and 2, for $\theta = 0°, 90°, 180°$ and $270°$ and $\delta\emptyset = 0°$

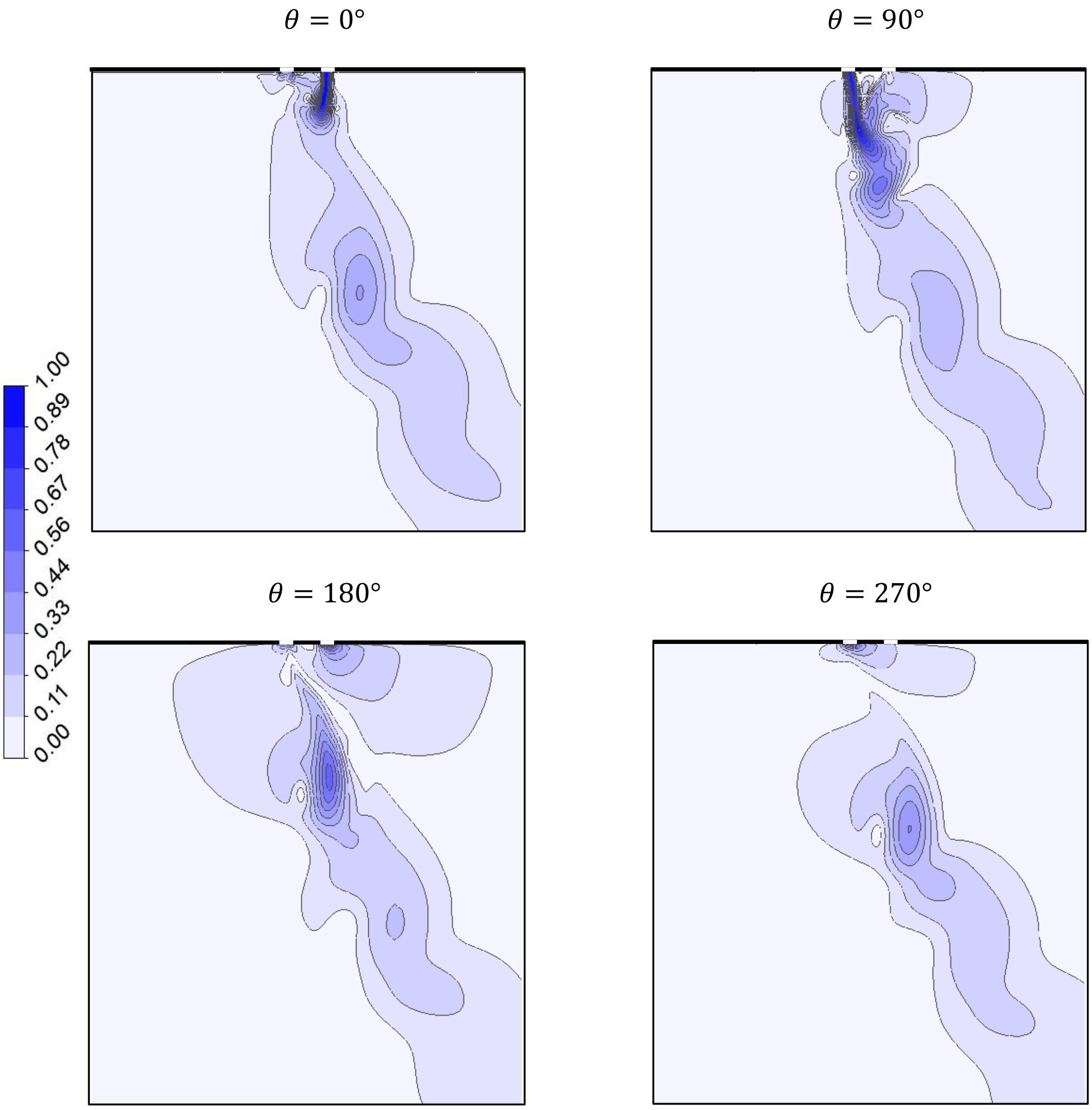
$\theta = 0°$
$\theta = 90°$
$\theta = 180°$
$\theta = 270°$
1.00
0.89
0.78
0.67
0.56
0.44
0.33
0.22
0.11
0.00

(a)

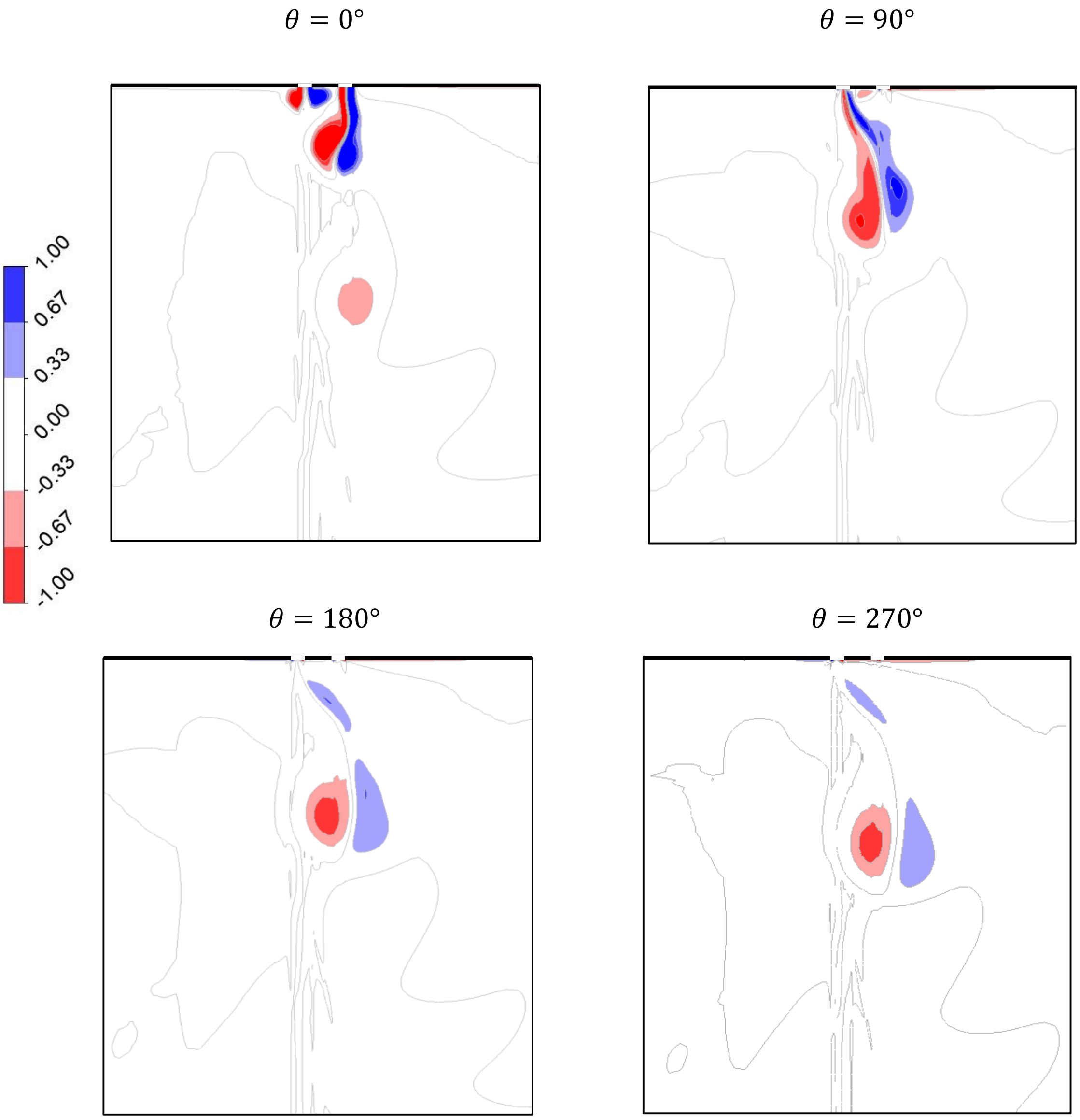

(b)

Figure 6-11. Numerical results for contours of (a). normalized velocity magnitude ($\sqrt{u^2+v^2}/U_0$) and (b). vorticity ($\omega D/U_0$) at 4 consecutive phase-resolved points in a full jet period: $\theta = 0°, 90°, 180°$ and $270°$ for $\delta\emptyset = 60°$

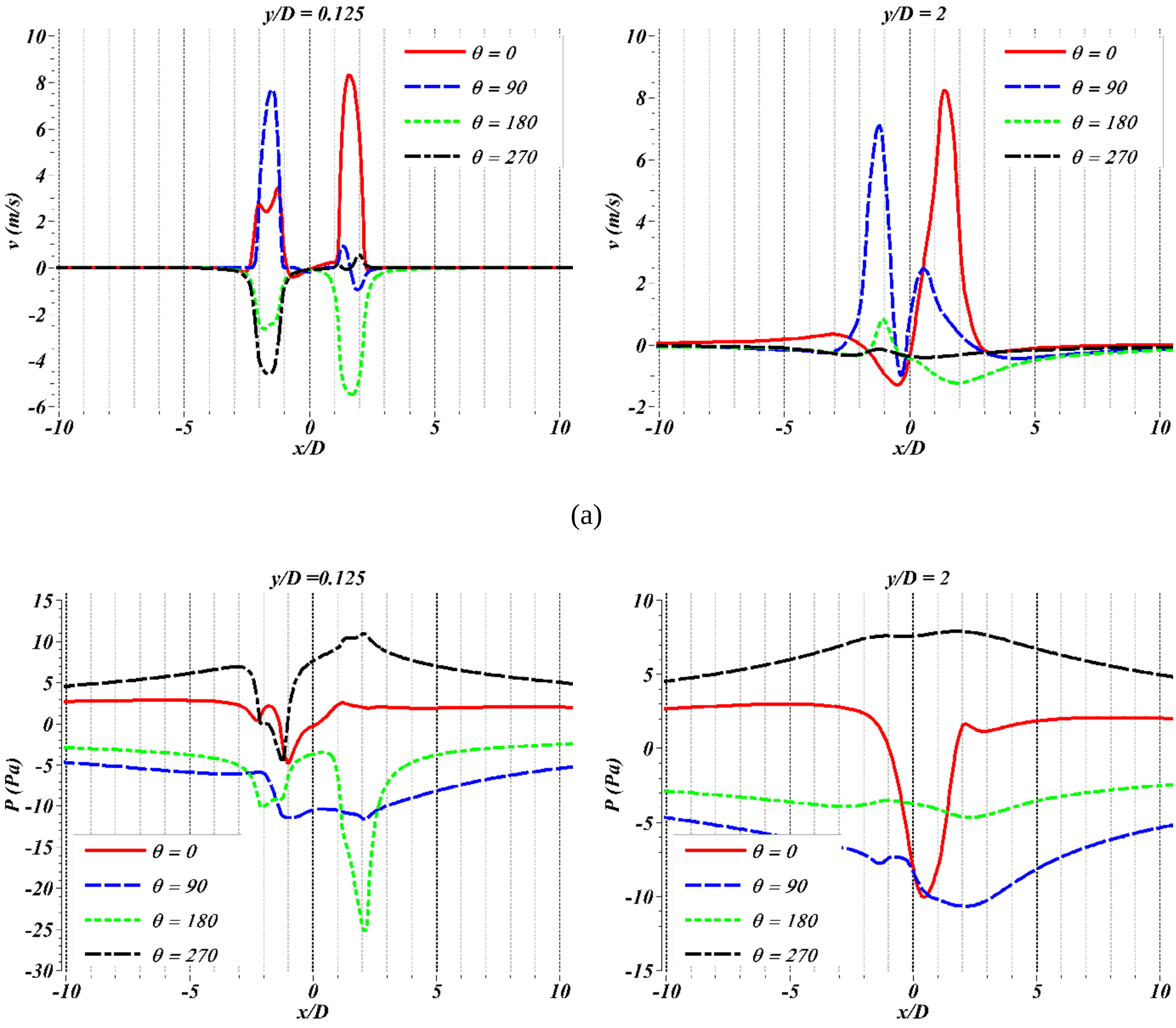

(a)

(b)

Figure 6-12. Numerical results for span-wise-distribution of (a). axial velocity, *v*, and (b). static pressure, *P*, at different non-dimensional stream-wise distances from the orifice exit plane, *y/D* = 0.125 and 2, for $\theta = 0°, 90°, 180°$ and $270°$ and $\delta\emptyset = 60°$

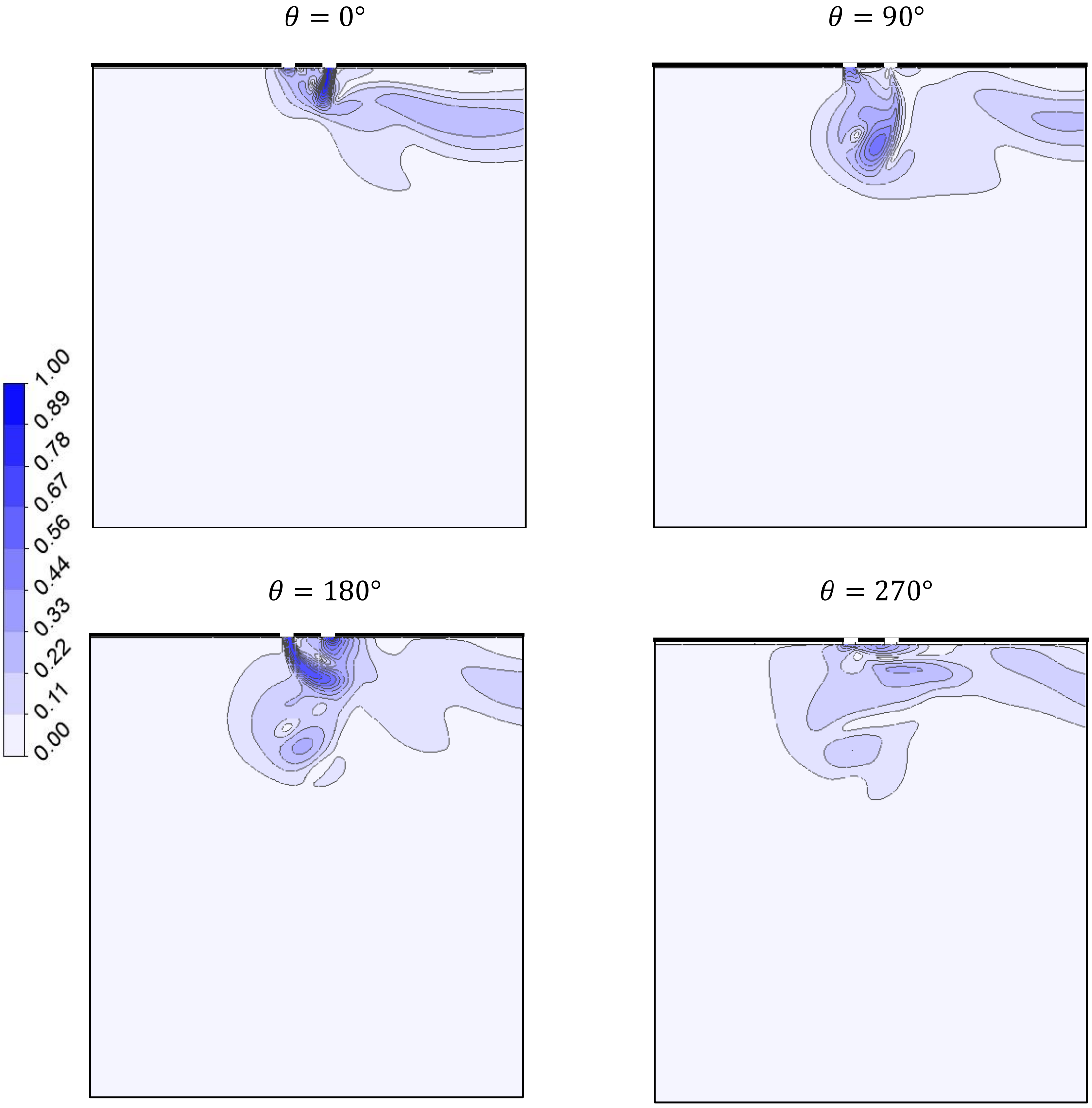
$\theta = 0°$
$\theta = 90°$
$\theta = 180°$
$\theta = 270°$
1.00
0.89
0.78
0.67
0.56
0.44
0.33
0.22
0.11
0.00

(a)

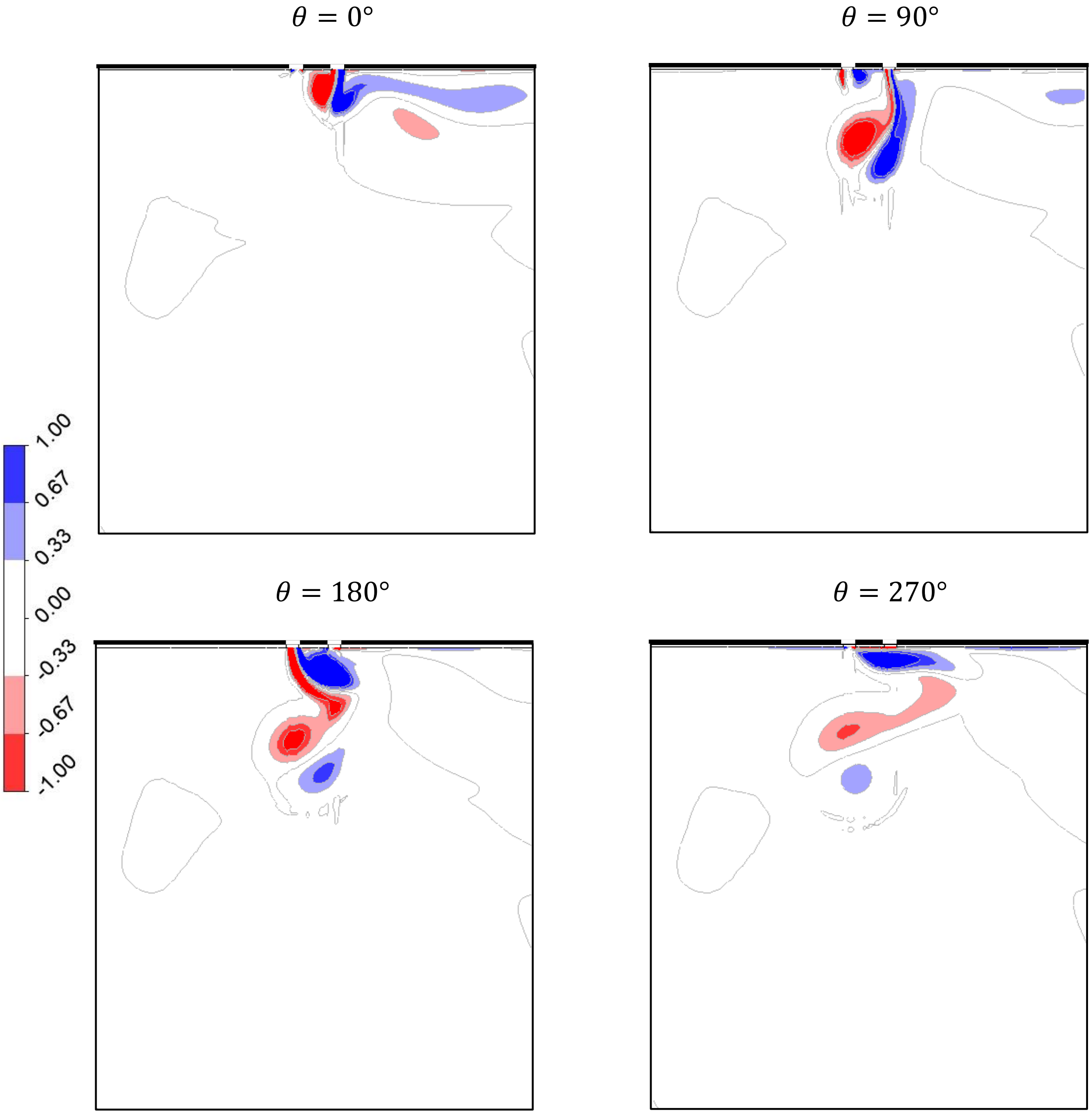

(b)

Figure 6-13. Numerical results for contours of (a). normalized velocity magnitude ($\sqrt{u^2 + v^2}/U_0$) and (b). vorticity ($\omega D/U_0$) at 4 consecutive phase-resolved points in a full jet period: $\theta = 0°, 90°, 180°$ and $270°$ for $\delta\emptyset = 130°$

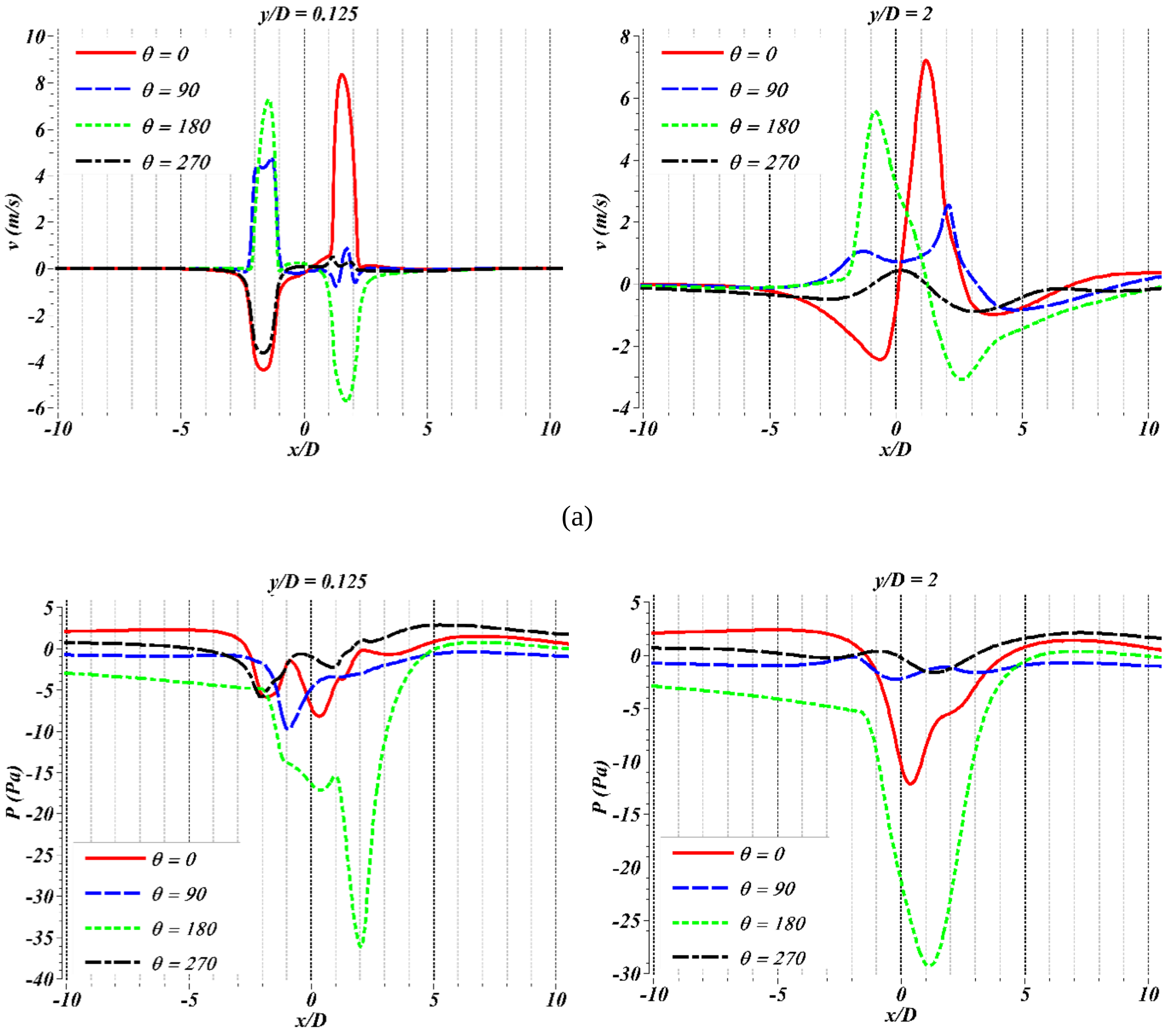

(a)

(b)

Figure 6-14. Numerical results for span-wise-distribution of (a). axial velocity, *v*, and (b). static pressure, *P*, at different non-dimensional stream-wise distances from the orifice exit plane, *y/D* = 0.125 and 2, , for $\theta = 0°, 90°, 180°$ and 270° and $\delta\emptyset = 130°$

6.4.3 Further analysis of the fluid mechanics of synthetic jet vectoring

Phase-resolved contours of instantaneous vorticity illustrate more clearly the evolution of interacting adjacent jets. The symbolization shown in Fig. 6-15 is used to clarify the discussion of vortical features of the flow. Similarly to the vorticity contour plots in Fig. 6-13, the counter-clockwise direction is taken as the positive direction of vortices. In this schematic diagram each vorticity symbol is marked with the direction of rotation (positive + or negative -) and the cavity side (left L or right R) from which vortices were formed. The pair of counter-rotating vortices further downstream are marked with the subscript ‘M’ which represents the merged jet vortices.

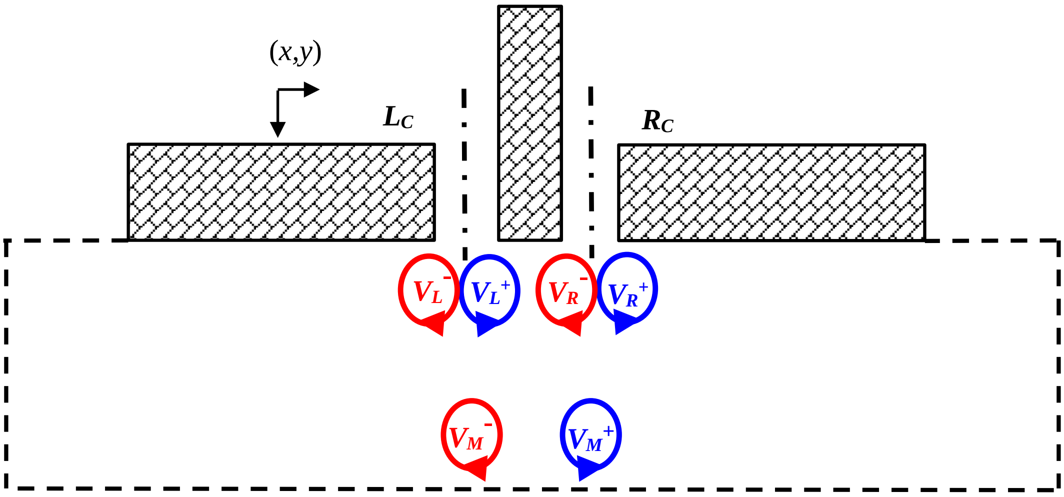

Figure 6-15. Symbolization used for clarifications of vortices induced by adjacent synthetic jets in the domain

When the two adjacent vortex pairs at the exit plane of the orifice slot ($V_L^{\pm}$ and $V_R^{\pm}$) start to roll down into the air, the remnants of the vortices from the previous blowing stroke ($V_M^{\pm}$) still exist downstream (Fig. 6-9, $\theta = 0^\circ$). New vortex pairs ($V_L^{\pm}$ and $V_R^{\pm}$) are fully formed at the peak of the blowing stroke, $\theta = 90^\circ$, and detach from the slot exit plane thus moving further downstream. The core of this pair of counter-rotating vortices is stretching in the direction of the flow at the same time. As shown in Fig. 6-4, the stream-wise centreline velocity decreases along the centreline. This is also evident since the newly formed vortex pairs ($V_L^{\pm}$ and $V_R^{\pm}$) show greater acceleration and propagate at a faster rate compared to the remnants of the previous stroke ($V_M^{\pm}$), for $\theta = 0^\circ$ to 90°. For $\delta\emptyset = 0^\circ$, Fig. 6-9 ($\theta = 0^\circ$ to 90°), $V_L^{\pm}$ and $V_R^{\pm}$ experience an acceleration almost 5 times greater than that of $V_M^{\pm}$.

Due to the smaller space between the two reversed inner vortices, V_L^+ and V_R^-, they are weaker than the two outer vortices, V_L^- and V_R^+. Increased mutual interaction between V_L^+ and V_R^- results in deceleration of the centreline flow velocity. Smith and Glezer [78] have reported that the self-induced velocity of the centre of vortex pairs is in the direction of the orifice exit plane. Therefore, the inner vortex pair, V_L^+ and V_R^-, have a tendency to become sucked toward the orifice exit, opposed by stronger general stream-wise flow motion emerging from the orifice at the same time.

For out of phase jets, $\delta\emptyset \neq 0°$, mutual interactions between left and right vortex pairs become more constructive. First, for further validation of the *CFD* model in terms of phase-resolved measurements, the consecutive snap shots of normalized vorticity contours are compared with the experimental result of Smith and Glezer [78] for $\delta\emptyset = 60°$. Fig. 6-16 (a-h), shows the phase-resolved maps at dimensionless time, $t^* = t/T$. The same parameter is used only for this comparison, in place of actuation phase θ. t^* is relative to the start of ejection or end of suction strokes, therefore, $t^* = 0$ and 0.5 is equivalent to $\theta = 270°$ and $90°$. Fig. 6-16 confirms the *CFD* model is able to replicate analogous results to *PIV* visualisations for various phase-resolved points, i.e. $t^* = 0.14, 0.22, 0.31,$ and 0.5. In the experimental results, the authors have use solid lines for vortices rotating in clockwise (+) and dashed lines for the ones rotating in contour-clockwise (-) directions.

Fig. 6-16 (a) and (e) contain phase-resolved normalized vorticity contour plots at $t^* = 0.14\,(\theta = 320.4°)$. The emerging vortex pair $V_R^{\pm}$, and the remnants of previous stroke, $V_M^{\pm}$, are evident in the domain for both experimental and numerical results with very similar concentrations. Comparison of stream-wise length scale, *x/D*, for Fig. 6-16 (a) and (e) shows $V_R^{\pm}$ and $V_M^{\pm}$ roll down for the same distance from the orifice, approximately *x/D* = 0.5 and 3 respectively. This agreement is also noticeable in the rest of the results shown in Fig. 6-16, i.e. both numerical and experimental plots display similar vortex magnitudes and comparable stream-wise and adjacent displacements of vortices in the domain.

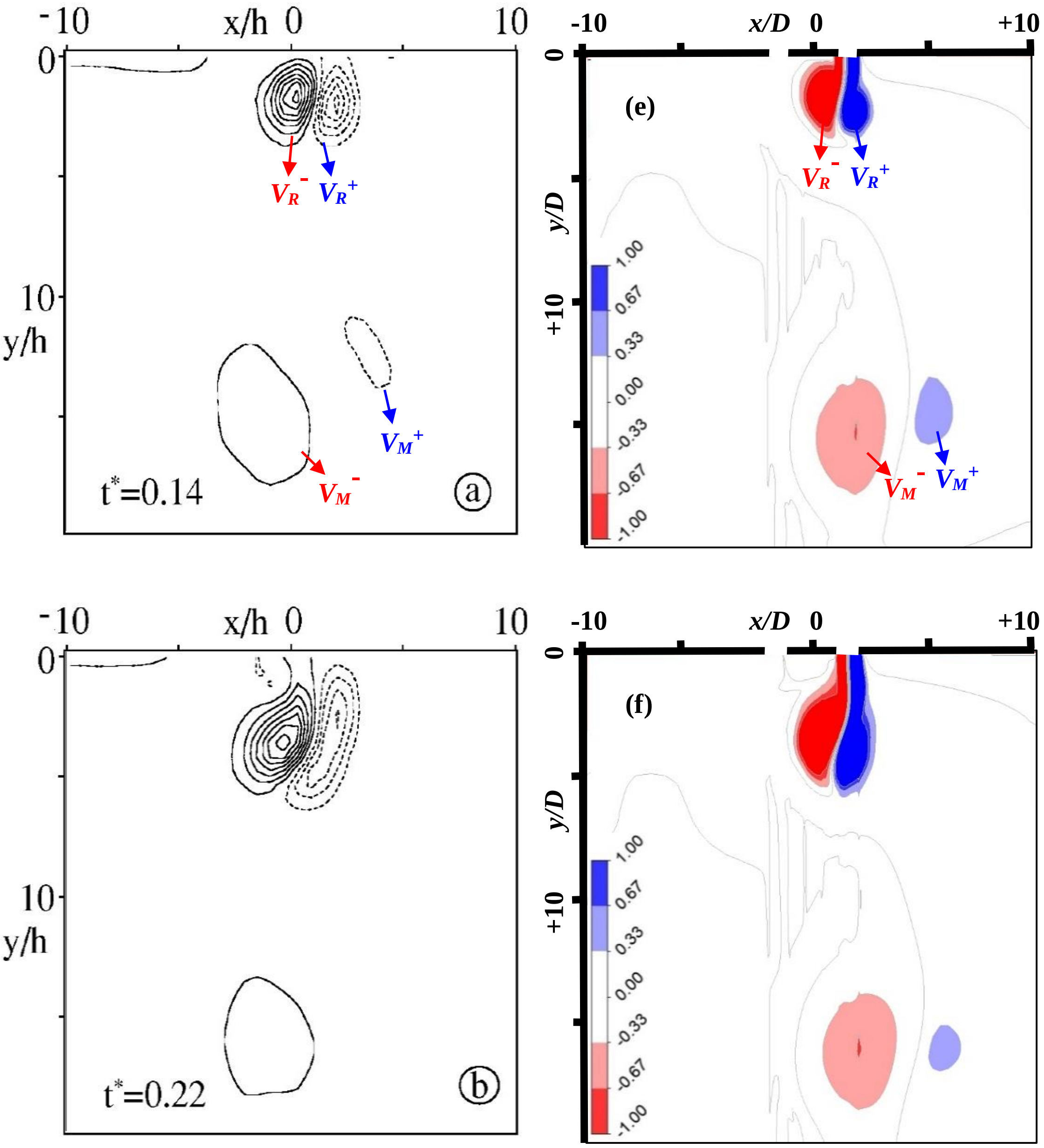

Figure 6-16. Comparison of experimental data [78] for 4 consecutive phase-resolved normalized vorticity contours (a-d) versus numerical results (e-h) for $\delta\emptyset = 60°$ (Re = 300, $L_0 = 29D$)

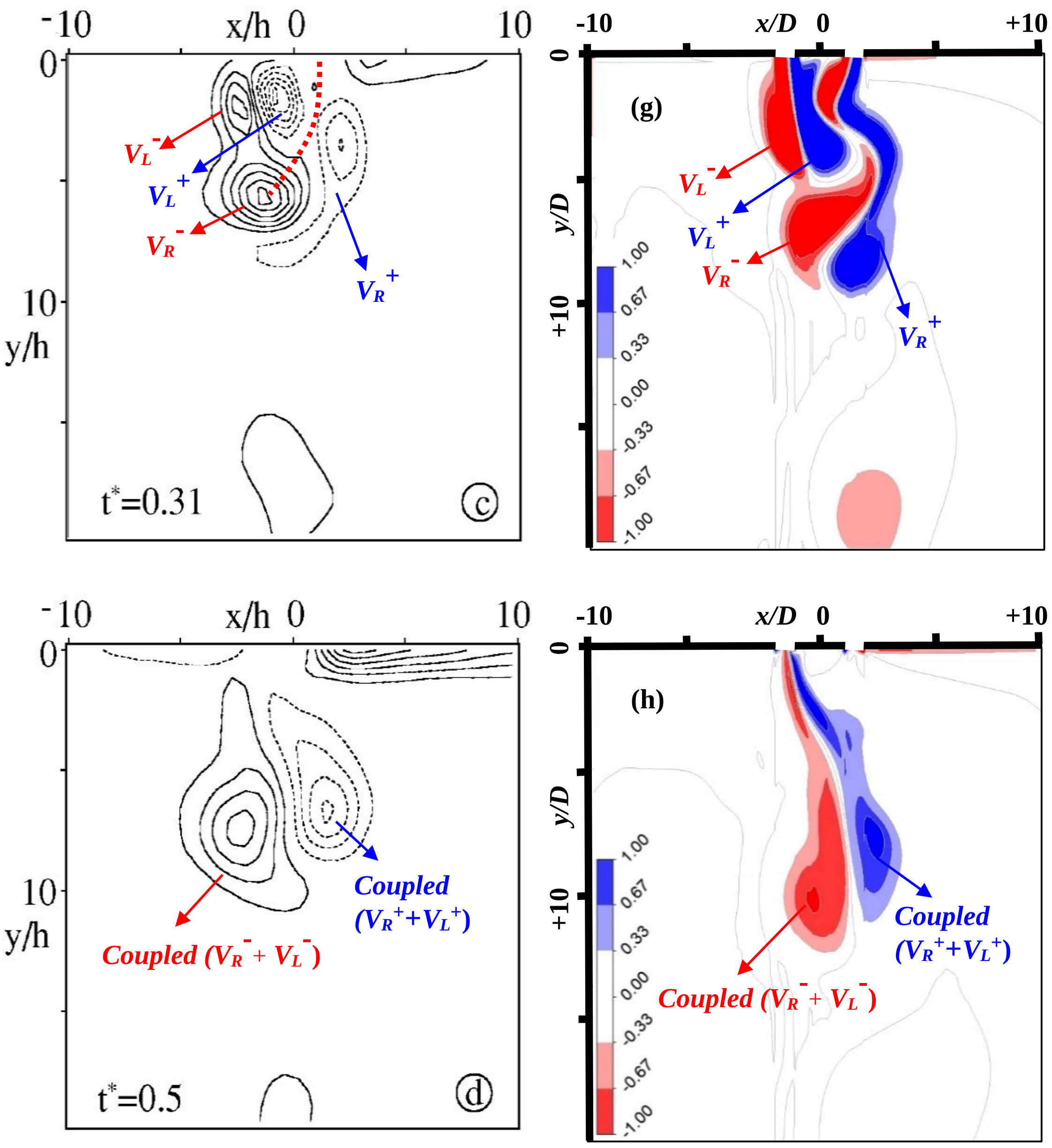

Fig. 6-16 (continued)

Visual differences in the numerical and experimental results are possibly due to the different approaches authors used in the post-processing stage of CFD, as described in section 5.2. A validated *CFD* model is obviously capable of capturing additional small-scale details in the domain, as it is less constrained with common problems of *PIV* visualisations, e.g. loss of vectors due to image resolution, camera frame rate limits, and noise-filtering issues. This is evident from examination of Fig. 6-16 (c) and (g). What can be understood from the *PIV* results shown in Fig. 6-16 (c) is that the left-hand side outer clockwise-rotating vortex (V_L^-) is displaced to a relatively larger extent and becomes stronger than the inner vortex, V_L^+, in the stream-wise direction, despite being ejected at the same time. The *CFD* results in Fig. 6-16 (g) suggest that this is likely to be a combination of V_L^- and V_R^-. The pair $V_R^\pm$ are in the domain, when $V_L^\pm$ is ejected with a delay of $\delta\emptyset = 60$. For $t^* = 0.22$ to 0.31 ($\theta = 349.2°$ to $21.6°$), the emerging pair $V_L^\pm$ interferes with $V_R^\pm$. The major interaction occurs when V_L^+ coalesces with V_R^-, separating its tip (Fig. 6-16 (g)). The detached tip of V_R^- couples with V_L^-, which appears as a strong V_L^- in the experimental data.

As shown above, the interaction of inner vortices, V_L^+ and V_R^-, has a major effect in vectoring of the merged jet. Figure 6-17 further explains this concept.

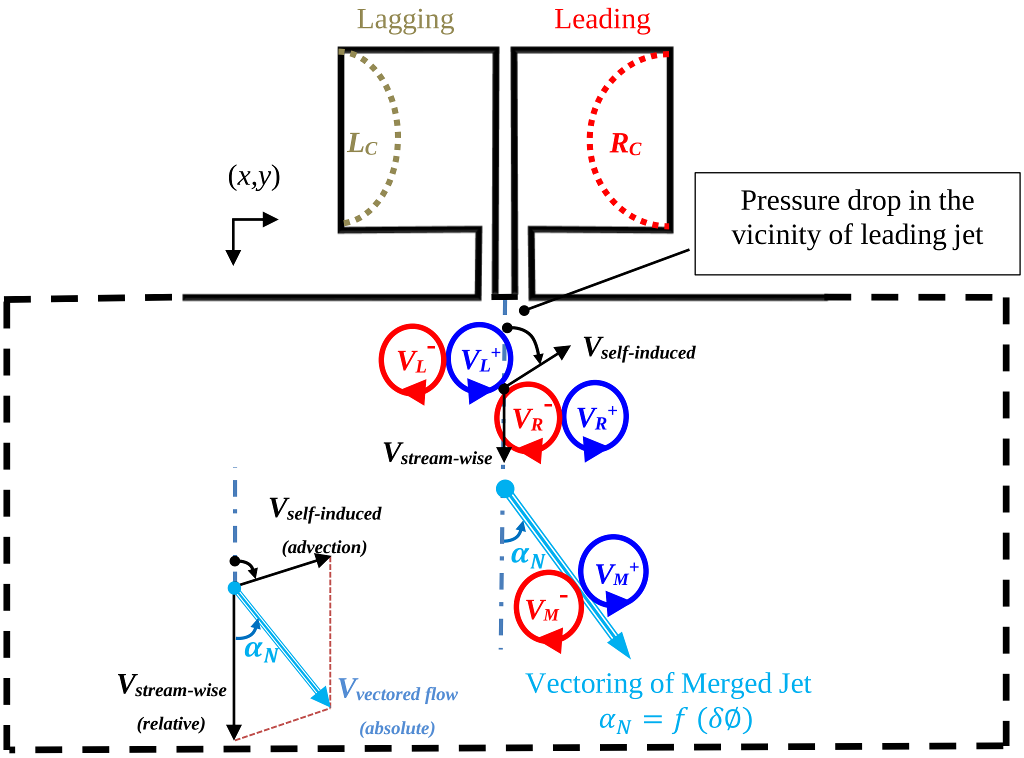

Figure 6-17. Schematic diagram for explanation of vectoring phenomenon

The nominal vectoring angle can proportionally change by variation of the phase difference. As described earlier for in-phase jets, there is a self-induced velocity component ($V_{self\text{-}induced}$) in the direction of the exit plane (upward/reverse). When $\delta\emptyset = 60°$, interaction of counter rotating vortices V_L^+ and V_R^- changes the direction of the component $V_{self\text{-}induced}$ towards the right (leading jet). In a similar manner to the concept of relative velocity in turbomachinery fundamentals, the terms $V_{vectored\ flow}$, $V_{self\text{-}induced}$ and $V_{stream\text{-}wise}$ are called absolute, relative and advection velocity components, respectively.

Contours of time-averaged pressure in the domain for different values $\delta\emptyset$ are shown in Fig. 6-18.

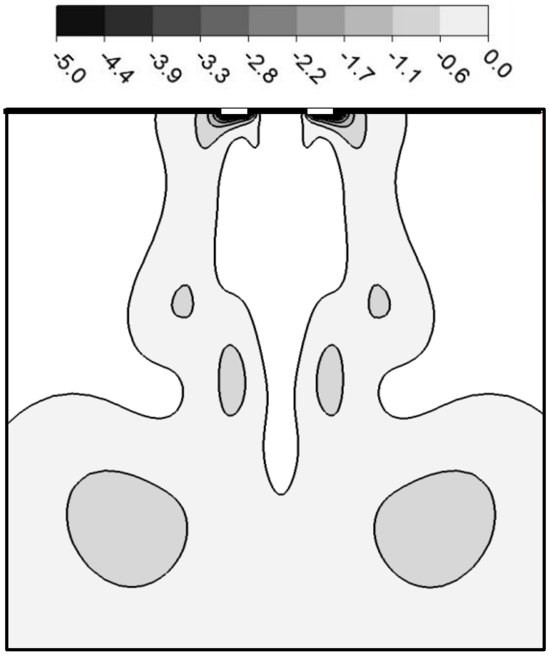

$\delta\emptyset = 0°$

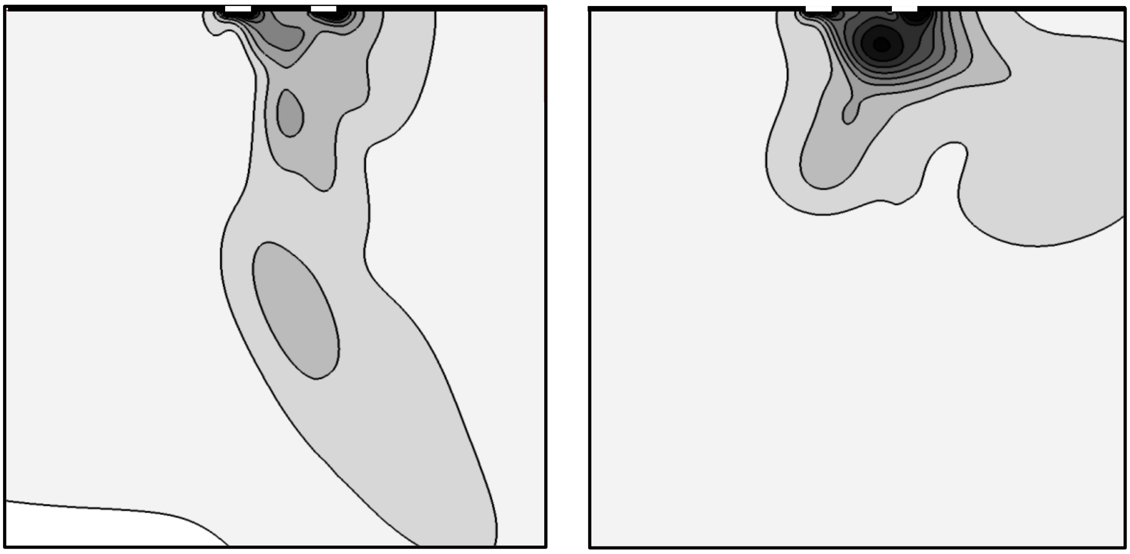

$\delta\emptyset = 60°$ $\delta\emptyset = 130°$

(a)

Figure 6-18. (a) Contours of time-averaged pressure in the domain for $\delta\emptyset = 0°, 60°$ and $130°$, Span-wise-distribution of time-averaged; (b and c). static pressure, *P*, at different non-dimensional stream-wise distances from the orifice exit plane, *y/D* = 0.125 and 2, for $\delta\emptyset = 0°, 60°$ and $130°$ (continued on the next page)

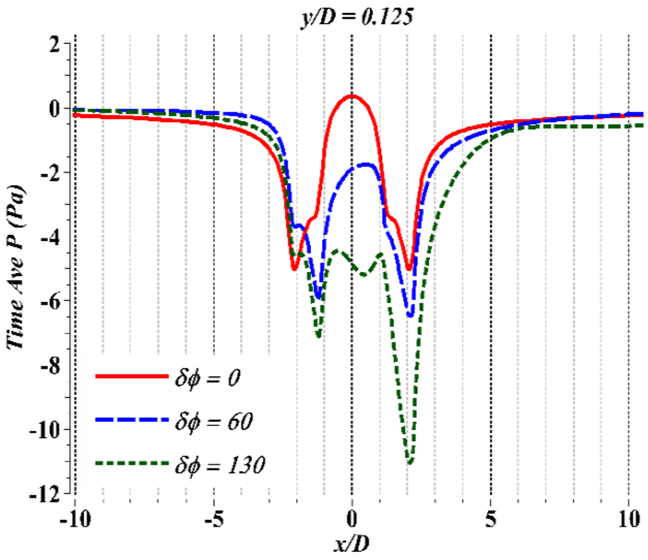

(b)

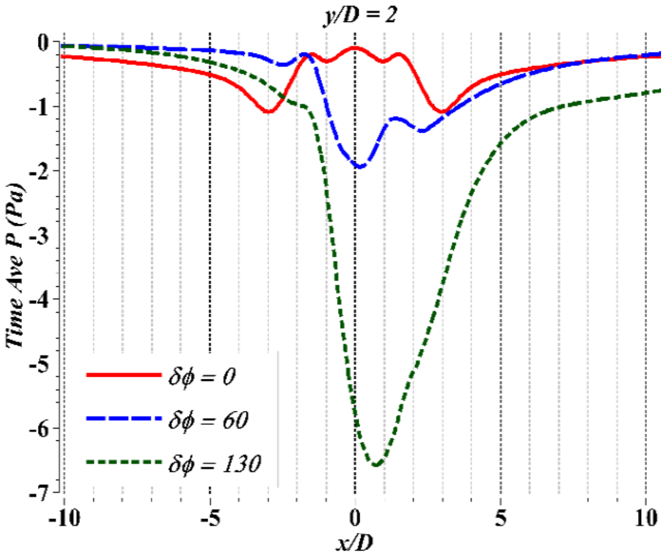

(c)

Fig. 6-18 (b, c)

The distribution of static pressure in the vicinity of the jets over a full jet period can describe the vectoring of the lagging jet better. Fig. 6-18 shows the span-wise distribution of P at two different stream-wise positions from the orifice exit plane, *y/D* = 0.125 and 2, for three different cases of $\delta\emptyset = 0°, 60°$ and $130°$. The formation of the phase-leading jet on the right results in lower static pressure on the right side of the orifice plate. The pressure difference tilts the merged jet to compensate for this.

The effect of vectoring on the magnitude and direction of mass transport by the merged jet is also characterized. Mass flow-weighted area averaged velocity, normal to the surface of averaging ($\overrightarrow{V_N}$) is calculated as follows:

$$\overrightarrow{V_N} = \frac{\iint \overrightarrow{V_N}\,\rho\left|\overrightarrow{V_N}.d\vec{A}\right|}{\iint \rho\left|\overrightarrow{V_N}.d\vec{A}\right|} = \frac{\sum_{i=1}^{n} \overrightarrow{V_N}_i \rho_i \left|\overrightarrow{V_N}_i.\vec{A}_i\right|}{\sum_{i=1}^{n} \rho_i \left|\overrightarrow{V_N}_i.\vec{A}_i\right|} \qquad (6\text{-}13)$$

Using $\overrightarrow{V_N}$, the area-averaged mass flow rate is calculated over the axial surface, i.e. *y/D* = 0 surface which splits the domain symmetrically. It is then time-averaged over a full actuation cycle, indicating a net mass transfer in the span-wise direction (*x* in Fig. 6-17) by operation of a pair of adjacent synthetic jets with a phase difference. This spatially and temporally averaged mass flow rate changes with phase difference such that $\bar{\dot{m}} = f(\delta\emptyset)$. This value is normalized with respect to the net area-averaged mass flow rate which emerges from one of the orifice slots during the ejection stroke, $\overline{\dot{m}_0} = \rho U_0 A_{orifice}$. Variation of the normalized net mass transfer by the merged jet versus phase difference is depicted in Fig. 6-19. According to the schematic Fig. 6-19, + and – signs respectively show mass transport to right and left directions. A nonlinear least-squares regression is performed to fit a *Gaussian* function through the set of data, resulting in the correlation reported as follows:

$$\begin{cases} \dfrac{\bar{\dot{m}}}{\overline{\dot{m}_0}} = ae^{-\left(\frac{\delta\emptyset - b}{c}\right)^2}; \qquad R^2 = 0.94 \\ a = 0.273, b = -0.6429, c = 0.4889 \end{cases} \qquad (6\text{-}14)$$

where $\delta\emptyset°$ values are normalized by mean and standard deviation values of 83 and 59.45.

The fitted correlation is also shown in Fig. 6-19 together with the confidence level bounds of 90%. The peak of the mass transfer by operation of a pair of adjacent synthetic jets under phase difference is located between $40° < \delta\emptyset < 50°$.

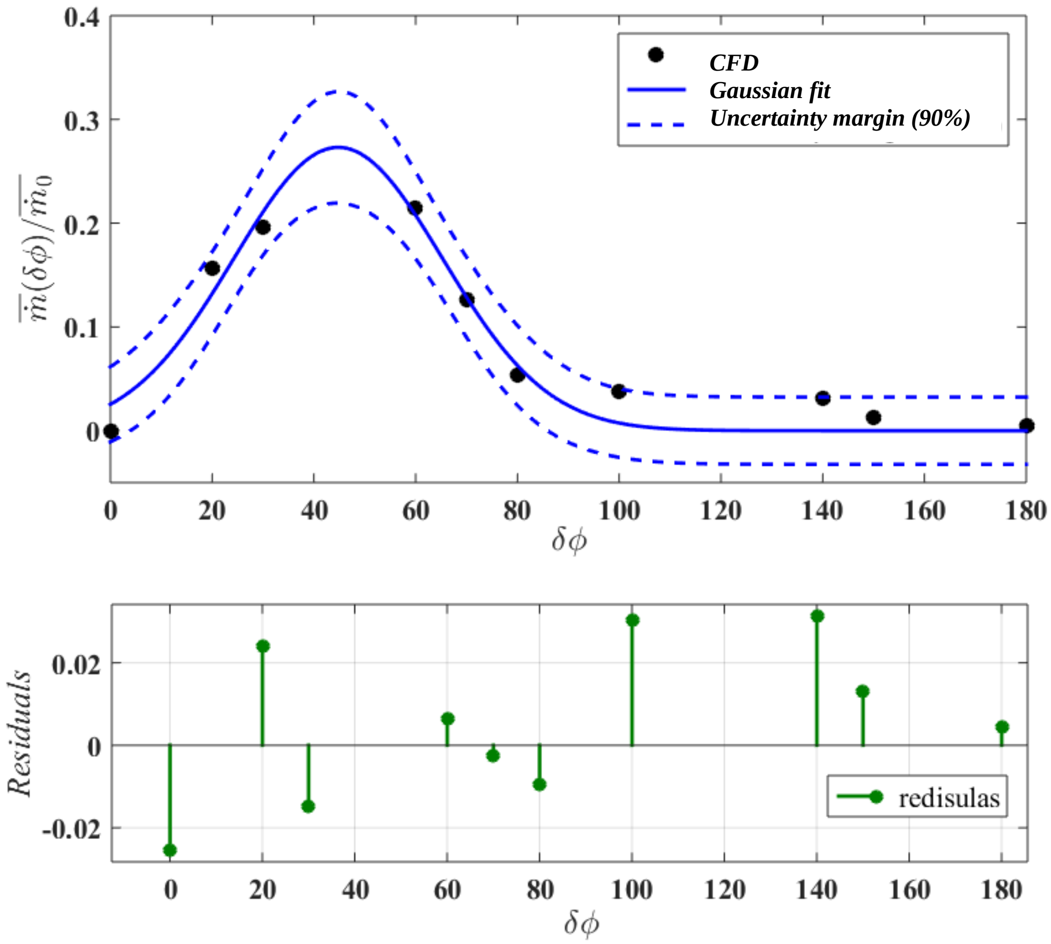

Figure 6-19. Net mass transfer ($\frac{\bar{\dot{m}}}{\dot{m}_0}$) variation with phase difference ($\delta\emptyset$)

6.5 Conclusion

For a pair of adjacent synthetic jets, computational fluid dynamics and particle image velocimetry techniques are used to study flow features. The investigation considers a jet pair issuing into quiescent air. A full simulation is performed of the internal flow in the jet cavities, as well as the external jet flow.

To assess the performance of the *CFD* model, the results are first carefully compared with experimental data. The target case to perform an experimental validation of *CFD* model is a pair of adjacent synthetic jets with a separation distance $s = 3.3D$, stroke length $L_0 = 29D$, and Reynolds number $Re = 300$.

For the variation of non-dimensional stream-wise time-averaged centreline velocity with stream-wise distances from the orifice exit plane, the agreement of the numerical result is considerably better when compared to *PIV* measurements performed by (Smith and Glezer 2005), while the deviation from *PIV* measurements in this chapter does not exceed a percentage error of 11% in $10 < y/D < 20$.

The time-averaged streamlines determined with *PIV* for adjacent jets with various phase differences, $\delta\emptyset = 0°,\ 60°,\ 70°,\ 80°,$ and $130°$, are compared to the numerical results. The relative phase difference of the jet actuators can be used to manipulate the merged jet which results in a great effect on the controlling ability of synthetic jet actuator. The merged jet is vectored to the right (i.e., toward the cavity that is leading in phase) with a very similar trend between experimental and numerical results.

The results shows that by keeping the non-dimensional L_0 and *Re* unchanged, without fully-defined cavity and slot geometries, the model predicts the flow very similar to that observed in the literature. The results suggest that the numerical model is almost independent of so called operating or synthetic jet formation conditions, and that the adjacent synthetic jets may experience the same 'Vectoring Phenomenon' under different conditions (e.g. frequency, cavity geometry, orifice slot width, etc.). The formation and evolution of jet is relatively independent of the cavity geometry and only depends on its stroke length (L_0) and Reynolds number (*Re*).

To look through complicated flow features, three cases with $\delta\emptyset = 0°, 60°$ and $130°$ are studied in more details to achieve a better understating of vectoring of adjacent synthetic jets. By the advance accomplishment of the ejection stroke with leading cavity, the momentum flux into the quiescent air and the generated vortices around it result in a low pressure region in the vicinity of the jet compared to the surrounding flow. The resulting pressure drop leads to vectoring of the merged jet. The evolution and interaction of adjacent jets are described more clearly using phase-resolved contours of instantaneous vorticity and also introducing the concept of absolute, relative and advection velocity components.

A nonlinear least-squares regression is performed to fit a *Gaussian* function through the set of data. This shows that averaged mass flow rate transported with the operation of a pair of adjacent synthetic jets with a phase difference, changes with phase difference such that $\bar{\dot{m}} = f(\delta\emptyset)$.

Some of the findings presented in this chapter have been published in Alimohammadi et al. [117] and [118].

7 Conclusions

7.1 Summary of the findings of this work

This study is a fundamental investigation of fluid flow and heat transfer to unsteady impinging jets. Of particular interest this includes documentation of a numerical methodology which is capable of handling a wide range of application and operating conditions, e.g. steady or unsteady jets, free or impinging jets, and fixed or moving geometries. The key point is the experimental validation of the numerical results versus the in-house detailed experimental measurements.

Based on the literature review, a limited number of studies have been performed on a wide-ranging numerical-experimental methodology for unsteady jets. The current research is accomplished through three major stages, that is to say steady, pulsating, and synthetic jets. These divisions are carefully selected based on the incremental progression of the complexity of the fluid flow and heat transfer from the first toward the highly intermittent synthetic jet flows. Accordingly, the findings at the end of each stage are combined with additional features and techniques with the purpose of developing the research toward the next stage study. This chapter highlights the main conclusions of the research base on the research objectives describe in chapter 3.

In the first place, realistic configurations of boundary conditions, computational domain, turbulence models, fluid properties and solution approach show that numerical modelling is able to precisely model the heat transfer of steady impinging jets. As a computationally low cost model, the shear stress transport (*SST*) coupled with modified curvature correction and also the *Gamma-Theta* transition model has been found to best capture the main flow features. The model shows a considerable improvement in accurate prediction of the position, intensity and extent of the secondary peak in the local Nusselt number distribution. A comprehensive sensitivity analysis of the most influential methods and parameters in the numerical modelling is reported [34].

The investigations performed on effect of the turbulent Prandtl number in the near-wall region confirm an important role in the prediction of turbulent heat transfer. It is found that turbulent Prandtl number can directly affect the level of heat diffusion. The best value to accurately capture the intensity and location of the secondary peak in the Nusselt number distribution is accordingly reported. The position of the secondary Nusselt number peak varies consistently with Reynolds number and nozzle-to-surface distance, both in the experiments and numerical results. The location of the secondary peak in the Nusselt number distribution is not affected significantly by the inlet turbulence intensity for large values of nozzle-to-surface distances. The turbulence created in the shear layer becomes dominant [34].

For a wide range of operating conditions, correlations based on the experimental and numerical heat transfer coefficient data are generated for the stagnation point Nusselt number, incorporating the effect of Reynolds number and nozzle-to-surface distance. The final outcome of steady impinging jets provides the base model for extending the methodology towards unsteady impingement flows such as synthetic or pulsating jets [34].

In the second stage, the effect of flow pulsation on fluid flow and heat transfer for impinging axisymmetric air jets is investigated. The main motivation is to characterise the stagnation and area-averaged enhancements (or degradations) in convective heat transfer rate achieved by flow pulsation, when compared to steady jets, for an extended range of operating conditions. This is of great value for the simulation of the operating conditions beyond experimental capabilities, i.e. considerably higher pulsation frequencies than the maximum experimental limit. The developed numerical model is now validated versus unsteady experimental results in terms of local Nusselt number distribution. Nusselt number exhibits larger enhancements showing a monotonic increase with frequency at different nozzle-to-surface values, while the stagnation *Nu* undergoes a reduction [35] & [38].

Using the numerical flow visualization of velocity and vorticity contours, a closer look at the radial distribution of near-wall components is presented. Monitoring the radial velocity gradient, the normal vorticity, and Reynolds stress components shows a direct dependency between the heat transfer behaviour of pulsating jets over the impingement surface and the aforementioned parameters. Considering the electronic thermal management application of pulsating impinging jets, they show great potential, while it is worth noting that jets highly depend on operating conditions, and adjusting the effective parameters appropriately can cause a significant enhancement [35] & [38].

To obtain the maximum enhancement in heat transfer, all of the mutually dependent conditions must be methodically investigated and understood for the effective optimization of performance. Wide-ranging correlations for the averaged and stagnation point Nusselt number enhancement in pulsating flow have been least-square fitted to the numerical data as a function of suitably modified Strouhal numbers [36] & [38].

For a pair of free adjacent synthetic jets at the final stage, numerical modelling is accompanied with particle image velocimetry techniques to study flow features. Using a dynamic mesh technique, a full simulation is performed of the internal flow in the jet cavities, as well as the external jet flow.

The time-averaged streamlines determined with *PIV* for adjacent jets with various phase differences are compared to the numerical results. The relative phase difference of the jet actuators can be used to manipulate the merged jet which results in a great effect on the controlling ability of synthetic jet actuator. The merged jet is vectored to the right (i.e., toward the cavity that is leading in phase) with a very similar trend between experimental and numerical results [78] & [117].

Without fully-defined cavity and slot geometries, maintaining the non-dimensional stroke length and Reynolds number unchanged can lead the numerical model to predict flow very similar to that of experiments. The numerical model is found to be almost independent of so called operating or synthetic jet formation conditions. The same 'vectoring phenomenon' may be experienced under various parameters. The fluid flow induced by operation of synthetic jets is independent of the cavity geometry and only depends on its stroke length and Reynolds number [117].

One possible reason for vectoring of the merged jet toward the cavity leading in phase is that the actuator leading in phase accomplishes the ejection stroke primarily. Therefore, the momentum flux into the quiescent air and the generated vortices around it result in a low pressure region in the vicinity of the jet compared to the surrounding flow. The pressure drop results in vectoring of the phase-lagging adjacent jet toward the leading jet. The resulting pressure drop leads to vectoring of the merged jet. The evolution and interaction of adjacent jets are described more clearly using phase-resolved contours of instantaneous vorticity. This helps to introduce the concept of absolute, relative and advection velocity components between two adjacent vortex pairs at the exit plane of the orifice slot [117]-[118].

Finally, to characterise the averaged mass flow rate transported with the operation of a pair of adjacent synthetic jets versus a phase difference, a nonlinear least-squares regression is performed to fit a general correlation through the set of data.

7.2 Future work

This research is mainly focused on constructing an experimentally validated numerical model, in terms of both fluid flow and heat transfer results. The computationally low cost numerical model is developed in a very flexible mode, open to further modifications and advancements. With the knowledge gained from this research, further investigations can be performed on improving the model to account for different dimensional cases, trying to visualise more intricate flow features in the computational domain. This would also include the case of impinging synthetic jets, by stretching the current model to include heat transfer predictions over a hot foil as the impingement surface.

The results in this research are always accompanied with general correlations through a wide-ranging set of data. By use of these correlations, a detailed practical analysis can be performed through the many applications of unsteady impinging jets in current engineering problems. Of particular interest is application of unsteady jets in thermal management of compact electronic devices and active flow control techniques. A parametric study can be performed on the validated model through the various cases and configurations. Based on the selected design parameter, e.g. drag coefficient and Nusselt number for flow control and electronic cooling applications respectively, suggestions can be provided for the optimal operating condition and dimensions of the desired unsteady jet configuration. This can also include an investigation of the effect of nozzle exit orientation which some studies have shown to have an enhancement effect on the evolution of the unsteady jet.

The data analysis may also include spectral and/or two-point correlation analysis, coherence analysis between fluid velocity and surface heat transfer coefficient, and proper orthogonal decomposition of both numerical and experimental phase-resolved fluid flow fields.

To accommodate the high levels of heat release in a data center, fundamental thermal management measures must be established. This will help IT managers to keep servers in data centers functioning properly, as their core responsibility. Investments on smart methods of electronic cooling can save a huge portion of the electricity usage. This might be as simple as finding the most efficient physical arrangement in a data center in such a way that the cold air can be passed into the system components effectively. Convective cooling using multiple rotary fans is currently the most common method of electronic cooling. The existing design of electronic devices is mainly based on preserving air as the coolant. The typical designs of the cooling systems are not satisfactory any longer for the current and next generation data centres. A research question is raised to recognise the framework of new energy efficient solutions. The impinging jets are regarded as efficient techniques which are investigated broadly in this study. The outcome of this research assists thermal engineers to design, optimise, and verify new cooling techniques based on the application of impinging jets, at a very early stage. Visualising the air flow induced by jets inside the equipment helps to develop innovative approaches that matches the major limitations in space, power, and budget.

8 Achievements

During the course of this three-year PhD project, I have disseminated my work in 3 peer-reviewed journal articles and 5 publications in international and regional conferences:

1) *Alimohammadi S., Persoons T., Murray D. B., Tehrani M. S., Farhanieh B., and Koehler J., 2013, "A Validated Numerical-Experimental Design Methodology for a Movable Supersonic Ejector Compressor for Waste-Heat Recovery", Journal of Thermal Science and Engineering Applications, 6, pp. 021001:1-10.*

2) *Alimohammadi S., Murray D., and Persoons T., 2014, Experimental Validation of a CFD Methodology for Transitional Flow Heat Transfer Characteristics of a Steady Impinging Jet, Journal of Heat Transfer. HT-14-1049 136(9), pp. 091703-9 doi: http://dx.doi.org/10.1115/1.4027840.*

3) *Alimohammadi S., Persoons T., and Murray D. B., 2014, "A Numerical-Experimental Study of Heat Transfer Enhancement using Unconfined Steady and Pulsating Turbulent Air Jet Impingement", Proc. 15th Int. Heat Transfer Conference, Kyoto, Japan, IHTC15-8765.*

4) *Alimohammadi S., Dinneen P., Persoons T., and Murray D. B., 2014, "Thermal Management Using Pulsating Jet Cooling Technology", Journal of Physics: Conference Series for Eurotherm Seminar 102 in Thermal Management of Electronic Systems, 525 012011; doi: http://dx.doi.org/10.1088/1742-6596/525/1/012011.*

5) *Alimohammadi S., Persoons T., and Murray D. B., 2014, "On the Numerical-Experimental Analysis and Scaling of Convective Heat Transfer to Pulsating Impinging Jets", International Journal of Thermal Sciences 98, pp. 296 - 311, THESCI4493, doi: http://dx.doi.org/10.1016/j.ijthermalsci.2015.07.022.*

6) *Alimohammadi S., Persoons T., Murray D. B., 2014, "Developing a Validated CFD Methodology for Convective Heat Transfer to Unsteady Impinging Jet Flows", 1st CADFEM Ireland Users' Meeting & ANSYS Regional Conference, Dublin, Ireland.*

7) *Alimohammadi S., Persoons T., Murray D. B., 2015, "A Validated Numerical Approach for Characterisation of Unsteady Impinging Jets", 18th Crossland Symposium, University of Limerick, April 2015.*

8) *Alimohammadi S., Fanning, E., Murray D. B. and Persoons T., 2015, "Fluid Flow & Heat Transfer of Adjacent Synthetic Jets", UK Heat Transfer Conference 2015, Edinburgh, Scotland.*

9) *Alimohammadi S., Persoons T., Murray D. B., 2015, "Vectoring Phenomenon in Adjacent Synthetic Jets: PIV and CFD approaches", submitted to Physics of Fluids (1994-present) Journal.*

List of completed taught modules and ECTS credits attained:

- *Core Module One of innovation academy: Creative Thinking & Innovation, University College Dublin UCD, May 2014 (10 ECTS)*

In the summer of 2014, I have attended the Department of Mechanical & Industrial Engineering, Indian Institute of Technology (IIT), Roorkee, India, as a visiting researcher. The main purpose of this travel was to meet with expert researchers in the specific field of numerical modelling of two-phase and multi-phase flows. This includes advanced computational fluid flow and heat transfer modelling techniques.

During this PhD study, I have collaborated in a part-time capacity on some additional research projects with other faculty members in the Department of Mechanical and Manufacturing Engineering in Trinity College Dublin, as listed below:

1) *Thermal readings of microwave heated specialized ceramics with* Fe_3O_4 *contents;* principal investigator: Dr. Anthony Robinson, October 2014.
2) *Computational Fluids Dynamics Modelling applied to parametric study of air curtains for airframe noise reduction*; principal investigator: Dr. Gareth J. Bennett, December 2014.
3) *Advanced low noise landing (main and nose) gear for regional aircraft (ALLEGRA),* principal investigator: Dr. Gareth J. Bennett, Dec. 2014 - present.
4) *Experimental performance analysis of lime-scale de-scalars;* principal investigator: Dr. Anthony Robinson, December 2014 - present.
5) *Low Noise Air Amplifiers, joint project with Purdue University, USA;* principal investigator: Dr. Tim Persoons, Jan. 2015 - present.

References

[1] Garimella S. V., Persoons T., Weibel J., and Yeh L., 2013, “Technological drivers in data centres and telecom systems: Multiscale thermal, electrical, and energy management”, *Applied Energy*, 107, pp. 66–80.

[2] Garimella S. V., Yeh L., and Persoons T., 2012, “Thermal management challenges in telecommunication systems and data centres”, *IEEE Transaction on Components, Packaging, and Manufacturing Technology*, 2, pp. 1307-16.

[3] Schlichting H., “Boundary layer theory”, *New York: McGraw-Hill Book Company,* Inc., 1960.

[4] Jambunathan, K., Lai E., Moss M. A., and Button B. L., 1992, “A review of heat-transfer data for single circular jet impingement”, *International Journal of Heat and Fluid Flow*, 13 (2), pp. 106–115.

[5] O’Donovan T. S., and Murray D. B., 2007, “Jet impingement heat transfer – Part I: Mean and root-mean-square heat transfer and velocity distributions”, *International Journal of Heat and Mass Transfer*, 50, pp. 3291–3301.

[6] O’Donovan T. S., and Murray D. B., 2007, “Jet impingement heat transfer – Part II: A temporal investigation of heat transfer and local fluid velocities”, *International Journal of Heat and Mass Transfer*, 50, pp. 3302–3314.

[7] Pakhomov M. A., and Terekhov V. I., 2012, “Second-moment closure simulation of flow and heat transfer in a gas-droplets turbulent impinging jet”, *International Journal of Thermal Sciences*, 60, pp. 1-12.

[8] Lytle D., and Webb B. W., 1994, “Air-jet impingement heat-transfer at low nozzle plate spacings”, *International Journal of Heat and Mass Transfer*, 37 (12), pp. 1687–1697.

[9] Lee J., and Lee S. S., 1999, “Stagnation region heat transfer of a turbulent axisymmetric jet impingement”, *Experimental Heat Transfer*, 12 (2), pp.137–156.

[10] Katti V., and Prabhu S. V., 2008, “Experimental study and theoretical analysis of local heat transfer distribution between smooth flat surface and impinging air jet from a circular straight pipe nozzle”, *International Journal of Heat and Mass Transfer*, 51 (17-18), pp. 4480–4495.

[11] Viskanta R., 1993, “Heat transfer to impinging isothermal gas and flame jets”, *Experimental Thermal and Fluid Science*, 6 (2), pp. 111–134.

[12] Shadlesky P. S., 1983, “Jet impingement to a plane surface”, *AIAA Journal*, 21(8), pp. 1214–1215.

[13] Persoons T., McGuinn A., and Murray D. B., 2011, “A general correlation for the stagnation point Nusselt number of an axisymmetric impinging synthetic jet”, *International Journal of Heat and Mass Transfer*, 54 (17-18), pp. 3900–3908.

[14] Wang T., Dhanasekaran T. S., 2010, “Calibration of a computational model to predict mist/steam impinging jets cooling with an application to gas turbine blades”, *Journal of Heat Transfer*, 132, pp. 122201:1-11.

[15] Draksler M., and Koncar B., 2009, “A numerical investigation on a submerged, axis-symmetric jet”, *Proceedings of the International Conference Nuclear Energy for New Europe 2009*, Slovenia, pp. 822.1-9.

[16] Caggese O., Gnaegi G., Hannema G., Terzis A., and Ott P., 2013, “Experimental and numerical investigation of a fully confined impingement round jet”, *International Journal of Heat and Mass Transfer*, 65, pp. 873–882.

[17] Hadziabdic M., and Hanjalic K., 2008, “Vortical structures and heat transfer in a round impinging jet”, *Journal of Fluid Mechanics*, 596, pp. 221–260.

[18] Cziesla T., Biswas G., Chattopadhyay H., and Mitra N. K., 2001, “Large-eddy simulation of flow and heat transfer in an impinging slot jet”, *International Journal of Heat and Fluid Flow*, 22 (5), pp. 500–508.

[19] Kubacki S., and Dick E., 2010, “Simulation of plane impinging jets with k–ω based hybrid RANS/LES models”, *International Journal of Heat and Fluid Flow*, 31 (5), pp. 862–878.

[20] Langtry R. B., and Menter F. R., 2005, “Transition modelling for general CFD applications in aeronautics”, *43rd AIAA Aerospace Sciences Meeting and Exhibit 2005,* Reno, Nevada, pp. 522.1-14.

[21] Menter F. R., Langtry R. B., Likki S. R., Suzen Y. B., Huang P. G., and Voelker S., 2006, “A Correlation-based transition model using local variables Part 1 – model formulation”, *ASME Journal of Turbomachinery,* 128 (3), pp. 413-422.

[22] Langtry R. B., 2006, “A correlation-based transition model using local variables for unstructured parallelized CFD codes, PhD thesis”, *Institute of Thermal Turbomachinery and Machinery Laboratory*, University of Stuttgart.

[23] Colucci D. W., and Viskanta R., 1996, “Effect of nozzle geometry on local convective heat transfer to a confined impinging air jet”, *Experimental Thermal and Fluid Science,* 13 (1), pp. 71-80.

[24] Persoons T., Balgazin K., Brown K., and Murray D. B., 2013, “Scaling of convective heat transfer enhancement due to flow Pulsation in an axisymmetric impinging jet”, *Journal of Heat Transfer,* 135 (11), pp. 111012:1-10.

[25] Azevedo L. F. A., Webb B. W., and Queiroz M., 1994, “Pulsed air jet impingement heat transfer”, *Experimental Thermal and Fluid Sciences,* 8, pp. 206–213.

[26] Camci, C., and Herr, F., 2002, “Forced convection heat transfer enhancement using a self-oscillating impinging planar jet”, *Journal of Heat Transfer,* 124(4), pp. 770.

[27] Zumbrunnen D. A., and Aziz M., 1993, “Convective heat-transfer enhancement due to intermittency in an impinging jet”, *Journal of Heat Transfer,* 635 115(1), pp. 91–98.

[28] Herwig H., and Middelberg G., 2008, “The physics of unsteady jet impingement and its heat transfer performance,” *Acta Mechanica*, 201(1–4), pp. 171–184.

[29] Xu P., Yu B., Qiu S., Poh H. J., and Mujumdar A. S., 2010, “Turbulent impinging jet heat transfer enhancement due to intermittent pulsation” *International Journal of Thermal Sciences*, 49, pp. 1247-1252.

[30] Liu T. S., and Sullivan J. P., 1996, “Heat transfer and flow structures in an excited circular impinging jet”, *International Journal Heat Mass Transfer*, 39(17), pp. 3695–3706.

[31] O'Donovan T. S., and Murray D. B., 2007, "Effect of acoustic excitation on the heat transfer to an impinging air jet", *Proc. of the ASME-JSME Thermal Engineering Summer Heat Transfer Conference*, Paper No. HT2007–32800.

[32] Poh H. J., Kumar K., and Mujumdar A. S., 2005, "Heat transfer from a pulsed laminar impinging jet," *International Communications in Heat and Mass Transfer*, 32, pp. 1317–1324.

[33] Mohammadpour J., Rajabi-Zargarabadi M., Mujumdar A. S., and Ahmadi H., 2014, "Effect of intermittent and sinusoidal pulsed flows on impingement heat transfer from a concave surface", *International Journal of Thermal Sciences*, 76, pp.118-127.

[34] Alimohammadi S., Murray D., and Persoons T., 2014, "Experimental validation of a CFD methodology for transitional flow heat transfer characteristics of a steady impinging jet", *Journal of Heat Transfer*, HT-14-1049 136(9), pp. 091703-9.

[35] Alimohammadi S., Persoons T., and Murray D. B., 2014, "A numerical-experimental study of heat transfer enhancement using unconfined steady and pulsating turbulent air jet impingement", *Proc. 15th International Heat Transfer Conference IHTC15-8765* (Kyoto, Japan).

[36] Alimohammadi S., Dinneen P., Persoons T., and Murray D. B., 2014, "Thermal management using pulsating jet cooling technology", *Journal of Physics: Conference Series for Eurotherm Seminar 102 in Thermal Management of Electronic Systems*, 525 012011.

[37] Alimohammadi S., Persoons T., Murray D. B., Tehrani M. S., Farhanieh B., and Koehler J., 2013, "A validated numerical-experimental design methodology for a movable supersonic ejector compressor for waste-heat recovery", *ASME Journal of Thermal Science and Engineering Applications*, 6 (2), pp. 021001:1-10.

[38] Alimohammadi S., Persoons T., and Murray D. B., 2014, "On the numerical-experimental analysis and scaling of convective heat transfer to pulsating impinging jets", *International Journal of Thermal Sciences* 98, pp. 296 - 311, THESCI4493.

[39] ANSYS, Inc., 2009, "ANSYS CFX-solver theory guide", Release 12.1.

[40] Vieser T., Esch W., and Menter F., 2002, "Heat transfer predictions using advanced two-equation turbulence models", *CFX Technical Memorandum* CFX: VAL 10/0602, ANSYS Inc.

[41] Mcguinn T. A., 2011, “A study of the heat transfer processes and related flows of a synthetic jet impinging perpendicular to a surface”, PhD Thesis, Trinity College Dublin.

[42] Dinneen, P., 2014, “Heat transfer to a pulsating jet”, Master Thesis, Trinity College Dublin.

[43] Parker Hannifin Corporation, “Series 9 2-Way and 3-Way High Performance Valve.”.

[44] Valiorgue P., Persoons T., McGuinn A., and Murray D. B., 2009, “Heat transfer mechanisms in an impinging synthetic jet for a small jet-to-surface spacing”, *Experimental Thermal and Fluid Science,* 33 (4), pp. 597–603.

[45] Celik I.B., Ghia U., Roache P.J., Freitas C.J., Coleman H., and Raad P.E., 2008, “Procedure for estimation and reporting of uncertainty due to discretization in CFD applications”, *Journal Fluids Engineering,* 130 (7), pp. 07800-1.

[46] Richardson L. F., and Gaunt J. A., 1927, “The deferred approach to the limit”, *Philosophical Transactions, R. Soc. London*, Ser. A, 226, pp. 299–361.

[47] Broadhead B. L., Rearden B. T., Hopper C. M., Wagschal J. J., and Parks C. V., 2004, “Sensitivity and uncertainty-based criticality safety validation techniques”, *Nuclear Science and Engineering,* 146, pp. 340–366.

[48] Ferziger, J. H., and Peric, M., 1996, “Further discussion of numerical errors in CFD”, *International Journal for Numerical Methods in Fluids*, 23, pp. 1263–1274.

[49] Gao N., and Ewing D., 2006, “Investigation of the effect of confinement on the heat transfer to round impinging jets exiting a long pipe”, *International Journal of Heat and Fluid Flow,* 27, pp. 33–41.

[50] Zuckerman N., and Lior N., 2006, “Jet impingement heat transfer: physics, correlations, and numerical modelling”, *Advances in Heat Transfer,* 39, pp. 565-631.

[51] Reynolds A. J., 1976, “The Variation of turbulent Prandtl and Schmidt Numbers in wakes and jets”, *International Journal of Heat and Mass Transfer,* 19, pp. 757-764.

[52] Antonia R. A., and Kim J., 1991, “Turbulent Prandtl number in the near-wall region of a turbulent channel flow”, *International Journal of Heat and Mass Transfer,* 34 (7), pp. 1905-1908.

[53] Mayer E., and Divoky D., 1966, "Correlation of intermittency with preferential transport of heat and chemical species in turbulent shear flows", *AIAA*, 4 (11), pp. 1995–2000.

[54] Patankar S. V., and Spalding D. B., 1967, "Heat and mass transfer in boundary layers", *Morgan Grampian*, London.

[55] Browne L. W. B., and Antonia R. A., 1983, "Measurements of turbulent Prandtl number in a plane jet", *Journal of Heat Transfer*, 105 (3), pp. 663-665.

[56] Kays W.M., 1994, "Turbulent Prandtl number - where are we?", *ASME Journal of Heat Transfer*, 116 (2) pp. 284-295.

[57] Kawamura H., Abe H., and Matsuo Y., 1999, "DNS of turbulent heat transfer in channel flow with respect to Reynolds and Prandtl number effects", *International Journal of Heat and Fluid Flow*, 20, pp. 196-207.

[58] Chidambaram N., Dash S.M., and Kenzakowski D.C., 2001, "Scalar variance transport in the turbulence modelling of propulsive jets", *Journal of Propulsion and Power*, 17, pp. 79–84.

[59] Churchill S. W., 2002, "A reinterpretation of the turbulent Prandtl number", *Industrial & Engineering Chemistry Research*, 41 (25), pp. 6393–6401.

[60] Roache P.J., 1997, "Quantification of uncertainty in computational fluid dynamics", *Annual Review of Fluid Mechanics*, 29, 1997, pp. 123-160.

[61] Radhakrishnan S., and Bellan J., 2012, "Explicit filtering to obtain grid-spacing-independent and discretization-order-independent large-eddy simulation of compressible single-phase flow", *Journal of Fluid Mechanics*, 697, pp. 399-435.

[62] Leonard B. P., "Comments on the policy statement on numerical accuracy", *Journal of Fluids Engineering*, 115, 1993 pp 339--340.

[63] Patankar S. V., 1980, "Numerical heat transfer and fluid flow", *Bristol, PA: Taylor & Francis*, edition 14th, ISBN 9780891165224.

[64] Cavadas A.S., Pinho F.T., and Campos J.B.L.M., 2012, "Laminar flow field in a viscous liquid impinging jet confined by inclined plane walls", *International Journal of Thermal Sciences*, 59, pp. 95-110.

[65] Koseoglu M.F., and Baskaya S., 2010, "The role of jet inlet geometry in impinging jet heat transfer, modelling and experiments", *International Journal of Thermal Sciences*, 49, pp. 1417-1426.

[66] Incropera, F.P., and DeWitt, D.P., 1985, "Fundamentals of heat and mass transfer", *John Wiley and Sons,* 6th edition, New York, NY.

[67] Angioletti M., Nino E., and Ruocco G., 2005, "CFD turbulent modelling of jet impingement and its validation by particle image velocimetry and mass transfer measurements", *International Journal of Thermal Sciences*, 44, pp.349-356.

[68] Langtry R. B., and Menter F. R., 2005, "Transition modelling for general CFD applications in aeronautics", *43rd AIAA Aerospace Sciences Meeting and Exhibit*, pp. 522.1-14.

[69] Menter F. R., Langtry R. B., Likki S. R., Suzen Y. B., Huang P. G. and Voelker S., 2006, "A correlation-based transition model using local variables Part 1 – model formulation", *ASME Journal of Turbomachinery,* 128 (3), pp. 413-422.

[70] Farrington R. B., and Claunch S. D., 1994, "Infrared imaging of large-amplitude, low-frequency disturbances on a planar jet" *AIAA Journal*, 32, pp. 317–323.

[71] Azevedo L. F. A., 1994, "Pulsed air jet impingement heat transfer," *Experimental Thermal and Fluid Science*, 8, pp. 206–213.

[72] Mladin E., and Zumbrunnen D., 1997, "Local convective heat transfer to submerged pulsating jets," *International Journal of Heat Mass Transfer,* 40, pp. 3305–3321.

[73] Hofmann H. M., Movileanu D. L., Kind M., and Martin H., 2007, "Influence of a pulsation on heat transfer and flow structure in submerged impinging jets", *International Journal of Heat Mass Transfer*, 50, pp. 3638–3648.

[74] Zulkifli R., and Sopian K., 2007, "Studies on pulse jet impingement heat transfer: flow profile and effect of pulse frequencies on heat transfer", *International Journal of Engineering and Technology*, 4, pp. 86–94.

[75] Launder B. E., Reece G. J., and Rodi W., 1975, "Progress in the development of a Reynolds-stress turbulence closure", *Journal of Fluid Mechanics.*, 68, pp. 537-566.

[76] Tennekes H., and Lumley J. L., 1972, "A first course in turbulence", *MIT Press*, Cambridge, MA.

[77] Bendat J. S., and Piersol A. G., 2012, “Random data: analysis and measurement procedures”, *Wiley,* 4th edition.

[78] Smith B. L., and Glezer A., 2005, “Vectoring of Adjacent Synthetic Jets”, *AIAA Journal,* 43, pp. 2117–2124.

[79] Smith B. L., and Glezer A., 1998, “The formation and evolution of synthetic jets”, *Physics of Fluids (1994-present),* 10, pp. 2281–2297.

[80] Holman R., Utturkar Y., Mittal R., and Smith B., “Formation criterion for synthetic jets”, AIAA journal, vol. 43, 2005, pp. 2110 – 2116.

[81] Zhang W., and Samtaney R., 2015, “A direct numerical simulation investigation of the synthetic jet frequency effects on separation control of low-Re flow past an aerofoil”, *Physics of Fluids (1994-present),* 27, p. 055101.

[82] Mittal R., and Rampunggoon P., 2002, “On the virtual aeroshaping effect of synthetic jets”, *Physics of Fluids (1994-present),* 14, pp. 1533–1536.

[83] Ozawa T., Lesbros S., and Hong, G., 2010, “LES of synthetic jets in boundary layer with laminar separation caused by adverse pressure gradient”, *Computers & Fluids,* 39, pp. 845–858.

[84] Jabbal M., and Zhong S., 2010, “Particle image velocimetry measurements of the interaction of synthetic jets with a zero-pressure gradient laminar boundary layer”, *Physics of Fluids (1994-present),* 22, p. 063603.

[85] Liu Y., Wang B., and Liu S., 20009, “Investigation of phase excitation effect on mixing control in coaxial jets”, *Journal of Thermal Science,* 18, pp. 364–369.

[86] Xia Q., and Zhong S., 2012, “A PLIF and PIV study of liquid mixing enhanced by a lateral synthetic jet pair”, *International Journal of Heat and Fluid Flow,* 37, pp. 64–73.

[87] Ibrahim I. H., and Skote M., 2012, “Simulations of the linear plasma synthetic jet actuator utilizing a modified Suzen-Huang model”, *Physics of Fluids (1994-present),* 24, p. 113602.

[88] Campbell J. S.J., Black W. Z., Glezer A., and Hartley J. G., 1998, “Thermal management of a laptop computer with synthetic air microjets”, *The Sixth Intersociety Conference on Thermal and Thermomechanical Phenomena in Electronic Systems*, ITHERM ’98, pp. 43–50.

[89] Smith B. L., and Swift G. W., 2003, "A comparison between synthetic jets and continuous jets", *Experiments in Fluids,* 34, pp. 467–472.

[90] Mahalingam R., 2007, "Modelling of synthetic jet ejectors for electronics cooling", *23rd Annual IEEE Semiconductor Thermal Measurement and Management Symposium,* SEMI-THERM 2007, pp. 196–199.

[91] Glezer A., and Amitay M., 2002, "Synthetic Jets", *Annual Review of Fluid Mechanics*, 34, pp. 503–529.

[92] Shuster J. M., and Smith D. R., 2007, "Experimental study of the formation and scaling of a round synthetic jet", *Physics of Fluids (1994-present),* 19, p. 045109.

[93] Mohseni K., and Mittal R., 2014, "Synthetic jets: fundamentals and applications", *CRC Press*.

[94] Kral L., Donovan J., Cain A., and Cary A., 1997, "Numerical simulation of synthetic jet actuators", *4th Shear Flow Control Conference*, American Institute of Aeronautics and Astronautics.

[95] Rizzetta D. P., Visbal M. R., and Stanek M. J., "Numerical investigation of synthetic-jet flow fields," AIAA Journal, vol. 37, 1999, pp. 919–927.

[96] Carpy S., and Manceau R., 2006, "Turbulence modelling of statistically periodic flows: Synthetic jet into quiescent air", *International Journal of Heat and Fluid Flow*, 27, pp. 756–767.

[97] Rumsey C. L., Schaeffler N. W., Milanovic I. M., and Zaman K. B. M. Q., 2007, "Time-accurate computations of isolated circular synthetic jets in crossflow", *Computers & Fluids*, 36, pp. 1092–1105.

[98] Wang Y., Yuan G., Yoon Y.-K., Allen M. G., and Bidstrup S. A., 2006, "Large eddy simulation (LES) for synthetic jet thermal management", *International Journal of Heat and Mass Transfer,* 49, pp. 2173–2179.

[99] Timchenko V., Reizes, J. and Leonardi, E., 2007, "An evaluation of synthetic jets for heat transfer enhancement in air cooled micro-channels", *International Journal of Numerical Methods for Heat & Fluid Flow,* 17, pp. 263–283.

[100] Hewakandamby B. N., 2009, "A numerical study of heat transfer performance of oscillatory impinging jets", *International Journal of Heat and Mass Transfer,* 52, pp. 396–406.

[101] Jain M., Puranik B., and Agrawal A., 2011, “A numerical investigation of effects of cavity and orifice parameters on the characteristics of a synthetic jet flow”, *Sensors and Actuators A: Physical*, 165, pp. 351–366.

[102] Bazdidi-Tehrani F., Eghbali A., and Karami M., 2013, “Influence of jet-to-surface distance and frequency on unsteady heat transfer and mass flow rate in an impingement synthetic jet”, *Journal of Enhanced Heat Transfer,* 20, pp. 115–136.

[103] Harinaldi C. D., and Rhakasywi D., 2012, “Effect of impinging distance for convective heat transfer of synthetic jet”, *World Applied Sciences Journal,* 20 (3), pp. 470-475.

[104] Silva L. A., and Ortega A., 2013, “Convective heat transfer in an impinging synthetic jet: a numerical investigation of a canonical geometry”, *Journal of Heat Transfer,* 135, pp. 082201–082201.

[105] Xia Q., Lei S., Ma J., and Zhong S., 2014, “Numerical study of circular synthetic jets at low Reynolds numbers”, *International Journal of Heat and Fluid Flow,*50, pp. 456–466.

[106] Ritchie B., and Seitzman J., 2000, “Controlled fuel-air mixing using a synthetic jet array”, *36th AIAA/ASME/SAE/ASEE Joint Propulsion Conference and Exhibit*, American Institute of Aeronautics and Astronautics.

[107] Luo Z., and Xia Z.-X., 2008, “PIV measurements and mechanisms of adjacent synthetic jets interactions”, *Chinese Physics Letters*, 25, p. 612.

[108] Persoons T., O’Donovan T. S., and Murray D. B., 2009, “Heat transfer in adjacent interacting impinging synthetic jets”, *ASME 2009 Heat Transfer Summer Conference*, pp. 955–962.

[109] Fanning E., Persoons T., and Murray D. B., 2015, “Heat transfer and flow characteristics of a pair of adjacent impinging synthetic jets”, *International Journal of Heat and Fluid Flow*, 54, pp. 153–166.

[110] Guo D., Cary A. W., and Agarwal R. K., 2003, “Numerical simulation of the interaction of two adjacent synthetic jet actuators”, *Computational Fluid Dynamics 2002,* S.W. Armfield, P. Morgan, and K. Srinivas, eds., Springer Berlin Heidelberg, 2003, pp. 751–756.

[111] Riazi H., and Ahmed N., 2011, "Numerical investigation on two-orifice synthetic jet actuators of varying orifice spacing and diameter," *29th AIAA Applied Aerodynamics Conference*, American Institute of Aeronautics and Astronautics.

[112] Luo Z., Xia Z., and Liu B., 2006, "An adjustable synthetic jet by a novel PZT-driven actuator with a slide block", *Journal of Physics: Conference Series*, 34, p. 487.

[113] Smith B. L., and Glezer A., 2001, "The formation and evolution of synthetic jets", *Physics of Fluids*, 10, pp. 2281–2297.

[114] Persoons T., and O'Donovan T. S., 2007, "A pressure-based estimate of synthetic jet velocity", *Physics of Fluids (1994-present)*, 19, p. 128104.

[115] Persoons T., 2012, "General reduced-order model to design and operate synthetic jet actuators", *AIAA journal*, 4, pp. 916-927.

[116] Stanislas M., Okamoto K., Kähler C. J., Westerweel J., and Scarano F., 2008, "Main results of the third international PIV Challenge", *Experiments in Fluids*, 45, pp. 27–71.

[117] Alimohammadi S., Fanning E., Murray D. B. and Persoons T., 2015, "Fluid flow & heat transfer modelling of adjacent synthetic jets", 1*4th UK Heat Transfer Conference 2015 Edinburgh*, UK.

[118] Alimohammadi S., Persoons T., Murray D. B., 2015, "Characterisation of vectoring phenomenon in adjacent synthetic jets: PIV and CFD approaches", *submitted to Physics of Fluids (1994-present) Journal*.

A Appendix

A.1 Simulation Results for a 13 mm Diameter Nozzle Pipe

The following sections compare the heat transfer results from steady and pulsating jet flows in the form of Nusselt number distribution over the impingement surface. The results are shown for *Re* = 6,000, *H/D* =1, 2, 3, 4 and 6 and *f* = 9, 18, 27, 32, 36, 40 and 55 Hz. This corresponds to Strouhal number, Sr, range of $0.017 \leq Sr \leq 0.102$. *Sr* numbers are reported in order to keep the current study comparable to other researches done in the scope of pulsating jet impingement with different operating conditions such as velocity, dimensions, etc.

A.1.1 Effect of Pulsation on Local Nusselt Number Distribution

The effect of pulsating inlet flow on the numerical results for local Nusselt number distribution, *Nu(r)*, is shown in Fig. A-1, in which the solid line represent the results for the steady flow (f =0), and the markers for the pulsating flow ($f = 9 – 55$ Hz).

As shown in Fig. A-1(a-e), for the lowest frequency (f = 9 Hz), a reduction in the heat transfer coefficient is clearly detectable in the stagnation zone. However, for higher frequencies (27 Hz $\leq f \leq$ 55 Hz), pulsating jet flow for $2 \leq H/D \leq 6$ generally increases the local Nusselt number distribution over the entire impingement surface, compared to the corresponding steady jet. For the radial distances of $r / D > 2$, after the secondary peak, the results show a gradual reduction in heat transfer distribution, and interestingly, the difference between the results of various frequencies after this region becomes insignificant. In addition, as the frequency of the pulsation increases, the second peak in the Nusselt number distribution becomes less intense while remaining at the same location ($1 \le r/D \le 2$). Although not shown here, similar behaviour has been observed for the entire range of Reynolds numbers investigated, $6{,}000 \le Re \le 14{,}000$.

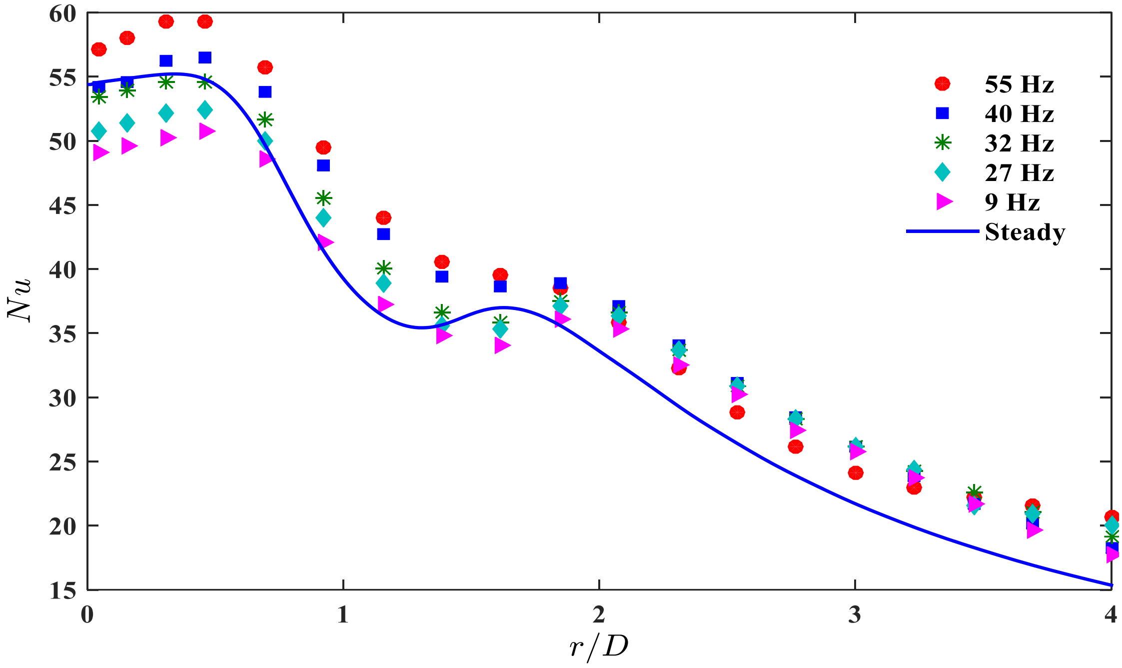

(a)

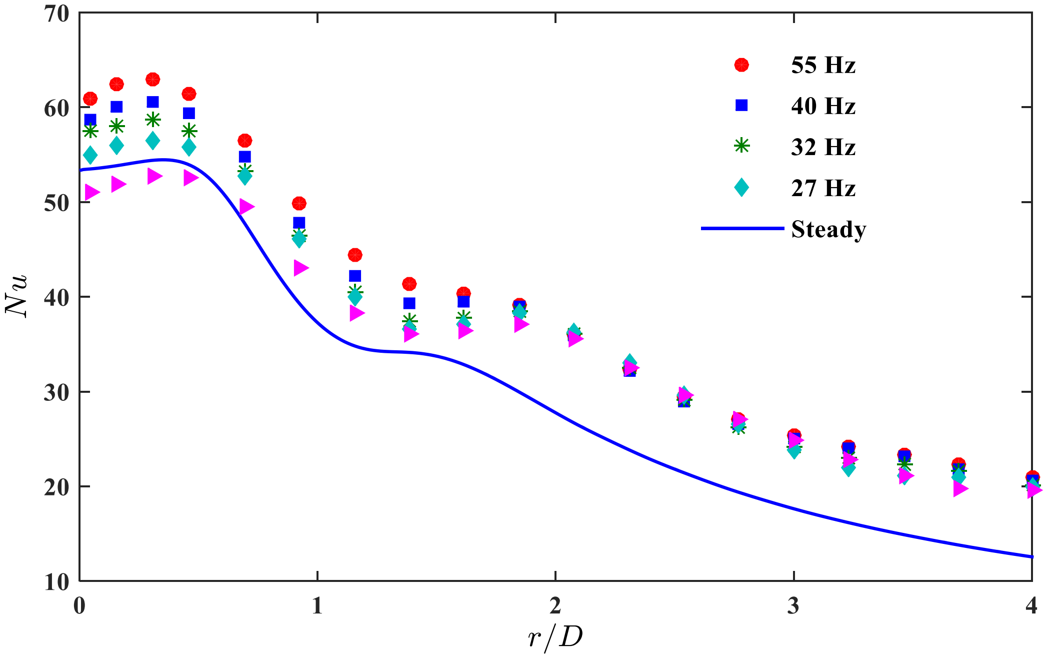

(b)

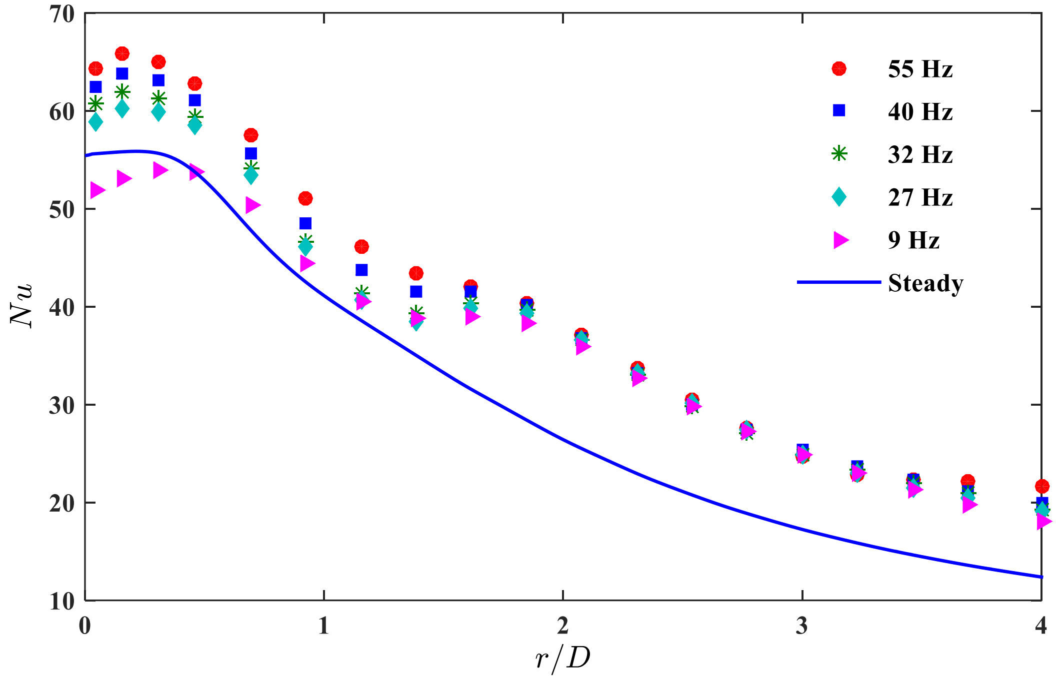
70
60
50
40
30
20
10
Nu
0
1
2
3
4
r/D
55 Hz
40 Hz
32 Hz
27 Hz
9 Hz
Steady

(c)

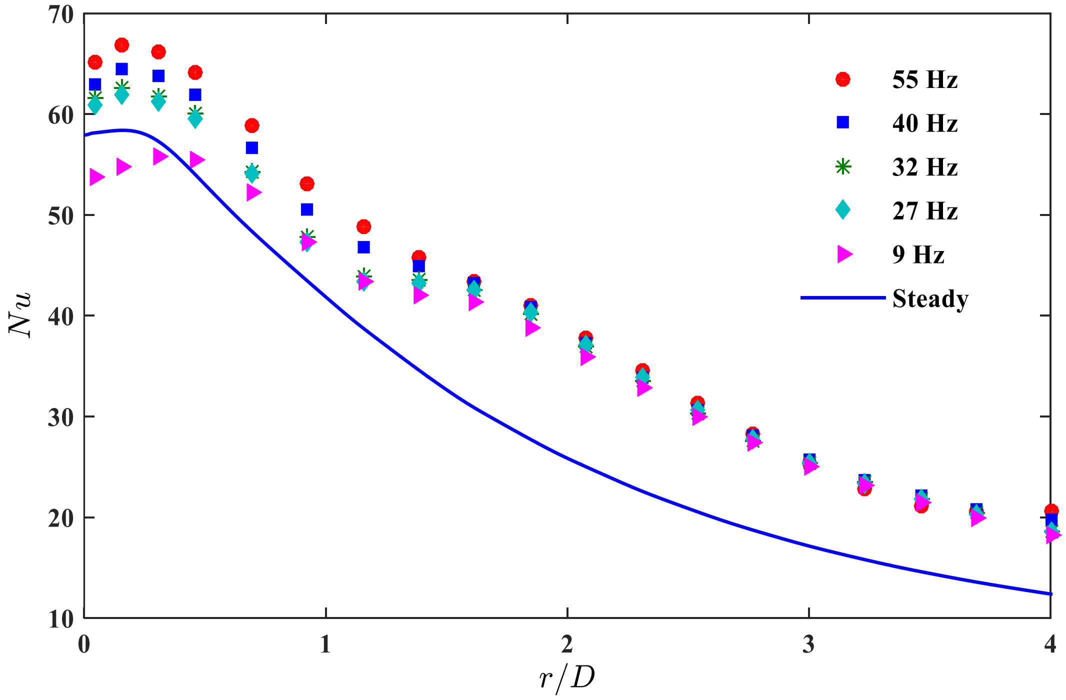
70
60
50
40
30
20
10
Nu
0
1
2
3
4
r/D
55 Hz
40 Hz
32 Hz
27 Hz
9 Hz
Steady

(d)

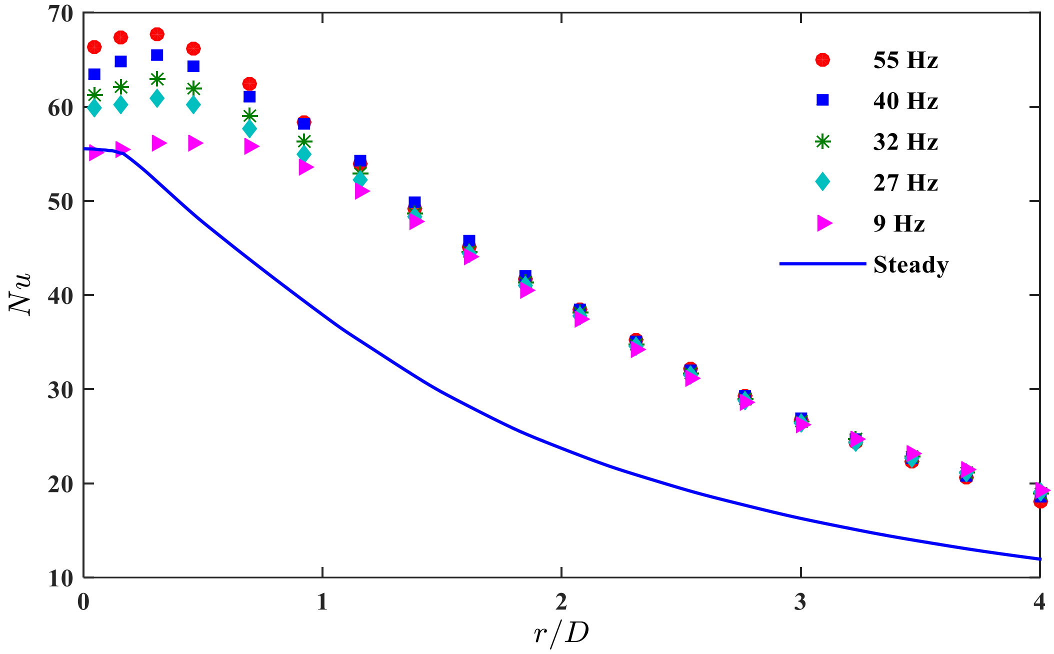

(e)

Figure A-1. Comparison of numerical results of local Nusselt number distribution for steady and pulsating flows at different frequencies (*f* = *9 – 55* Hz; *Re* = 6,000) for: (a). *H/D* = 1, (b). *H/D* = 2, (c). *H/D* = 3, (d). *H/D* = 4 and (e). *H/D* = 6

A.2 Enhancement in Stagnation Nusselt Number

The stagnation point enhancement using the pulsating flow is quantified by using: $\delta Nu_0 = Nu_0^{(Pulsating)}/ Nu_0^{(Steady)}-1$. Figure A-2 depicts numerical results of the δNu_0 for different frequencies and *H/D* values.

For *f* = 9 Hz, a degradation in the stagnation Nusselt number occurs when pulsation is used, followed by increases with increasing frequency from 9 to 55 Hz. For *H/D* of 1, the maximum reduction of -10% of the steady Nusselt number is observed (*f* = 9 Hz, *Sr* = 0.017), and only at the uppermost frequency of 55 Hz, is an increase of the stagnation point Nusselt number detectable (Fig. A-2). On the other hand, as shown in Fig. A-2, for larger nozzle-to-surface distance ($2 \leq H/D \leq 6$), the pulsating jet flow enhances the heat transfer coefficient in the stagnation zone, compared to the equivalent steady jet. The maximum stagnation point enhancement is 19% at *H/D* = 6, *f* = 55 and *Sr* = 0.102.

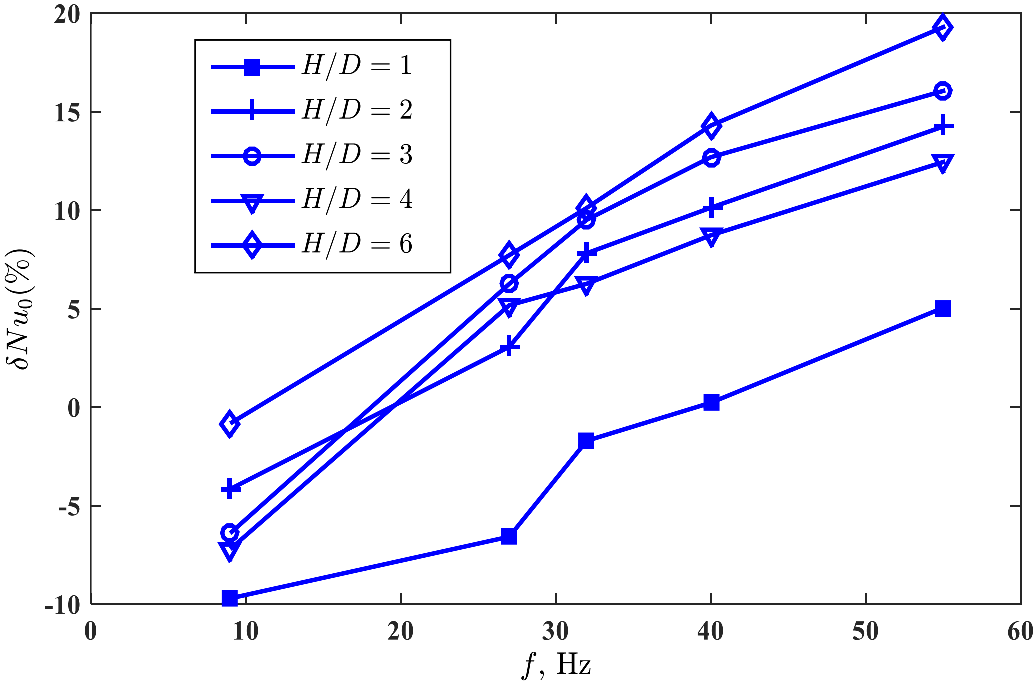

Figure A-2. Numerical results for Stagnation Nusselt number enhancement, δNu_0 (%), using pulsating flows at different frequencies (*f* = 9 – 55 Hz; *Re* = 6,000) for *H/D* = 1 - 6

A.2.1 Enhancement in Area-Averaged Nusselt Number

As shown in section 4.1, the flow pulsation mainly increases the heat transfer in the wall jet region, rather than in the stagnation region ($r/D \leq 1$), so the largest enhancement effect of pulsating flow is generally detectable in the wall jet region ($r/D > 1$). The effect of pulsation on the area-averaged Nusselt number ($\mathrm{Nu}_{ave-domain} = \frac{2}{R^2}\int_{r=0}^{R} \mathrm{Nu}(r) r dr;\ here: R = 6D$) can provide a better indication of the global performance of the pulsating flow. The numerical results for heat transfer enhancement of area-averaged Nusselt number ($\delta Nu_{ave} = Nu_{ave}^{(\mathrm{Pulsating})} / Nu_{ave}^{(\mathrm{Steady})} - 1$) for different frequencies, compared to the steady jet at the same *Re* and *H/D*, are shown in Fig. A-3.

As evident from Fig. A-3, flow pulsation generally increases the heat transfer rate. The level of area-averaged enhancement (δNu_{ave}) increases with frequency (or Strouhal number). *H/D* strongly affects the area-averaged heat transfer. The results for two higher frequencies, 40 and 55 Hz, are very close; this becomes more evident at $H/D = 6$, where the maximum δNu_{ave} of 63% occurs ($f = 55$, $Sr = 0.102$). The lowest enhancement is equal to 10% for $H/D = 1$ ($f = 9$ Hz, $Sr = 0.017$). As a result, Fig. A-3 confirms that the increased δNu_{ave} outweighs the reductions in δNu_0 (Fig. A-2). Furthermore, comparison of Figs. A-2 and A-3 shows that the stagnation and area-averaged Nusselt numbers exhibit similar trends with frequency and nozzle-to-surface distance. The variation of enhancement in stagnation and area-averaged Nusselt numbers with *f* and *H/D* are consistent with experimental data of Persoons et al. [24].

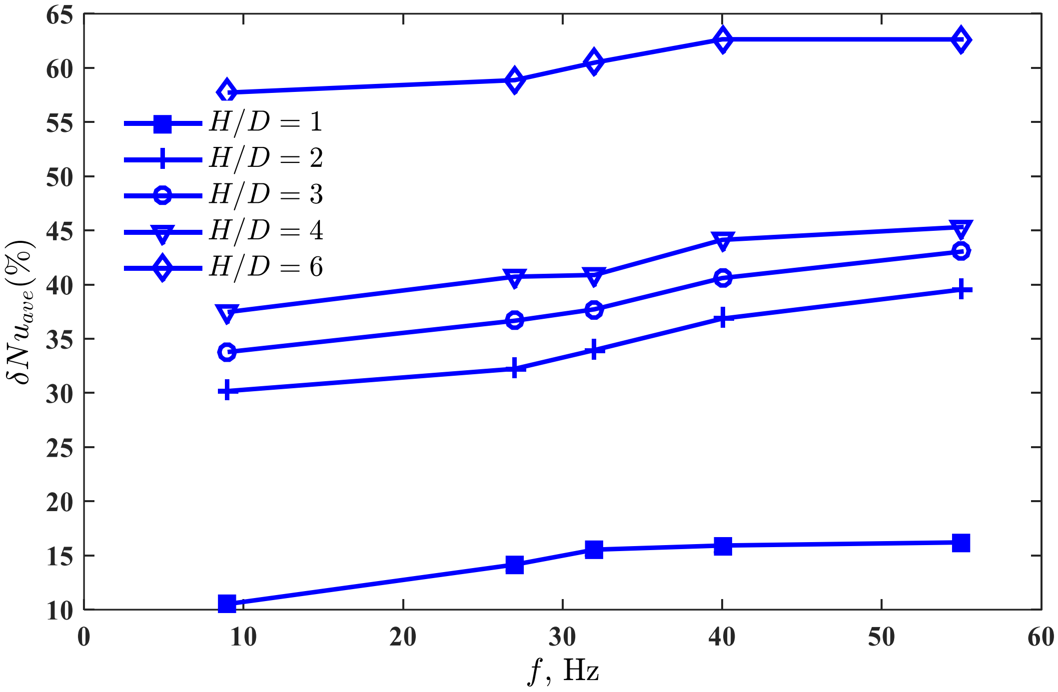

Figure A-3. Numerical results for area-averaged Nusselt number enhancement (%) using pulsating flows at different frequencies (*f* = 9 – 55 Hz; *Re* = 6,000) for: *H/D* = 1 – 6

A.3 Grid Convergence Index (GCI) Method

The Grid Convergence Index (GCI) method, based on Richardson Extrapolation, described hereafter is a commonly used method that has been evaluated over several hundred CFD cases [45]-[48].

A.3.1 Recommended Procedure for Estimation of Discretization Error

Step 1. Define a representative cell, mesh, or grid size h. For example, for three-dimensional calculations,

$$h = \left[\frac{1}{N}\sum_{i=1}^{N}(\Delta V_i)\right]^{1/3} \tag{A-1}$$

For two dimensions,

$$h = \left[\frac{1}{N}\sum_{i=1}^{N}(\Delta A_i)\right]^{1/2} \tag{A-2}$$

where ΔV_i is the volume, ΔA_i is the area of the ith cell, and N is the total number of cells used for the computations. Equations shown above are to be used when integral quantities, e.g., drag coefficient, are considered. For field variables, the local cell size can be used. Clearly, if an observed global variable is used, it is then appropriate to use also an average “global” cell size. The area should be interpreted strictly according to the mesh being used, i.e., the mesh is either *2D* (consisting of areas) or *3D* (consisting of volumes) irrespective of the problem being solved.

Step 2. Select three significantly different sets of grids and run simulations to determine the values of key variables important to the objective of the simulation study, for example, a variable ϕ critical to the conclusions being reported. It is desirable that the grid refinement factor r=h_{coarse} /h_{fine} be greater than 1.3. This value of 1.3 is based on experience and not on formal derivation. The grid refinement should, however, be done systematically, that is, the refinement itself should be structured even if the grid is unstructured. Use of geometrically similar cells is preferable.

Step 3. Let $h_1 < h_2 < h_3$ and $r_{21}=h_2 / h_1$, $r_{32}=h_3 / h_2$, and calculate the apparent order p of the method using the expression,

$$h = \frac{1}{\ln(r_{21})} \left|\ln|\varepsilon_{32}/\varepsilon_{21}| + q(p)\right| \tag{A-3a}$$

$$q(p) = \ln\left(\frac{r_{21}^{p}-s}{r_{32}^{p}-s}\right) \tag{A-3b}$$

$$s = 1.\operatorname{sgn}\left(\varepsilon_{32}/\varepsilon_{21}\right) \tag{A-3c}$$

where $\varepsilon_{32} = \phi_3 - \phi_2$, $\varepsilon_{21} = \phi_2 - \phi_1$ and ϕ_k denotes the solution on the *k*th grid. Note that $q(p) = 0$ for r = const. Eq. (5-3) can be solved using fixed-point iteration, with the initial guess equal to the first term. The absolute value in Eq. (A-3a) is necessary to ensure extrapolation toward h=0. Negative values of $\frac{\varepsilon_{32}}{\varepsilon_{21}} < 0$ are an indication of oscillatory convergence. If possible, the percentage occurrence of oscillatory convergence should also be reported. The agreement of the observed apparent order with the formal order of the scheme used can be taken as a good indication of the grids being in the asymptotic range; the converse should not necessarily be taken as a sign of unsatisfactory calculations. It should be noted that if either $\varepsilon_{32} = \phi_3 - \phi_2$ or $\varepsilon_{21} = \phi_2 - \phi_1$ is "very close" to zero, the above procedure does not work. This might be an indication of oscillatory convergence or, in rare situations, it may indicate that the "exact" solution has been attained. In such cases, if possible, calculations with additional grid refinement should be performed; if not, the results may be reported as such.

Step 4. Calculate the extrapolated values from

$$\phi_{ext}^{21} = (r_{21}^{p}\phi_1 - \phi_2)/(r_{21}^{p} - 1) \tag{A-4}$$

similarly, calculate ϕ_{ext}^{32}.

Step 5. Calculate and report the following error estimates, along with the apparent order p.

In approximate relative error,

$$e_a^{21} = \left|\frac{\phi_1 - \phi_2}{\phi_1}\right| \tag{A-5}$$

In extrapolated relative error,

$$e_{ext}^{21} = \left|\frac{\phi_{ext}^{12} - \phi_1}{\phi_{ext}^{12}}\right| \tag{A-6}$$

In the fine-grid convergence index,

$$GCI_{fine}^{21} = \frac{1.25 e_a^{21}}{r_{21}^{p} - 1} \tag{A-7}$$

When computed profiles of a certain variable are presented, it is recommended that numerical uncertainty be indicated by error bars on the profile, analogous to the experimental uncertainty. It is further recommended that this be done using the GCI in conjunction with an average value of $p = p_{\text{ave}}$ as a measure of the global order of accuracy [45]-[48].

A.4 Turbulence Models

It is important to have a good idea of differences between various types of turbulence models used in this study. The following section tries to introduce the turbulence concept and to give a detailed description of different models; it is all based on ANSYS CFX-solver theory guide [39]. Turbulence consists of fluctuations in the flow field in time and space. It is a complex process, mainly because it is three dimensional, unsteady and consists of many scales. It can have a significant effect on the characteristics of the flow. Turbulence occurs when the inertia forces in the fluid become significant compared to viscous forces, and is characterized by a high Reynolds Number.

In principle, the Navier-Stokes equations describe both laminar and turbulent flows without the need for additional information. However, turbulent flows at realistic Reynolds numbers span a large range of turbulent length and time scales, and would generally involve length scales much smaller than the smallest finite volume mesh, which can be practically used in a numerical analysis. The Direct Numerical Simulation (DNS) of these flows would require computing power which is many orders of magnitude higher than available in the foreseeable future.

To enable the effects of turbulence to be predicted, a large amount of CFD research has concentrated on methods which make use of *turbulence models*. Turbulence models have been specifically developed to account for the effects of turbulence without recourse to a prohibitively fine mesh and direct numerical simulation. Most turbulence models are statistical turbulence models, as described below.

A.4.1 Statistical Turbulence Models and the Closure Problem

When looking at time scales much larger than the time scales of turbulent fluctuations, turbulent flow could be said to exhibit average characteristics, with an additional time-varying, fluctuating component. For example, a velocity component may be divided into an average component, and a time varying component.

In general, turbulence models seek to modify the original unsteady Navier-Stokes equations by the introduction of averaged and fluctuating quantities to produce the Reynolds Averaged Navier-Stokes (RANS) equations. These equations represent the mean flow quantities only, while modelling turbulence effects without a need for the resolution of the turbulent fluctuations. All scales of the turbulence field are being modelled. Turbulence models based on the RANS equations are known as Statistical Turbulence Models due to the statistical averaging procedure employed to obtain the equations.

Simulation of the RANS equations greatly reduces the computational effort compared to a Direct Numerical Simulation and is generally adopted for practical engineering calculations. However, the averaging procedure introduces additional unknown terms containing products of the fluctuating quantities, which act like additional stresses in the fluid. These terms, called 'turbulent' or 'Reynolds' stresses, are difficult to determine directly and so become further unknowns.

The Reynolds (turbulent) stresses need to be modelled by additional equations of known quantities in order to achieve "closure." Closure implies that there is a sufficient number of equations for all the unknowns, including the Reynolds-Stress tensor resulting from the averaging procedure. The equations used to close the system define the type of turbulence model.

A.4.2 Reynolds Averaged Navier-Stokes (*RANS*) Equations

As described above, turbulence models seek to solve a modified set of transport equations by introducing averaged and fluctuating components. For example, a velocity U_i may be divided into an average component, $\overline{U}_i$, and a time varying component, u_i.

$$U_i = \overline{U}_i + u_i \tag{A-8}$$

The averaged component is given by:

$$\overline{U}_i = \frac{1}{\Delta t}\int_t^{t+\Delta t} U_i \, dt \tag{A-9}$$

where Δt is a time scale that is large relative to the turbulent fluctuations, but small relative to the time scale to which the equations are solved. For compressible flows, the averaging is actually weighted by density (Favre-averaging), but for simplicity, the following presentation assumes that density fluctuations are negligible.

For unsteady flows, the equations are ensemble-averaged. This allows the averaged equations to be solved for unsteady simulations as well. The resulting equations are sometimes called URANS (Unsteady Reynolds Averaged Navier-Stokes equations).

Substituting the averaged quantities into the original transport equations for mass and momentum results in the Reynolds averaged equations given below. In the following equations, the bar is dropped for averaged quantities, except for products of fluctuating quantities.

$$\frac{\partial \rho}{\partial t} + \frac{\partial}{\partial x_j}\left(\rho U_j\right) = 0 \tag{A-10}$$

$$\frac{\partial \rho U_i}{\partial t} + \frac{\partial}{\partial x_j}\left(\rho U_i U_j\right) = -\frac{\partial p}{\partial x_i} + \frac{\partial}{\partial x_j}\left(\tau_{ij} - \rho\overline{u_i u_j}\right) + S_M \tag{A-11}$$

where τ is the molecular stress tensor (including both normal and shear components of the stress).

The continuity equation has not been altered but the momentum and scalar transport equations contain turbulent flux terms additional to the molecular diffusive fluxes. These are the Reynolds stresses, $\rho\overline{u_i u_j}$. These terms arise from the nonlinear convective term in the un-averaged equations. They reflect the fact that convective transport due to turbulent velocity fluctuations will act to enhance mixing over and above that caused by thermal fluctuations at the molecular level. At high Reynolds numbers, turbulent velocity fluctuations occur over a length scale much larger than the mean free path of thermal fluctuations, so that the turbulent fluxes are much larger than the molecular fluxes.

The Reynolds averaged energy equation is:

$$\frac{\partial \rho h_{tot}}{\partial t} - \frac{\partial p}{\partial t} + \frac{\partial}{\partial x_j}\left(\rho U_j h_{tot}\right) = \frac{\partial}{\partial x_j}\left(\lambda \frac{\partial T}{\partial x_j} - \rho \overline{u_j h}\right) + \frac{\partial}{\partial x_j}\left[U_i\left(\tau_{ij} - \rho \overline{u_i u_j}\right)\right] + S_E \qquad \text{(A-12)}$$

This equation contains an additional turbulence flux term, $\rho \overline{u_j h}$ compared with the instantaneous equation. The $\frac{\partial}{\partial x_j}\left[U_i\left(\tau_{ij} - \rho \overline{u_i u_j}\right)\right]$ term in the equation is the viscous work term that can be included by enabling Viscous Work in CFX-Pre.

The mean Total Enthalpy is given by:

$$h_{tot} = h + \frac{1}{2} U_i U_i + k \qquad \text{(A-13)}$$

Note that the Total Enthalpy contains a contribution from the turbulent kinetic energy, k, given by:

$$k = \frac{1}{2} \overline{u_i'^2} \qquad \text{(A-14)}$$

Similarly, the Additional Variable ϕ may be divided into an average component, $\bar{\phi}$, and a time varying component, φ. After dropping the bar for averaged quantities, except for products of fluctuating quantities, the Additional Variable equation becomes

$$\frac{\partial \rho \phi}{\partial t} + \frac{\partial}{\partial x_j}\left(\rho U_j \phi\right) = \frac{\partial}{\partial x_j}\left(\Gamma \frac{\partial \phi}{\partial x_j} - \rho \overline{u_j \phi}\right) + S_\phi \qquad \text{(A-15)}$$

where $\rho \overline{u_j \phi}$ is the Reynolds flux.

Turbulence models close the Reynolds averaged equations by providing models for the computation of the Reynolds stresses and Reynolds fluxes. CFX models can be broadly divided into two classes: eddy viscosity models and Reynolds stress models.

A.4.3 Eddy Viscosity Turbulence Models

One proposal suggests that turbulence consists of small eddies which are continuously forming and dissipating, and in which the Reynolds stresses are assumed to be proportional to mean velocity gradients. This defines an “eddy viscosity model”.

The eddy viscosity hypothesis assumes that the Reynolds stresses can be related to the mean velocity gradients and eddy (turbulent) viscosity by the gradient diffusion hypothesis, in a manner analogous to the relationship between the stress and strain tensors in laminar Newtonian flow:

$$-\rho\overline{u_i u_j} = \mu_t\left(\frac{\partial U_i}{\partial x_j} + \frac{\partial U_j}{\partial x_i}\right) - \frac{2}{3}\delta_{ji}\left(\rho k + \mu_t\frac{\partial U_k}{\partial x_k}\right) \tag{A-16}$$

where μ_t is the eddy viscosity or turbulent viscosity, which must be modelled.

Analogous to the eddy viscosity hypothesis is the eddy diffusivity hypothesis, which states that the Reynolds fluxes of a scalar are linearly related to the mean scalar gradient:

$$-\rho\overline{u_i\phi} = \Gamma\frac{\partial \phi}{\partial x_i} \tag{A-17}$$

where Γ_t is the eddy diffusivity, and this has to be prescribed. The eddy diffusivity can be written as:

$$\Gamma_t = \frac{\mu_t}{Pr_t} \tag{A-18}$$

where Pr_t is the turbulent Prandtl number. Eddy diffusivities are then prescribed using the turbulent Prandtl number.

The above equations can express turbulent fluctuations in terms of functions of the mean variables only if the turbulent viscosity, μ_t, is known. Both the $k-\varepsilon$ and $k-\omega$ two-equation turbulence models use this variable.

Subject to these hypotheses, the Reynolds averaged momentum and scalar transport equations become:

$$\frac{\partial \rho U_i}{\partial t}+\frac{\partial}{\partial x_j}\left(\rho U_i U_j\right)=-\frac{\partial p'}{\partial x_i}+\frac{\partial}{\partial x_j}\left[\mu_{eff}\left(\frac{\partial U_i}{\partial x_j}+\frac{\partial U_j}{\partial x_i}\right)\right]+S_M \tag{A-19}$$

where S_M is the sum of the body forces, and μ_{eff} is the Effective Viscosity defined by:

$$\mu_{eff}=\mu+\mu_t \tag{A-20}$$

and p' is a modified pressure, defined by:

$$p'=p+\frac{2}{3}\rho k+\frac{2}{3}\mu_{eff}\frac{\partial U_k}{\partial x_k} \tag{A-21}$$

The term $\frac{2}{3}\mu_{eff}\frac{\partial U_k}{\partial x_k}$ involves the divergence of velocity. It is neglected in ANSYS CFX, although this assumption is strictly correct only for incompressible fluids.

The Reynolds averaged energy equation becomes:

$$\begin{aligned}\frac{\partial \rho h_{tot}}{\partial t}-\frac{\partial p}{\partial t}+\frac{\partial}{\partial x_j}\left(\rho U_j h_{tot}\right)\\ =\frac{\partial}{\partial x_j}\left(\lambda\frac{\partial T}{\partial x_j}+\frac{\mu_t}{Pr_t}\frac{\partial h}{\partial x_j}\right)+\frac{\partial}{\partial x_j}\left[U_i\left(\tau_{ij}-\rho\overline{u_i u_j}\right)\right]+S_E\end{aligned} \tag{A-22}$$

Note that although the transformation of the molecular diffusion term may be inexact if enthalpy depends on variables other than temperature, the turbulent diffusion term is correct, subject to the eddy diffusivity hypothesis. Moreover, as turbulent diffusion is usually much larger than molecular diffusion, small errors in the latter can be ignored.

Similarly, the Reynolds averaged transport equation for Additional Variables (non-reacting scalars) becomes:

$$\frac{\partial \rho \phi}{\partial t} + \frac{\partial}{\partial x_j}\left(\rho U_j \phi\right) = \frac{\partial}{\partial x_j}\left[\left(\Gamma_\phi + \frac{\mu_t}{\sigma_\phi}\right)\frac{\partial \phi}{\partial x_j}\right] + S_\phi \tag{A-23}$$

Eddy viscosity models are distinguished by the manner in which they prescribe the eddy viscosity and eddy diffusivity.

A.4.3.1 The Zero Equation Model in ANSYS CFX

Very simple eddy viscosity models compute a global value for μ_t from the mean velocity and a geometric length scale using an empirical formula. Because no additional transport equations are solved, these models are termed ‘zero equation.’

The zero equation model in ANSYS CFX uses an algebraic equation to calculate the viscous contribution from turbulent eddies. A constant turbulent eddy viscosity is calculated for the entire flow domain.

The turbulence viscosity is modelled as the product of a turbulent velocity scale, U_t, and a turbulence length scale, l_t, as proposed by Prandtl and Kolmogorov,

$$\mu_t = \rho f_\mu U_t l_t \tag{A-24}$$

where f_μ is a proportionality constant. The velocity scale is taken to be the maximum velocity in the fluid domain. The length scale is derived using the formula:

$$l_t = \left(V_D^{\frac{13}{3}}\right)/7 \tag{A-25}$$

where V_D is the fluid domain volume. This model has little physical foundation and is not recommended.

A.4.3.2 Two Equation Turbulence Models

Two-equation turbulence models are very widely used, as they offer a good compromise between numerical effort and computational accuracy. Two-equation models are much more sophisticated than the zero equation models. Both the velocity and length scale are solved using separate transport equations (hence the term 'two-equation').

The $k-\varepsilon$ and $k-\omega$ two-equation models use the gradient diffusion hypothesis to relate the Reynolds stresses to the mean velocity gradients and the turbulent viscosity. The turbulent viscosity is modelled as the product of a turbulent velocity and turbulent length scale.

In two-equation models, the turbulence velocity scale is computed from the turbulent kinetic energy, which is provided from the solution of its transport equation. The turbulent length scale is estimated from two properties of the turbulence field, usually the turbulent kinetic energy and its dissipation rate. The dissipation rate of the turbulent kinetic energy is provided from the solution of its transport equation.

A.4.3.3 The k-epsilon Model

k is the turbulence kinetic energy and is defined as the variance of the fluctuations in velocity. It has dimensions of ($L^2\ T^{-2}$); for example, m^2/s^2. $\boldsymbol{\varepsilon}$ is the turbulence eddy dissipation (the rate at which the velocity fluctuations dissipate), and has dimensions of k per unit time ($L^2\ T^{-3}$); for example, m^2/s^3.

The $k-\varepsilon$ model introduces two new variables into the system of equations which are earlier represented in Eqs. (A-10) and (A-11) as continuity and momentum equations.

The $k-\varepsilon$ model, like the zero equation model, is based on the eddy viscosity concept. The $k-\varepsilon$ model assumes that the turbulence viscosity μ_t used in Eq. (A-20) for effective viscosity μ_{eff} is linked to the turbulence kinetic energy and dissipation via the relation:

$$\mu_t = C_\mu \rho \frac{k^2}{\varepsilon} \tag{A-26}$$

wehre C_μ is the model constant.

The values of k and ε come directly from the differential transport equations for the turbulence kinetic energy and turbulence dissipation rate:

$$\frac{\partial(\rho k)}{\partial t} + \frac{\partial}{\partial x_j}\left(\rho U_j k\right) = \frac{\partial}{\partial x_j}\left[\left(\mu + \frac{\mu_t}{\sigma_k}\right)\frac{\partial k}{\partial x_j}\right] + P_k - \rho\varepsilon + P_{kb} \tag{A-27}$$

$$\frac{\partial(\rho \varepsilon)}{\partial t} + \frac{\partial}{\partial x_j}\left(\rho U_j \varepsilon\right) = \frac{\partial}{\partial x_j}\left[\left(\mu + \frac{\mu_t}{\sigma_\varepsilon}\right)\frac{\partial \varepsilon}{\partial x_j}\right] + \frac{\varepsilon}{k}\left(C_{\varepsilon 1} P_k - C_{\varepsilon 2}\rho\varepsilon + C_{\varepsilon 1} P_{\varepsilon b}\right) \tag{A-28}$$

$C_{\varepsilon 1}$, $C_{\varepsilon 2}$, σ_k and σ_ε are model constants.

P_{kb} and $P_{\varepsilon b}$ represent the influence of the buoyancy forces. P_k is the turbulence production due to viscous forces, which is modeled using:

$$P_k = \mu_t\left(\frac{\partial U_i}{\partial x_j} + \frac{\partial U_j}{\partial x_i}\right)\frac{\partial U_i}{\partial x_j} - \frac{2}{3}\frac{\partial U_k}{\partial x_k}\left(3\mu_t\frac{\partial U_k}{\partial x_k} + \rho k\right) \tag{A-29}$$

For incompressible flow, $\partial U_k/\partial x_k$ is small and the second term on the right side of above equation does not contribute significantly to the production. For compressible flow, $\partial U_k/\partial x_k$ is only large in regions with high velocity divergence, such as at shocks.

A.4.3.4 The RNG k-epsilon Model

The RNG $k-\varepsilon$ model is based on renormalization group analysis of the Navier-Stokes equations. The transport equations for turbulence generation and dissipation are the same as those for the standard $k-\varepsilon$ model, but the model constants differ, and the constant $C_{\varepsilon 1}$ is replaced by the function $C_{\varepsilon 1RNG}$.

The transport equation for turbulence dissipation becomes:

$$\frac{\partial(\rho\varepsilon)}{\partial t}+\frac{\partial}{\partial x_j}\left(\rho U_j\varepsilon\right)=\frac{\partial}{\partial x_j}\left[\left(\mu+\frac{\mu_t}{\sigma_{\varepsilon RNG}}\right)\frac{\partial\varepsilon}{\partial x_j}\right]+\frac{\varepsilon}{k}(C_{\varepsilon 1RNG}P_k-C_{\varepsilon 2RNG}+C_{\varepsilon 1RNG}P_{\varepsilon b}) \tag{A-30}$$

where:

$$C_{\varepsilon 1RNG}=1.42-f_\eta \tag{A-31}$$

and:

$$f_\eta=\frac{\eta\left(1-\frac{\eta}{4.38}\right)}{(1+\beta_{RNG}\eta^3)} \tag{A-32}$$

$$\eta=\sqrt{\frac{P_k}{\rho C_{\mu RNG}\varepsilon}} \tag{A-33}$$

A.4.3.5 The k-omega Model

One of the advantages of the $k-\omega$ formulation is the near wall treatment for low-Reynolds number computations. The model does not involve the complex nonlinear damping functions required for the $k - \varepsilon$ model and is therefore more accurate and more robust. A low Reynolds $k - \varepsilon$ model would typically require a near wall resolution of $y^+ < 0.2$, while a low-Reynolds number $k - \omega$ model would require at least $y^+ < 2$. In industrial flows, even $y^+ < 2$ cannot be guaranteed in most applications and for this reason, a new near wall treatment was developed for the $k - \omega$ models. It allows for smooth shift from a low-Reynolds number form to a wall function formulation.

The $k - \omega$ models assumes that the turbulence viscosity is linked to the turbulence kinetic energy and turbulent frequency via the relation:

$$\mu_t = \rho \frac{k}{\omega} \tag{A-34}$$

The starting point of the present formulation solves two transport equations, one for the turbulent kinetic energy, k, and one for the turbulent frequency, ω. The stress tensor is computed from the eddy-viscosity concept. This is generally called Wilcox k-omega model.

k equation:

$$\frac{\partial(\rho k)}{\partial t} + \frac{\partial}{\partial x_j}\left(\rho U_j k\right) = \frac{\partial}{\partial x_j}\left[\left(\mu + \frac{\mu_t}{\sigma_k}\right)\frac{\partial k}{\partial x_j}\right] + P_k - \beta' \rho k \omega + P_{kb} \tag{A-35}$$

ω equation:

$$\frac{\partial(\rho \omega)}{\partial t} + \frac{\partial}{\partial x_j}\left(\rho U_j \omega\right) = \frac{\partial}{\partial x_j}\left[\left(\mu + \frac{\mu_t}{\sigma_\omega}\right)\frac{\partial \omega}{\partial x_j}\right] + \alpha \frac{\omega}{k} P_k - \beta \rho \omega^2 + P_{\omega b} \tag{A-36}$$

In addition to the independent variables, the density, ρ, and the velocity vector, U, are treated as known quantities from the Navier-Stokes method. P_k is the production rate of turbulence, which is calculated using Eq. (A-29).

The model constants are given by:

$\beta' = 0.09$

$\alpha = 5/9$

$\beta = 0.075$

$\sigma_k = 2$

$\sigma_\omega = 2$

P_{kb} and $P_{\omega b}$represent the influence of the buoyancy forces.

A.4.3.6 The Baseline (BSL) k-Omega Model

The main problem with the Wilcox model is its well-known strong sensitivity to free stream conditions. Depending on the value specified for ω at the inlet, a significant variation in the results of the model can be obtained. This is undesirable and in order to solve the problem, a blending between the $k-\omega$ model near the surface and the $k-\varepsilon$ model in the outer region. It consists of a transformation of the $k-\varepsilon$ model to a $k-\omega$ formulation and a subsequent addition of the corresponding equations. The Wilcox model is thereby multiplied by a blending function F_1 and the transformed $k-\varepsilon$ model by a function $1-F_1$. F_1 is equal to one near the surface and decreases to a value of zero outside the boundary layer (that is, a function of the wall distance).

Wilcox $k-\omega$ model:

$$\frac{\partial(\rho k)}{\partial t} + \frac{\partial}{\partial x_j}\left(\rho U_j k\right) = \frac{\partial}{\partial x_j}\left[\left(\mu + \frac{\mu_t}{\sigma_{k1}}\right)\frac{\partial k}{\partial x_j}\right] + P_k - \beta' \rho k \omega \tag{A-37}$$

$$\frac{\partial(\rho\omega)}{\partial t} + \frac{\partial}{\partial x_j}\left(\rho U_j \omega\right) = \frac{\partial}{\partial x_j}\left[\left(\mu + \frac{\mu_t}{\sigma_{\omega 1}}\right)\frac{\partial \omega}{\partial x_j}\right] + \alpha_1 \frac{\omega}{k} P_k - \beta_1 \rho \omega^2 \tag{A-38}$$

Transformed $k-\varepsilon$ model:s

$$\eta\frac{\partial(\rho k)}{\partial t}+\frac{\partial}{\partial x_j}\left(\rho U_j k\right)=\frac{\partial}{\partial x_j}\left[\left(\mu+\frac{\mu_t}{\sigma_{k2}}\right)\frac{\partial k}{\partial x_j}\right]+P_k-\beta'\rho k\omega \tag{A-39}$$

$$\begin{aligned}\frac{\partial(\rho\omega)}{\partial t}+\frac{\partial}{\partial x_j}\left(\rho U_j\omega\right)\\ =\frac{\partial}{\partial x_j}\left[\left(\mu+\frac{\mu_t}{\sigma_{\omega 2}}\right)\frac{\partial\omega}{\partial x_j}\right]+2\rho\frac{1}{\sigma_{\omega 2}\omega}\frac{\partial k}{\partial x_j}\frac{\partial\omega}{\partial x_j}+\alpha_2\frac{\omega}{k}P_k\\ -\beta_2\rho\omega^2\end{aligned} \tag{A-40}$$

Now the equations of the Wilcox model are multiplied by function F_1, the transformed $k-\varepsilon$ equations by a function 1-F_1 and the corresponding $k-$ and $\omega-$ equations are added to give the BSL model. Including buoyancy effects the BSL model reads:

$$\frac{\partial(\rho k)}{\partial t}+\frac{\partial}{\partial x_j}\left(\rho U_j k\right)=\frac{\partial}{\partial x_j}\left[\left(\mu+\frac{\mu_t}{\sigma_{k3}}\right)\frac{\partial k}{\partial x_j}\right]+P_k-\beta'\rho k\omega+P_{kb} \tag{A-41}$$

$$\begin{aligned}\frac{\partial(\rho\omega)}{\partial t}+\frac{\partial}{\partial x_j}\left(\rho U_j\omega\right)=\frac{\partial}{\partial x_j}\left[\left(\mu+\frac{\mu_t}{\sigma_{\omega 3}}\right)\frac{\partial\omega}{\partial x_j}\right]+(1-F_1)2\rho\frac{1}{\sigma_{\omega 2}\omega}\frac{\partial k}{\partial x_j}\frac{\partial\omega}{\partial x_j}\\ +\alpha_3\frac{\omega}{k}P_k-\beta_3\rho\omega^2+P_{\omega b}\end{aligned} \tag{A-42}$$

The coefficients of the new model are a linear combination of the corresponding coefficients of the underlying models:

$$\phi_3=F_1\phi_1+(1-F_1)\phi_2 \tag{A-43}$$

All coefficients are listed again for completeness:

$\beta'=0.09$

$\alpha_1=5/9$

$\beta_1 = 0.075$

$\sigma_{k_1} = 2$

$\sigma_{\omega_1} = 2$

$\alpha_2 = 0.44$

$\beta_2 = 0.0828$

$\sigma_{k_2} = 1$

$\sigma_{\omega_2} = 1/0.856$

A.4.3.7 The Shear Stress Transport (*SST*)

The $k - \omega$ based SST model accounts for the transport of the turbulent shear stress and gives highly accurate predictions of the onset and the amount of flow separation under adverse pressure gradients.

The BSL model combines the advantages of the Wilcox and the $k - \varepsilon$ model, but still fails to properly predict the onset and amount of flow separation from smooth surfaces. The main reason is that both models do not account for the transport of the turbulent shear stress. This results in an over prediction of the eddy-viscosity. The proper transport behaviour can be obtained by a limiter to the formulation of the eddy-viscosity:

$$v_t = \frac{\alpha_1 k}{\max(\alpha_1 \omega, SF_2)} \tag{A-44}$$

where

$$v_t = \mu_t/\rho \tag{A-45}$$

Again F_2 is a blending function similar to F_1, which restricts the limiter to the wall boundary layer, as the underlying assumptions are not correct for free shear flows. S is an invariant measure of the strain rate.

The blending functions shown above are critical to the success of the method. Their formulation is based on the distance to the nearest surface and on the flow variables.

$$F_1 = tanh(arg_1^4) \tag{A-46}$$

$$arg_1 = min\left[max\left(\frac{\sqrt{k}}{\beta'\omega y}, \frac{500\upsilon}{\omega y^2}\right), \frac{4\rho k}{y^2 CD_{k\omega}\sigma_{\omega_2}}\right] \tag{A-47}$$

where y is the distance to the nearest wall, υ is the kinematic viscosity and:

$$CD_{k\omega} = max\left(2\rho\frac{1}{\sigma_{\omega_2}\omega}\frac{\partial k}{\partial x_j}\frac{\partial \omega}{\partial x_j}, 1.0 \times 10^{-10}\right) \tag{A-48}$$

$$F_2 = tanh(arg_2^2) \tag{A-49}$$

$$arg_2 = max\left(\frac{2\sqrt{k}}{\beta'\omega y}, \frac{500\upsilon}{\omega y^2}\right) \tag{A-50}$$

A.5 Computational efficiency

Configurations of the personal computer workstation used for the numerical studies in this project are detailed as follows.

Processor: Intel® Core™ i7-4770K Processor (8M Cache, up to 3.50 GHz)

Installed memory (RAM): 16.0 GB

Using the above described computational workstation, the comparison of computational time for three different unsteady turbulence modeling approaches, namely Large Eddy Simulation (*LES*), Detached Eddy Simulation (*DES*), and Unsteady Reynolds-Averaged Navier Stokes (*URANS*), is presented in Fig. A-4. This is done for a sample case including a pair of adjacent synthetic jets with a phase difference $\delta\varnothing = 60°$, Reynolds number $Re = 300$, and stroke length $L_0 = 29D$. The solutions using different unsteady approaches are continued for several cycles (i.e. 80 cycles) up to the same flow time (i.e. 1.4 seconds) when the flow is fully converged.

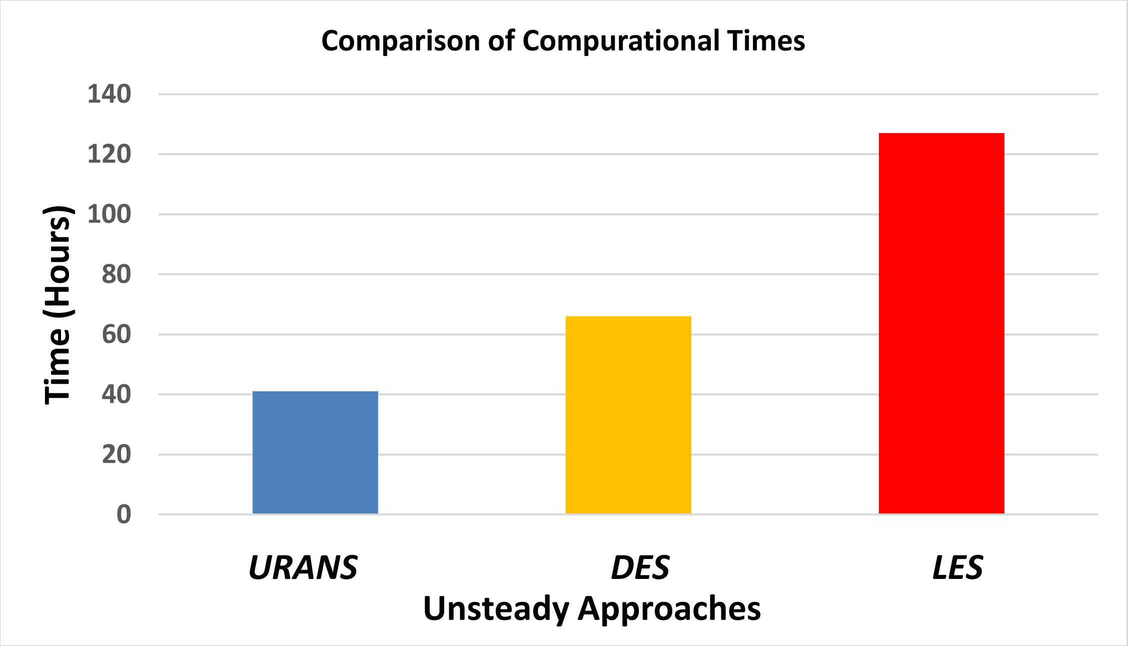

Figure A-4. Comparison of *URANS*, *DES* and *LES* in the simulation of a pair of adjacent synthetic jets with $\delta\varnothing = 60°$, $Re = 300$, and $L_0 = 29D$

Based on Fig. A-4, it is observed that in terms of computational cost, *URANS* resolves the domain at lowest time compared to *DES*, with a moderate computational cost, and *LES*, with high computational costs.

As described earlier, there is a need to establish a reliable numerical methodology to investigate unsteady impinging jets at low computational costs, as a major motivation in this study. Though the employment of the *DES* and *LES* approaches can considerably help to enhance the accuracy of results, these methods are not computationally efficient enough for a typical industrial design and engineering environment. As a compromise between low computational costs and reliably modelling the major flow features in unsteady jets, *URANS* based approaches are employed throughout this study.

A.6 Inner cavity flow field (a pair of adjacent synthetic jets)

Various snapshots of the fluid flow (including the inner cavity flow field) are shown for a pair of adjacent synthetic jets with and without a phase difference in figures below. For jets with no phase difference, $\delta\emptyset = 0°$, presented in Fig, A-5, and for out of phase jets with $\delta\emptyset = 60°$ and $\delta\emptyset = 130°$, the results are shown in Figs. A-6 and A-7, respectively.

Figure A-5 displays that two in-phase adjacent vortex pairs exit plane of the orifice slot and start to roll down into the air. The remnants of the vortices form the last blowing stroke are noticeable downstream. The cores of the pair of counter-rotating vortices stretch in the direction of the flow.

For $\delta\emptyset = 60°$, as shown in Fig. A-6, the merged jet is vectored toward the right with a nominal angle of $\alpha_N = 17°$ based on the *PIV* results. In comparison, for the numerical results, the asymmetric streamlines of the merged jet show an approximate vectoring angle of 19°.

For $\delta\emptyset = 130°$, according to the result in Fig. A-7, the merged jet is fully vectored toward the right with an approximate nominal angle of $\alpha_N = 90°$, almost parallel to the confinement plate.

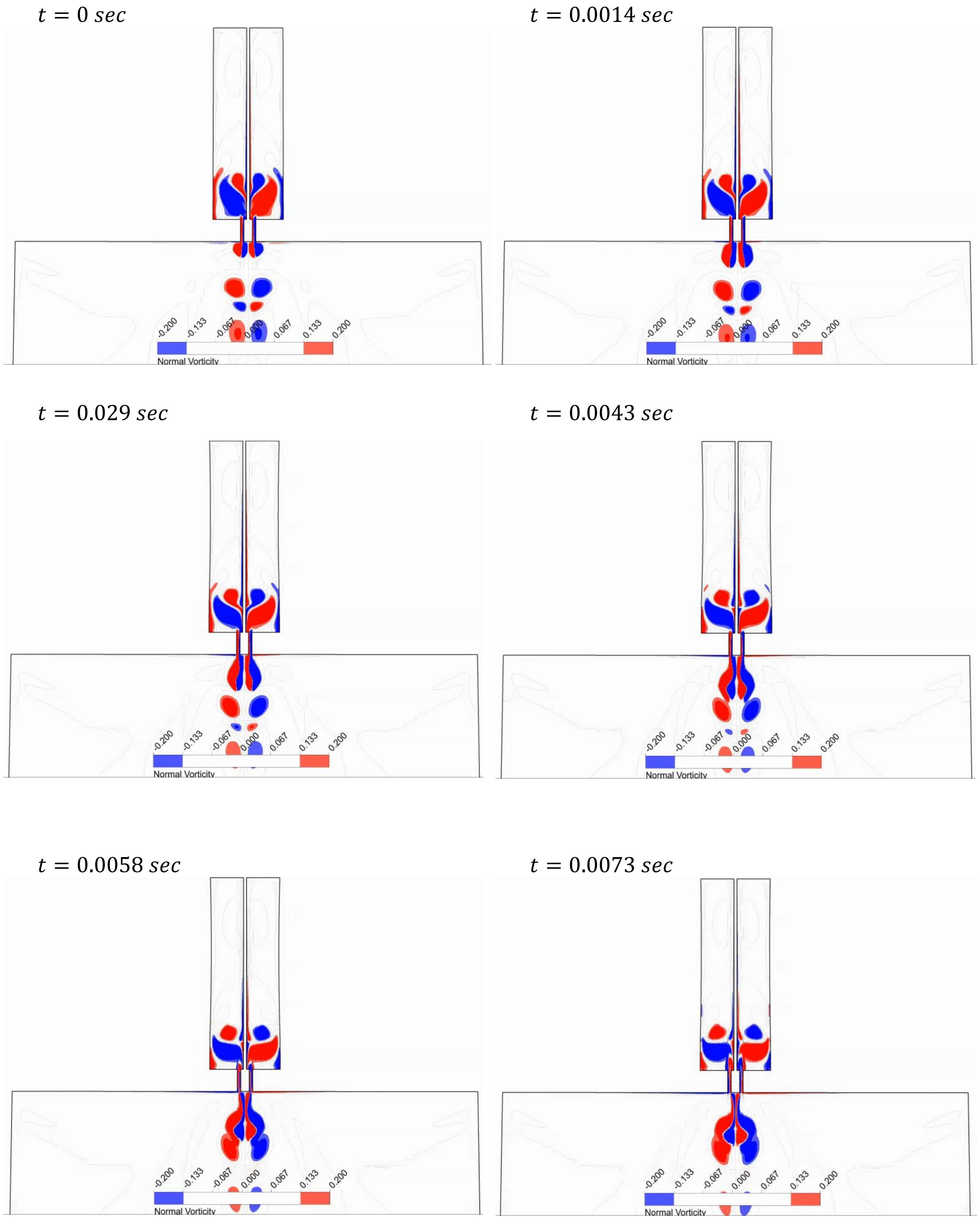

$t = 0\ sec$

$t = 0.0014\ sec$

$t = 0.029\ sec$

$t = 0.0043\ sec$

$t = 0.0058\ sec$

$t = 0.0073\ sec$

Figure A-5. (a) Instantaneous vorticity snapshots of the flow induced by a pair of adjacent synthetic jets with $\delta\emptyset = 0°$, $Re = 300$, and $L_0 = 29D$ ($f = 57$ Hz)

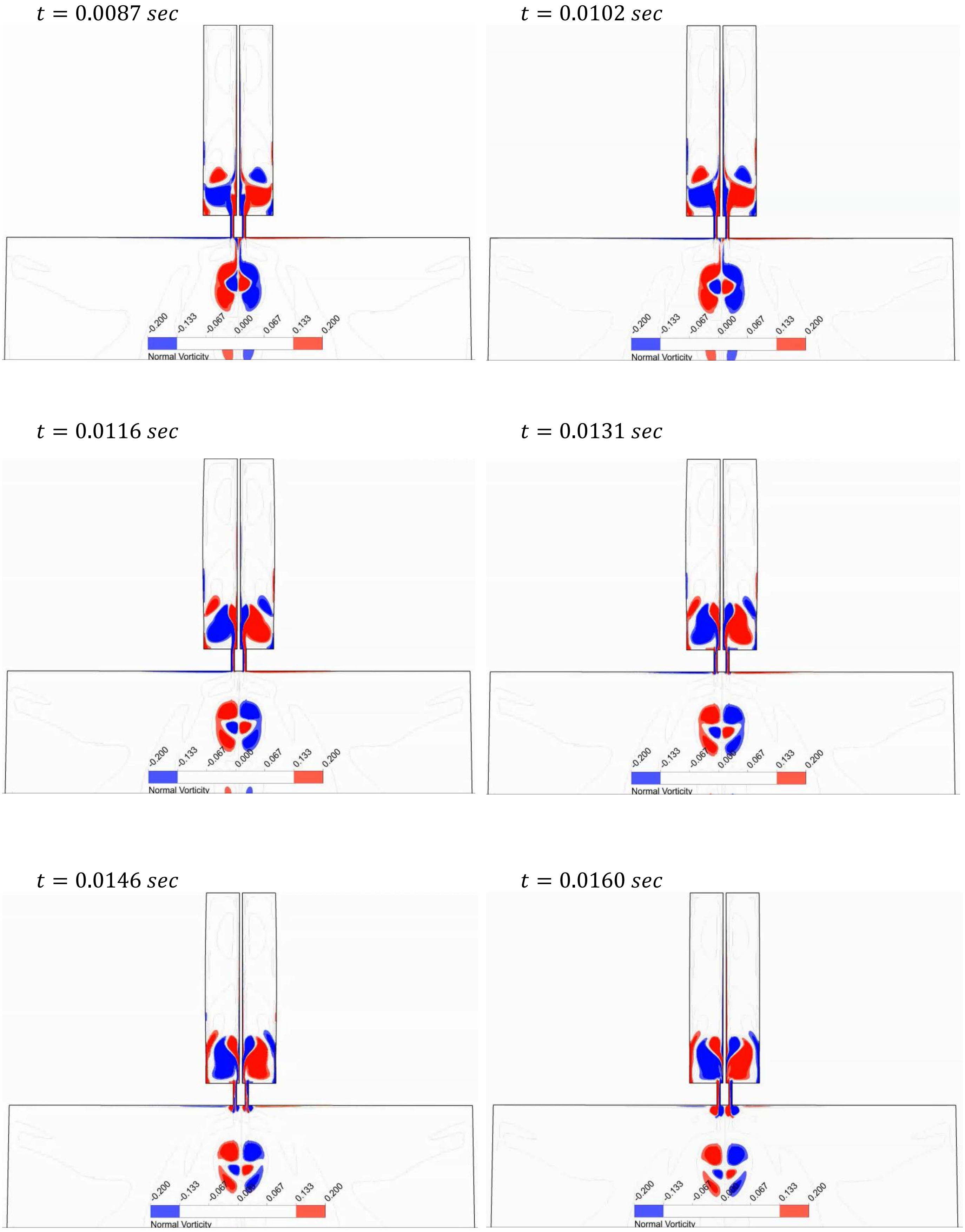

$t = 0.0087\ sec$ $t = 0.0102\ sec$

$t = 0.0116\ sec$ $t = 0.0131\ sec$

$t = 0.0146\ sec$ $t = 0.0160\ sec$

Figure A-5. (b)

$t = 0\ sec$ $t = 0.0014\ sec$

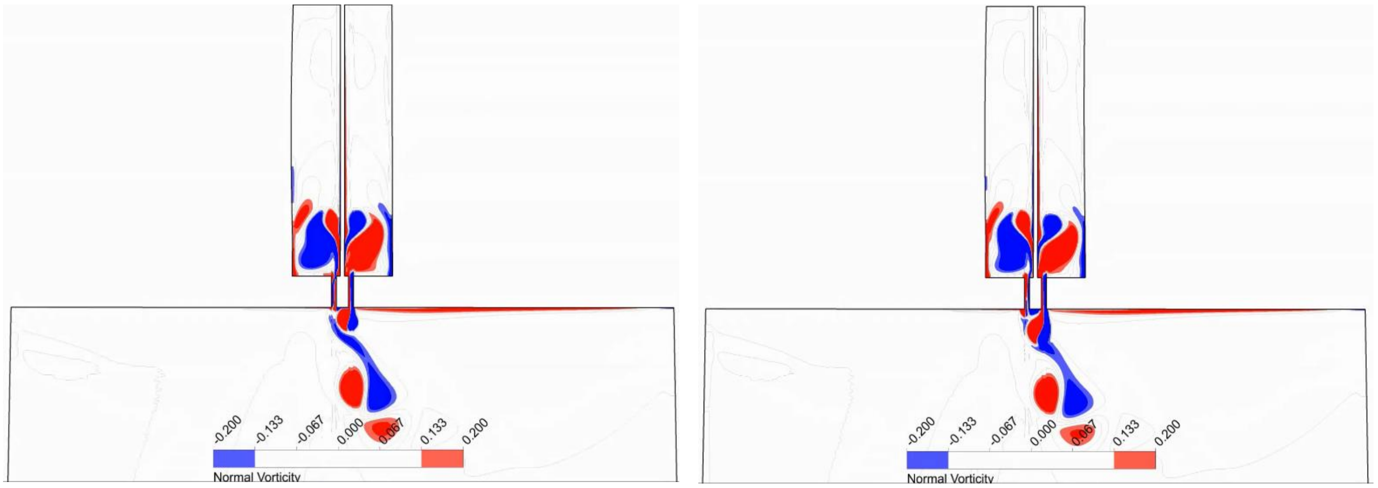

$t = 0.029\ sec$ $t = 0.0043\ sec$

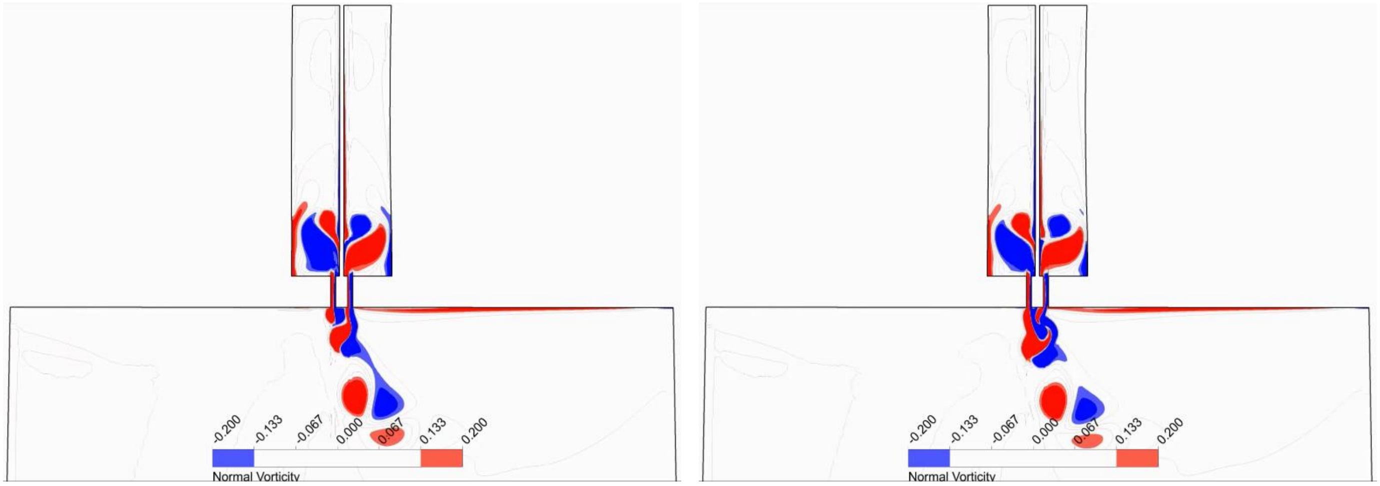

$t = 0.0058\ sec$ $t = 0.0073\ sec$

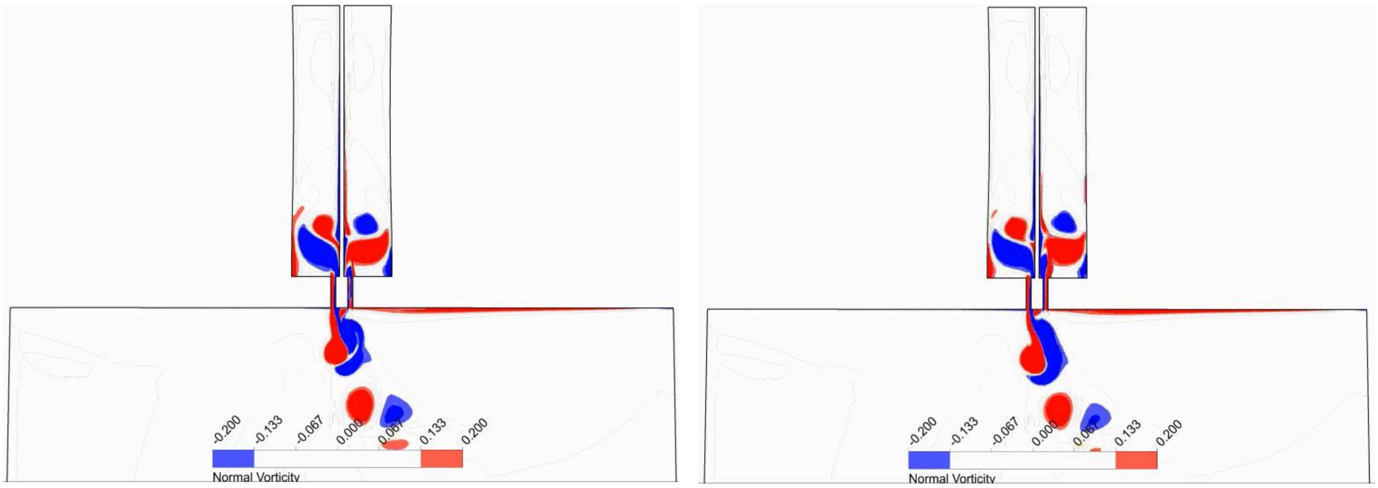

Figure A-6. (a) Instantaneous vorticity snapshots of the flow induced by a pair of adjacent synthetic jets with $\delta\emptyset = 60°$, *Re* = 300, and $L_0 = 29D$ (f = 57 Hz)

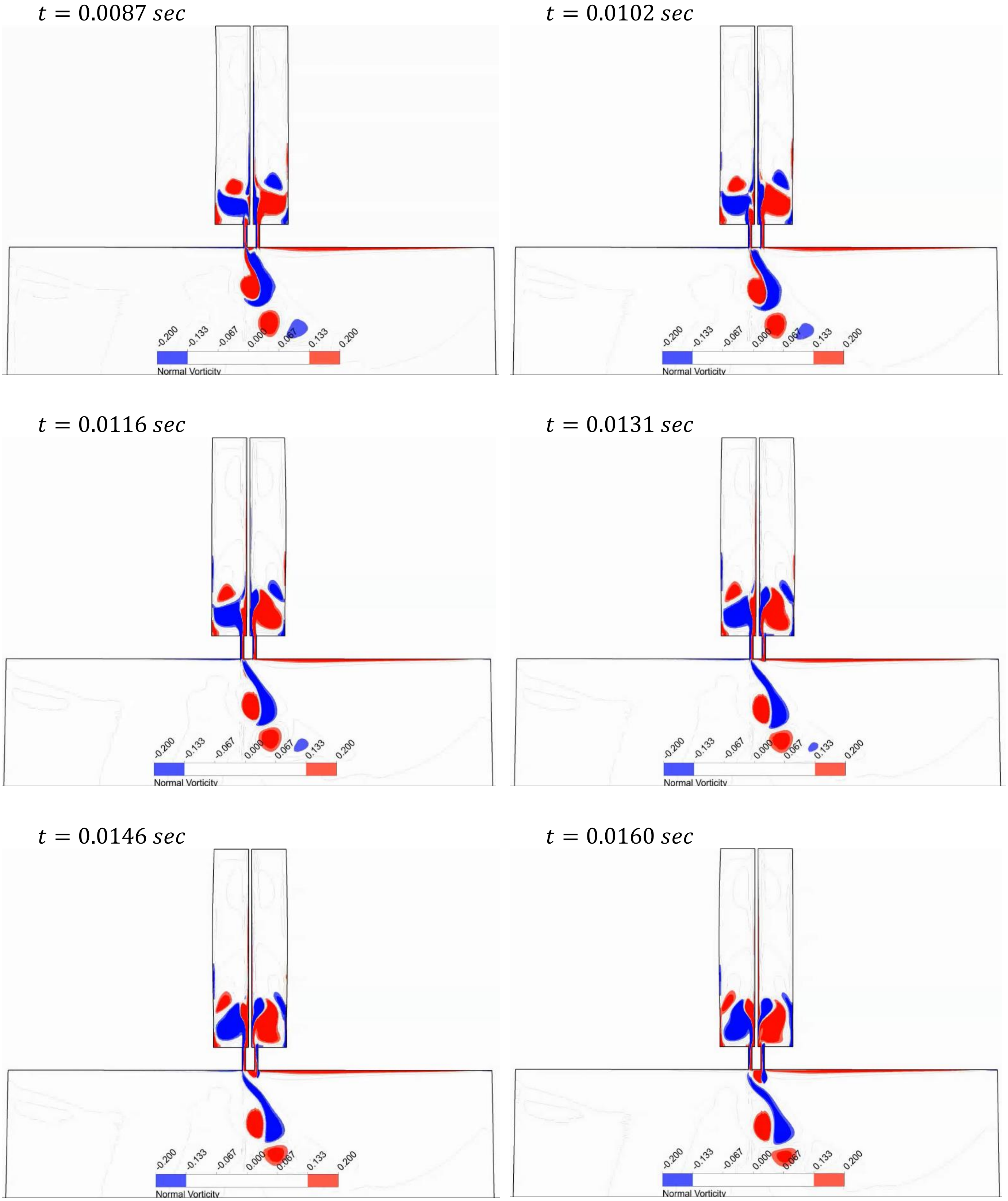

$t = 0.0087\ sec$ $t = 0.0102\ sec$

$t = 0.0116\ sec$ $t = 0.0131\ sec$

$t = 0.0146\ sec$ $t = 0.0160\ sec$

Figure A-6. (b)

$t = 0\ sec$ $t = 0.0014\ sec$

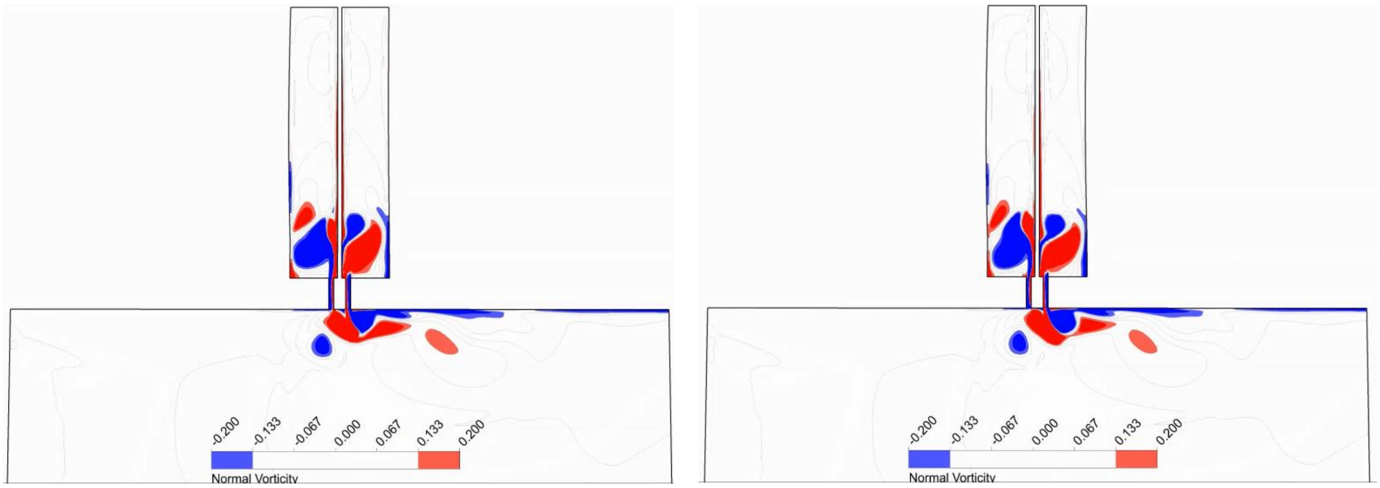

$t = 0.029\ sec$ $t = 0.0043\ sec$

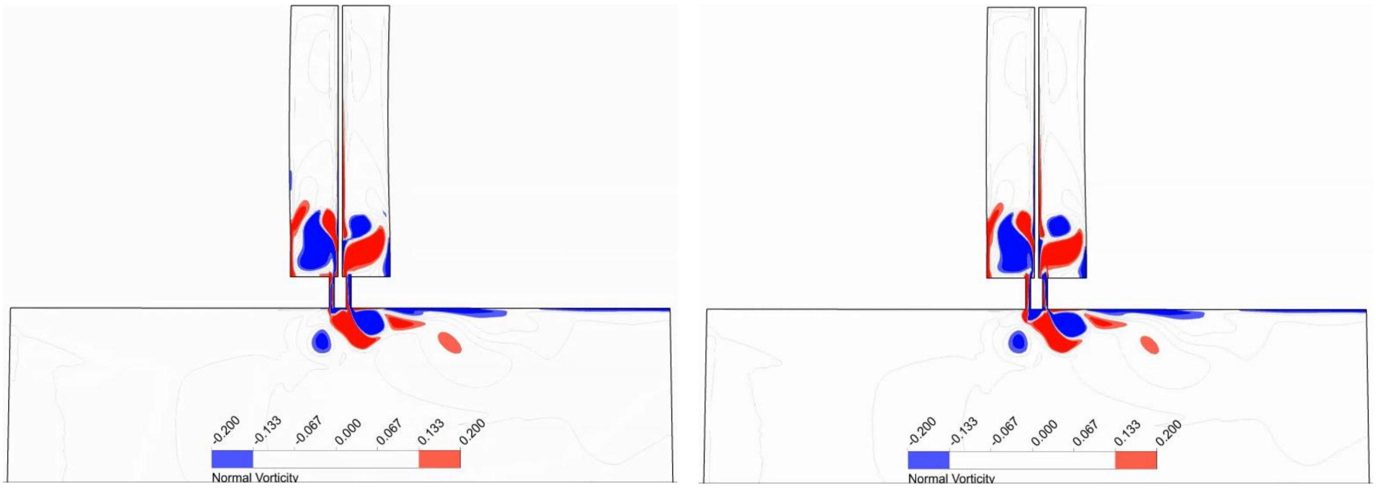

$t = 0.0058\ sec$ $t = 0.0073\ sec$

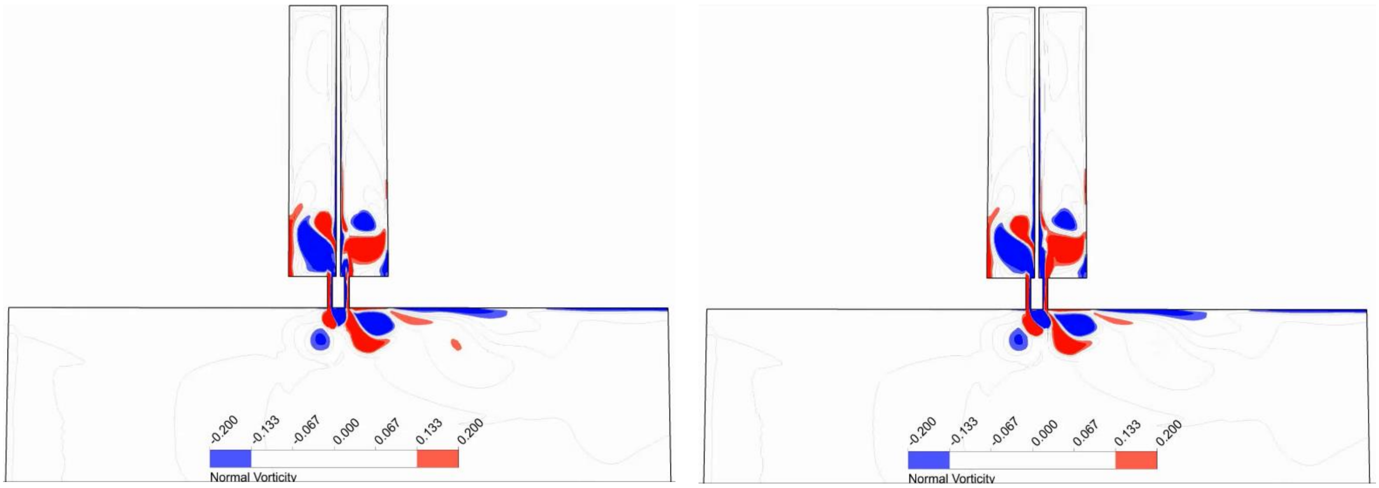

Figure A-7. (a) Instantaneous vorticity snapshots of the flow induced by a pair of adjacent synthetic jets with $\delta\emptyset = 130°$, *Re* = 300, and $L_0 = 29D$ ($f = 57$ Hz)

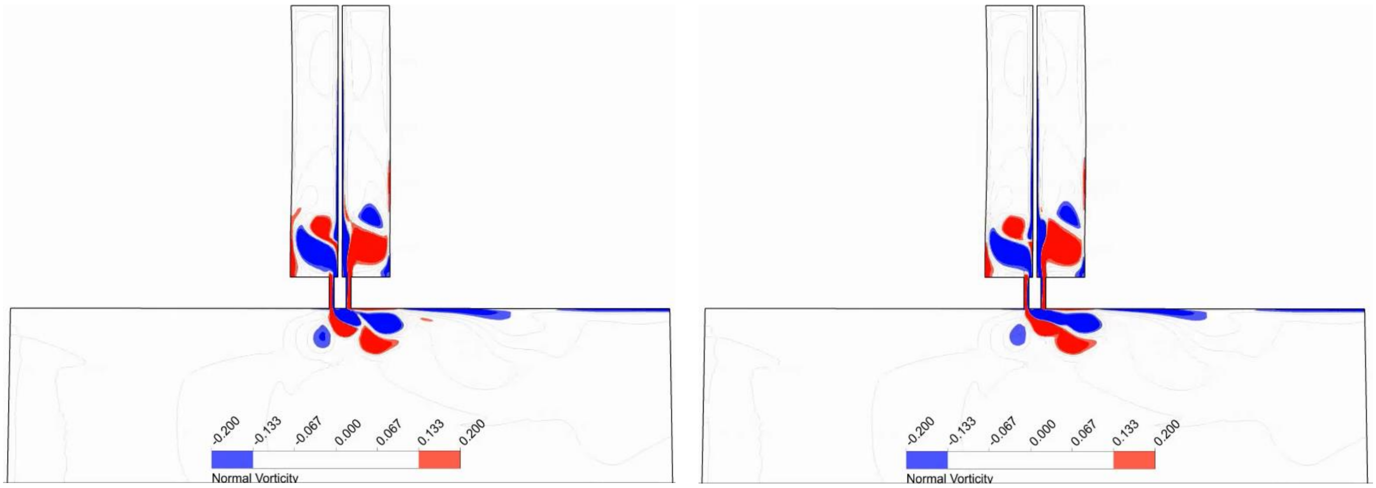
$t = 0.0087\ sec$ $t = 0.0102\ sec$

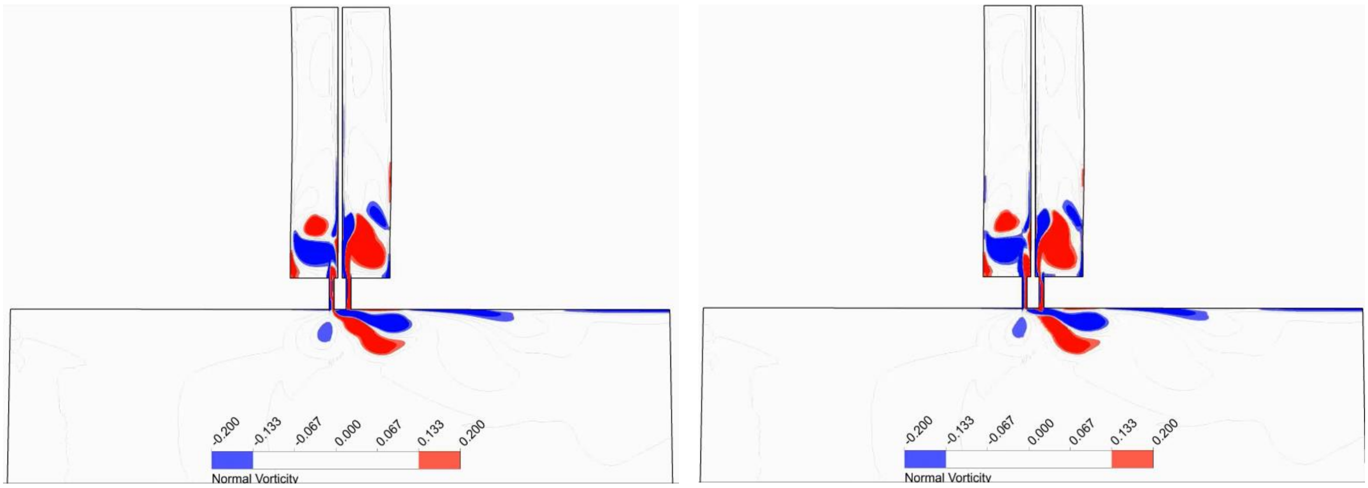
$t = 0.0116\ sec$ $t = 0.0131\ sec$

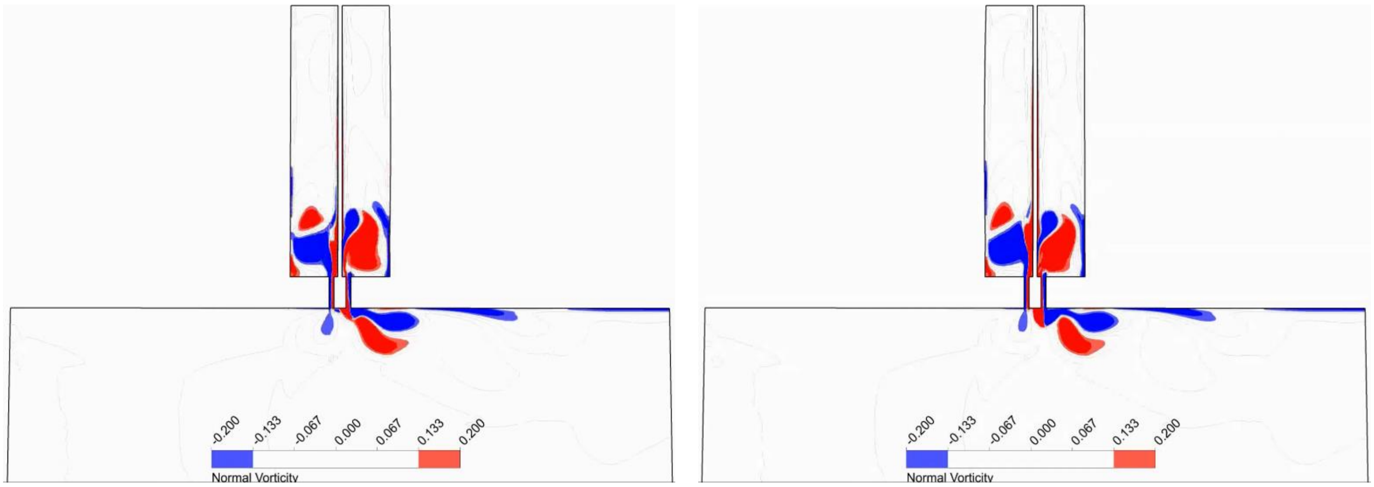
$t = 0.0146\ sec$ $t = 0.0160\ sec$

Figure A-7. (b)